Tampere University

SURAJ PANICKER

Knowledge-based Modelling of Additive Manufacturing for Sustainability Performance Analysis and Decision Making

Tampere University Dissertations 745

Tampere University Dissertations 745

SURAJ PANICKER

Knowledge-based Modelling of Additive Manufacturing for Sustainability Performance Analysis and Decision Making

ACADEMIC DISSERTATION
To be presented, with the permission of
the Faculty of Engineering and Natural Sciences
of Tampere University,
for public discussion in the auditorium K1702
of the Konetalo building, Korkeakoulunkatu 6, Tampere,
on 10th of February 2023, at 14 o'clock.

ACADEMIC DISSERTATION
Tampere University, Faculty of Engineering and Natural Sciences,
Finland

Responsible supervisor and Custos	Professor Eric Coatanéa Tampere University Finland	
Supervisor	Associate Professor Karl R. Haapala Oregon State University USA	
Pre-examiners	Associate Professor Yaoyao Zhao McGill University Canada	Assistant Professor Guha Manogharan Penn State University USA
Opponents	Engineering Specialist Ric Roca Aerospace Corporation USA	Assistant Professor Guha Manogharan Penn State University USA

The originality of this thesis has been checked using the Turnitin Originality Check service.

Cover design: Roihu Inc.

ISBN 978-952-03-2756-9 (print)
ISBN 978-952-03-2757-6 (pdf)
ISSN 2489-9860 (print)
ISSN 2490-0028 (pdf)
http://urn.fi/URN:ISBN:978-952-03-2757-6

PunaMusta Oy – Yliopistopaino
Joensuu 2023

To my parents.

ACKNOWLEDGEMENTS

The dissertation is part of a larger research effort that was carried out over a period of four years (March 2018 to June 2022) at Tampere University, Finland. During this period there were many changes that happened globally in our society. These changes (positive and negative) had a profound impact on my personal and professional life. I take this opportunity to acknowledge all the people who have been part of this journey.

First and foremost, I would like to express my sincere gratitude to my supervisors, Professor Eric Coatanéa and Associate Professor Karl R. Haapala for their support, guidance, and inputs. Their mentoring has been instrumental in providing direction to the work. I am much obliged to the examiners of the dissertation, Associate Professor Yaoyao Zhao, Associate Professor Guha Manogharan and Dr. Ric Roca for accepting the invitation to be part of the committee and their valuable feedback, critique, and guidance. I am grateful for the help and support provided by the administrative and technical support staff at the university. A shout out to Anna Nykänen, Merja Ritola, Jaakko Kotiranta, Jorma Vihinen, and Antti Heikkilä for their help with the research, study, and training aspects. I am grateful to Tampere University Foundation and Business Finland for providing the financial backing for the research projects.

I would like to dedicate this work to my family, their help and support has been a constant guiding force. My parents, P.G. Balakrishna Panicker and M. G. Komalakumariamma for being constant pillars of support. Aditya Panicker for always being there for me. I love you brother, and you have/will always be the person I look up to. My sister-in-law (Ammu Sreekumar) and my lovely niece (Natasha Panicker) for their support and encouragement. Finally, my deepest gratitude to all my friends and colleagues including Hari P.N. Nagarajan, Saigopal Vasudevan, Ahalya Ganesh, Hossein Mokhtarian, Jari Tuominen, Madan Patnamsetty, Tiina Salmi, Mika Lyly, Dmitry Sotnikov, Inigo Flores, Joonas Coatanéa, Antoine Queguineur, Shahriar Bakrani, and Olli Wiikinkoski for making this a memorable experience.

ABSTRACT

Additive manufacturing (AM) has been considered viable for complex geometries, topology optimized parts, and parts that are otherwise difficult to produce using conventional manufacturing processes. Despite the advantages, one of the prevalent challenges in AM has been the poor capability of producing functional parts at production volumes that are competitive with traditional manufacturing. Modelling and simulation are powerful tools that can help shorten the design-build-test cycle by enabling rapid analysis of various product designs and process scenarios. Nevertheless, the capabilities and limitations of traditional and advanced manufacturing technologies do define the bounds for new product development. Thus, it is important that the designers have access to methods and tools that enable them to model and simulate product performance and associated manufacturing process performance to realize functional high value products. The motivation for this dissertation research stems from ongoing development of a novel high temperature superconducting (HTS) magnet assembly, which operates in cryogenic environment. Its complexity requires the convergence of multidisciplinary expertise during design and prototyping. The research applies knowledge-based modelling to aid manufacturing process analysis and decision making in the design of mechanical components of the HTS magnet. Further, it explores the feasibility of using AM in the production of the HTS magnet assembly. The developed approach uses product-process integrated modelling based on physical experiments to generate quantitative and qualitative information that define process-structure-property-performance interactions for given material-process combinations. The resulting interactions are then integrated into a graph-based model that can aid in design space exploration to assist early design and manufacturing decision-making. To do so, test components are fabricated using two metal AM processes: wire and arc additive manufacturing and selective laser melting. Metal alloys (stainless steel, mild steel, high-strength low-alloyed steel, aluminium, and copper alloys) commonly used in structural applications are tested for their mechanical-, thermal-, and electrical properties. In addition, microstructural characterization of the alloys is performed to further understand the impact of manufacturing process parameters on material properties. The integrated modelling approach combines the collected experimental data,

existing analytical and empirical relationships, and other data-driven models (e.g., finite element models, machine learning models) in the form of a decision support system that enables optimal selection of material, manufacturing technology, process parameters, and other control variables for attaining desired structure, property, and performance characteristics of the final printed component. The manufacturing decision making is performed through implementation of a probabilistic model i.e., a Bayesian network model, which is robust, modular, and can be adapted for other manufacturing systems and product designs. The ability of the model to improve throughput and quality of additive manufacturing processes will boost sustainable manufacturing goals.

TIIVISTELMÄ

Additiivista valmistusta on pidetty käyttökelpoisena monimutkaisissa geometrioissa, topologisesti optimoiduissa kappaleissa ja kappaleissa joita on muuten vaikea valmistaa perinteisillä valmistusprosesseilla. Eduista huolimatta, yksi additiivisen valmistuksen vallitsevista haasteista on ollut heikko kyky tuottaa toimivia osia kilpailukykyisillä tuotantomäärillä perinteisen valmistuksen kanssa. Mallintaminen ja simulointi ovat tehokkaita työkaluja, jotka voivat auttaa lyhentämään suunnittelun, rakentamisen ja testauksen sykliä mahdollistamalla erilaisten tuotesuunnitelmien ja prosessiskenaarioiden nopean analyysin. Perinteisten ja edistyneiden valmistusteknologioiden mahdollisuudet ja rajoitukset määrittelevät kuitenkin rajat uusille tuotekehityksille. Siksi on tärkeää, että suunnittelijoilla on käytettävissään menetelmät ja työkalut, joiden avulla he voivat mallintaa ja simuloida tuotteen suorituskykyä ja siihen liittyvän valmistusprosessin suorituskykyä, toimivien korkea arvoisten tuotteiden toteuttamiseksi. Motivaation tämän väitöstutkimuksen tekemiselle on, meneillään oleva kehitystyö uudenlaisen korkean lämpötilan suprajohtavan (high temperature superconducting (HTS)) magneettikokoonpanon kehittämisessä, joka toimii kryogeenisissä lämpötiloissa. Sen monimutkaisuus edellyttää monitieteisen asiantuntemuksen lähentymistä suunnittelun ja prototyyppien valmistuksen aikana. Tutkimus hyödyntää tietopohjaista mallinnusta valmistusprosessin analysoinnin ja päätöksenteon apuna HTS-magneettien mekaanisten komponenttien suunnittelussa. Tämän lisäksi, tutkimus etsii mahdollisuuksia additiivisen valmistuksen toteutettavuuteen HTS-magneettikokoonpanon tuotannossa. Kehitetty lähestymistapa käyttää fysikaalisiin kokeisiin perustuvaa tuote-prosessi-integroitua mallinnusta tuottamaan kvantitatiivista ja laadullista tietoa, joka määrittelee prosessi-rakenne-ominaisuus-suorituskyky-vuorovaikutuksia tietyille materiaali-prosessi-yhdistelmille. Tuloksina saadut vuorovaikutukset integroidaan kaaviopohjaiseen malliin, joka voi auttaa suunnittelutilan tutkimisessa ja täten auttaa varhaisessa suunnittelu- ja valmistuspäätöksenteossa. Tätä varten testikomponentit valmistetaan käyttämällä kahta metallin additiivista valmistus prosessia: lankakaarihitsaus additiivista

valmistusta (wire arc additive manufacturing) ja selektiivistä lasersulatusta (selective laser melting). Rakenteellisissa sovelluksissa yleisesti käytetyistä metalliseoksista (ruostumaton teräs, pehmeä teräs, luja niukkaseosteinen teräs, alumiini ja kupariseokset) testataan niiden mekaaniset, lämpö- ja sähköiset ominaisuudet. Lisäksi tehdään metalliseosten mikrorakenteen karakterisointi, jotta voidaan ymmärtää paremmin valmistusprosessin parametrien vaikutusta materiaalin ominaisuuksiin. Integroitu mallinnustapa yhdistää kerätyn kokeellisen tiedon, olemassa olevat analyyttiset ja empiiriset vuorovaikutus suhteet, sekä muut tietopohjaiset mallit (esim. elementtimallit, koneoppimismallit) päätöksenteon tukijärjestelmän muodossa, joka mahdollistaa optimaalisen materiaalin, valmistustekniikan, prosessiparametrien ja muitten ohjausmuuttujien valinnan, lopullisen 3d-tulosteun komponentin halutun rakenteen, ominaisuuksien ja suorituskyvyn saavuttamiseksi. Valmistuspäätöksenteko tapahtuu todennäköisyysmallin, eli Bayesin verkkomallin toteuttamisen kautta, joka on vankka, modulaarinen ja sovellettavissa muihin valmistusjärjestelmiin ja tuotesuunnitelmiin. Väitöstyössä esitetyn mallin kyky parantaa additiivisien valmistusprosessien suorituskykyä ja laatua, täten edistää kestävän tuotannon tavoitteita.

CONTENTS

List of Figures

List of Tables

ABBREVIATIONS

ABS	Acrylonitrile butadiene styrene
AC	Alternating current
AHP	Analytic hierarchy process
AM	Additive manufacturing
BN	Bayesian network
CERN	European organization for nuclear research
CPU	Central processing unit
CT	Cryogenic treatment
DAH	Direct age hardening
DC	Direct current
DCT	Deep cryogenic treatment
DED	Directed energy deposition
DGCM	Directed graphical causal models
DIMT	Deformation induced martensite transformation
DSS	Decision support system
FEM	Finite element modelling
GMAW	Gas metal arc welding
HIP	Hot isostatic pressing
HTS	High temperature superconductor
IC	Integrated circuits
ITER	International thermonuclear experimental reactor
LHC	Large hadron collider
LPBF	Laser powder bed fusion
LTS	Low temperature superconductor
MAG	Metal active gas
MIG	Metal inert gas
MRI	Magnetic resonance imaging
MWnF	Metal working nanofluid
NMR	Nuclear magnetic resonance
OEM	Original equipment manufacturer

PIM	Processing in memory
PLA	Polylactic acid
RRR	Residual resistance ratio
SC	Superconductivity
SEM	Scanning electron microscope
SLM	Selective laser melting
SMES	Superconducting magnet energy storage
TIG	Tungsten inert gas
TRIP	Transformation induced plasticity characteristics
TRL	Technology readiness level
UTS	Ultimate tensile strength
YS	Yield strength

LIST OF ORIGINAL PUBLICATIONS

Publication I Investigation of thermal influence on weld microstructure and mechanical properties in wire and arc additive manufacturing of steels

S. Panicker, H.P.N. Nagarajan, J. Tuominen, M. Patnamsetty, E. Coatanéa and K.R. Haapala. Material Science and Engineering A, https://doi.org/10.1016/j.msea.2022.143690

Publication II Graph-based metamodelling for characterizing cold metal transfer process performance

H.P.N. Nagarajan, **S. Panicker**, H. Mokhtarian, T Remy-Lorit, E. Coatanéa, R. Prod'hon, H. Jafarian, K.R. Haapala and A. Chakraborti. ASTM Smart and Sustainable Manufacturing, https://doi.org/10.1520/SSMS20190026

Publication III Systematic manufacturability evaluation using dimensionless metrics and singular value decomposition: a case study for additive manufacturing

E. Coatanéa, H.P.N. Nagarajan, **S. Panicker**, R. Prod'hon, H. Mokhtarian, A. Chakraborti, H. Paris, I.F. Ituarte and K.R. Haapala. IJAMT, https://doi.org/10.1007/s00170-020-06158-0

Publication IV Probabilistic modelling of defects in additive manufacturing: a case study in powder bed fusion technology

H. Mokhtarian, A. Hamedi, H.P.N. Nagarajan, **S. Panicker**, E. Coatanéa, and K.R. Haapala. Procedia CIRP, https://doi.org/10.1016/j.procir.2019.03.234

Publication V Tracing the interrelationship between key performance indicators and production cost using Bayesian networks

S. Panicker, H.P.N. Nagarajan, H. Mokhtarian, A. Hamedi, A. Chakraborti, E. Coatanéa, K.R. Haapala and K.T. Koskinen. Procedia CIRP, https://doi.org/10.1016/j.procir.2019.03.136

Publication VI A dimension reduction method for efficient optimization of manufacturing performance

A. Chakraborti, H.P.N. Nagarajan, **S. Panicker**, H. Mokhtarian, A. Hamedi, E. Coatanéa, and K.T. Koskinen. Procedia Manufacturing, https://doi.org/10.1016/j.promfg.2020.01.070

Publication VII Optimization-driven design to explore and exploit the process-structure-property-performance linkages in digital manufacturing

I. Flores Ituarte, **S. Panicker**, H.P.N. Nagarajan, E. Coatanéa, and D. W. Rosen. Unpublished Manuscript

AUTHOR'S CONTRIBUTIONS

The dissertation is based on compilation of journal and conference publications. The author's contribution to each of the publications is presented here:

Publication I: The author was main contributor to the journal article. The planning of the research, experimental work, and data collection was performed by the author. The manuscript was written and revised by the author. Hari P.N. Nagarajan collaborated in performing the experiments, writing, and review process. Jari T. and Madan P. helped with data collection and analysis. All the co-authors helped revise the manuscript.

Publication II: The author was part of the research planning and execution. Hari P.N. Nagarajan lead the experiments, writing, and review process. The author developed the Bayesian network model as part of the graph-based modelling approach proposed in the work. The author also contributed towards writing of the manuscript. All the co-authors helped revise the manuscript.

Publication III: The contribution of the author to this work was limited. The author was involved in developing the case study and selection of the design cases that formed the case study. In addition, the author helped with validation of data and the models. The author wrote the background section and helped to revise the manuscript. All the co-authors helped revise the manuscript.

Publication IV: The author assisted in development of the research plan and case study. The author was responsible for development of the probabilistic model for defects characterization. The author helped in writing and revision of the manuscript. All the co-authors helped revise the manuscript. Lastly, the author presented this research work at the CIRP CMS conference.

Publication V: The author was the main contributor for this conference publication. The planning of the research, development of case study, and writing was done by the author. Hari P.N. Nagarajan and Hossein M. helped develop the case study and simulation models. The development of the modelling approach and analysis of results was done by the author. The author presented this research work at the CIRP CMS conference. All the co-authors helped revise the manuscript.

Publication VI: The author was part of planning of the research and development of case study. The development of the graph-based model used in the paper was done by Hossein M., and the author. Ananda C. was the main contributor who developed the optimization case study, wrote, revised, and presented the work at FAIM conference. All the co-authors helped revise the manuscript.

Publication VII: The author contributed to the methodology developed in this journal publication. The author integrated the different surrogate models presented in the work to develop and simulate the Bayesian network. The BN model is crucial in representation of the process-material-property linkages and helps perform design space exploration at embodiment design phase of product development. The author contributed towards writing and reviewing of the manuscript. All the co-authors helped revise the manuscript.

1 INTRODUCTION

Complex engineering designs in industry sectors such as aerospace, defence, and energy often require special materials, tools, processes, and process adjustments to meet product specification during manufacturing. In addition, mission critical components often operate in extreme work environments, and replicating the work environment for carrying out testing is often resource intensive and not feasible. A workaround for replicating the working environment is the ability to develop models and simulations that mirror the real-world working environments. Modelling and simulation are powerful tools that can help shorten the design-build-test cycle in new product development. Nevertheless, the capabilities and limitations of existing manufacturing technologies do often define the bounds for development of a new product. Along with the limitations of the manufacturing technology, another important factor is the availability of technical expertise to be able to realize functional high value products. A successful roll out of a product is dependent upon the decisions made during the early design stage. It is essential that an immersive early design phase exploration is carried out by a multi-disciplinary design team to ensure informed decision making. Inputs from end users, manufacturing engineers, the sales and marketing team (for commercial products) and other stakeholders helps designers to improve the product design. Thus, it is important that the designers have access to methods and tools that enable them to model and simulate their product performance and associated manufacturing process performance.

The motivation for this research comes from one such complex engineering project for design, development, and prototyping of high temperature superconducting (HTS) magnet components using conventional and additive manufacturing (AM) processes. HTS magnet technology involves complex multi-scale, multi-physics phenomena, which has limited their availability and commercial relevance due to technology development and prototyping challenges. Challenges exist in the production of HTS magnet technology, preventing wide-scale adoption of the technology despite proven advantages (Lvovsky et al., 2013). Some of the

challenges include high geometric tolerancing standards, manufacturing process variability resulting in poor quality HTS conductor tapes, high sensitivity, and inability to maintain stable operating conditions and environment. Be that as it may, the potential for use of HTS technology in these four key applications namely, portable systems for bulk superconductivity, high field magnet systems for portable medical devices, ultra-light superconducting rotating machines for next-generation transport and power applications, and magnetic shielding applications for electric machines, equipment and other high-field devices is promising (Durrell et al., 2018). It is to be noted that HTS technology operates in cryogenic temperatures above 77K.

Stautner et al. (2017) in their publication highlighted the potential benefits the use of additive manufacturing technology can bring to component designs for cryogenic applications. AM has been considered viable for complex geometries, topology optimized parts, and parts that are otherwise difficult to produce using conventional manufacturing processes. Despite the advantages, one of the prevalent challenges in AM has been the poor capability of producing functional parts at production volumes that are competitive with traditional manufacturing (Colosimo et al., 2018). These challenges are being addressed through collaborative research and development activities performed by research institutes and industry.

The parts made using AM processes must meet the design requirements and safety considerations. Along with being able to meet the physical properties (mechanical, thermal, and electrical), the AM processes must ensure desired surface finish, geometrical tolerances, repeatability within the batch, across batches, and across building platforms. Hence, for adoption of AM technologies for production of components used in cryogenic applications (such as HTS technology), it is important for the components to meet mechanical, electrical, and thermal property standards in cryogenic and room temperature environments. During the early design phase of a component for cryogenic application, having simulation models representing the relationships between materials, processes, and properties across operational range (working temperature range) will aid in design and manufacturing decision support. As part of this work, the focus is on combining design and manufacturing considerations to explore the possibility of using AM for enhancing the technical performance of the superconducting magnet assembly (mechanical components). Since the mechanical components of the HTS magnet will be operational in cryogenic environments (11K-90K), a detailed exploration of material characteristics of metal additive parts in these environments is warranted.

Developing simulation models to represent the process-structure-property and performance of components produced using AM process is crucial in improving the efficiency of the product development cycle.

1.1 Overarching research goal

The dissertation aims to develop knowledge integrated metamodels that can assimilate process-structure-property and performance relationships prevalent in additive manufacturing processes to analyse the impact of design and manufacturing decisions on the performance of the manufactured products.

For a given material-process combination, the research utilizes a novel hybrid modelling methodology that relies on physical experiments to generate quantitative and qualitative information that defines process-structure-property-performance interactions. The resulting interactions are then developed into a graph-based model that can aid in design space exploration to assist early design stage and manufacturing decision-making support. The graph-based model can help in selection of the material, manufacturing technology, process parameters, and other control variables that will result in attaining desired structure, property, and performance characteristics for the manufactured component.

1.2 Research Questions

The dissertation is an effort towards answering the following research questions:

1. What process-structure-property and performance relationships are crucial for modelling and simulation of additive manufacturing processes?
2. How can different forms of knowledge be integrated through metamodelling for additive manufacturing processes?
3. How can metamodel-based simulation aid in design space exploration, process parameter optimization, product quality enhancement, and material property tailoring?

1.3 Research Tasks

For finding the answers to the posed research questions, the following research tasks were executed:

1. An in-depth study of existing literature in the relevant domains.
2. Identification of specific additive manufacturing cases that can be studied within the scope of the work.
3. Establishing a suitable experimental research plan for data collection and analysis.
4. Conducting the experiments and classifying the information gathered.
5. Based on the collected data, exploring the different modelling and simulation methods.

1.4 Summary

The different research tasks were executed at various stages of the research project and the results were published in a series of conference and journal publications. These publications are attached towards the end of the dissertation. The rest of the dissertation document is distributed over four chapters.

Chapter 2 forms the background study that provides the reader with the state of the art in multiple domains of engineering needed for comprehending this work. Chapter 3 contains the description of the modelling approaches developed in the dissertation. In this chapter, the readers will learn about the intricacies of model development and their applications. Chapter 4 reports the results and discussion. Insights related to specific case studies, challenges encountered during the execution of the research tasks, and contributions of the work are provided. Lastly, Chapter 5 will highlight and reiterate the findings of the dissertation and present the conclusions and future directions for the research.

The research done in this work is reported in a compilation of scientific publications. The publications are part of the dissertation and are provided as appendices towards the end of the book. Figure 1 represents how each publication is linked with the research questions.

	Publication I	Publication II	Publication III	Publication IV	Publication V	Publication VI	Publication VII
Research Question I	X	X					X
Research Question II			X	X	X	X	X
Research Question III		X	X	X	X	X	X

Figure 1: Mapping of the research questions and associated publications

2 BACKGROUND

State of the art in the fields of cryogenics, superconducting magnet technology, additive manufacturing, and modelling and simulation, are integral to the work presented in the dissertation. A general outline of the past and ongoing research work in forementioned fields is provided for understanding of the reader, with an emphasis on specific technologies of interest for the work related to this dissertation.

2.1 Cryogenics

The U.S. National Institute of Standards and Technology (NIST) considers working environments that involve temperatures below -180 °C (93K) to be classified as cryogenic. A wide range of scientific and industrial applications require cryogenic environments to achieve superconductivity, control liquification of gases, and attain desired material mechanical properties or device operational performance. Industrial cryogenic technology applications include cryogenic manufacturing processes (e.g., machining and surface treatment), cryogenic fuels for rocket propulsion, nuclear magnetic resonance (NMR), magnetic resonance imaging (MRI), cryogenic food freezing, power generation, electricity transmission lines, and transportation.

2.1.1 Industrial applications needing cryogenic systems

Superconducting (SC) magnets are used for several critical applications. The magnetic field generated by SC magnets is used to confine atomic-scale particles and control their motion within the plasma of nuclear fusion devices (Vaghela et al., 2021). SC magnets require stable cryogenic operating environments, and their stability is ensured through meticulous design and management of cryogenic cooling systems. Thermal loads are generated in the coils of SC magnets due to alternating current (AC) losses, nuclear heating, and high currents flowing through the coiled

conductors, and must be removed to maintain stable operating temperatures. In addition to fusion reactors, research has been focusing on leveraging superconductivity in electric motors and propulsion units for aerospace and naval transportation applications (Gubser, 2003). SC motors and generators provide tactical advantages such as higher power, compact size and reduced weight, and low acoustic noise in comparison to traditional powertrains and induction motors (W. Cao, 2011; Rehman et al., 2020).

Cryogenic heat exchangers play a crucial role in industrial applications such as process cooling, separation and distillation of gas mixtures, and liquefaction for transportation and storage of natural gas, oxygen, nitrogen, and hydrogen (Popov et al., 2019). Cryogenic heat exchangers have higher performance requirements and demanding operating cycles compared to regular heat exchangers. The operating conditions, which include a large operating temperature range with precise temperature regulation, multiple flow streams in separate channels, multi-component mixtures with flow injection and removal, require heat exchanger designers to use models that reflect close-to-real thermodynamics and fluid dynamics (viz., reducing the number of assumptions that are generally used to simplify the design problem) of the process. As a result, the design and manufacturing of these specialized heat exchangers have been restricted to a few original equipment manufacturers. Moreover, cryogenic heat exchangers are being used to separate and capture CO_2 from flue gases generated from burning of fossil fuels in the energy and manufacturing sector, which is of interest for pursuing climate change mitigation strategies (C. Song et al., 2019).

2.1.2 Cryogenics in manufacturing technology

Subsection 2.1.1 looked at cryogenic systems as auxiliary units for industrial applications. Moving forward, the focus will be on use of cryogenics in machining, materials used in cryogenic applications, and unique challenges related to manufacturing for cryogenic applications. In the 1940s, scientists observed that metals exhibit higher wear resistance when exposed to low temperatures (Jawahir et al., 2016). In 1966, the Cryotech Company (Detroit, MI, USA) demonstrated a 200-400% increase in metal tool life through the process of cryo-tempering. Cryogenic manufacturing processes include cryogenic material removal operations (such as grinding, milling, and cutting) wherein cryogens are used as coolant/lubricants, and

cryogenic processing operations (like heat treatment but performed at different cryogenic temperature ranges).

Metal cutting processes have traditionally used water and oil-based coolant and lubricants for reducing tool wear, increasing the tool-life, ease of chip removal from the cutting zone and to avoid fusion of chips to the tool face due to excessive heat generation, while allowing better surface finish, faster cutting speeds, and feed rates. In recent years, researchers have studied the use of metal working nanofluids (MWnF) as these have better performance characteristics for thermal conductivity and lubricity resulting in increased tool-life (Niyaghi et al., 2014). The environmental impact of end-of-life phases of traditional metal working fluids and the MWnf has been a major cause of concern as these fluids are often toxic and hazardous to living beings. Cryogenic machining uses liquified gases such as nitrogen, carbon dioxide, and helium as alternative coolants to traditional oil and water-based coolant and/or lubricant. These cryogens are naturally occurring in the atmosphere and the controlled release of these gases to the atmosphere is relatively safer. Researchers who have studied cryogenic machining and grinding processes have reported extensively on the benefits they observed on the tool life, surface finish, dimensional accuracy, and residual stresses for a range of steels (Paul & Chattopadhyay, 1995, 2006). Others have studied the effectiveness of cryogenic cooling in machining of difficult-to-machine materials such as titanium alloys (Z. Y. Wang & Rajurkar, 2000).

Cryogenic processing of metal alloys as part of heat treatment have proven to positively impact material properties, e.g., increasing wear resistance, improving fatigue life, increasing hardness, and reducing residual stresses (Bowes, 2008). Under ordinary cooling, 10-20% austenite is retained in steels and cast iron, while the retained austenite percentage reduces as the austenite transforms to martensite with cryogenic processing, hence increasing strength and hardness (Firouzdor et al., 2008). An extensive literature review was performed by Singla et al., classifying prior work based on the observed effects of cryogenic treatment (CT) on microstructural characteristics observed in different metallic samples, cryogenic processing cycles, and processing parameters (Singla et al., 2018). One form of CT, deep cryogenic treatment (DCT), refers to treatment in the temperature range of 113-77 K, carried out by exposing the metal alloy to liquid nitrogen (Ray & Das, 2017).

2.1.3 Engineering materials used in cryogenic applications

Several polymers and metals are finding use in cryogenic applications. Polymer materials, such as ABS (acrylonitrile butadiene styrene), PLA (Polylactic acid), and nylon-66, are commonly used in electrical and thermal insulators, non-magnetic supports, vacuum seals, and composite matrix materials in cryogenic environments (G. Hartwig, 1995). Thermo-mechanical characterization of ABS at 77K is reported for 3D-printing of ABS, which allows for rapid prototyping, fabrication of complex shapes, and aggregated part designs (Bartolomé et al., 2017). Characterization of thermo-mechanical and electrical properties for a variety of polymers at cryogenic temperatures has been documented (Kalia & Fu, 2013). Composites made using thermoplastic graphite-reinforced cryogenic tank have been used to contain liquid H_2 and other rocket propulsion fuels (D. Chen et al., 2021). At cryogenic temperatures, fibre-reinforced polymer-based composite structures are subjected to combined thermal and mechanical loads, which initiate microcracks well below the ultimate tensile strength (UTS) of the composite material. The propagation of these microcracks may result in a premature failure of the component. Improving the mechanical strength and toughness properties of the polymer composites is desirable for broadening the utility of high-performance composites in cryogenic environments.

Moving on from polymers and composites to metals used in cryogenic applications, welding of dissimilar metal alloys is of interest to cryogenic applications related to aerospace industry, high pressure pipelines, and chemical and vacuum systems. Welding of dissimilar metals has posed a wide variety of challenges including formation of brittle intermetallic compounds (IMCs) that result in lowered strength of the joints (Vyas et al., 2020). Hence, for cylindrical components such as piping, friction welding has been pursued as an effective joining method. The WAAM process enables production of multi-material parts. Austenitic stainless steels (e.g., 308 and 316L) are commonly used as structural materials for cryogenic temperatures below 77K due to their relatively high strength (>1200MPa) at these temperatures (Paredes et al., 2020). Bidulský and co-workers (2020) performed mechanical property characterization, including yield strength (YS), ultimate tensile strength (UTS), toughness, and uniform elongation (UE), for austenitic stainless steels produced using laser powder bed fusion (LPBF). Tensile tests were performed on samples in as-built and stressed-relieved configurations at 298K, 77K, and 4.2K.

Fractured surfaces were observed under field emission scanning electron microscope. Heat treatment was carried out for stress relief (soaking at 400 °C for 60 minutes). Martensitic formation is observed to be more prominent at cryogenic temperatures during the first and second hardening range, explaining the increased mechanical resistance. The movement of dislocations is reduced at cryogenic temperatures, reducing plastic deformation (necking) and leading to more brittle failure. Inclusions in the microstructure act as regions of stress concentrators, facilitating cleavage and brittle fracture micro-mechanisms in the necking region. Microstructural defects in LPBF were classified as spherical porosities, irregular fusion holes, or cracks. Spherical porosities were randomly distributed throughout the sample, while fusion holes were generally distributed between the tracks and layers. These defects were responsible for crack initiation and propagation. Karthik and co-authors (2021) studied the role of cellular dislocations in improving the strength, simultaneously improving the mechanical stability of austenite and retardation of deformation induced martensite transformation (DIMT) of the austenite at cryogenic temperature (77K). This retardation in the DIMT lead to improved strength-ductility synergy in DED laser-melted 316L stainless steel compared to wrought processed samples. The layer-wise (additive) fabrication of parts and the complex thermal cycles resulted in a heterogenous grain structure, sub-grain cellular structure, texture, and anisotropy.

Much recent work has demonstrated metal additive manufacturing provides advantages over traditional manufacturing processes due to significant reductions in cost and lead times, production of highly-efficient and lightweight components through application of topology optimization and design for additive manufacturing principles, and ability to manufacture consolidated parts that have unique complex design solutions and are otherwise impossible to manufacture using traditional manufacturing (Blakey-Milner et al., 2021). These advantages of metal additive manufacturing are utilized in commercial applications in the aerospace industry for manufacturing of liquid-fuel rocket engines, heat exchangers, turbomachinery, valves, propellant tanks, satellite components, and repair and remanufacturing of existing components.

As in case of any specialized technology, cryogenic applications have challenges associated with design, manufacturing, materials, use-phase operating conditions, and end-of-life planning (Stautner et al., 2017). Researchers have identified specific cryogenic component designs that can greatly benefit from additive manufacturing

including but not limited to, bimetallic structures, cryogenic suspension and support systems, tubes and shells, cooling tubes, seals, heat switches, thermal insulation for HTS magnets, microchannel heat exchangers, porous plugs, and gas storage vessels (Stautner et al., 2017). Due to the challenging and complex thermal, electrical, and mechanical functional requirements of cryogenic systems, there is a need for reliable computational models, tools, and techniques to ensure competing component design goals are met. Such models would support manufacturing decision making, and thus be able to represent information related to general material properties, process parameters, and product-process performance interactions. Other key areas of research interest in the metal additive manufacturing domain include ensuring process repeatability, porosity control, and surface finish; refining inspection methods; evaluation of thermal cycles; and development of new superalloys and surface coatings with high reflectivity.

In summary, Section 2.1 provides readers with background information related to the recent developments in the field of cryogenic applications, the uses of cryogenics, design, manufacturing, materials, and associated challenges in the field. A more focused review of HTS magnet technology is provided in Section 2.2.

2.2 High temperature superconductivity

Superconductivity was first discovered in 1911, the superconductors were classified in two types: type 1(LTS) and type 2 (HTS) (Uglietti, 2019). During the 1960s, superconducting magnets were developed using NbZr, MoRe, and NbTi, all of these were type1 LTS materials. Projects like Large Hadron Collider (LHC) at CERN and tokamak fusion device at ITER (International Thermonuclear Experimental Reactor), among others will benefit from increased peak magnetic field, higher operating temperatures that are offered by HTS materials. Superconducting magnets find their use in steady state operating conditions due to economic advantages in comparison to resistive magnets which has a higher power demand and require large cooling systems. LTS superconducting magnetic energy storage systems (SMES) were first developed in the early 1960s, with the first successful charging and discharging test done in 1971 (Mukherjee & Rao, 2019). The SMES are developed mainly for power stability purpose. The type 1 LTS materials such as NbTi and Nb_3Sn conductors are difficult to work with due to their brittleness. Low cost HTS

type material like RE-$Ba_2Cu_3O_{7-\delta}$ (REBCO) coated conductor is a possible alternative to the Nb_3Sn conductors.

HTS materials due to their high current densities and lower losses offers higher specific power and efficiency over conventional conductors (Hull & Murakami, 2004). HTS materials can generate large magnetic flux densities that remain constant over time. These favourable properties have influenced researchers to study feasibility of using HTS materials in applications ranging from current leads, fault-current limiters (FCLs), flywheel systems for energy storage, magnetic levitation, superconducting motors, and generators. Potential applications of bulk superconducting materials fall in three categories: flux shielding applications (magnetic shielding and magnetic lenses), flux pinning applications (levitation, flywheel energy storage, magnetic bearings) and flux trapping applications (motors/generators, MRI and NMR) (Durrell et al., 2018).

Bulk materials such yttrium-barium-copper-oxide (YBCO), bismuth-strontium-calcium-copper-oxide (BSCCO) and rare-earth-barium-copper-oxide (REBCO) are commonly used in manufacture of HTS tapes (Hull & Murakami, 2004). Superconducting state of HTS materials are extremely stable when compared to LTS counterparts due to the large heat capacity and higher operating temperatures, in addition the HTS filaments generate less heat per unit volume and the high thermal conductivity matrix around the filaments effectively redistribute the heat. Both YBCO and REBCO materials are prone to phenomena known as flux jumping or flux avalanche which drops the overall stability of the superconductor. The superconducting filaments have lower thermal conductivities, this in conjunction with insufficient cooling results in generation of localized zones within the bulk material with raised temperatures. These regions have higher electrical resistivities in comparison to the rest of the bulk material, as a result there is movement of fluxoids from surrounding regions, this phenomenon is known as flux pinning, in turn gives rise to flux avalanches. Flux pinning in BSCCO is extremely weak due to strong anisotropy in the microstructure, hence BSCCO bulk materials are used to produce current leads in fault-current limiters.

Power systems can experience large transient current increases (20-30 times the rated value) caused due to lightning, short circuit, or other faults; the surge in currents can damage equipment connected to the power line. To protect the equipment, traditionally mechanical breakers have been used. FCLs have better response time (within one cycle) characteristics compared to the mechanical

breakers, hence in principle can reduce the complexity of the system (B. Li et al., 2018). FCLs are developed to utilize the non-linear resistance property of superconductors, meaning when the current in the line exceeds a certain critical value, the superconducting material transitions from superconductor state to a resistive state and helps limit the fault current. This transition is passive, therefore avoiding the need complex control circuitry.

Another application that can benefit from use of HTS materials is high-capacity transmission lines that can carry out power transfers in gigawatt (GW) ranges (Doukas, 2019). Minimized land use and environmental footprint (for the overhead power lines), reduction in energy losses, low-voltage operation, lower electromagnetic field (causing interference with surrounding environment), and cable-embedded FCL capabilities are some of the potential advantages of using HTS cables in power transmission. AC and DC transmission lines have been developed and prototype cables have been tested by integrating them in the real power grid systems. Liquid nitrogen cooled reliable and cost-efficient high-capacity underground AC transmission lines are being developed for the urban environment. These cables are compact, carry higher power, and with the latest advancements in HTS materials manufacturing technology, segments that are few hundreds of meters long are available before additional joints are needed. DC power transmission lines made with HTS cables offer similar advantages and has been considered for long distance transmission of power from distant isolated renewable energy sources to centrally located load centres. Advancement in converter technologies (AC to DC and vice versa) will allow for use of HTS DC power transmission lines to further reduce on transmission losses. The new convertors developed are cost efficient, less bulky, and have low-voltage operation, hence allowing more flexibility in integration of transmission lines to mixed AC/DC systems. At present, the technology readiness level (TRL) for HTS DC and AC cables are at 5 and 7 respectively, and by 2030 it is expected that the TRLs for both these cables will reach 9. The major hurdles for large scale adoption of the HTS cables is still in cost to performance metric (€/kAm), and secondary costs associated with the cooling systems. Manufacturing process for the wire manufacturing and related power equipment is still a niche area with limited players. There is a need for increased testing and development of standardized manufacturing process plans for ensuring quality of the cables. Long term risk and reliability assessments, damping and stability concerns, and development of accurate

multi-physics models for HTS cables are some of the technical hurdles that need to be addressed (Marchionini et al., 2017).

The diamagnetic behaviour of superconductors along with the ability to lock magnetic field lines in pinning centres within the HTS, allows for stable levitation of permanent magnets above or below an HTS (Hull & Murakami, 2004). This levitation property is of interest to make HTS bearings. Flywheels for energy storage are another application where HTS bearings are used. Traditional flywheels with conventional bearings experience high speed idling losses of about 1% per hour. In contrast, the rotational energy losses of a HTS bearing are about 0.001%, considering the energy demand from auxiliary cryostat system, it is believed that energy losses of the HTS bearings can be as low as 0.1% per hour.

Use of HTS superconductors to make electrical transformers is another application of interest considering the potential reduction in losses (<30%), volume (~50%), and weight (~70%) (M. Chen et al., 2004). The feasibility of HTS transformers was demonstrated by ABB 3-phase 630KVA (20kV/0.42kV) prototype, that was operational on the live grid for one year. Oak Ridge National labs and Siemens have independently made and tested 1MVA prototype devices. The large-scale implementation of these devices requires reliable cost competitive cooling and reduction in the HTS superconductor costs. HTS cables need to be stable and robust under various mechanical, electrical, and thermal conditions. Hartwig et al., designed and experimentally qualified vacuum pressure impregnated, insulated, partially transposed, extruded, and roll-formed (VIPER) cables, these cables were tested for thousands of cycles of mechanical cycles, electromechanical force levels, multiple cryogenic cycles, and dozens of transient quench like events (Z. S. Hartwig et al., 2020). The conclusions of the study were promising, it showed the cables demonstrated high mechanical strength, cryostability, and rapid quench detection. The performance of the cables was predictable and repeatable.

Dissertation titled 'High Temperature Superconductor Accelerator Magnets' submitted to the University of Twente by Dr. Jeoren van Nugretren explores the different challenges and opportunities of developing HTS magnets for future circular collider applications (Van Nugteren, 2016). As part of the dissertation a new network model is developed that can analyse the transient electro-magnetic and thermal behaviour of coated conductor cables. The model allows for solving complex and critical issues related to coated conductors, such as, thermal stability, quench propagation, and field quality.

Table 1: HTS applications and related design and manufacturing decisions.

HTS Application	Functional requirements	Design constraints	Design and Manufacturing Decisions
Magnetic plasma confinement in fusion reactors	1. Steady state operations with constant magnetic flux. 2. Higher magnetic fields	Cannot operate with nitrogen cooled SC	1. Requires working temperature ranges of helium or hydrogen cooling media (Bruzzone et al., 2018) (Uglietti, 2019)
HTS application defines the design and type of cable to be used	HTS tape/cable configuration selection for stable operation and prevention of quenching.	Axial, transversal, bending, shear, and/or torsional forces are developed based on different design alternatives	1. Need to define the geometry, final shape, number of tapes etc., based on design constraints (Bykovsky et al., 2015)
HTS ring magnets for rotating electric machine	1. Coreless/air-core topology for light weight design. 2. The magnets must have high power and torque densities 3. AC losses must be reduced for high efficiency electric machines	1. High rpm operating conditions (160000-24000 rpm) 2. Size, weight, and power density are important. 3. Magnetic field homogenization	1. The field homogeneity can be ensured by studying different stacking alternatives. (Yazdani-Asrami et al., 2021)
	4. Effective cooling of the tapes must be ensured for increase in current densities and thereby increase in the attainable magnetic field	4. Yoke and stator design can determine the cooling efficiency 5. Material selection for these support structures can determine effective field strengths that can be achieved	2. Mechanical support structures (yokes, collars) can provide means for removing excess heat generated. 3. Multi-objective design optimization problem to be solved using machine learning algorithms.

HTS in MRI and NMR	High magnetic field homogeneity	1. Short piece lengths 2. Brittleness of the cables and tapes 3. High cost of the HTS tapes 4. Cables do not provide the needed resolution	High field solenoids with thick winding and small bore. (Iwasa, 2006)

It is important to note the importance given to quench protection of the magnets and the overall mechanical support structure design of the magnets. Challenges and technical difficulties of working with the ReBCO Roebel cables especially delamination and disintegration of the cables during winding. Quenching in superconducting research field jargon is a process in which due to process irregularities, hot spots generate in certain regions of the superconducting tape material resulting in the local temperature of the material rising above the critical temperature. The rise in temperature results in the loss of superconducting behaviour of the material. This would mean that the material will have high resistance and with the high ampere current flowing through the material, Joule heating will result in complete burnout of the superconducting cables.

In conclusion, having looked at the different aspects connected with design and manufacturing of HTS materials, the reader should now have a better understanding of the functional requirements, design constraints, and material selection decisions. These aspects have been summarized in Table 1. The next subsection will address topics related to metal additive manufacturing.

2.3 Additive manufacturing

Additive manufacturing has revolutionized the manufacturing industry by enabling the creation of customized products, reducing product development cycles, reducing manufacturing lead times and costs, increasing focus on sustainability, and leading to the development of new business models (Mazzucato et al., 2019). Advantages of AM technology over conventional manufacturing methods include part consolidation (design for assembly), topology optimization of parts to achieve higher strength to weight ratios, production of complex geometries without the need for costly custom tooling, and creation of multi-material components(Pérez et al., 2020).

Additive manufacturing plays a central role in the shift towards industry 4.0, smart manufacturing, and factories of the future paradigms (Mazzucato et al., 2019). Industrial firms, however, are sceptical of AM technologies due to inherent issues of reproducibility, part quality, and productivity, limiting large scale acceptance. There are also unresolved concerns over part qualification (e.g., for aerospace, automotive, and biomedical applications). It is expected that AM technologies will soon be mature enough to resolve these underlying uncertainties.

ISO/ASTM 52900 classifies AM technologies under seven categories as shown in Table 2 (ISO/TC 261 & ASTM Committee F42, 2021). Various materials (e.g., ceramics, composites, metals, and polymers) are used as AM process feedstocks in sheet, wire, powder, and liquid form. Research advancements for two directed energy deposition (DED) processes, wire arc additive manufacturing and selective laser melting, are discussed below.

Recent advancements in materials and process technology for laser powder bed fusion (LPBF) and laser directed energy deposition (LDED) have been reviewed and discussed in detail by Gu and co-workers (Gu et al., 2021), highlighting the need for development of models with variable fidelity, that will better integrate the material-structure-performance relationships of AM parts for optimized process and part quality. Multi-material printing involves a mismatch in physical properties (e.g., melting temperature, laser absorptivity, coefficient of thermal expansion, and thermal conductivity) giving rise to interlayer and inter-material bonding defects (Reichardt et al., 2021).

Development of components with electronic sensors integrated to the structure during manufacturing using the laser DED and/or LPBF processes is active research that tackles challenges such as requirements for high surface finish tolerances, reduced porosity, increased structural precision, and spatial resolution (Espalin et al., 2014). Design for AM has led to implementation of topology optimized structural components that replace primitive designs serving the same functional requirement with relatively less material and energy use (S. Das & Sutradhar, 2020). By combining advanced computing capabilities and sophisticated finite element modelling (FEM) and simulation tools, designers can create multiple prototypes and simulate different loading conditions to test the designs. Topology optimized structural components are capable of meeting complex multi-disciplinary design goals such as reduced materials use, uniform stress distribution, improved heat conduction, desired electromagnetic properties, and longer service life.

Table 2: Additive manufacturing classification

Technology	Process	Material
Vat polymerization	Stereo-lithography (SLA)	Polymers
Material jetting	Drop on Demand (DOD)	Photopolymers and casting wax
Material extrusion	Fused deposition modelling (FDM)	Polymer filaments
Sheet lamination	Laminated object manufacturing (LOM)	Plastics, composites, metal foils, and ceramics
	Ultrasonic additive manufacturing	Metal sheets and strips
	Solid foil polymerization	Plastics
Directed energy deposition	Laser metal deposition (LMD)	Metal wire feedstock and powder metal
	Rapid plasma deposition	Metal wire
	Wire and arc additive manufacturing (WAAM)	Metal wire
	Laser engineered net shaping (LENS)	Metal powder
Binder jetting	3D printing (3DP)	Metal powder
Powder bed fusion	Electron beam melting (EBM)	Metal powder
	Selective laser sintering (SLS)	Metal powder
	Selective laser melting (SLM	Metal powder
	Direct metal laser sintering (DMLS)	Metal powder

Recent research developments for two metal AM processes relevant to this dissertation are discussed in more detail in the following subsections. The discussion focuses on work devoted to improving process quality and productivity through the application of design, manufacturing, and materials science research methods.

2.3.1 Wire arc additive manufacturing

Wire arc additive manufacturing (WAAM) is a DED process that revolutionizes the metal printing industry with its high material deposition rates and printing speed. In conventional arc welding, the high deposition rates are often associated with very high heat input, an unstable arc, and spatters, which is also noticed in WAAM processes that utilize this welding technology. Cold metal transfer (CMT) is a novel welding technology that mitigates these issues in WAAM by carrying out on/off arcing in three phases, namely, boost, burn phase, and short-circuit phase, to reduce the overall heat input to the weld (Mezrag et al., 2015).

Figure 2: Wire arc additive manufacturing (WAAM) setup used in this research

The arc is on during the boost and burn phase of the welding cycle, while no current flows during the short circuit phase when metal is deposited using the controlled dip transfer mechanism. Metal is transferred by dipping the molten

droplet into the melt pool and retracting the wire back at a specific frequency (50~130 Hz), forcing the droplet to detach due to surface tension. The fast retraction movement ensures spatter free welding since no metal transfer occurs in the gap between the wire and base material (Almeida & Williams, 2010). In addition, heat input to the weld only occurs during the arcing period and detachment of droplets occurs when the process is current free (Välimäki, 2017). The experimental work performed as part of this dissertation has been conducted using WAAM setup comprised of a Fronius CMT Advanced 4000 welding machine, and an ABB (4600 40/2.55) 6-axis robot in conjunction with a 3-axis worktable as shown in Figure 2. It should be noted that the Fronius CMT welder can be used in different welding modes (i.e., metal inert gas (MIG), metal active gas (MAG), tungsten inert gas (TIG), and cold metal transfer (CMT)).

2.3.1.1 Process description, opportunities, and challenges in WAAM

One of the major manufacturing sectors that has seen a rise in the use of AM technologies is the aerospace industry. The requirements for aircraft parts qualification and certification (Q&C) are regulated by guidelines set up by the Federal Aviation Authority (FAA) and similar national and international organizations (Seifi et al., 2017). Based on the functionality of the components, these guidelines provide definitions for the level of part criticality under various degrees of specificity. There are rules related to the materials, fabrication methods, and testing methods to name a few. Often, these rules do not define the specific acceptable testing procedures or compliance methods. Instead, they are defined by the applicant (for instance, by the original equipment manufacturers of a specific manufacturing technology) as part of the means of compliance (MoC) definition, which are then reviewed and approved by certification authorities. Hence, for AM technologies there is a need to develop standardized testing procedures considering the unique nature of AM material systems such as anisotropy, material anomalies, multi-material phases, location specific properties, and residual stresses. At present, the Q&C of AM technologies rests upon the shoulders of OEMs, multinational corporations, and well-funded research organizations and relies on their willingness to share/make public their findings. Standards development organizations (SDOs) can bolster the accessibility and use of AM technology by small and mid-sized companies and research units via

development of baseline specifications and standards pertaining to use of AM technologies for different industry sectors.

September 2015 saw the first joint workshops in the U.S. organized by the FAA and Air Force Research Laboratory (ARFL), which was attended by personnel from government, industry, and academia, to promote technical dialog and knowledge sharing between key stakeholder groups. Over the years, the stakeholder group has expanded to include international organizations such as the European Aviation Safety Agency (EASA). Presenters at the workshop identified the following specific areas of interest for AM processes that need to be addressed to advance Q&C:

- Process monitoring and control
- Process-related anomaly and defect detection, characterization, and control.
- Effect of post process machining, heat treatments, and stress-relief processing
- Quality and control for raw materials used for AM (for instance powders, wires, and sheets)
- Characterizing of as-built and post processed parts to compare final product durability
- Defining the needs, capabilities, and requirements of non-destructive testing methods to evaluate AM parts
- Characterization of orientation- and location-dependent properties of AM parts (Seifi et al., 2017)

2.3.1.2 Material characterization in WAAM

The literature reviewed in this section focuses on material characterization research conducted for WAAM technology. The study of characterization is crucial for addressing some of the opportunities and challenges mentioned in the previous section.

Le and Mai (2020) characterized the microstructural evolution and mechanical properties of 308L stainless steel parts printed using gas metal arc welding based additive manufacturing (GMAW-AM). The authors printed thin-walled structures, which were primarily comprised of columnar dendrites in the bottom and middle regions of the wall, while the top region was comprised of equiaxed dendrites along the build direction. Equiaxed dendrites were also found in the heat affected zones

(HAZ) between adjacent layers. The material was composed of small amounts of δ-ferrite phases in the γ-austenite dendrites. The microhardness of the printed specimens ranged from 155 ± 1.20 HV0.1 to 169 ± 5.67 HV0.1. The ultimate tensile strength (UTS), yield strength (YS), and elongation for the samples taken in the vertical direction were 537.78 ± 4.52 MPa, 343.67 ± 7.53 MPa, and 39.58 ± 1.38 %, respectively, while these measured 552.95 ± 4.96 MPa, 352.69 ± 8.12 MPa, and 54.13 ± 1.29 %, respectively, for samples in the horizontal direction.

Fatigue crack growth in multi-pass welding of 308L was studied by Jang et al., who observed fatigue crack growth rate depended on dendrite alignment and residual stress distribution in the weld (Jang et al., 2010). The anisotropy in the microstructures formed during welding results in variable fracture toughness within the weld. ASTM standard E647-15 was adopted to perform the fatigue crack growth experiments under ambient conditions under Mode 1 loading. Gordon et al., (2018) studied the fatigue properties and fracture behaviour of stainless steel 304L walls fabricated using WAAM. Standard light microscopy, electron back scatter diffraction (EBSD), and X-ray diffraction (XRD) were carried out for as-printed and heat-treated samples. Skeletal and lathy δ-ferrite formations were found in the microstructure. Grain sizes varied largely due to the epitaxial growth pattern and formation of columnar grains along the build direction, which were surrounded by smaller equiaxed grains. Grain sizes varied significantly, some measured up to 600μm wide and 4000μm long. As-printed and heat-treated samples showed surface residual stress distributions that were compressive in nature. The horizontal tensile test specimen displayed a higher UTS and strain hardening coefficient values (523.81 ± 13.08 MPa, 0.3317 ± 0.002) than the vertical specimen (499.11 ± 6.76 MPa, 0.283 ± 0.002). Both the horizontal (296.33 ± 12.60 MPa) and vertical (305.75± 5.57 MPa) specimens surpassed the YS of wrought steel (202 MPa). The Young's Modulus values of the as-printed samples were 40% lower than conventionally processed 300 series stainless steels, due to the texture and residual stress resulting in anisotropic elastic behaviour.

The study done by Le et al., (2021) investigated the influence of process parameters (such as welding current, voltage, and travel speed) on the obtained geometry of single bead welds using response surface methodology (RSM) and ANOVA. In addition, microstructure and mechanical characteristics of stainless steel 308L parts printed using WAAM were studied. The microstructure was comprised of dendrites of austenite growing vertically along the build direction and

residual ferrite existing in grain boundaries of the austenite matrix. The microhardness was found to be 163 $HV_{0.1}$. Values for UTS, YS, and elongation were found to be 553 MPa, 344-353 MPa, and 40-54% respectively. A dwell time of 40s was maintained between printing of two consecutive layers. The variations observed in microhardness along the vertical axis agrees with microstructures that were observed, as explained by the Hall-Petch relationship. The hardness of the material is higher for finer grain sizes. The morphologies of the fracture surfaces of the horizontal and vertical tensile test specimens were observed using SEM imaging. There were many dimples with homogenous distribution on the fracture surfaces of both the horizontal and vertical test specimens, demonstrating good toughness for 308L parts made with GMAW-AM. Better toughness values in the depositing (horizontal) direction is explained by the presence of more refined dimple depth and sizes observed in the fracture surface of the horizontal test specimen.

Lu et al. (2017) studied the formability, microstructure, and mechanical properties of printed WAAM parts made from AWS ER70S-6 alloy, by performing evaluation using optical microscopy, scanning electron microscopy, microhardness, and microtensile tests. The microstructure consisted of granular ferrite and residual austenite and had traces of pearlite in the intermediate zone. Horizontal tensile test specimens had better mechanical properties compared to the vertical counterparts. The results obtained for the tensile tests are similar to prior work, reinforcing the relationship between mechanical properties and the anisotropic behaviour of WAAM-printed parts. The YS and UTS values of horizontal specimens (519.5 $\pm$ 8.3 MPa and 693.5 $\pm$ 8.5 MPa) were higher than specimens taken along the build direction (461.5 $\pm$ 6.3 MPa and 618.5 $\pm$ 10.8 MPa). The elongation of specimens along the horizontal and vertical directions were found to be 36.8 $\pm$ 0.2 and 28.2 $\pm$ 0.5 percent, respectively.

In their state-of-the-art review, Rodrigues et al. (2019) provided insights into ongoing WAAM process research, with a focus on studies for dimensional quality, mechanical strength, and welding path planning for different metal wire feedstocks. They discussed the different types of welding technologies used in WAAM, common defects in WAAM printed parts, and stress relief strategies to improve mechanical strength. Studies reported that residual stress build up due to inhomogeneous heat distribution was a common occurrence in WAAM. Employing stress relief strategies such as cold interlayer rolling, machine hammer peening, or laser peening was found

to help achieve grain growth refinement, providing better control of mechanical properties, path width, and surface finish.

In addition, Rodrigues and co-workers found that interlayer temperature, or interpass temperature, had a high influence on final printed part quality and microstructure (Rodrigues, Duarte, Avila, et al., 2019). A higher interpass temperature generally provides finer grain structure and improved toughness for certain high-strength steels. However, this characteristic reverses as interpass temperature exceeds 260 °C; increasing the interpass temperature beyond this limit causes the weld pool to puddle and collapse, affecting the quality of the part (X. L. Wang et al., 2017). The wait time for cooling to the required interpass temperature is influenced by the cooling rate of the layer, which varies as a function of energy density and product height. Increasing part height influences conduction, convection, and radiation and, in turn, causes a reduction in the cooling rate of subsequent weld layers. Thus, controlling the thermal cycles during the process to maintain stable interpass temperatures is essential for achieving high quality welds.

Sun et al. (2020) investigated the microstructure and mechanical properties of low-carbon, high-strength steel fabricated using WAAM. A 907-steel alloy plate substrate and an A-Fe-W-86 welding alloy wire feedstock were used. They found the microhardness values varied from 290 HV to 260 HV along the build direction of the welded part. In addition, the average UTS of longitudinal specimens (976.53 MPa) was significantly lower than transverse specimens (1017.8 MPa), confirming anisotropic behaviour. The inclusion of more interlayer zones in the microstructure resulted in higher stress concentrations in the longitudinal specimens. The order of occurrence of the phases also corresponded with the microhardness results, where hardness decreased along the build direction. Additionally, two crucial control parameters were found to influence the microstructure formation: temperature gradient (G) and solidification velocity (SV). Based on solidification theory, the G/SV ratio determines the microstructure formation. When G/SV is extremely high (approaching infinity), planar grains form, when G/SV is relatively high, columnar grains form, and when G/SV is small, equiaxed grains form.

Rodrigues et al. (2019) investigated the thermal influence of WAAM on microstructure and mechanical properties of high-strength, low-alloy steel using a commercial-grade wire electrode (AWS A5.28 ER110S-G) deposited onto a mild steel substrate. The microstructural analysis in the study found that ferrite, bainite, martensite, and retained austenite were present for both levels of heat input. Further,

it was reported that heat input directly affected the cooling rates, interlayer temperatures, and residence times in the 800 °C to 500 °C cooling interval. Two primary cooling intervals (1300 °C to 800 °C and 800 °C to 500 °C) are known to promote phase transformations and grain growth development. Austenite grain growth occurs in the 1300 °C to 800 °C range, while in the 800 °C to 500 °C range, a phase transformation from austenite to distinct ferrite morphologies and bainite can be observed. Despite using different heat inputs for the two samples, no significant difference was observed in the microstructure of the parts. Both samples had the same phase constituents (i.e., ferrite, and bainite). Uniaxial tensile tests and Charpy impact tests found the mechanical properties in the build and travel directions to be similar, exhibiting isotropic behaviour.

From the discussion presented so far in Section 2.3, it can be inferred that process-structure-property relationships and part functionality/performance are critical aspects of AM technologies that must be better understood to bridge the gap in knowledge with their conventional manufacturing counterparts. A similar review of research work done for selective laser melting process is presented in Section 2.3.2.

2.3.2 Selective Laser Melting

Selective laser melting (SLM) technology has revolutionized the manufacturing of products in aerospace, automotive, medical prosthetics and implants, and consumer goods. With inherent advantages such as realization of complex geometry parts, reduced manufacturing times, ability to process a wide spectrum of materials, ability to tune properties during processing of parts, and production of near-net shapes, SLM will continue to be one of the leading AM technologies adopted in industry (Maconachie et al., 2019). Printing of alloys of titanium, nickel, aluminium, iron, and steels have been subject to ongoing research efforts to address a variety of process-related challenges, improving process knowledge and uncovering opportunities for research. Porosity, incomplete deposition, balling phenomena, keyhole effects, incomplete fusion holes, cracking, oxidation, delamination, warping, and impurities in the powder are some of the major defects that severely affect the part quality and performance (B. Zhang et al., 2017). Incorrect process parameter selection, feedstock powder quality, and errors in design considerations can result in the above-mentioned defects. In addition, there are defects such as metallic inclusions,

segregations, residual stresses, and metallurgical imperfections that result from the multiple thermal cycles that the printed part undergoes.

Apart from the challenges and defects encountered in SLM printing of regular metal alloys, working with feedstock materials like pure copper and copper alloys introduces newer challenges arising from the high thermal conductivity and laser reflectivity of the material (Tran et al., 2019). The printed layer surface reflects the laser beam falling on the subsequent powder layer resulting in lower energy transfer to the printed layer. The high thermal conductivity of copper results in fast dissipation of heat away from the melt pool often causing incomplete deposition and delamination. Research efforts have been made toward printing of pure copper and copper alloy, resulting in various strategies such as using a lower laser power, using a green laser (wavelength better absorbed by copper), and varying the feedstock powder size. Also, AM technologies like electron beam melting (EBM) and bound metal deposition (BMD) have had better success in printing denser and defect-free copper parts (Guschlbauer et al., 2018). Delamination defects result from instability of the process melt pool. The delamination can be aggravated further due to the presence of thermally induced stresses. Studies have observed differences in the relative density of copper parts, where internal regions of the parts tend to have higher relative densities than the boundary regions. The high thermal conductivity of pure copper results in higher heat dissipation rates at the boundary regions, resulting in partial melting and higher porosity at the extremities.

Jia et al. (2021) reviewed the progress in research specific to implementation of various scanning strategies for SLM, and related impact on the part quality, mechanical properties, and microstructure. Defects such as large residual stresses and balling effects can be effectively controlled by careful selection of scanning strategy. Long scanning lines or vectors induce excessive accumulation of stresses, which can be reduced by following the island scanning strategy, wherein the overall printing area is divided into smaller sections, or islands. Presence of equiaxed grains is preferred over columnar grains in the microstructure as equiaxed grains favour isotropy in the mechanical properties. By reducing the ratio between heat gradient and solidification rate, the refinement of microstructure can be ensured (improves chances of equiaxed grain formation). The contour strategy improves the density of the microstructure and the overall surface roughness of the printed part. Studies have shown improvement in the surface quality of SS316 alloy and Hastelloy X following a contour scanning strategy (Salman et al., 2019; Tian et al., 2017). Large hatch

spacing results in low energy density; hence, causing insufficient melting leading to balling phenomena. Meanwhile, small hatch spacing results in highly concentrated laser energy, leading to vaporization of powder, pore formation, and keyhole defects. Rotation of the scanning vector while printing subsequent layers is beneficial for the overall improvement in mechanical and microstructure properties. Improved mechanical properties caused by remelting of powder has been reported in several studies (Xin et al., 2020). The effect of scanning strategy and its impact on the residual stress has been documented, where a high-temperature gradient can result in high residual stresses, lowering critical mechanical properties such as strength, ductility, and fatigue life (Cheng et al., 2016; Salman et al., 2019; Y. Song et al., 2020).

Contradictory observations have been reported by researchers regarding the presence of anisotropy in the mechanical properties of metal AM parts. Each metal AM process is unique, and the physical phenomena associated with the process of melting and solidification of the metal alloy is complex. Kok et al. (2018), in their review article, highlight findings of some of the studies reporting the nature of anisotropy in parts fabricated using metal AM process. In metal additive manufacturing including SLM processes, a general observation was the formation of epitaxial columnar grain growth along the build direction (Kok et al., 2018; Qian et al., 2005). The formation of these columnar grains has been cited as the reason for existence of anisotropy in material properties (such as mechanical and electrical). Higher fatigue strengths are reported in the horizontal direction compared to vertical orientation for PBF parts, and the cycles to failure for as-built parts are lower compared to wrought parts. Fatigue strength properties for AM parts can be improved through post-process stress relief heat treatments and surface machining (Lewandowski & Seifi, 2016; P. Li et al., 2016). With optimized process parameters, a refined microstructure with equiaxed grains and homogenous properties can be achieved. Microstructural heterogeneity is another cause for the presence of anisotropy; variation in powder size (for powder-based processes), chemical composition, morphology, and orientation lead to differences in melt pool behaviour, thermal gradients, and solidification rates at the micro- and meso-scale, leading to variations in the final microstructures obtained.

Phase transformation affects microstructure and is a complex phenomenon that depends upon the chemical composition of the alloy, thermal cycles experienced by the part, heating and cooling rates, exposure to environmental conditions, and processing time (Tan et al., 2016). Layer banding is another common phenomenon

to metal AM processes, which is the formation of distinguishable bands that result from the cyclic thermal history of the part due to deposition of multiple layers (Kelly & Kampe, 2004; Martina et al., 2015). The layer bands have been known to improve the ductility of certain alloys in specific loading directions (Todai et al., 2017). Numerical modelling of multi-physics phenomena, i.e., the fluid-flow and thermal profile of the AM process is crucial in understanding the microstructural evolution and determining the expected physical properties of the part. Costa et al. (2005) developed a finite element model representing the thermo-kinetic behaviour of the LPBF process via modelling of the heat transfer mechanisms, phase transformation data, and microstructure-property relationships.

Shifting the focus away from the general directions in powder-based metal AM research, let us look at studies conducted on alloys of specific interest to this dissertation, namely copper alloys, pure copper, Invar36, and steel alloys. Invar36 is difficult-to-machine nickel-based alloy due to work hardening and high ductility. Thus, SLM is a promising process technology to produce near net shape Invar36 parts and would be beneficial to the industrial sectors that use Invar36 as an essential material, e.g., aerospace, metrology devices, and precision instruments and tooling. Yakout et al. (2021) presented an in-situ monitoring setup using thermal imaging for detecting spatter formation and delamination during SLM printing of Invar36. Process conditions that lead to instabilities, excessive spattering, and delamination were identified. Methods such as preheating of the build plate and powder bed were shown to considerably reduce spattering. Spattering causes formation of metal inclusions that can be three times the size of the feedstock powder. The studies conducted used energy densities that lie between the balling and keyhole regimes (41.7-156.3 J/mm^3). Lack-of-fusion porosity was observed at low laser energy density (41.7-86.8 J/mm^3), while high energy density (above 86.8 J/mm^3) inputs resulted in delamination and hot spots around the melt track.

A prior study investigating process-structure-property relationships by the same authors (Yakout et al. (2019)), studied the impact of process parameters on the bulk density, material composition, fracture behaviour, tensile properties, and residual stresses for SLM-printed Invar36 and stainless steel 316L using a full factorial design of experiments. Optimum process windows were identified, and the residual stresses were classified in two categories: microscopic and macroscopic residual stresses. Song et al. (2020) studied the influence of five different scanning strategies on the crystallographic morphologies and mechanical properties of 316L stainless steel

alloy printed using SLM. Introducing an angle of rotation to the scan pattern at the start of each successive layer benefited the overall development of the microstructure by deterring the formation of columnar grains, thereby promoting equiaxial grain growth. The equiaxial grains increased the tensile strength and ductility of the parts. A rectangular scanning pattern improved the microhardness properties of the part. The work highlighted the contribution of scanning strategy towards the overall energy input, and thereby its effect on the meso- and micro- scale structure and behaviour of alloys. The island scanning strategy was used in the study to define subareas within the entire printing bed, wherein, different scanning patterns could be used simultaneously. Four rectangular scanning patterns and one hexagonal pattern were used in the study. The rectangular scanning pattern with parallel scanning in sub-areas and a 47° rotation between deposited layers had the highest tensile strength and ductility properties.

Qiu et al. (2016) studied the microstructure and mechanical properties of SLM fabricated Invar36. They kept the laser power constant at 400W while varying the laser scanning speed for each part. With the laser power constant, increasing the scan speeds above 3200 mm/s resulted in increase in the porosity. The sample printed at 4000 mm/s showed maximum porosity. Large vertical columnar grains (45μm width on average) were observed throughout the samples. In addition, more complex fan-like clusters of grains (20μm in width) were observed in the upper regions of the samples.

Silbernagel et al. (2019) printed pure copper with medium power (200-watt, ytterbium fibre continuous wavelength laser) laser powder bed fusion (LPBF) technology. Printing of pure copper has been challenging due to the inherent properties of the material. Copper's high thermal conductivity means heat is dissipated away from the melt zone through the previous deposited layers, resulting in incomplete deposition. It is particularly challenging to carry out remelting of the previous layer for better deposition due to the high reflectivity of the deposited copper. The highest density obtained was 85.8%, found using optical measurement techniques. Average resistivity for parts printed in the vertical direction was 24% higher than the other orientations. The study involved testing different combinations of the parameter settings for single scan tracks, thin walls, and cubes. Scan speed, powder layer thickness, laser power, laser point distance, hatching distance, and scanning pattern were varied for the three different geometries in order to achieve the desired geometric and material properties. Resistivity measurements were carried

out on the test bars that were printed following the cube parameters that resulted in the highest part density. The average resistivity of the as-built specimens was found to be 8.18 μΩ-cm, for the samples heat treated at 1000 °C for a duration of four hours, the resistivity reduced to 3.69 μΩ-cm. The lowest average resistivity of 3.45 μΩ-cm (equates to 50.3% IACS) was found for heat-treated samples with 45 ° orientation. Note, %IACS corresponds to International Annealed Copper Standard, and it's a comparative unit to denote conductivity of metal alloys. The disruptions arising from imperfections in the crystal lattice of pure copper contributes to the higher electrical resistance. Larger grains have fewer grain boundaries and, therefore, result in lower resistivity compared to structures with smaller grains. Along with grain boundaries, porosity and other imperfections in the microstructure influence the resistivity of the printed part. The percentage porosity in high purity copper LPBF parts can be reduced via post process treatment such as hot isostatic pressing (HIP).

Jadhav et al. (2019) printed crack-free pure copper parts with relative densities exceeding 98% using a high-power fibre laser SLM. It was noted that relationships between laser scan parameters and crystallographic textures were easily established for the top surfaces of the part, while the textures in the core of the sample were random due to the successive remelting and altered temperature gradients induced due to the 90° scan rotation introduced between subsequent layers. The electrical conductivity of the printed copper part was found to be 88% IACS. Two limitations that restricted up-scaling of SLM technology were the existence of a small process window that resulted in a stable sample geometry and the damaging effects of the high reflectivity of the newly formed copper surface on the dielectric coating of the optical mirror.

Mechanical, electrical, and microstructure characterization of SLM printed Cu-10Zn were studied by Zhang et al. (2019). The authors printed single track and cube specimens to establish suitable processing parameters for the alloy. With scanning speed, laser power, and hatching space determined, the authors printed specimens for tensile tests, microhardness tests, electrical measurement, and microstructure evaluation. Strength and electrical conductivity results obtained for SLM printing were similar to annealed samples fabricated using forging for the same alloy. The authors observed anisotropic behaviour in the microhardness values in the horizontal and vertical directions; further, the microstructure observed in the vertical direction showed presence of columnar grains. The grain boundary densities were

higher for the cross-sectional samples (horizontal), resulting in higher hardness values in this orientation. The electrical conductivity values were measured and averaged for three samples and found to be 43.19% IACS. Yan et al. (2020) studied the properties of SLM printed pure copper. Linear energy density parameters were identified for different combinations of scanning velocity and laser power. An energy density parameter range of 0.35 – 0.5 J/mm resulted in prints with high relative part density, therefore good quality prints. Microhardness and tensile tests for samples printed using the identified process parameters had similar or better values than wrought parts.

Computer-based machine learning approaches such as Bayesian networks, neural networks, transfer learning, and clustering methods have been utilized to analyse, assess, and optimize the data collected in AM processes (Bi et al., 2021). Craeghs et al. (2012) developed a feedback control system for SLM using optical sensors. Rodriguez et al. (2012) used infrared imaging cameras to collect the thermal profile of the powder bed in EBM process in order to provide corrections to process parameters for the subsequent build layers. Khanzadeh et al. (2017) used a self-organizing map (SOM), an unsupervised learning method, to establish relationships between process parameters and geometrical accuracy in AM parts. Garg et al. (2015) used genetic programming to discover hidden non-linear relationships between process parameters and porosity in the SLS process. In addition, big data plays a crucial role in the application of DFAM through the implementation of various topology optimization algorithms, part redesign, part aggregation, and reduction in the number of supports used. For improving the process efficiency and part quality of metal AM, it is important to delve into the progresses made in of modelling and simulation research pertaining to AM, as briefly explored in the next section.

2.4 Modelling and Simulation

The following subsection provides background information related to modelling and simulation in additive manufacturing.

2.4.1 Causal ordering

Causality and causal relationships have been an area of interest for research in philosophy and sciences. The literature on causality deals with causal discovery, causal inference, and statistical inferences (Vuković & Thalmann, 2022). Causal reasoning is another domain that deals with qualitative physics reasoning based on the system architecture. Identification of causal relationships based on data and other forms of knowledge is addressed by causal discovery. Casual inference assumes existence of known causal structure and deals with identification and estimation of causal effects. Finally, statistical inference is concerned with processing and testing of a hypothesis and establishing cause-effect relationships between entities by applying various mathematical methods. Statistical inferences use information in the form of data sets and distributions (Eberhardt, 2017).

For causal discovery, information from existing knowledge on variables, system architecture, and elementary principles from domains of physics, chemistry, and biology that are integral to the system behaviour are gathered and presented as functions, organs, and decompositions to fundamental units (e.g., mass, length, time, and temperature) (A. Simon & Iwasaki, 1988; de Kleer & Brown, 1986; Iwasaki & Simon, 1994; Mokhtarian et al., 2016). Taxonomies and rules have been developed by different researchers, which extract and represent knowledge to aid in causal discovery. Causal discovery can be conducted using causal graph modelling (CGM) techniques, e.g., cyclic and acyclic bond graphs and directed acyclic graphs (DAGs) (Filippo et al., 1991; Pearl, 2000). DAGs, for example, are used to represent Bayesian networks (see Section 2.4.4).

Glymour et al. (2019) reviewed the different causal discovery methods and algorithms, which can be classified as constraint-based, score-based, and functional causal models. The traditional method for discovering causal relationships involved use of interventions or randomized experiments. These experiments are expensive, time-dependent, and at times impractical. As a result, causal discovery through

analysis of purely observational data gained popularity (Spirtes et al., 2000). The development of algorithms and advanced computation techniques have advanced the combination of observational and experimental data to establish causal relationships between variables in the ecology, clinical medicine, genomics, economics, neurosciences, and engineering domains. Conditional independence (Markov chains) relationships in data are used to uncover underlying causal structure. Algorithms like PC and fast causal inference (FCI) are constraint-based algorithms, PC uses a set of statistical tests and rules to determine the conditional independence of the variables in the graph. The PC procedure starts with forming a completely connected undirected graph representing all the variables and then eliminating the different edges based on conditional independence tests. Like the PC algorithm, FCI does pruning of the undirected graph based on statistical independence judgements; in addition, FC can identify unknown confounding variables that exist in the network. The discovery of these confounding variables informs the user that a certain variable that was not considered as part of the initial causal graph plays a significant role in defining the system. The algorithms rely upon predefined causal architecture, and through iterative statistical procedures modify the graph to represent nodes that satisfy conditional independence.

Directed graphical causal models (DGCM) have the following components: a set of variables, directed edges between pairs of variables, and joint probability distribution over the entire network of connected variables. The network is comprised of variables that may be time-indexed and may also include a set of causally related stochastic processes, unmeasured variables, measurement errors, omitted sources of variation (noises or disturbances), and choice biases. The variable states can be categorical, ordinal, or continuous. Structural equation models (SEMs), or functional causal models (FCMs), form a class of DGCM that assumes each variable is a deterministic function of its direct causes and disturbances represented in the graph (Goudet et al., 2018; Petersen & van der Laan, 2014).

Probabilistic causation has had a paradigm shift from absolute determination of an effect due to occurrence of a cause to the occurrence of cause increasing the probability of an effect. Pseudo-indeterminism assumes that the specified cause alone is not sufficient to determine an effect, but it does so in conjunction with unspecified causes (Steel, 2005). Cause-effect relationships falling under the assumption of pseudo-indeterminism may be encoded into graphical structure known as directed acyclic graph (DAG). Availability of field knowledge of causality

helps represent the manufacturing process in form of causal graph models. These models can form the basis for developing data-driven models that have improved robustness and prediction power for shifting distributions of input data. The statistical independence and invariance properties of causal graph modelling allow it to neglect the effects of confounding disturbances. Thus, causal graph models are effective in retaining information while successfully discarding the disturbances.

Section 2.4.2. summarizes the research work in modelling and simulation of wire arc additive manufacturing and powder bed fusion processes using finite element modelling method.

2.4.2 Finite element modelling for additive manufacturing

The numerical simulation models for powder bed fusion (PBF) introduce computationally expensive and complex-coupled physical phenomena such as melt pool behaviour, heat transfer, fluid dynamics, vaporization, and chemical reactions within the melt pool (Luo & Zhao, 2018). The complexity of finite element (FE) models is dependent on the geometry of the part, inherent coupled physics models, and mesh properties. These parameters along with the computational capabilities of the processing system can prolong the time required for evaluating the simulation. The primary purpose of FE simulations of the PBF process is to investigate the relationship between process parameters and quality (geometric and mechanical properties) of the printed part. Material properties of metal alloys such as thermal conductivity, specific heat, thermal expansion coefficient, density, and viscosity are temperature dependent; hence, to obtain accurate simulation results, the changes in these properties as a function of temperature need to be accounted for during model development. However, average values for these properties are often assumed in FE modelling to reduce the computational cost.

Mesh properties determine the convergence of the numerical computation, accuracy of the results, and computation efficiency. The regions of interest such as the deposited bead or layer can have a refined mesh, while the base plate or the extremities of the powder bed can have a coarser mesh. Heat source models are critical to accurately simulate the heat input provided to the powder bed or the wire. Goldak's double ellipsoidal Gaussian heat source model for welding torch is a widely accepted heat source model used in most FE simulations (Goldak et al., 1984). Adaptions of this model are used in FE simulations of laser-based and arc-based

metal AM process (Montevecchi et al., 2016; Velaga & Ravisankar, 2017). Boundary conditions are predefined for the different heat transfer modes: conduction, convection, and radiation. Assumptions related to convection and radiation are made to reduce computational cost; however, these assumptions introduce minor errors in the result of the simulation.

Latent heat during phase changes is usually neglected to simplify FE models. Some studies have considered temperature load rather than using heat source models in order to reduce computational cost (Zaeh & Branner, 2010a). A line heat source model has been introduced to replace the Gaussian moving point heat source, with claims that the model has a 10% displacement error in each time step, while the overall time to convergence is reduced to 1/10th of the moving heat source model (Irwin & Michaleris, 2016). The FE model for PBF includes non-linear transient thermal analysis and quasi-static elastoplastic mechanical analysis. The temperature field data generated in the thermal analysis is used as an input in the mechanical analysis to approximate the thermal stresses and deformation. Weakly coupled thermo-mechanical simulations are performed due to the reduction in computation time (Cheng et al., 2016).

The element birth and death technique is utilized to simulate the effect of thermal-mechanical phenomena (Michaleris, 2014). The geometric model of the powder bed and the printed part is created first. The geometric model mesh elements are deactivated at the start of the simulation. Based on the laser movement, specific zones of the geometric model are activated using an activation function. The activation function follows the real experimental laser beam trajectory to simulate the deposition process. Table 3 summarizes recent work involving FEM simulations for SLM and WAAM processes. The FEM simulations are an important asset to model and validate multi-physics phenomena in AM. The simulation models can be validated for specific material-process combinations via conducting physical experiments (fabrication). The data collected from the validation experiments can help improve the FEM model accuracy by revisiting some of the model assumptions and parameter settings.

Table 3: Literature on FEM used in SLM and WAAM processes

Study Objective	Material	Highlights	Article
SLM Process			
Developed Multi-layer deposition simulation	Ti-6Al-4V	Melting pool shape and dimensions were predicted and validated. Temperature gradient and thermal history for multi-layer build up were generated.	(Fu & Guo, 2014)
To predict temperature distribution	90W-7Ni-3F	Reduced layer thickness, narrower scan interval, and slower scan velocity improved temperature control in the powder bed.	(D. Q. Zhang et al., 2010)
Developed models for Thermo-mechanical stress	Ti-6Al-4V	Method to account stress relaxation in thermo-elastic-plastic simulations	(Denlinger et al., 2015)
Simulated models for residual stress and deformation	Tool Steel X3NiCoMo Ti 18-9-5	The simulation results for residual stress measurements were slightly higher compared to the neutron diffractometry method	(Zaeh & Branner, 2010b)
Simulation models for temperature field	316L	The static temperature field during melt pool formation was simulated	(X. Yang et al., 2021)
WAAM			
Developed models for temperature field	AZ31 (mg alloy) & G4Si1 (steel)	Influence of wire feed rate and weld path orientation on temperature evolution was modelled	(Graf et al., 2018)

Modelled thermal behaviour for idle time prediction	235JR steel	Methods helps maintain constant interpass temperature and molten pool size	(Montevecchi et al., 2018)
Transient thermal history and stress distribution	2Cr13	Von Mises stress distribution for developed for the weld layers and baseplate	(Ge et al., 2019)
Thermo-mechanical model	IN718, SS316, 800H	The results of FEM simulation and experiment studies were used to validate the prediction accuracy of two ML models: ANN and random forest	(Wu et al., 2020)

The FEM models can provide valuable process-physics data which can be used in other modelling approaches to move towards generalisability within a specific process-material combination. Section 2.4.3., provides summary about these other modelling approaches that can benefit from data of the FEM simulation models.

2.4.3 Meta models and multidisciplinary optimization

The typical engineering design approach is composed of four phases, namely, (i) planning and clarification, (ii) conceptual design, (iii) embodiment design, and (iv) detail design (Pahl et al., 2007). Traditionally, product design applied a linear process wherein different departments (e.g., sales, customer service/feedback, design, production, and management) provided inputs at different stages of the product design cycle leading to inefficiencies and poor choices of materials and manufacturing alternatives, resulting in unreliable and lacklustre products. The advent of concurrent engineering philosophy meant inputs from all stakeholders were integrated into the product design cycle early on. The result was development of structured functions/requirements and identification of constraints for the various design alternatives. The different inputs and requirements provided by stakeholders increases the complexity of the design problem as multiple design goals need to be satisfied.

The current state-of-the-art in heuristic optimization methods applied to AM is largely focused on MDO methods for specific problem formulations. For example, part build orientation has been studied to optimize trade-offs of surface quality and part quality in direct metal laser sintering (P. Das et al., 2015). Researchers have also formulated MDO problems to perform topology optimization and improving mechanical properties (Mirzendehdel & Suresh, 2015; Plocher & Panesar, 2019).

Modelling and simulation has been key to advancing research efforts in AM. Accessibility to these developed AM models and proprietary software is restrictive (Witherell et al., 2014). There is a need for consolidated efforts by researchers in academia and industry towards developing composable and reusable AM models that can be adapted for different process-material combinations. The modelling and simulation efforts in AM are towards these three goals: (1) optimization of process parameter settings, (2) in-situ monitoring and real-time control of the process for part quality, and (3) part qualification.

In case of powder bed fusion models, the simulation models need to address the following multidisciplinary phenomena of powder melting, thermo-fluid mechanics, heat transfer, and material behaviour and mechanics. To do so the models need to include definitions for the heat source model, heat transfer behaviour, melt pool formation, and solidification. The physical and metallurgical phenomena are described in the model using set of governing ordinary or partial differential equations involving parameters and variables. Based on the level of abstraction, the metamodels developed can be classified as high-level, specialized, and low-level models (Witherell et al., 2014). High-level models represent the general overarching phenomena, while specialized models are process- and material- specific, and low-level models have the maximum level of detail. Ontologies are an effective means to represent the components (parameters and constraints) of the model.

Roh et al., (2016) provided a proof of concept for ontology based metamodels in additive manufacturing was developed using Protégé software. The visualization for the model was in the form of a graph that represented the role-relation hierarchies for the process using NavigOwl ontology visualization tool. The approach developed a framework for establishing these relationships and connections but lacked the mathematical engine to provide simulation results. Predictive metamodels using response surface modelling and kriging models have been utilized to improve accuracy and reliability of AM process (Al-Ahmari et al., 2016; L. Cao et al., 2021; J. Li et al., 2021) . Yang et al., (Z. Yang et al., 2016) proposed

use of minimum Euclidean distance and maximum predictive error updating method to improve the metamodel prediction through selection of different combinations of samples from a list of full-factorial design of experiments.

Metamodels can be used to represent the AM process, additionally it can aid in manufacturing decision making, process monitoring and control. Decision support systems (DSS) solutions for complex decision making and problem solving became widespread in the 1970s with the growth of computer technology. Over the past several decades, the utility of DSS has improved, and with manufacturing moving towards more automated processes, solutions have been developed leading to intelligent decision support systems (IDSS) and cyber-physical production systems (CPPS) (Eom & Kim, 2006; Zhou et al., 2008). DSS can serve as passive, active, or cooperative systems depending upon their functionality. The available literature categorizes DSS into five types, namely, model-driven, data-driven, knowledge-driven, document-driven, and communication-driven systems.

A model-driven DSS is typically not data intensive, rather it uses analytical models, simulation tools, and optimization methods to generate multiple experiments depicting the effects of alternative decisions. Monte Carlo simulation, discrete event simulation, probabilistic forecasting, agent-based and multi-agent simulation, system dynamics, and visual simulation are some of the common simulation methods used in a model-driven DSS (Hilletofth et al., 2016; C. Li et al., 2016; F. Zhang et al., 2016). A data-driven DSS, on the other hand, utilizes structured data, such as internal and external company data, time-series data, and real-time data (Power, 2001). Business intelligence systems or online analytical processing (OLAP) are examples of data-driven DSS that enable better decision support by formulating decisions through triggering, manipulating, and/or analysing data. However, accurate and structured data are a key requirement in developing data-driven solutions and, thus, efficient data processing could enable fast and accurate decision making (Chaudhuri et al., 2011; Pillai, 1990). Knowledge-based DSS (e.g., machine learning using neural networks, fuzzy logic, and genetic algorithms) have evolved from their predecessors, known as rule-based expert systems. Such rule-based expert systems used heuristics to solve problems with the help of human expert knowledge stored in databases. In the age of big data, the challenges pertaining to the properties of data (i.e., volume, variety, velocity, veracity, validity, and value) need to be addressed to improve the process of decision making (Kaisler et al., 2013; L. Zhang, 2014).

Decision support for manufacturing process selection has been of key interest for the AM research community. Such systems require evaluation of design and manufacturing capability to choose the right process for a specific design. Selection criteria for design elements are often objective and can be expressed in the mathematical form to be either maximized or minimized. However, trade-offs involving conflicting selection criteria may introduce a certain level of subjectivity which, when combined with the existing complexity of the evaluated problem, makes the selection process difficult. In addition, for AM, material selection, process selection, and shape selection are not to be considered as independent, mutually exclusive entities, rather they must be addressed with a focus on overlaps and interrelationships (Lovatt & Shercliff, 1998). Wang et al. (2018) developed a DSS for AM process selection using a hybrid multi-criteria decision-making method. They used the analytic hierarchy process (AHP) combined with a technique for order preference by similarity to an ideal solution to explore and refine the solution space and to rank suitable alternatives. Technical and economic aspects of processes were considered when making decisions, however, the method required development of probabilistic models for representing each process and its capabilities for initial sampling based on customer preferences obtained through the AHP. Such an approach implies the need for large amounts of data relating to each technical or economic aspect of interest for training.

2.4.4 Bayesian networks

In additive manufacturing, machine learning (ML) algorithms can help in performing design and topology optimizations, optimizing of process parameter settings, targeted tailoring of materials, in-situ monitoring and control of the process (C. Wang et al., 2020). The ML algorithms can be classified as unsupervised, semi-supervised, and supervised models. Unsupervised models are used to train unlabelled data, it is a data-driven methodology that can uncover hidden patterns in random data and perform clustering. It is mainly used for anomaly detection, market segmentation, and recommendation systems (Raina et al., 2007). Semi-supervised models such as reinforcement learning, do not require training data sets, instead the models interact with the environment to adapt and perform the most suitable actions which will result in a reward (reward when positive and punishment when negative) (Khan et al., 2012). Lastly, supervised models are set of algorithms that require

labelled datasets during training phase, to predict unlabelled datasets in validation and test phases (Alloghani et al., 2020).

Wang et al., (2020) provide a detailed account of the different ML models used in various AM research work. Uncertainty quantification (UQ) needs to be considered during the development of models representing AM process (Hu & Mahadevan, 2017). The UQ methods presently reported follow experimental approaches performed at process level. There are uncertainties arising from natural variability in the system known as aleatory uncertainty. These cannot be eliminated (e.g., particle size and shape in PBF, mechanical properties, and material coefficients). Another type, epistemic uncertainties arise from the lack of completeness of the models and data uncertainties.

Bayesian Network (BN) models have been proven to model uncertainties into the models (Nannapaneni et al., 2016). BN allows for forwards and backwards simulations. The forwards simulations allow for aggregation of knowledge from varying sources (e.g., data, other models, expert opinion) to quantify the overall uncertainty in process outputs measure such as cost, materials, and energy consumption. While the backwards simulations are used for fault diagnostics, process parameter tuning, and performance optimization. BN is a probabilistic graph-based model with the Bayes' probability theorem at its core. The network comprises of nodes and connections between the nodes (arcs). These arcs are unidirectional arrows which relates the parent node to child nodes. A few of the recent studies that have used BN in the additive manufacturing context are listed in Table 4.

Table 4: Recent works in additive manufacturing field with emphasis on Bayesian network

Reference	Objective	Outcomes
(Jing & Ma, 2020)	Framework for implementation of fuzzy Bayesian Network-based models for exploration of adaptability of AM processes.	1. Defined the influencing factors under two categories: (a) Fundamental features and (b) System characteristics 2. Expert knowledge and engineering experience is represented using fuzzy linguistic terms 3. Sensitivity analysis was performed to identify the significance of the different influencing factors
(Hertlein et al., 2020)	Bayesian network model in hybrid domain relating four process parameters (laser power, scan speed, hatch spacing, and layer thickness) of SLM to part quality characteristics.	1. n-dimensional complex hull is constructed for successful builds based on known training data. 2. the convex hull relies on empirical data rather than process physics-based reasoning. 3. Training feedback loop to accept new observed data into the BN model
(Haruna & Jiang, 2022)	A framework is developed using Fuzzy BN for DFAM decision-making.	1. Probability fluctuations are computed to carry out sensitivity analysis on DFAM adaptiveness based on the six parent nodes (C, D, E, F, X, and Y). 2. Conflict measure was used in the decision making to identify uncertain knowledge representation and probabilistic reasoning.
(Ye et al., 2021)	BN approach is used to carry out uncertainty quantification analysis for AM simulation models comprising of a suite of hierarchically linked PSPP simulation models.	1. Two Gaussian process surrogate models are established to link the inputs and outputs of the hierarchical physics-based simulation models of finite element thermal models and phase field microstructure model. 2. The outputs of the GP models are then translated into DAG to create BN model representing the complete simulation models. Hyperparameters are introduced to account for the model bias and calibrated based on observed experimental data.

		3. Demonstrated the use of BN to develop coupled surrogate models defining the PSPP interactions.
(R. Chen et al., 2021)	Development of ontology-based BN model representing causal relationships between AM process parameters and quality control requirements.	1. Hybrid learning algorithm was integrated with ontology graph to identify causal relationships between variables in AM to create the BN graph. 2. The efficacy of the network learned with and without the integration of the AM ontology in the hybrid learning algorithm was established.
(Nagarajan et al., 2020)	Systematic literature review on welding and it's impact on worker health in order to develop BN model.	1. Developed a causal graph linking process parameters in welding to intermediate parameters such as fume generation rate, composition of the fume, cumulative fume exposure to final impact on worker health. 2. Proposed the use of BN model to integrate manufacturing process information (experimental data collection), impact on health (statistical data from literature), and safety measures (regulations and safety equipment) to develop online monitoring for worker safety.
(Goguelin et al., 2021)	Bayesian optimization to determine optimal build orientation to reduce the need for support structure in printing overhang geometries.	1. Bayesian optimization, grid, and random search technique algorithms were tested to determine the best possible orientation to reduce the number, volume, and length of supports for overhang structures. 2. Bayesian optimizer outperformed both the grid and random search optimizers in identifying the best solution in least number of iterations. 3. Global maximum solution is not guaranteed using the Bayesian optimizer, but the median solution obtained in near the global optima.
(Aminzadeh & Kurfess, 2019)	Computer vision and Bayesian inference is used as online part quality monitoring system for LPBF process	1. Bayesian classifier is trained based on live images capture in-situ the layer deposition.

	2. Supervised learning approach was implemented, wherein the training dataset was labeled for each image. 3. Overall the performance of the classifier developed and trained was commendable with high true positive rate (89.5%) and high true negative rate (82%)

2.5 Summary

Chapter 2 provided a detailed overview of the research activities in the field of cryogenics, high temperature superconductors, additive manufacturing, and modelling and simulations methods. The following text summarizes the chapter and establishes the research gap existing in the field of modelling and simulation for additive manufacturing.

Depending on the application, the functional requirements of the product and operating conditions for which they are designed can be extreme. Section 2.1.2. (Cryogenics in manufacturing applications), provided insight to the benefits of using cryogenic machining for working with metal alloys. It also highlighted how the exposure of metallic alloys to extremely low temperatures (70K – 120K) can bring about changes in the microstructure and mechanical properties. To the best of author's knowledge there were not many works reporting the behaviour of metal parts made using AM processes tested in cryogenic temperature ranges. The information on these may not be easily accessible due to the proprietary nature of the research. Nevertheless, the work done in this dissertation has provided the opportunity to perform these tests and report the results in public forum. Section 2.2 (High temperature superconductivity) summarized the ongoing research work done specific to development of HTS magnet technology. It is important for the readers of this dissertation to get familiarized with some of the functional requirements and challenges (design and manufacturing) in HTS magnet development to better understand the underlying motivation of the work. Section 2.3. (Additive manufacturing) highlights the ongoing research activities in this field. The literature study focuses on two processes wire and arc additive manufacturing and selective laser melting. The studies discussed in the section hint towards the need

to have models in AM that are generalisable, modular, composable, and can be easily adopted across process-platform limitations. Section 2.4. (Modelling and Simulation), provides the recent advances in the field of modelling and simulation techniques used in the additive manufacturing context.

The thesis work contributes towards development of modelling methodology that can aid in early design and manufacturing decision-making and optimization. Chapter 3 Methodology covers the different steps involved in development of these models. The text in the subsequent chapters will refer to the publications that are attached towards the end of the dissertation. The methods were developed and reported in series of seven publications. Chapter 4 Result and Discussions provide an overview of the findings of these research articles. Chapter 5 Conclusions highlight the contributions of the work and future research opportunities.

3 METHODOLOGY

This chapter introduces the methodology developed as part of the dissertation to address some of the challenges and limitations identified via the review of literature in the domains of cryogenic applications, high-temperature superconductor technology, additive manufacturing, and manufacturing process modelling and simulation. The chapter briefly summarizes the steps involved in development and implementation of a hybrid modelling methodology for product design and manufacturing decision support. The contents of the chapter are excerpts from the publications that are part of this dissertation research.

3.1 Data collection methodology

As seen from discussions in Section 2.4, systems can be modelled based on different forms of knowledge. Here, the different types of information used in creation of the models are discussed in detail. Experimental data involves manufacturing process parameters, design of experiments used to identify influential process parameters, results from mechanical and material property characterization of the fabricated parts, data from sensors and monitoring devices, and metrology data. The raw data collected undergoes data processing before it can be used in suitable modelling and simulation methods. These steps are described in more detail below to support modelling of two additive manufacturing processes: wire and arc additive manufacturing (WAAM) and selective laser melting (SLM).

3.1.1 Manufacturing process data collection

In Publication I (Panicker et al., 2022), WAAM was used to produce thin walls from two feedstock materials (mild steel and high-strength low-alloy steel). The experimental setup for the manufacturing process and data collection process are

described here. The WAAM-CMT setup (shown in Figure 3) consists of a welder and wire feeder (Fronius CMT Advanced 4000), a 6-axis industrial robot with 3-axis worktable (ABB 4600 40/2.55), and an inert shielding gas supply.

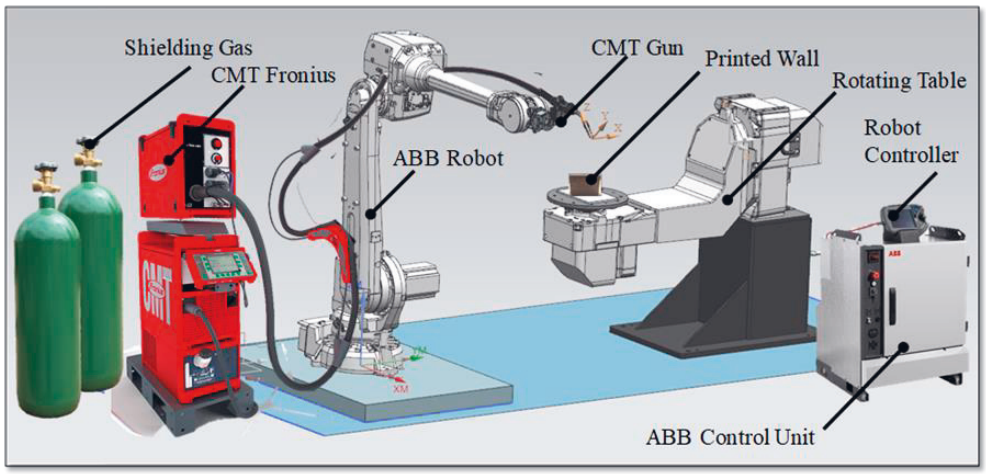

Figure 3: Wire and arc additive manufacturing (WAAM) setup used in this research

The robot path program was generated using Robot Studio 6. An infrared pyrometer (Micro-Epsilon) in tandem with temperature measurement software (Compact Connect v1.9) was used to measure and record the temperature of the weld during fabrication. In addition, a contact-type digital thermal probe (Center 314 humidity temperature meter with a K-type thermocouple) was used to monitor the interpass temperature between consecutive weld passes. Welding was performed with cold metal transfer (CMT) technology, which alters arc length and thermal input during welding by controlling material transfer (droplet removal) to the melt pool through a short-circuiting phase. During this phase, the wire feeder dips the molten droplet into the weld pool and retracts the wire at a specific frequency (50-120 Hz) to detach the droplet through surface tension. The controlled wire oscillating motion in the nozzle is carried out at zero current, lowering heat input to the weld. The fast-retracting motion results in near spatter-free droplet transfer. Further, the lowering of heat input enables the fabrication of thin-walled structures (a few millimetres in thickness). Table 5 shows chemical composition of the different wire feedstocks that were used for fabrication of test components using WAAM technology.

*Table 5: Wire feedstock chemical composition (*reported in Publication I)*

Elements	G4Si1* (wt. %)	AM70* (wt. %)	SS316L (wt. %)	AL4043 (wt. %)
C	0.090 %	0.08 %	0.02%	-
Mn	1.670 %	1.700 %	1.80%	0.15%
Si	0.87 %	0.60 %	0.80%	5.00%
S	0.006-0.010 %	0.000 %	0.015%	-
P	0.004-0.010 %	0.000 %	0.015%	-
Cr	0.000 %	0.200 %	18.50%	-
Mo	0.000 %	0.500 %	2.70%	-
Ni	0.000 %	1.500 %	12.00%	-
Fe	98.133 -98.143 %	95.42%	64.05%	0.6%
Cu	-	-	0.1%	0.3%
Mg	-	-	-	0.2%
Al	-	-	-	93.35%
Ti	-	-	-	0.15%
Zn	-	-	-	0.10%
Others	-	-	-	0.15%

To collect data representing the mechanical and microstructural properties of the materials processed using WAAM, thin walls of given dimensions were fabricated and characterized as shown in Figure 4.

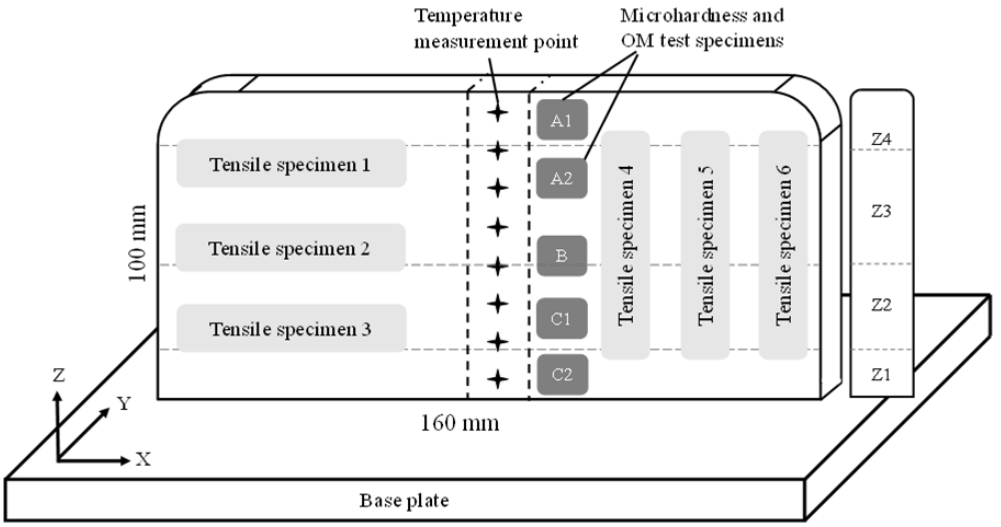

Figure 4: Schematic for deposition wall with locations of temperature measurement and mechanical samples marked

Similarly, specimens were printed to evaluate the tensile strength, hardness, microstructural characteristics, and electrical and thermal properties of materials processed using SLM. Table 6 provides the chemical composition of the four alloys that were considered in this work. The powders used in the process were purchased from SLM Solutions AG. CuNi2SiCr, Invar36, and SS316L alloys were printed by an industry partner (3DStep Oy) using an SLM 280HL printer.

Pure Cu samples were printed in collaboration with EOS Manufacturing Turku. The process parameter settings used for printing of pure Cu are proprietary. Along with samples for the various characterization tests, a mechanical component used in a miniature prototype HTS magnet was printed using the EOS powder-based system.

Table 6: Chemical composition of powder stock used in SLM process

Elements	Pure Cu (wt. %)	Invar36 (wt. %)	SS316L (wt. %)	CuNi2SiCr (wt. %)
C	0.0 %	0.10 %	0.03%	-
Mn	0.00 %	0.50 %	0.00%	0.10%
Si	0.00 %	0.50 %	0.80%	0.60%
S	0.00 %	0.00 %	0.00%	-
P	0.00 %	0.00 %	0.00%	-
Cr	0.00 %	0.50 %	18.00%	0.25%
Mo	0.00 %	0.00 %	2.25%	-
Ni	0.00 %	36.00 %	13.00%	2.50%
Fe	0.00%	61.90%	65.92%	0.15%
Cu	99.95%	-	0.00%	96.3%
Others	0.05%	0.50%	-	0.10%

The print bed layout is shown in Figure 5. Design details for the prototype HTS magnet is proprietary and hence withheld from publication in this dissertation. However, residual stress analysis using X-ray diffraction was conducted for the prototype, and the results have been presented in this work.

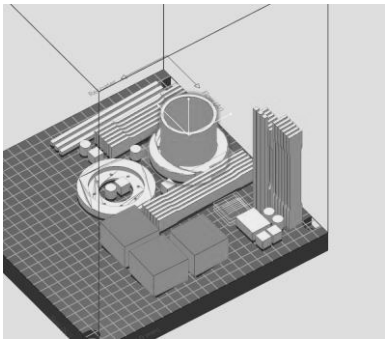

Figure 5: Print bed layout for printing of pure copper samples

As-built and heat-treated mechanical test specimens were studied. The heat treatment was performed for stress relief based on the recommendation in the material data sheet of the powders (EOS, 2022; SLM Solutions, 2019).

3.1.2 Mechanical characterization

The thin walls printed using WAAM were separated from the base plate using a band saw. Next, a CNC milling machine was used to remove specimens for hardness and microstructure evaluation. The tensile test specimens were face milled to ensure uniform thickness (~2.5 mm), as shown in Figure 6. Microhardness tests were performed in accordance with ASTM test standard E92-17 using a Vickers microhardness tester (Matsuzawa MMT-X7) with a test load of 9.8 N and dwell time of 10 s. Tensile properties (i.e., YS, UTS, and percent elongation) were investigated according to EN ISO 6892-1:2019 (Annex B) with tests conducted using an Instron 8800. A crosshead speed of 0.01 mm/s and an initial strain rate of 0.00025/s were set, based on the test standard.

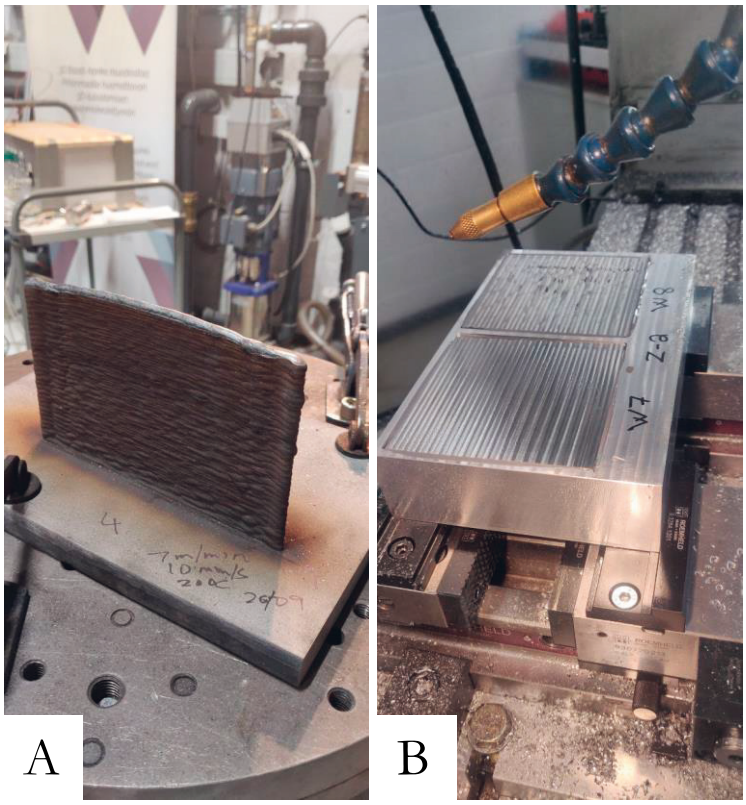

Figure 6: (A) Stainless steel wall printed with WAAM & (B)Face milling of the wall

Along with tensile test and microstructure specimens, specimens were cut from the wall for electrical resistivity and thermal conductivity characterization.

3.1.3 Electrical resistivity and thermal conductivity characterization

Electrical resistivity and thermal conductivity of the printed metal AM specimens were measured using a conduction cooled cryostat and in a liquid nitrogen bath. A conduction cooled cryostat consists of eight components (identified in Figure 7). The main components of the cryostat are multi-layer insulation (a), a radiation shield (c), a Dewar or vacuum chamber (d), a helium gas compressor (e), a two-stage cryocooler (f), and a sample holder (h), as well as two auxiliary systems: vacuum pumps (b) and an instrumentation cluster (g).

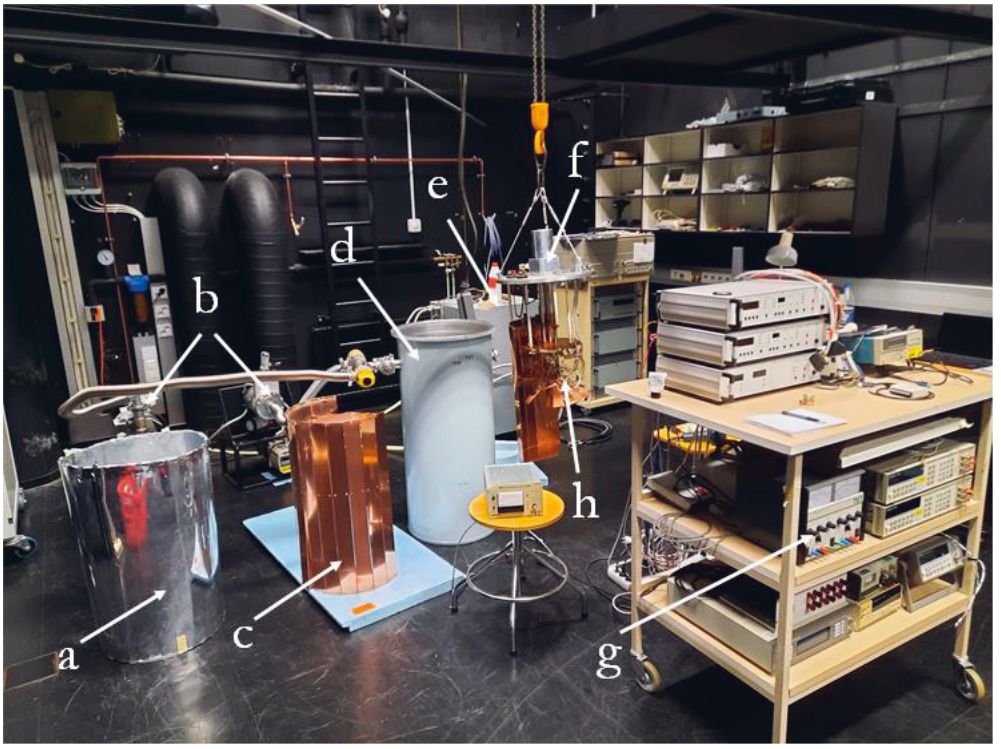

Figure 7: Different components of a cryostat (see accompanying text for details)

The Cryomech GB-04 cryocooler is connected to a He-compressor (CP640COPW7). Temperature is regulated using additional heating elements, as it is not possible to directly control the cooling power of the cryocooler. The lowest achievable temperature depends on heat load, vacuum level, and cooling capacity of the cryocooler. The cryostat is divided in two regions (two stages): the first stage is closer to the cryocooler (maintained between ~57-80 K) and the second stage (maintained between 11.5-50 K). The second stage has additional heating elements which are used to regulate the temperature in this region. For the experiment, the cryostat is cooled down to 11.5 K at $2e^{-5}$ mbar vacuum pressure. It takes approximately 20 hours for the cryostat to cool down to the above-mentioned temperature. Once the cryostat is stable and operating at the set temperature, heating elements are used to raise the temperature of the second stage. The sample holders for performing the electrical resistivity and thermal conductivity measurements are attached to the second stage of the cryostat. These sample holders are shown in

Figure 8. Additional heaters and temperature sensors are mounted on the sample holders for monitoring and control purposes.

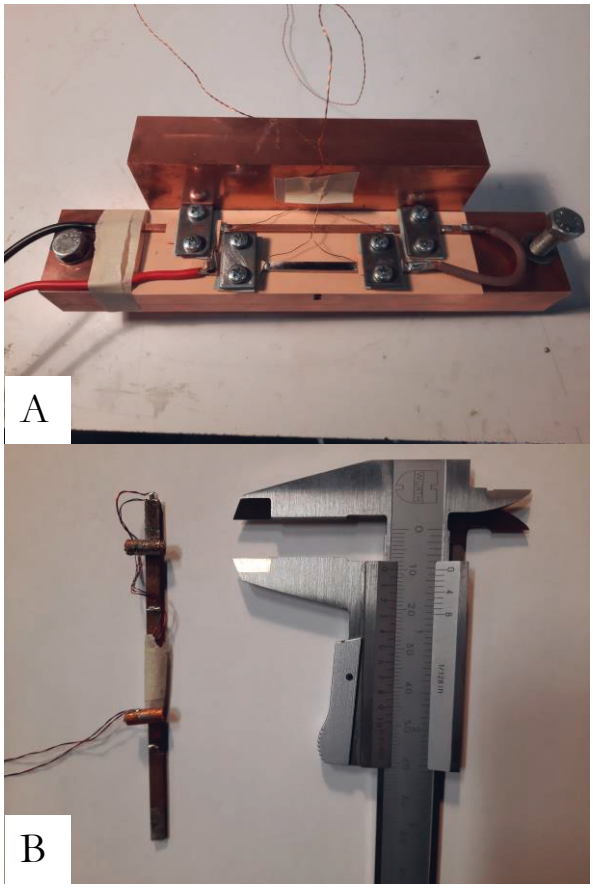

Figure 8: (a) Sample holders for electrical resistivity (b) Soldered caps for mounting Cernox sensors

The two sample holders provide mechanical support, ease of installation for instrumentation, and a thermal interface between the mounted sample and second stage of the cryostat. Electrical insulation between the sample and sample holder was provided using a thermally-conductive silicon rubber. Apiezon N grease was used to improve the thermal contact between samples and the holder. Temperature readings of the sample were recorded using Cernox sensors that are rated for use in cryogenic applications. Cernox sensors were also mounted on the sample holder and the first stage of the cryostat for monitoring and control of the temperature inside the Dewar.

The sample holder allowed for simultaneous measurement of electrical properties of two samples of differing length. The four-point probe resistivity measurement technique was used to estimate sample resistivity over a range of temperatures (see Table 9 and Figure 26). Measurements at 77 K were performed by emersion of the samples directly in a liquid nitrogen bath. A known current was applied using a cryogenic magnet power supply through the samples connected in series. All connections were soldered. Resistivity (ρ) was then derived from the Equation 1:

$$\rho = \frac{U}{I} \times \frac{A}{l} \quad \text{Eq. (1)}$$

where U, I, A, and l are the voltage, applied current, sample cross-sectional area, and distance between voltage taps, respectively. HP 3458A digital multi-meters were used for measuring voltage. Data logging and current supply control was performed automatically via LabVIEW.

Thermal conductivity measurement for the metal AM samples was carried out following a similar procedure as reported in the work of Hiltunen and colleagues (Hiltunen, 2010; Hiltunen et al., 2009).

3.1.4 Microstructure characterization

To characterize material microstructure, the metal alloy specimens were first mechanically polished using a Struers Tegramin-30 polisher and etched using a suitable chemical solution for each alloy. Microstructures of the prepared specimens were then observed and recorded using a Leica DMi8 optical microscope. The microstructural images were used to estimate grain sizes in Leica Application Suite X (LAS X version 5) software following the ASTM E112 standard using the Jeffries planimetric method (ASTM, 2021). In addition, scanning electron microscopy (SEM) and electron backscatter diffraction (EBSD) studies were conducted for the different metal alloys to identify the different phases, inclusions, and presence of defects in the printed parts.

3.1.5 Data from other sources

The previous subsections described the experimental approaches and methods utilized for data collection. Other techniques used to source information are

discussed in this subsection. Publication IV (Mokhtarian et al., 2019) used analytical hierarchy process (AHP) to capture experts' knowledge and preferences for defining the geometric dimensions and the number of supports required for printing a defect-free cantilever beam structure using powder bed fusion technology. AHP is an efficient tool to deal with complex decision-making problems since it reduces the complexity of a decision to a series of pairwise comparisons (Saaty, 1980). AHP was developed to help identify important variables in multi-criteria decision problems. The process involves three steps: decomposition, measurement of preferences, and priority synthesis. Decomposition starts with defining the goal of the study. Next, criteria and sub-criteria are defined as a basis on which the decision is evaluated. Finally, pair-wise comparison between these criteria is carried out. In the case study of a cantilever beam printed using powder bed fusion technology, a questionnaire was developed that presented experts with different scenarios for the geometric features of the cantilever beam, the overall mass of the beam, and heat energy input. The experts provided their rating (1 to 9, from equal importance to extremely more important) for each support structure design scenario. Once all preferences were captured from these pairwise comparisons, AHP was used to generate a weight for each interval, in a way that the sum of all individual interval weights was equal to one. Hence, the weights generated by AHP are equivalent to the probability of selection of that interval by experts. The process of capturing experts' preferences continued until all independent variables were considered. The weights were then used to generate the conditional probability tables for these variables in the Bayesian network model (discussed in Section 3.3).

Publication V (Panicker et al., 2019) developed a modelling methodology to integrate product sustainability performance indicators into the product development process for making better-informed design and manufacturing decisions. The model represented manufacturing decisions, design and material choices, and sustainability metrics (economic, environmental, and social). Product manufacturing cost was used as the economic metric. A bottom-up cost modelling approach was used to model the manufacturing cost. Manufacturing cost was modelled using seven cost components, namely, facility cost, capital cost, utility costs, raw materials cost, raw materials transportation cost, labour cost, and maintenance cost. These cost components are dependent upon various factors such as manufacturing location, type of manufacturing process, raw materials used, source of raw materials, and transportation modes. A holistic system model was developed

in which system variables, constraints, and decisions are clearly defined. To demonstrate the modelling methodology, two additive manufacturing (AM) processes were selected to be investigated under the approach, namely, wire arc additive manufacturing (WAAM) and electron beam melting (EBM). The sustainability performance of these processes were evaluated for the production of a shell and tailpipe assembly for a gas turbine. The design of the two components were predefined. Seven KPIs were used to evaluate the performance of the system under different domains: social performance (labour productivity), production performance (order-to-delivery lead-time and setup rate), environmental performance (energy intensity and percentage of recycled materials in manufacturing), production quality (scrap ratio), and product complexity (shape complexity).

Publication III (Coatanéa et al., 2020) formulated a set of dimensionless performance metrics to conduct manufacturability assessment of laser powder bed fusion (LPBF) for producing different components. Metrics are often used as a means of evaluating product functions during the design phase. The use of dimensionless numbers helps create generic performance metrics that can be applied to a broader spectrum of functional use cases. The use of dimensionless metrics to represent functions is explained using an additive manufacturing case study. In LPBF, the build volume rate V (mm^3/s) is an important indicator for assessing building time and, consequently, production rate and cost. V is dependent on the layer thickness, D_S (μm), scan speed, V_{scan} (mm/s), and the scan line distance between parallel laser tracks, Δ_{ys} (μm). Other important variables affecting the overall product cost are part height, H (mm), part orientation, part surface area, SP (mm^2), and total printing time, t_b (s). A printing process is represented as a high-level functional model in Figure 9, where the high-level function is "to print". Analytical (physics-based) models of multiple low-level functions are integrated to form the model of the high-level function.

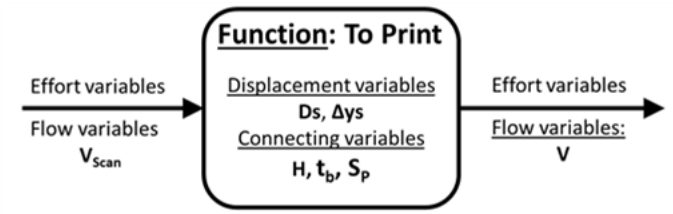

Figure 9: High-level functional diagram representing the LPBF printing

The granularity of low-level model function descriptions focuses on the key outputs of the manufacturing machine sub-functions, i.e., for LPBF: to create a layer of powder and to move the laser with respect to the powder layer. Parameters related to the different functions as well as those that specify part properties and part position on the printing table are considered. To demonstrate this approach, the development of two dimensionless metrics is explained in Publication III.

Publication VI (Chakraborti et al., 2019) developed a modelling and optimization approach towards targeted optimization of manufacturing process parameters and manufacturing cost for the mechanical support components of a high field superconducting magnet. Dimensional analysis conceptual modelling (DACM) was used to create a graph model that defines the functions and requirements of the system under study (Mokhtarian et al., 2016). First, the important manufacturing process parameters and product design parameters were identified. Information from established laws of physics (Lorentz force) and manufacturing process data (milling parameters) were then used to create the graph models. A weighted-page rank algorithm along with a graph centrality algorithm were then used to identify the important hubs (influential variables) in the graph model. Hence, the variables were separated into two clusters: high influence variables and low influence variables. A multi-objective optimization problem was formulated using the identified high influence variables to minimize manufacturing cost and the stress developed in the part.

Section 3.1. highlighted the different sources of information used in the models developed in the work. Next, the process of integrating this information to create knowledge-based models explained in Section 3.2.

3.2 Knowledge integration

Data collected from various sources must be processed to facilitate integration into graph models. Depending on the type of data and the models being developed, data pre-processing steps may include normalization, logarithmic transformation, and clustering. These steps were followed in the case studies in Publication III and VI.

In Publication III, after defining and developing the 13 dimensionless metrics related to the additive manufacturing process, 10 different part designs were chosen to be evaluated against an ideal part design meant for the PBF process (shown in

Figure 10). The matrix, comprised of the dimensionless metrics and corresponding scores for each part, was populated. This matrix was then normalized between -1 and +1. Following normalization, SVD and other clustering methods were implemented to establish the relative distances between each of these parts. The Euclidian distances of each real part to an ideal part were then calculated.

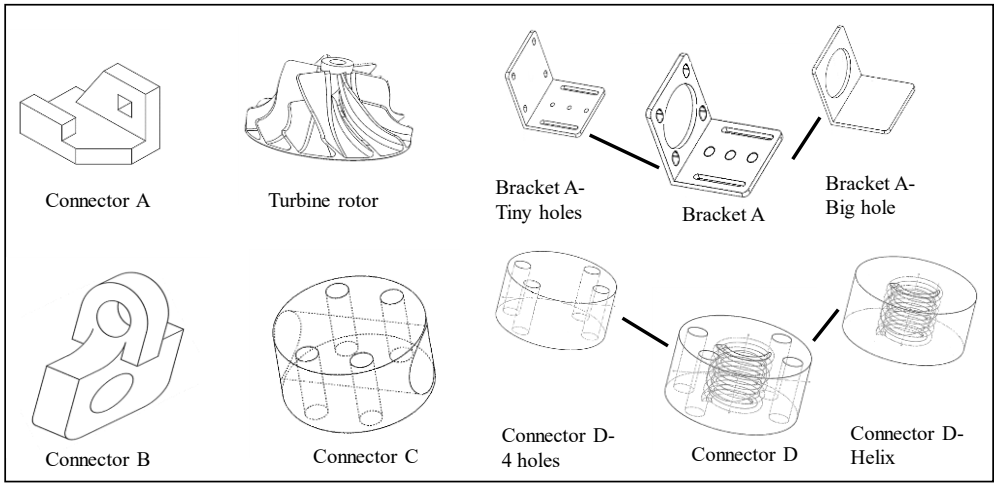

Figure 10: The case study parts used in the study

The assessed part designs were then ranked in ascending order based on their proximity to the ideal part's point in space. An interesting observation was that the ranking changes based on the number of singular values that were chosen for the evaluation. In this work, the use of mathematical tools such as SVD, logarithmic transformations, and matrix operations to facilitate computation of Euclidean and Cosine distances was realized. The Euclidean distances were visualized by plotting on a Cartesian coordinate system for ease of comprehension (Figure 11). The next work (Publication VI) discusses how information can be extracted from graphical models in order to perform mathematical operations.

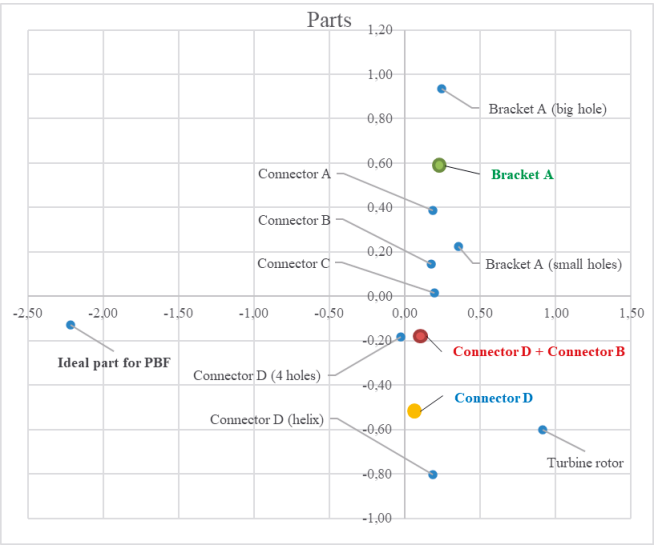

Figure 11: Spatial arrangement of case study parts with respect to ideal part based on Euclidean distances

Publication VI develops a cause-effect relationship diagram (Figure 12) based on the functional model of a simplified high temperature superconducting magnet design. The arcs that connect the nodes represent the interconnections between variables, and also note the exponent of each connection from existing equations. A "+" is assigned on the arc if an increase in the nth node increases the $(n+1)^{th}$ node. A "–" is assigned if an increase in the nth node decreases the $(n+1)^{th}$ node. Next, a multiple domain matrix (MDM) is developed from the causal graph. The MDM is a sparse, square matrix representation of the system's structure that condenses knowledge of all the variables across the functional, design, and manufacturing process domains with their weights obtained from the causal graph (network). The MDM can be considered as a collection of design structure matrices (DSM) in each domain, mapping variables in the domain to itself, as well as variables from other domains to represent the entire structure of the system. The first column of the MDM consists of all the variables in the system. The MDM is a scalable matrix capable of handling very large structures, where each DSM can contain any finite number of variables. The matrix representation of the system facilitates application of ranking algorithms and graph centrality measures to find the most influential variables of the system.

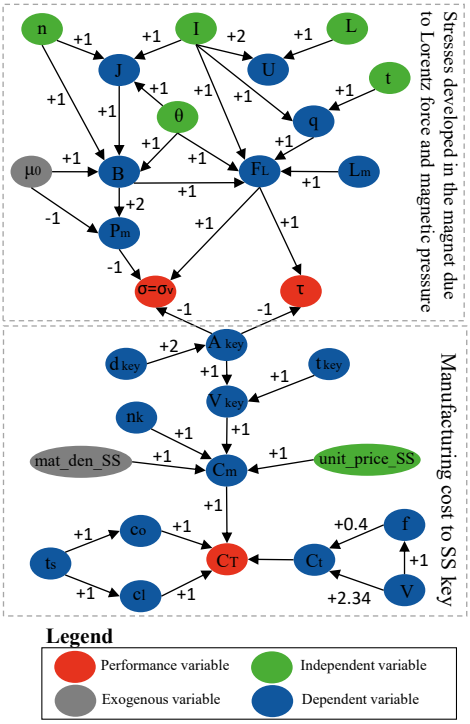

Figure 12: Cause-effect diagram connecting design and manufacturing requirements

Publication II undertook and experimental study of WAAM-CMT to develop a metamodel that associates the various welding process parameters to the geometric properties of the final part. Nine parameters of importance were identified, and single bead geometries were printed following a Taguchi design of experiments. Of the nine independent parameters, eight could be set to four different levels each and the one remaining was varied at three levels. In all, a full-factorial experiments for these nine process parameters would result in total of 196608 ($3^1 * 4^8$) individual beads to be printed. A mixed-level orthogonal plan (L32) was adopted for the design of experiments, which reduced the number of experiments to 96 single-beads. The welding process parameters for single- and multi-bead geometries are shown in Table 7. Data collected for the 96 single-bead experiments were normalized, and a two-way analysis of variance (ANOVA) test was performed. This statistical analysis helped identify five of the nine process parameters that had significant impact on the output (height and width of the printed beads).

Table 7: Study settings for single and multi-bead prints (Nagarajan et al., 2019)

	Single bead	**Multi-bead**
Base plate size (material)	300*200*20 mm (Mild steel)	300*200*20 mm (Mild steel)
Bead length (material)	50 mm (TD MAK-10S)	80 mm (TD MAK-10S)
Robot	ABB 4600 40/2.55	ABB 4600 40/2.55
DOE type (number of experiments)	Taguchi L32 (96)	Full factorial (27)
Measurement of outputs	Laser scanning	CMM
Parameter of study (levels)		
Ignition time (t_{ign})	(100, 200, 300, 400) ms	**F** (400) ms
Ignition current (I_{ign})	(90, 100, 110, 120) A	(46, 47.7, 49.2) A
Arc length correction (ALC)	(-15, -10, 0, 15) %	**F** (0) %
Wire feed rate (WFR)	(53.3, 58.3, 63.3, 68.3) mm/s	(33.34, 41.66, 50) mm/s
Travel speed (TS)	(6.67, 8.34, 10, 11.67) mm/s	(10, 11, 12) mm/s
Shielding gas flow rate (SGFR)	(14, 16, 18, 29) L/min	**F** (14) L/min
Torch angle (Φ)	(70, 90, 120) degree	**F** (90) degree
Ending time (t_{end})	(100, 200, 300, 400) ms	**F** (400) ms
Ending current (I_{end})	(125, 135, 145, 155) A	*(46, 47.7, 49.2) A
Number of layer (n)	**F** (1) layer	(9, 12, 15) layers
Wire stick-out length	**F** (15) mm	**F** (15) mm
Interpass temperature	**N/A**	150 °C
Note: **F**- Fixed parameter; *-Dependent on wire feed rate		

Wire feed rate, travel speed, torch angle, ignition- and ending- time, and ending currents seemed to have greater influence on the final geometry of the part. The initial statistical processing of data collected from the single-bead geometry helped narrow down the design space for the experiments done for the multi-bead

geometry. The modelling and simulation related to the multi-bead geometry is discussed in Section 3.3.

An extension of this work was the research that culminated in Publication I, which investigated the influence of thermal phenomena on the mechanical properties of two low-carbon steels. The influence of thermal cycles on the macro-, micro-, and meso-scale properties of additively manufactured parts is essential for development of AM models. This work was carried out to obtain data needed to develop models representing process-structure-property relationships for the two steel alloys printed using the WAAM-CMT process. Mechanical characterization tests were done to estimate tensile strength, hardness, and ductility. The tests were done on specimens obtained from horizontal and vertical orientations from the weld geometry (shown in Figure 4, above). The impacts of the process parameters and specimen orientation on the mechanical properties of the two steel alloys were explored and discussed in the publication. The high magnification light microscopy images revealed the grain sizes, grain boundaries, and phases that were formed during the solidification of the weld (shown in Figure 13). Leica Application Suite X (LAS X version 5), an image processing software was used to quantify the grain types, sizes, and phases present in the two steel alloys. Image analysis was done in accordance with the ASTM E112 standard. The results of the studies are discussed in further detail in Chapter 4. In addition to the image analysis for estimating the grain sizes and phase content, a Ferritescope was used to validate the ferritic phase content in these steels.

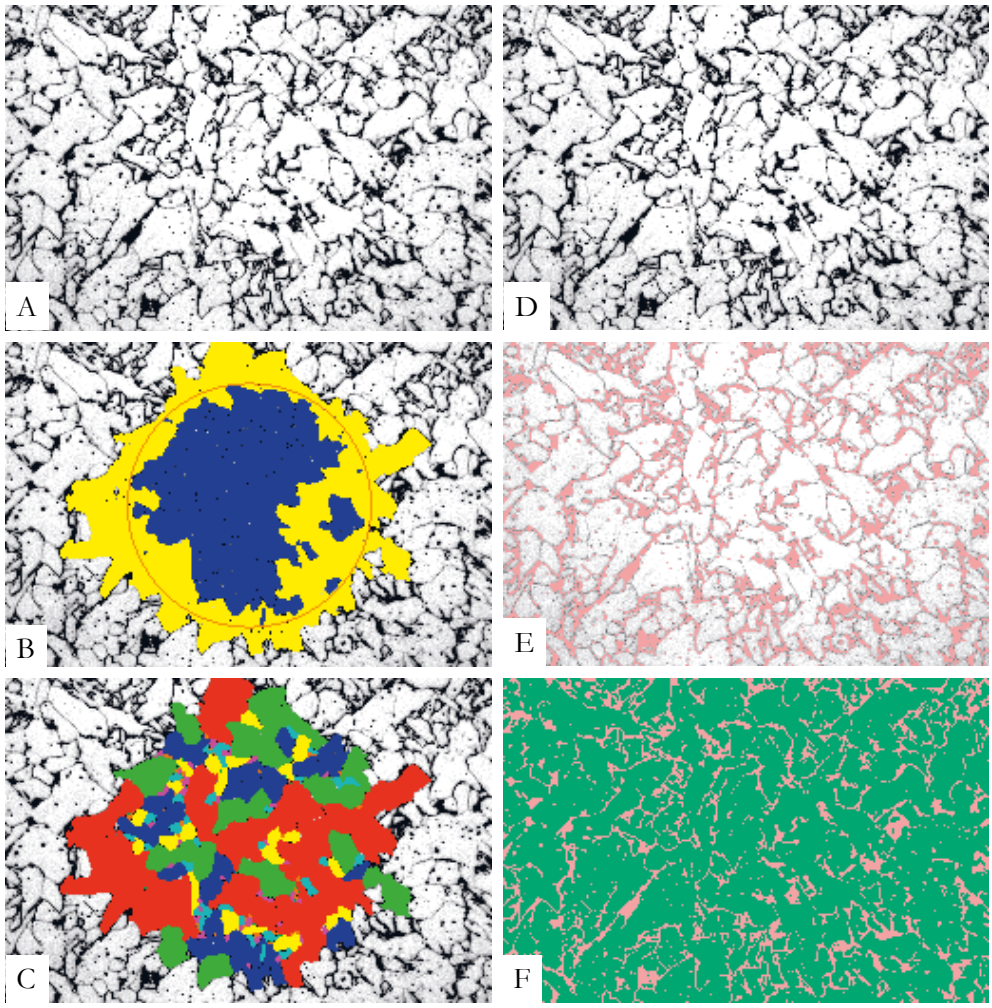

Figure 13: Left-hand side column (A-C) represents the Jeffries Planimetric method for grain size analysis & right-hand side column (D-F) represents steps involved in phase analysis performed for mild steel alloy

Publications III, IV, V, and VII showcase the different capabilities of the integrated process modelling methodology towards manufacturing decision-making, design space exploration, and sustainability assessment. The different meta-models developed in these studies are backed by presence of process data, expert knowledge, simulation model data, analytical equations, empirical equations, causal relationships, regression, and machine learning models. The integration of these different forms of data and the challenges associated with the process are discussed in the subsequent sections.

3.3 Development of integrated knowledge models

Following data collection and pre-processing, the next step is development of the models. All the publications comprising this dissertation work contribute towards advancing the modelling methodology in additive manufacturing.

In Publication II (Nagarajan et al., 2019), the experimental design space for a multi-bead geometry was narrowed down by analysing the influence of nine welding processing parameters on the height and width of a single bead. Wire feed rate (WFR) and travel speed (TS) were found to have the most significant impact on the output. In addition, the number of layers (n) was introduced as a third influential parameter for producing multi-bead geometries. Thus, a full-factorial design of experiments with three process parameters at three different levels each for the multi-bead geometry was selected. Multi-variable nonlinear regression (power law form) was used to generate a regression curve fit of the obtained experimental inputs and outputs. The regression equations obtained via the power law approach are then used to develop a Bayesian network (BN) model. The fundamental advantage of the modelling method applied in this study is its ability to generate BN models from a causal graph, which enables two-way simulation for forward prediction (prognosis) of targets and backward prediction (diagnosis) of input parameters. The simulation of the BN model allows the user to choose values for WFR, TS, and n for obtaining required target values and simultaneously allows visualizing the effects of inputs on the target values. Backward prediction is useful in manufacturing since the dimensions of the part are defined by the design requirements. It can be noted that application of BN modelling provides a validated approach to generate a grey box model in which analytic knowledge in form of equations can be used with experimental data. The results of this work are discussed further in Chapter 4.

Publication III developed a methodology to evaluate different part designs and their suitability to be printed using the laser powder bed fusion (LPBF) process. In Section 3.1.5, the creation of dimensionless metrics for evaluating LPBF was discussed. The steps ensuing metric development are presented in more detail below, with the complete manufacturability evaluation methodology shown in Figure 14.

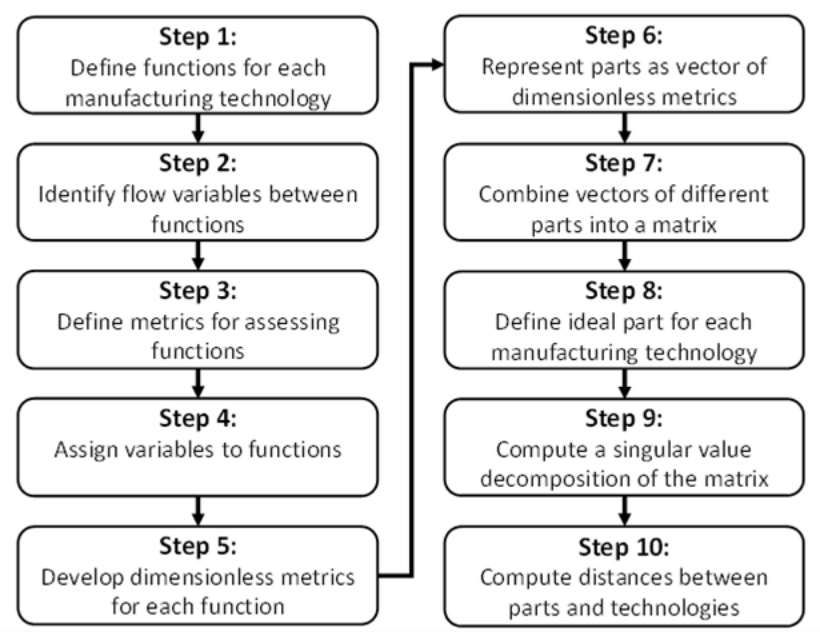

Figure 14: Manufacturability evaluation methodology (Coatanéa et al., 2020)

Matrix X is created with the different dimensionless metrics in columns and the parts to be evaluated forming the rows. This matrix is decomposed using singular value decomposition (SVD), to compute the distances of the parts under evaluation from an ideal part. The general form of the decomposition of matrix X using SVD is represented in Equation 2:

$$[X] = [U].[W].[V]^T \qquad \text{Eq (2)}$$

Matrix W is a diagonal matrix comprised of singular values. These singular values have similarities to the principal components obtained through principal component analysis. The values of the diagonal matrix are arranged in descending order. The SVD approach develops a reduced model linking parts, metrics, and manufacturing processes. The required level of accuracy can be selected by choosing the number of singular values retained in the reduced model. The model can be reconstructed using a select number of singular values and reversing the matrix operations. Sensitivity is evaluated by carrying out the operation for multiple selection of singular values.

Figure 11 above represents the distance of the parts being evaluated in comparison to the ideal part on a 2D graph. Two methods, cosine similarity and Euclidean distances, are used to determine the distances. Cosine similarity is a measure of similarity between two non-zero vectors of an inner product space based

on the cosine of the angle between them. Cosine similarity is usually used in positive design space, wherein the outcome is bounded in [0,1]. It is assumed that the set of metrics developed is also bounded in [0,1]. Thus, the input data is normalized in order to obtain values in the range of zero (0) to one (1). Cosine similarity is used when the magnitude of the vector distances is not crucial.

In this research, however, the reference technologies (parts) play the role of ideal targets, and the magnitude of the distances must be computed between these ideal parts and the evaluated alternative parts. Hence, the Euclidean distance method is chosen to rank parts based on their relative distances from an ideal part for a specific manufacturing process technology.

Publications IV and V were directed towards the use of integrated knowledge models for prediction of defects in LPBF and manufacturing decision making in additive manufacturing during early design phase for metal products, respectively. Publication IV developed a systematic approach towards developing probabilistic models based on cause-effect relationships of variables for a given manufacturing process. In laser powder bed fusion, the curling defect occurs during the fabrication process in part designs having cantilever/overhang geometries that are not provided with sufficient support in preceding layers. Excessive heat energy input, uneven heat dissipation, and non-uniform thermal conductivity of the loosely packed powder layers under the overhang results in a thermo-mechanical stress gradient which, in turn, can result in deformation of the printed part. To control the occurrence of curling, the underlying thermo-mechanical phenomena were be modelled. Figure 15 shows the steps involved in the development of the probabilistic model for prediction of curling defects in LPBF.

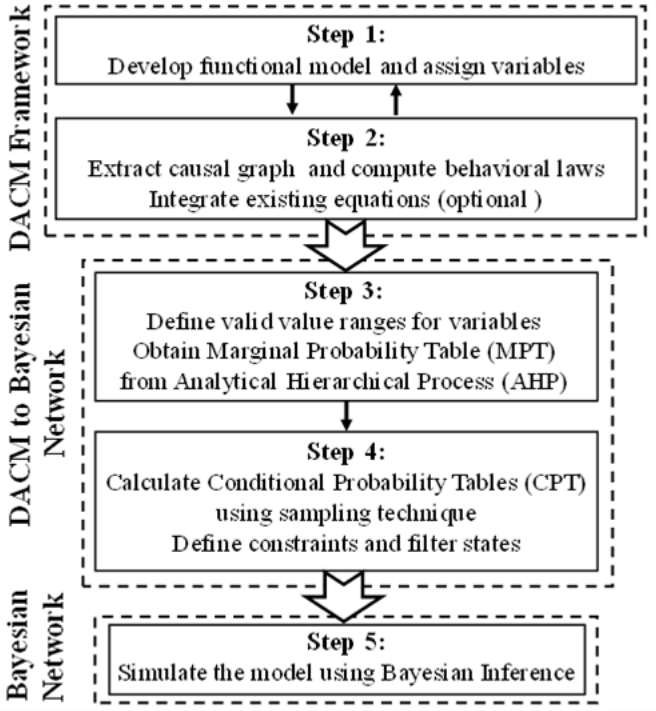

Figure 15: Model development steps to evaluate occurrence of curling defects in LPBF

Step 1 required the use of dimensional analysis conceptual modelling (DACM) to extract causal rules and establish the governing relationships between variables. The given problem was represented in the form of three functional models: working of the LPBF process, desired functions of support structure (effective heat sink and limit deflection), and undesired functions of supports (generation of unnecessary thermal constraints and resulting deflection). In step 2, the analytical equations that represent the functions were identified and transformed to dimensionless pi (π) numbers expressed as power laws of the involved variables. The temperature gradient and equations for deflection, inertia, and heat transfer were substituted with dimensionless pi numbers.

The developed functional model and the corresponding final network structure for the process is reproduced here in Figure 16. For ease of comprehension, the model variables are assigned a colour-coded convention such that the independent variables are green, while dependent variables, exogenous variables, and performance variable are assigned blue, grey, and red colours, respectively. The variables can be continuous, discrete, and/or categorical in nature.

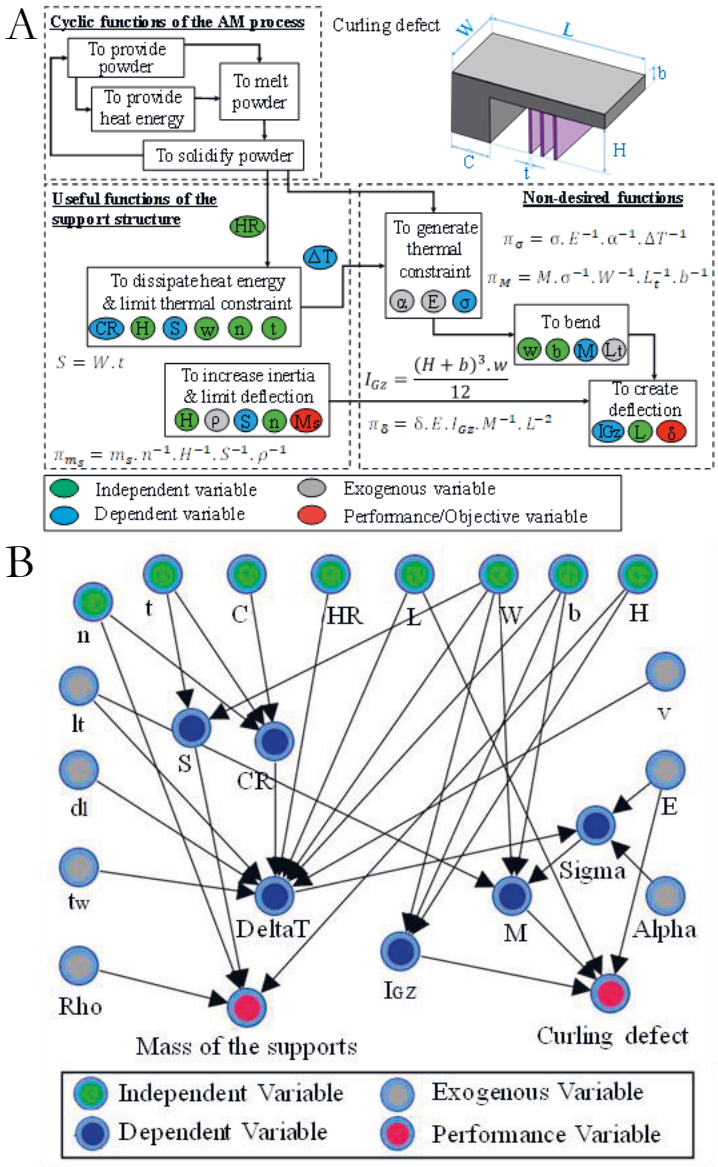

Figure 16: (A) Functional model and (B) Bayesian network representation

The range (set of all values the variable can take) for a continuous variable is discretized to form multiple states. These states can be normalized following a specific distribution or can be custom defined. Once the skeletal framework of the model is created, the probability of occurrence of each variables needs to be assigned.

In step 3 and step 4, the different types of data collected (raw data from sensors, mathematical equations, and expert knowledge) are integrated into the network, and the marginal and conditional probability tables of the variables are filled. Finally, with the complete network variables populated, simulation can be performed to determine the impact of manufacturing decisions, such as process parameter selection and support structure design, on the final part deformation. Table 8 shows the list of study variables and their ranges used in forming the model.

Table 8: Study variables and their ranges

Variable (Symbol)	Unit	(Range of states) **Marginal Probability (%)**		
Part length (L)	mm	(15,45)	(45,75)	(75,120)
		11.11	**66.67**	**22.22**
Part height (H)	mm	(3, 9)	(9, 18)	(18, 36)
		9.53	**24.99**	**65.48**
Part width (W)	mm	(3, 9)	(9, 18)	(18, 36)
		23.85	**62.50**	**13.65**
Part base (C)	mm	(4, 12)	(12, 21)	(21, 33)
		10.95	**30.90**	**58.16**
Part thickness (b)	mm	(2, 6)	(6, 12)	(12, 18)
		19.63	**65.71**	**14.66**
Support thickness (t)	mm	(0.3, 1)	(1, 1.8)	(1.8, 3)
		65.86	**26.28**	**7.86**
Number of supports (n)	-	(1,5)	(6,10)	(11,15) (16,20)
Cooling rate (CR)	°C/s	(18, 25)		
Heating rate (HR)	°C/s	35		
Elasticity modulus (E)	MPa	$113.8 * 10^3$		
Thermal expansion (α)	1/K	$8.6 * 10^{-6}$		
Density (ϱ)	g/mm^3	$4.43 * 10^{-3}$		
Powder layer thickness (l_t)	mm	0.1		
Laser diameter	mm	0.115		
Laser scan velocity (v)	mm/s	1000		

Publication V focused on developing a manufacturing decision-making system that can help in evaluating the consequences of decisions such as the selection of manufacturing processes, materials, material supplier locations, manufacturing locations, and transportation modes on sustainability metrics through the lens of key performance indicators. The relationship between the different manufacturing decisions, key performance indicators, and the production costs were mapped. Seven KPIs were used to evaluate the performance of a manufacturing system under five domains: economic performance (production cost), social performance (labor

productivity), environmental performance (energy intensity and percentage of recycled materials in manufacturing), production performance (order-to-delivery lead time and setup rate), and production quality (scrap ratio). The overall network graph followed similar colour-coded convention as described for the curling defect case study (Publication IV), shown in Figure 17.

The conditional probability tables for the network were formed using a sampling technique in which the governing equations propagate several samples from parent nodes to the child nodes. The final computed network (a BN) allows the user to compare the impacts of different decisions on KPI values and production cost. For instance, selection of production processes results in use of different manufacturing equipment, hence affecting facility cost, capital cost, maintenance cost, utilities costs, labor cost, production performance, and environmental performance of the system. Similarly, each decision is linked to several or all cost and performance metrics. Thus, it is important to simulate, record, and visualize the impact of these decisions on cost and performance metrics. A thorough analysis of what-if scenarios using the network during the design and manufacturing planning phases can help avoid expensive or negatively impactful decisions. Based on the level of accuracy and granularity that is required for the BN, the production targets can be represented as ranges or as precise estimates. The rationale for implementing cost models in a BN is to leverage the benefit of characterizing the impact of intrinsic and extrinsic factors on the different cost categories. Factors such as market forecasts, supply chain uncertainties, and market fluctuations can be modelled into the BN as extrinsic factors under certain boundary conditions. Implementation of the approach reduces the effective person-hours and effort required to estimate production costs for scenario analysis done during the manufacturing decision making process. The usability of the developed method is demonstrated for estimating production cost and the above-mentioned KPIs for different manufacturing decisions. The network developed (Figure 17) is modular, and new elements (sub systems) and other metrics can be added into the network with relative ease. After ensuring the connections developed between newly introduced subsystems and the existing network are complete and accurate, the new version of the model is capable of resampling and calculating the new conditional and joint probabilities.

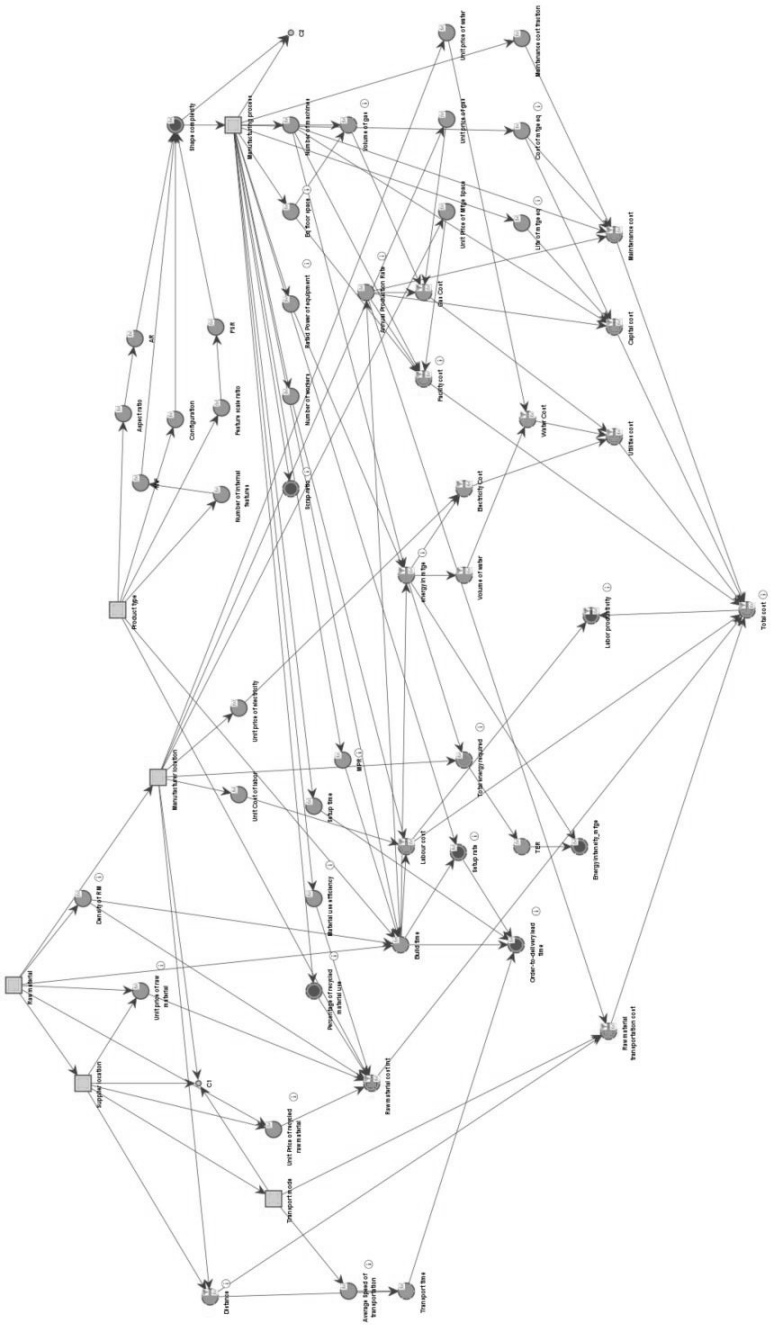

Figure 17: The BN model layout for product sustainability performance analysis

Publication VII integrated the different elements of material systems, design engineering, and manufacturing systems to aid in the development of a holistic metamodel which is capable of design space exploration during the embodiment design phase of a product. The metamodel was used to simulate process-structure-property-performance relationships and identify a focused region of design space solutions for a product (prosthetic device) produced using multi-material polymer binder jetting process. The product development process was split into three interconnected domains: material (D1), manufacturing (D2), and design (D3). Table 9 shows the design of experiments for the three domains.

Table 9: Design of experiments followed for the different subsystems

Variables (Domain)	Nomenclature	Levels
Volume fraction (Xd1)	Vf	0.0, 0.2, 0.4, 0.6, 0.8, 1.0
Height (Xd2)	H (cm)	2 – 10 – 18
Build area (Xd2)	A (cm^2)	582 – 1170 – 1728
Average volume fraction (Xd2)	$\overline{Vf}$	0 – 0.5 – 1
Rigid region thickness (Xd3)	Rt (mm)	5 – 10 – 15 – 20 – 25
Material - rigid region (Xd3)	Vf_{Rigid}	0.4, 0.6, 0.8, 1
Soft region thickness (Xd3)	St (mm)	6
Material - soft region (Xd3)	Vf_{Soft}	0

A BN model presents a modular and efficient representation of the joint probability distribution of a set of domain variables. Based on the dependencies between different variables, the joint probability distribution (JPD) of a BN can be factorized into a set of conditional probability tables at the nodes given their parent nodes. Use of BN models for embodiment design and MDO problem formulation is explained below. A colour-coded directed acyclic graph (DAG) depicting the process, structure, property, and performance (PSPP) linkages for the prosthetic device design was created, as shown in Figure 18, based on the set of equations and the associated ranges of values.

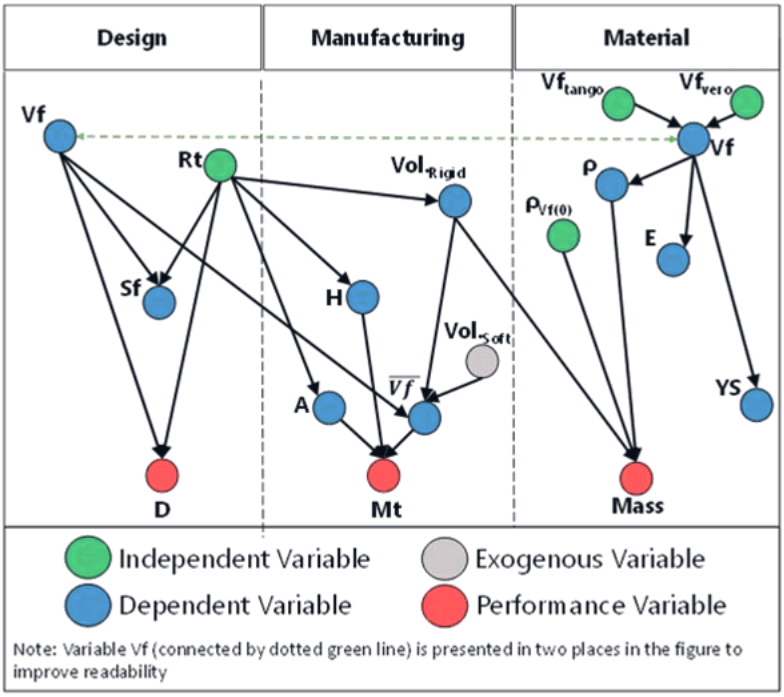

Figure 18: Directed acyclic graph representing the complete design-manufacturing-material domain system

The relationships between the parent nodes and child nodes are modelled using the surrogate models presented in the publication. Based on these relationships, the domain of the variable (child nodes) is calculated and assigned to equal states within the node. Conditional probability tables (CPT) are then computed within the network for the child nodes, given the probability of their respective parent nodes. Finally, the target nodes (Mass, Mt, and D) are performance variables in the system model represented in red. The target nodes are child nodes for which conditional probability tables are computed like other child nodes. Once all the nodes and their connections are defined, the BN model can be simulated for variables of interest by providing evidence to the nodes of the network. It is important to note that the underlying mechanism for developing the DAG and, hence, the BN is modular and is dependent on the variable interactions represented as equations. Designers can simulate and assess the three subsystems collectively and independently. For specific levels of granularity warranted, designers can redefine or update system boundaries, add or remove the connections and nodes, and make changes to their states and value ranges within each node. In this research, more states are provided for nodes R_t and V_f than others to aid in the design of space exploration.

3.4 Summary of the modelling approach

The knowledge integrated modelling methodology developed as part of this work has been implemented and validated for different case studies involving several additive manufacturing processes. Based on the requirements presented in the case studies, the model has been adapted to perform process parameter tuning, design space exploration, sustainability assessment, multi-disciplinary optimization, and manufacturing decision making. Overall, modularity, robustness, operability across different levels of granularity, applicability across domains, and ability to integrate process-structure-property linkages have been demonstrated.

Extension of this research will support development of additional sub-system modules which will provide information on the behaviour of the metal AM parts in cryogenic environments. Ongoing work is gathering the necessary data and information on material properties (mechanical, electrical, and thermal) to support future model development.

Before presenting the results and learnings of the developed modelling approach, it is necessary to highlight several limitations of this current work:

1. The accuracy of the models is dependent on the correctness of the causal graph produced from the knowledge encoding phase. Causal graphs can be generated from functional models or from equations, dimensional analysis, and datasets. For the present work, considerable time and effort were needed to create the oriented causal graphs that represent the investigated additive manufacturing processes.
2. The models were developed to assist design phase analysis and decision making and offline control of the additive manufacturing processes studied. The evaluation of capabilities of these models to help with online control of the processes was not explored in the present study.
3. The work undertakes event-based probabilistic inferences rather than quantitative simulations and system dynamics.
4. The modelling approach is envisioned to help generate metamodels capable of representing complex multi-domain phenomena in a modular framework. The modules are building blocks of the system, and can be a combination of white-, grey-, and black- box models. As a result, some modules/sub-

modules can be defined as causal models (well defined cause-effect relationships) and others are based on statistical correlations, with temporal ordering.

5. As discussed in the background section, mathematical tools have been used to establish cause-effect relationships. Some of these tools require big data sets to establish these relationships with high degree of certainty. The enquiry into these mathematical models for causal discovery was not part of the scope of the present work due to lack of availability of large data sets for the manufacturing process case studies, but also to restrict the focus of the work to a well-defined boundary.

Data and knowledge collection, extraction, and processing is central to the causal modelling framework presented in this work. Focus is given to different ways information can be collected and integrated. One of the key objectives has been to develop system models capable of representing the process with small datasets. The next chapter will highlight some of key results and learnings based on the developed models.

4 RESULTS AND DISCUSSION

To restate the overarching research objective of the dissertation, the aim is to develop knowledge integrated metamodels that can assimilate process-structure-property- and performance relationships prevalent in additive manufacturing processes to analyse the impact of design and manufacturing decisions on the products. Towards this goal, research tasks were identified, and case studies were developed. Those case studies were reported as seven scientific publications, and the results of those publications are discussed in this chapter.

4.1 Exploring the suitability of metamodelling for defect characterization in the laser powder bed fusion process.

Publication IV successfully demonstrated the development of a computationally efficient modelling and simulation tool, which can represent the powder bed fusion manufacturing system and predict the cascading impacts of the choices made for the different design variables on the outcome (deformation of the final part).

As part of the study two scenarios were evaluated. First, the effect of defining the values for design variables on the deflection generated in the part (shown in Figure 16 on page 86) was observed. Second, the desired output targets for deflection, mass of supports, and the length of the overhang were defined to estimate the other geometric dimensions of the part and the number of supports that need to be printed. The forward simulation models the effect of the design variables on the resulting curling defect for additive manufacturing of the L-shaped part. During simulation of the Bayesian network model, it was seen that the probability of curling increased in the high value state (final curling defect <=1.0), 44.78% (as shown in Figure 19.A.), when the values for part height (H, 9-18 mm), width (W, 9–18 mm), length (L, 45-75 mm), and thickness (b, 12-18 mm) were set as evidence (e.g., input information).

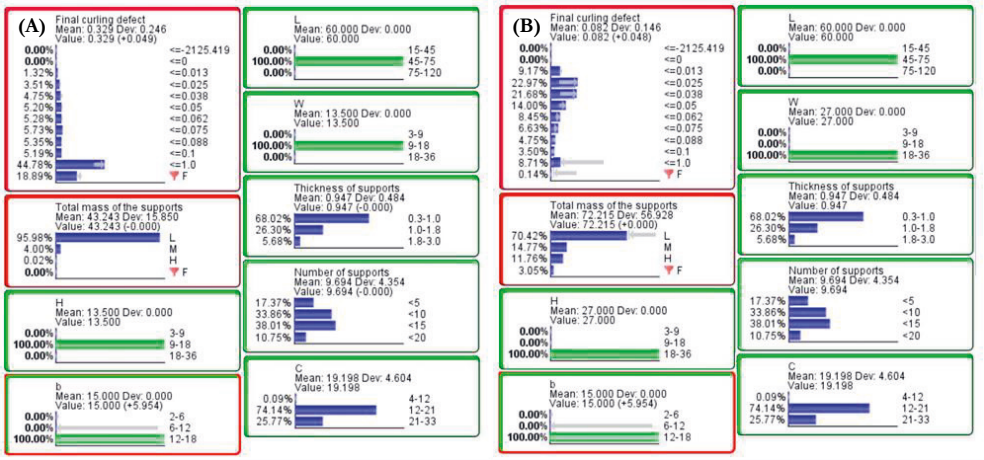

Figure 19: Simulation results for the LPBF case study

New evidence (shown in Figure 19.B.) for part width (W, 18–36 mm) and part height (H, 18-36 mm) was presented to characterize the effect of these changes on the curling defect. The probability that the final curling defect lies in low value states of the variable (<=0.025, <=0.038, and <=0.05) increased to 22.97%, 21.68%, and 14%, respectively, representing a significant increase in the probability of curling occurring in these ranges.

The research demonstrated an approach to generate a Bayesian network model to characterize the influence of design and manufacturing parameters on the curling defect in laser-based additive manufacturing for a part with an overhang structure. The approach developed herein is generic and could be expanded to explore other defects resulting from non-homogenous temperature gradients in additive manufacturing. The Bayesian network model allows for forward- and backward-simulation of the system under study. First, the model estimates the probability of output targets occurring based on fixed design parameters. Second, it allows the user to set evidence for known output targets and then uses the model to update the probability value ranges for the input values (i.e., part geometric dimensions) to attain those targets. This two-way simulation helps designers make better-informed decisions about changes in product geometry early in the design stage. Such evaluation can eliminate costs associated with design changes later in the product development cycle.

4.2 Developing metamodels to assist product sustainability performance evaluation and manufacturing decision making

AM processes have been beset with challenges such as inconsistency in part quality, reproducibility, and ability to meet tolerance requirements; models that can predict and reduce geometric defects play a crucial role in improving part manufacturability and process sustainability performance. Publication III developed dimensionless metrics that can be used to evaluate the suitability of manufacturing processes for producing parts with specific geometric features. The proposed approach was derived from latent semantic analysis and dimensional analysis and can be used to evaluate parts and their production for a variety of selected metrics. The selected metrics serve as descriptors of design features and manufacturing functions and were developed using functional modelling and dimensional analysis theory. Singular-value decomposition (SVD) and Euclidean distance measurement techniques were used to determine the relative manufacturability for a set of parts produced using laser powder bed fusion technology.

There has been a recent shift towards implementation of data-intensive machine learning (ML) models in manufacturing research (discussed in Section 2.4). Developing ML process models with limited data is challenging, especially in AM where parameters often reflect non-linear relationships, requiring more intensive model training. One of the thematic ideas of this dissertation research is to explore the possibility of developing process models with a paucity of data. When comparing ML modelling with analytical modelling strategies, a key difference is the ability of ML models to continuously learn and update. The process modelling approach drew upon meta-learning domain theory and internalized metric-based, model-based, and optimization-based approaches to improve learning ability (Vilalta & Drissi, 2002). First, a metrics-based approach was established using dimensional analysis theory (DAT) and the Vashy-Buckingham theorem. The approach was applied to manufacturing decision-making. Model-based and optimization-based approaches were then combined using SVD to perform part evaluation.

The methodology presented in Publication III was demonstrated for ranking a set of parts based on their manufacturability using laser powder bed fusion (LPBF) technology. The detailed accounts of part rankings, comparisons within parts, and the methods to evaluate the vector distances can be found in the publication. An important factor in the manufacturability ranking is the number of singular values

selected. Based on the number of singular values selected the ranking order for the parts changes. Thus, any model reduction efforts must consider two factors: the average error generated by the reconstruction of a reduced model and the variation in the ranking based on the number of singular values considered.

Another interesting observation is that some metrics appear in clusters when represented in a 2D graph (shown in Figure 20). For example, Metric 1 (individual part production rate), Metric 2 (batch production rate), and Metric 4 (the need for internal support structures) form a cluster and are related to production time. In addition, Metric 6 (minimum feasible vertical hole size), Metric 7 (difficulty of de-powdering), and Metric 10 (internal lattice structures) each indicate part complexity and form a cluster. Metrics 11 and 12, design rules relating to ease of clamping and presence of overhanging features, respectively, appear to be somewhat correlated. In this work, no specific clustering method was used, but methods such as k-means could be employed to examine clustering and drivers of correlation that can better inform designers and process planners.

It is interesting to note the clustering of metrics provides an opportunity to combine metrics together to develop new ones that are more representative of a given process. The principles presented are highly flexible and facilitate feature/part composability and metric ranking. The developed method enables isolated evaluation of individual features comprised in a part, but also allows for combining features or parts for aggregate evaluation of complex parts and sub-assemblies. Thus, the method promotes design for manufacturing and assembly through its ability to separate or combine features and parts and perform evaluation of both individual and aggregated features/parts. In addition, the graphical representation of the design space can enable design space exploration to find new combinations of parts and/or new metrics to aid design and manufacturing analysis.

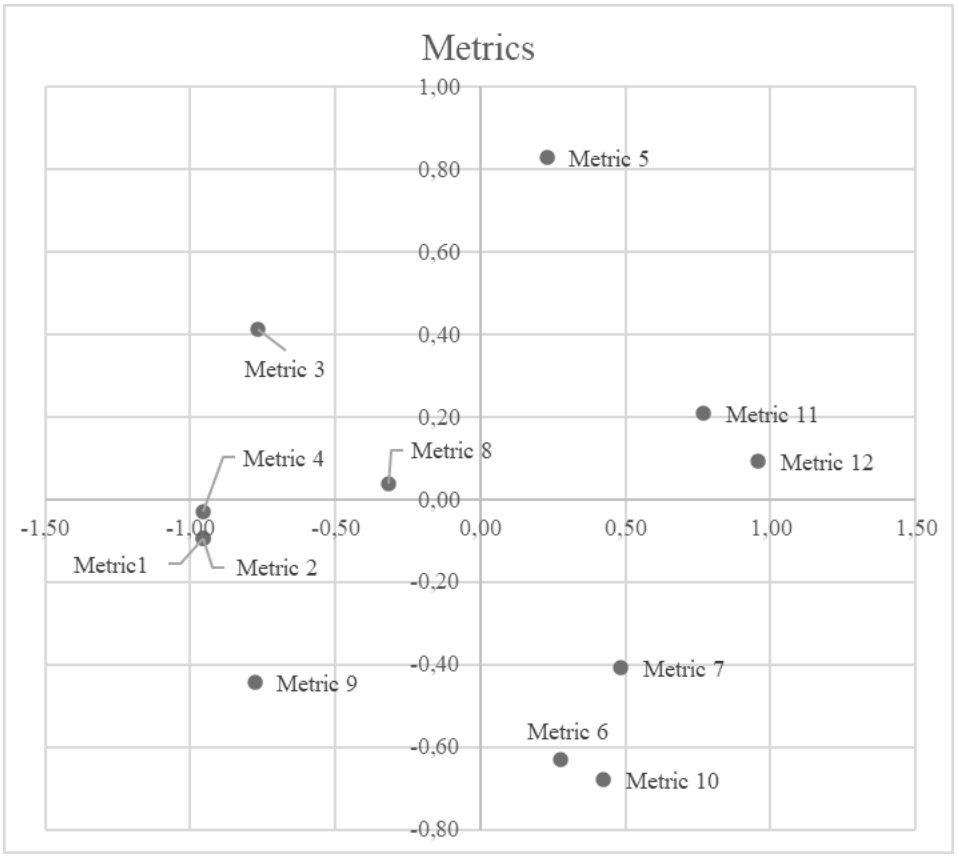

Figure 20: Spatial arrangement of the metrics

Next, the development of probabilistic models to aid in manufacturing decision making for advancing sustainability goals was explored in Publication V. The study examined the effect of six manufacturing decisions on a set of selected performance indicators (economic, social, and environmental) to produce turbine components using additive manufacturing processes (shown in Table 10). The relative effects of the various decision choices were simulated using Bayesian network modelling. Two scenarios were evaluated, where: (1) the impact of manufacturing decisions on the final production cost and KPIs were observed and (2) the desired cost and KPI targets were provided to the network to determine the manufacturing decisions that are most likely to yield those results. The two scenarios provided insights on the consequences of different design and manufacturing choices on overall sustainability performance.

Table 10: Manufacturing decision choices and key performance indicators

Decisions	**Choices**		
Product	Shell and Tailpipe		
Manufacturing process	WAAM and EBM		
Raw material	Titanium and Aluminium		
Manufacturing location	USA and China		
Raw material supplier location	USA, China, and India		
Transport mode	Rail, Road, and Sea		
KPI	**Description**		
Scrap ratio	Ratio between scrap quantity and processed product quantity		
Setup rate	Ratio between actual unit setup time and actual unit processing time		
Recycled material use	Percentage of materials used that are recycled input materials		
Energy intensity	Ratio of electricity generation and transmission losses (based on locational electricity mix) to the total direct energy required to manufacture the product		
Order-to-delivery lead time	Latency between the initiation and execution of process		
Labour productivity	Ratio between value of monthly product shipped and monthly labour expenditures		
Variable Material processing rate	**Unit** kg/hr	**Ranges / Discrete values** **EBM**	**WAAM**
Equipment floor space	square meters	0.2	2.9
Setup time	hours	4.46	24.15

The main advantage of the Bayesian network model is its ability to add new modules, including information about new manufacturing processes, materials, KPIs, and locations. Bayesian network-based KPI modelling is well-suited for characterizing complex systems where knowledge and data from multiple engineering domains needs to be integrated. Such integrated models can allow for fast simulation of various manufacturing scenarios and aid users in streamlining their choices.

4.3 Integrating process-structure-property relationships through metamodelling to optimize AM process performance

For developing holistic metamodels of manufacturing processes that encompass various physical phenomena, material structure, and mechanical properties, there is a need to develop and implement a number of subsystem modules. The work of developing these smaller modules was carried out over a series of publications, namely, Publication I, Publication II, and Publication VII. The outcome of this work is shown schematically using a directed-acyclic graph (DAG) in Figure 21.

The necessary experimental data needed to create the process-structure-property models to represent wire and arc additive manufacturing technology was collected and reported in Publication I. Publication II helped in development of geometric models for welding thin-walled structures using WAAM. The models associated the impact of process parameters on the geometric features (height and width) of the beads. As shown in Figure 21, the process parameters such as wire feed rate (WFR) and travel speed (TS) play a crucial role in determining the heat energy input during the arcing. While interpass temperature (T_0) determines how much of the heat energy is allowed to dissipate to the surrounding environment before the deposition of the next layer begins. The dissipation of the heat energy happens through conduction, convection, and radiation. The primary source of heat loss is through conduction to the baseplate. Convection and radiation are secondary mode of heat loss happening over exposed surface area of both the deposited weld and the baseplate. The scope of the study is limited to natural cooling of part. The cooling rate of the weld determines the grain nucleation, grain growth, and the phase transformations undergone by the steel. Relationships exist in literature connecting the grain sizes to hardness properties and so on. In addition, the different phases in steels have different characteristic properties and depending upon the technical requirement having certain phases in the microstructure is desirable.

Therefore, metamodels developed for specific process-material combinations will provide capabilities for manufacturing and material science engineers make AM parts that have specific microstructural features and mechanical properties. These models will also reduce defects through optimized parameter selection.

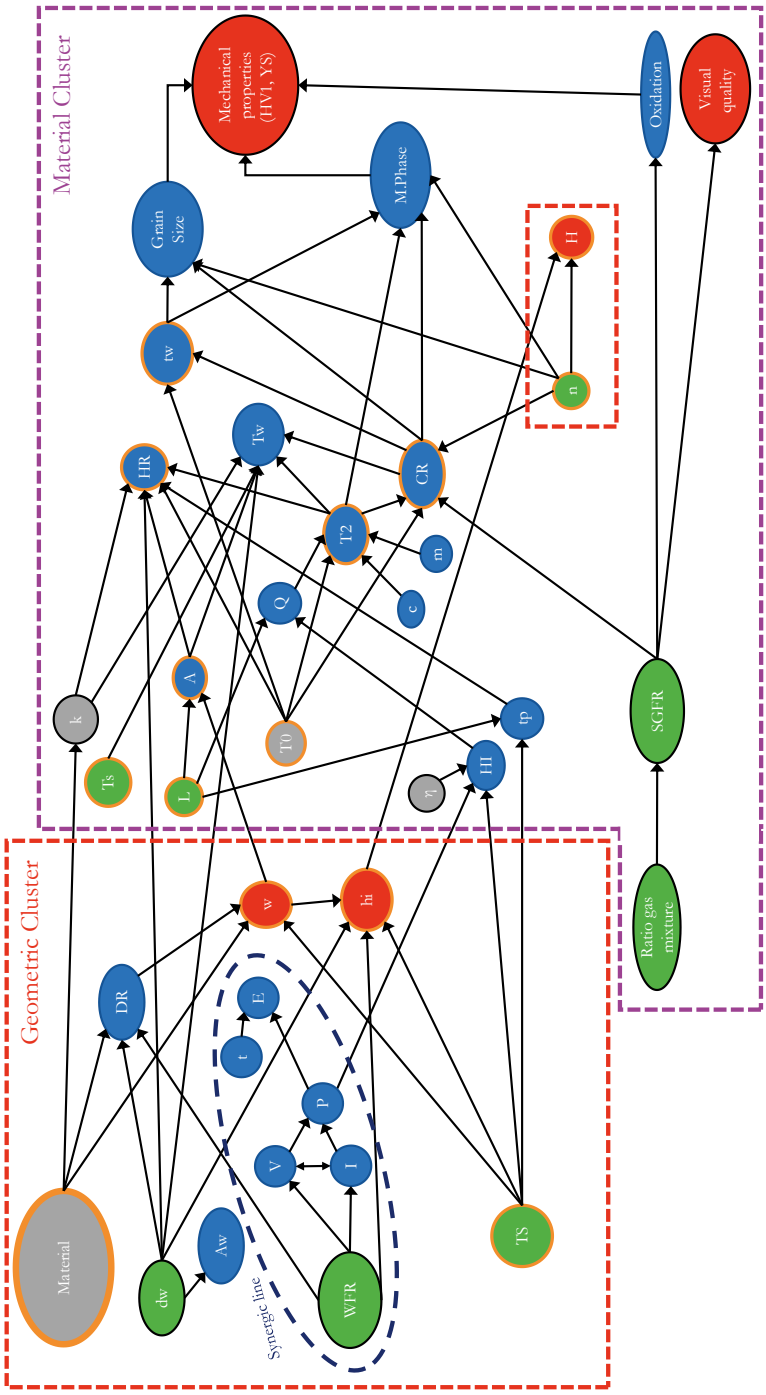

Figure 21: Directed acyclic graph representing the WAAM process

The contributions reported in this dissertation are an outcome of ongoing effort towards gathering the necessary information and reducing the uncertainties existing in the modelling methodology for AM. Towards this goal, Publication VII developed a proof of concept of the modelling methodology via a product development case study using binder jetting process. Process-structure-property and performance linkages were integrated in a modelling framework to develop probabilistic simulation model which is capable of design space exploration. The additional knowledge gained through the design space exploration was utilized to perform a multi-disciplinary optimization towards improvement of the product.

Publication I studied the impact of thermal cycles on the microstructure and mechanical properties of two steel alloys. The interrelationships between process parameters, heating and cooling cycles of the welded part, and the resultant microstructure and mechanical properties were characterized. Microstructural analysis identified the presence of acicular ferrite and equiaxed ferrite structures in G4Si1 welds, as well as a small volume fraction of pearlite along the ferrite grain boundaries (Figure 22.B.). Analysis of AM70 welds found acicular ferrite, martensite, and bainite structures (Figure 22.A.). The hardness of both materials decreased with increasing build height due to decrease in the temperature gradient and cooling rate. Image analysis was used to identify the grain sizes and microstructure phase constituents of the printed specimens. The walls produced using AM70 (M2E1 and M2E2), resulted in a fine-grained steel consisting of ferrite, martensite, and bainite, along with trace amounts of inclusions.

Acicular ferrite is a desired phase in inoculated steels owing to its influence on the overall toughness of the material (Bhadeshia & Christian, 1990). Acicular ferrite grains are usually formed at intragranular nucleation sites formed at inclusions. Similar to bainite, which nucleates at austenite grain boundaries and grows inwards as sheaves or plates, transformation to acicular ferrite occurs below the bainite start temperature. The growth of acicular ferrite may be favoured over bainite based on the prior austenite grain size and inclusion density in the alloy used for printing. In addition, the presence of Widmanstätten ferrite and allotriomorphic ferrite along prior austenite grain boundaries have been seen to favour growth of acicular ferrite over bainite. The increased amount of acicular ferrite grains may be desired in applications where higher ductility is warranted. Similar to acicular ferrite, the presence of bainite may also bring good strength to ductility performance, but with higher hardness.

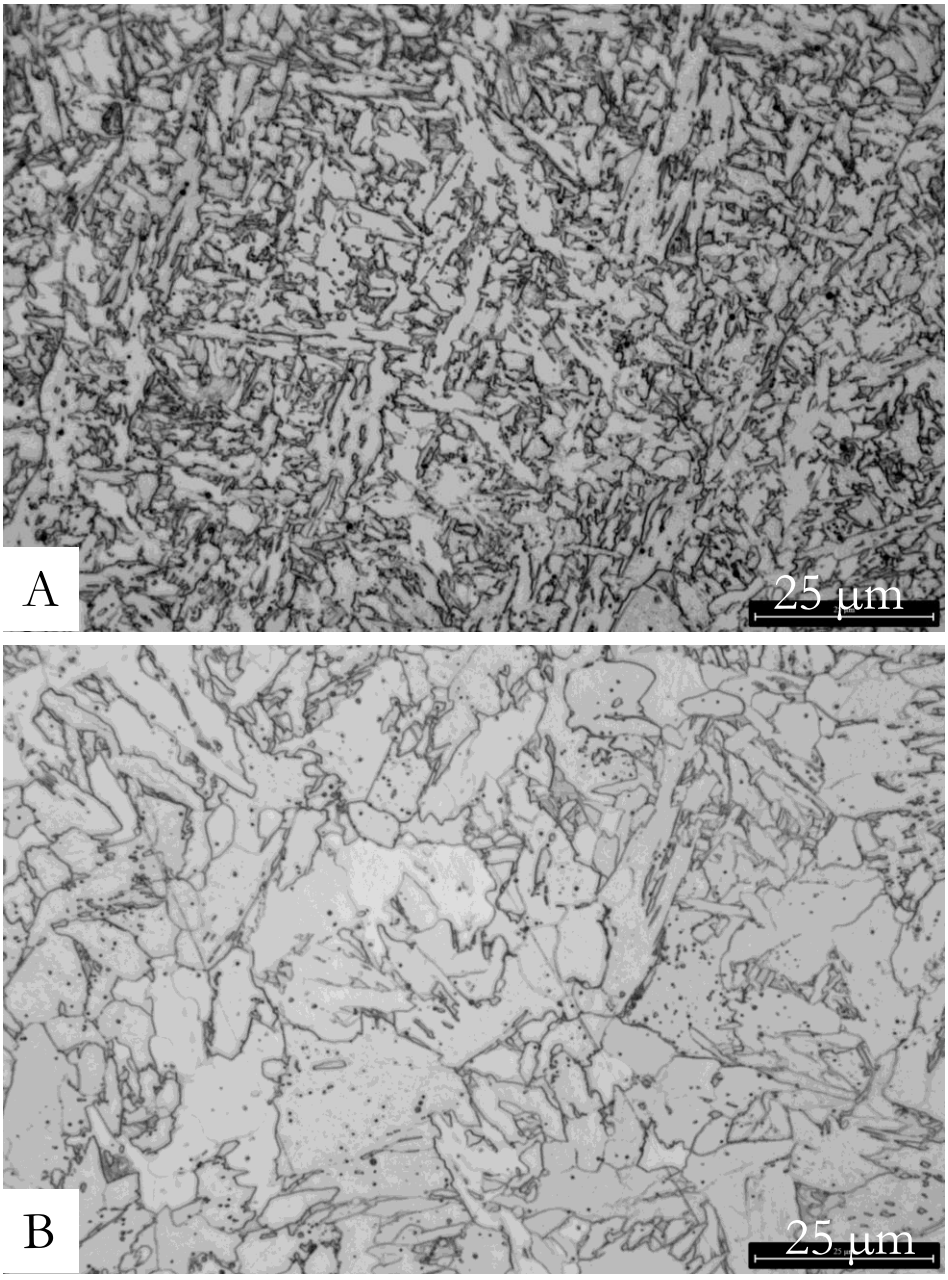

Figure 22: Microstructure evolution of two steels (A) AM70 & (B) G4Si1; Scale bar is 25µm

The lower ductility of AM70 may be associated with the large number of fine inclusions found throughout the welded microstructure, which can aggravate microcracks and their propagation in the weld (Shown in figure 23).

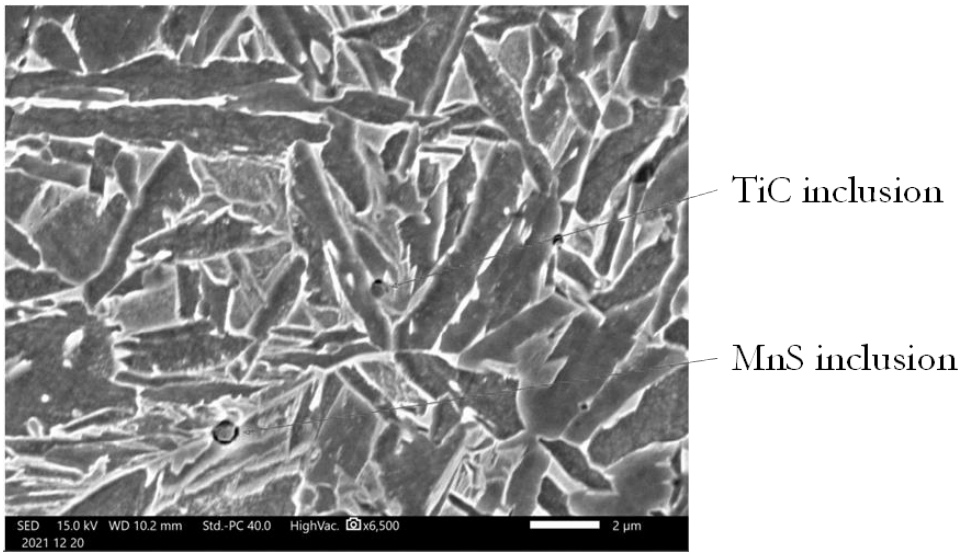

Figure 23: Metallic inclusions in AM70 microstructure identified by SEM

The hardness and strength of fully bainitic microstructures decrease during tempering; this change is more evident in high strength steels (Bhadeshia & Christian, 1990). The repeated heating and cooling cycles in the WAAM process results in a non-uniform tempering of the printed part. Consequently, a clear variation in the microstructure and mechanical properties was seen due to the layer-by-layer building approach.

As a part of the dissertation research, similar studies have been conducted for other alloys processed using WAAM and SLM technologies. Inclusions, defects, and elemental map counts were performed using SEM for alloys such as stainless steel, copper alloys, and Invar36. Figure XX shows the various image analysis performed for CuNi2SiCr alloy printed using SLM technology. Figure 24A identified the presence of Columnar grains along the build direction. Figure 24B and 24C, represents the surface and the cross section of the tensile test specimen respectively.

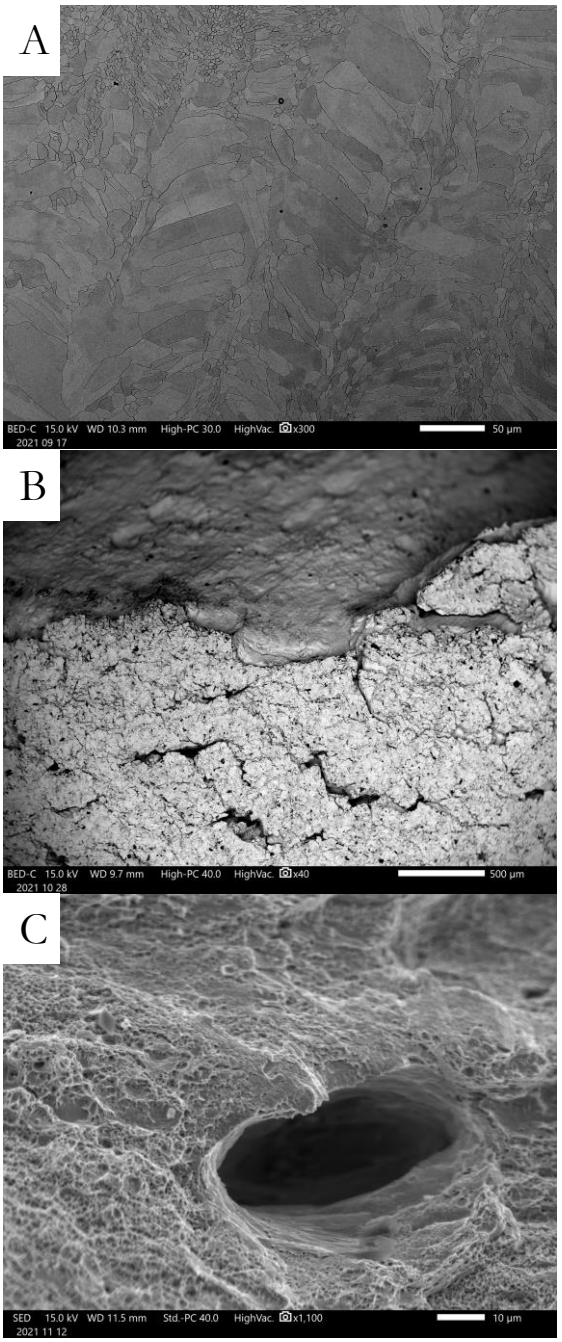

Figure 24: SEM imaging of SLM printed CuNi2SiCr alloy, (A) microstructure comprising of elongated grains (B) Microcracks on the surface of tensile test specimen near the fracture region (C) presence of large and small dimples in the fracture region

The presence of micro-voids and dimples in the fractography images suggests a ductile failure. The tensile tests for copper alloys and Invar36 were carried out at both room temperature and -50 °C. Microhardness (Vickers hardness) characterization was performed for the two alloys (shown in Figure 25). Hardness value of pure extruded copper is provided as reference in the figure.

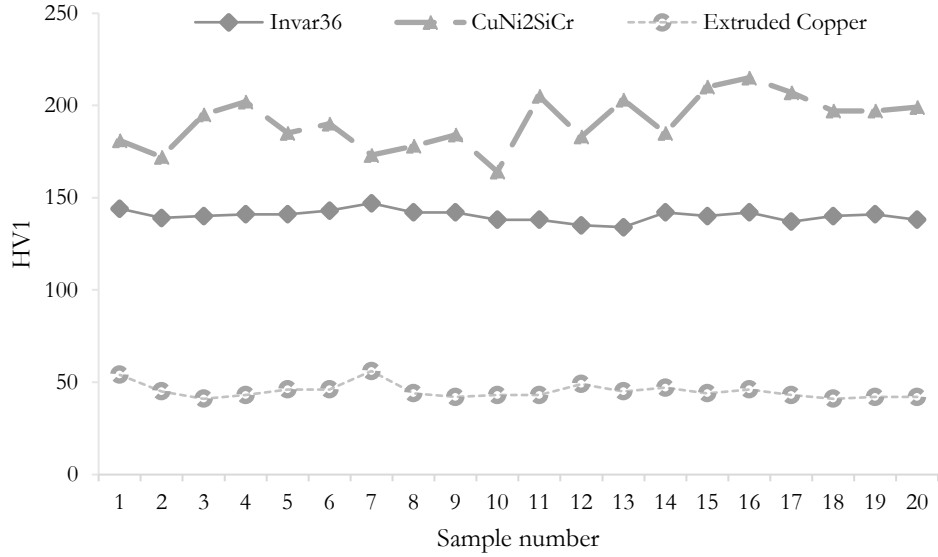

Figure 25: Hardness profile for Invar36 and CuNi2SiCr printed using SLM compared to reference extruded pure copper

The electrical resistivities of pure copper, CuNi2SiCr, and Invar 36 were measured at room temperature and in cryogenic environment. The geometric dimensions of the samples used for the measurement of electrical resistivity is given in Table 11. The resistivity values for the pure copper samples are compared against a reference sample with residual resistivity ratio (RRR) of 113 from literature (Russenschuck, 2010).

Similarly, reference plots were found for other alloys. The resistivity of the specimen was measured at fixed intervals between 12K to 298.5K, the results are presented in Figure 26.

Table 11: Dimensions of the samples used in electrical resistivity measurements

Geometric Dimensions	Pure Cu (Luvata Oy)	CuNi2SiCr	Invar36	EOS Pure Cu Horizontal	EOS Pure Cu Vertical
Distance between voltage taps, [mm]	74.9	38.3	40.0	40.0	28.00
Width of samples [mm]	3.34	4.00	3.92	4.7	4.15
Thickness of samples [mm]	2.53	2.00	3.31	4.15	4.15
Area of cross section [mm^2]	8.45	8.00	12.98	19.05	17.22

For the heat-treated specimen of the CuNi2SiCr alloy that was printed using SLM technology, the values for resistivity at room temperature was close to the value found in the material data sheet. In addition, the %IACS value was calculated to be 43. 29% which was close to the 40% reported in the material data sheet.

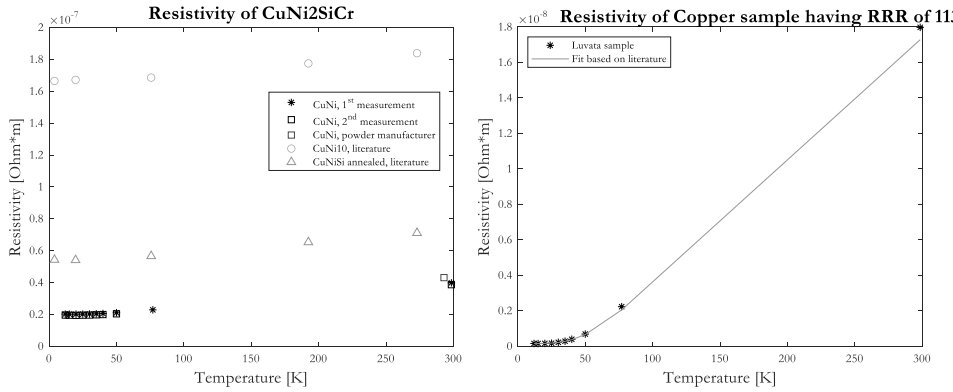

Figure 26: Resistivity measurements for SLM printed Cu alloy and pure copper sample from Luvata Oy.

To validate the accuracy of resistivity measurement setup, we measured the resistivity values of pure annealed copper sample provided by Luvata Oy (manufacturers of copper products). The sample we measured was rated to be of RRR 113. The measured results were within 10% margin. Figure 27 shows the measurements results for Invar 36 alloy printed using SLM and Pure copper printed using EOS laser powder bed system. Three different Invar36 samples printed using SLM technology were measured: (1) *htm* represents heat-treated and machined, (2) *ab* represents as-built samples and (3) ht represents heat treated samples with no post process machining.

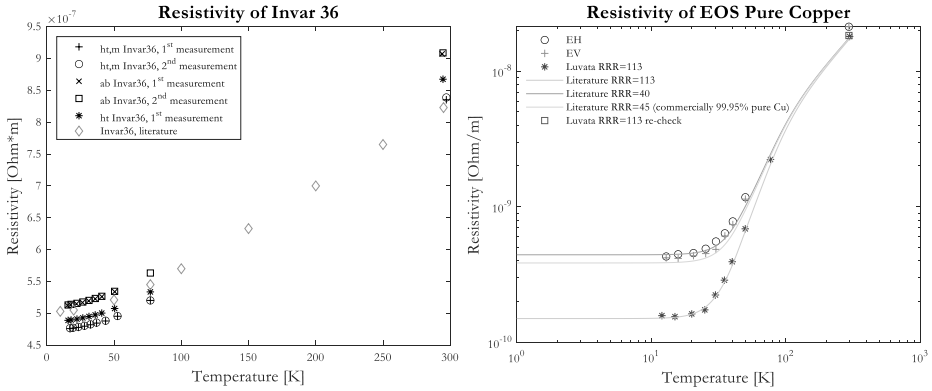

Figure 27: Resistivity Measurements of Invar36 and pure copper samples (EH & EV)

The *htm* (heat-treated and machined) samples were measured twice for ensuring measurement process reproducibility. The measurement of the samples takes one day for sample preparation and preparation of the cryostat for cooldown. The cooldown to cryogenic temperatures takes about 24 hours, and finally the measurements in the temperature range (12K – 50K) requires two days. In each cooldown, two samples for electrical resistivity and one sample for thermal conductivity can be measured. Note in Figure 27, the plot of resistivity of for EOS pure copper sample is represented as a logarithmic plot for better readability. It was found that the samples printed in the horizontal orientation had higher resistivity values compared to the samples in the vertical orientation, a possible explanation for this is the presence of larger number of grain boundaries in the horizontal direction (horizontal plane). The SLM and LPBF copper samples were seen to have elongated and columnar grains growing in the vertical direction (lesser number of grain boundaries). Hence, the importance of understanding the process-structure-

property relationships is emphasized. The printed pure copper samples closely resemble the trend for resistivity, as seen in literature for copper with same purity (99.95%) and RRR value of 40. Similar measurements are being conducted for WAAM printed steels and other alloys. These measurements provide a positive assertion that additive manufacturing can fabricate components that have similar or better property performance as traditional manufacturing methods.

As part of the dissertation work, fabrication of mechanical components of a high temperature superconducting magnet was carried out using two manufacturing process: selective laser melting and subtractive milling. The fabricated components were inspected using X-ray diffraction method to evaluate the surface residual stresses generated during the manufacturing process (shown in Figure 28). Both processes induced compressive and tensile residual stresses in different regions of the components (shown in Figure 29). Overall, it was found that the SLM process showed lower variability in stress values in the components for both measurement orientations (0° and 90°). It is important to note that the residual stress measurements are performed only at the surface level of the components.

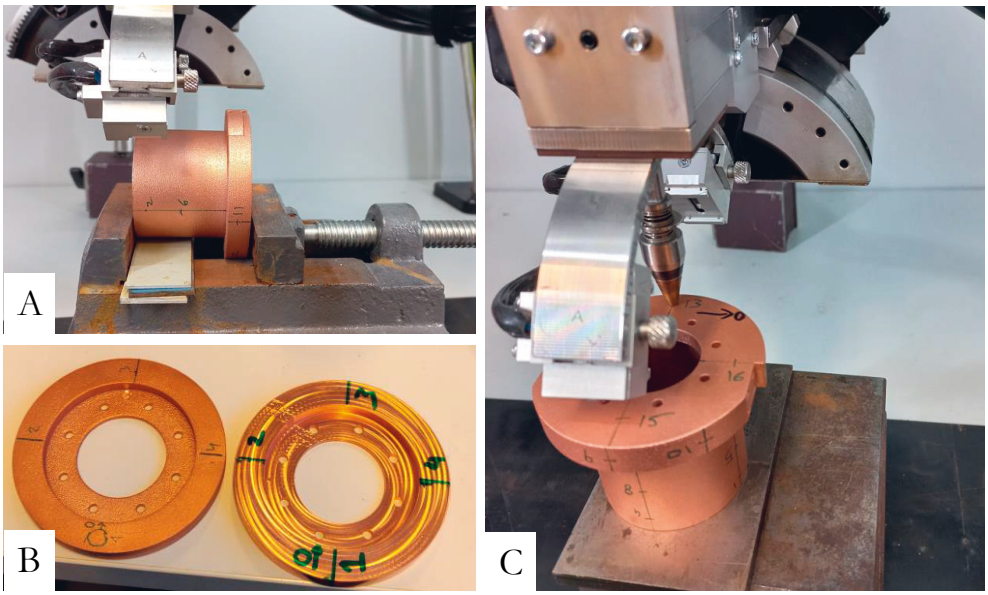

Figure 28: (A) & (C) Ongoing residual stress measurement of AM printed base component. In image (B), top cap component manufactured using SLM (Left hand side) and CNC-mill (Right hand side)

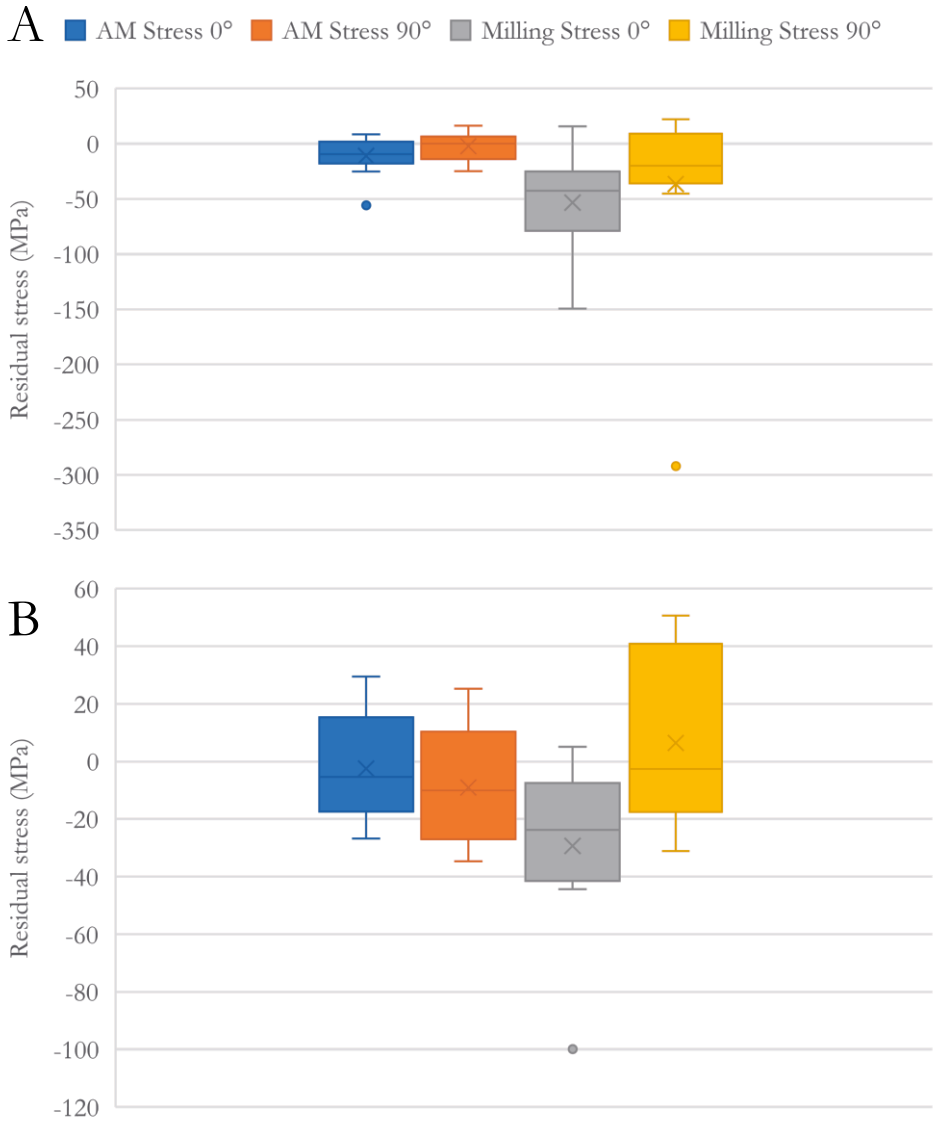

Figure 29: Residual stress variation observed in (A) top cap & (B) base assembly components fabricated using AM & milling

Publication II investigated the use of metamodels in predicting part geometry (height and width) based on welding process parameters. Cause-effect relationship models were established for both single bead and multi-bead geometries. As discussed in Section 3.2, statistical analysis of single-bead experiments identified the

influential process parameters to reduce the design space for multi-bead experiments. The full-factorial design of experiments for multi-bead prints necessitated 27 experiments.

Regression models based on power laws were developed that predicted the output variables based on input process parameters. Using these models, a Bayesian network (BN) was developed to predict two geometric dimensions (i.e., wall height and width) for an additively manufactured part. Validation experiments were performed to evaluate regression model error. Five validation experiments were performed for forward simulation, wherein the users defined the wire feed rate (WFR), travel speed (TS), and number of layers (n). In addition, three backward simulation experiments were performed, wherein the user defined height and width target values, and the BN model predicted the probable WFR, TS, and n values. The BN model predicted the WFR (2.5 mm/min), TS (11 mm/s), and n (9 layers) to achieve a target width (3.6 mm) and height (11.0 mm). The printed part using these inputs was measured using a coordinate measurement machine (CMM). The average error for the predicted wall width and height was found to be 7.72% and 8.76%, respectively. The modelling approach and error computations for the different models are explained in detail in the publication.

In Publication VII, a probabilistic model is developed to perform design space exploration to identify a smaller feasible solution region within the complete design space. The model developed accounted for three domains: design, material, and manufacturing. Case study of fabrication of artificial prosthetic limb using binder jetting process was evaluated. The Bayesian network model was implemented to run scenario analysis. The BN was simulated to optimize the disciplinary objectives in two scenarios. Scenario 1: minimizing both mass (J1) and manufacturing time (J2), along with minimizing the total deformation (J3) of the product to obtain the stiffest socket design. Scenario 2: minimizing both the mass (J1) and manufacturing time (J2) while maximizing the total deformation (J3) to obtain the most flexible design.

The BN model is simulated backwards to perform the exploration study for the different scenarios. It is important to note that a forward simulation could also be executed to perform predictive analysis moving from independent variables to the targets. The resulting contour plot of Rt and Vf as a function of the total deformation (D) is mapped in Figure 30. The contour also combines the results obtained from the BN exploration scenarios, defining a narrower design space for the detail design stage. The observation results from the BN simulations provide the

region that leads to optimal outcomes for both scenarios and can define a resampling plan for additional FEA simulations to increase local accuracy at the detail design and exploitation phase.

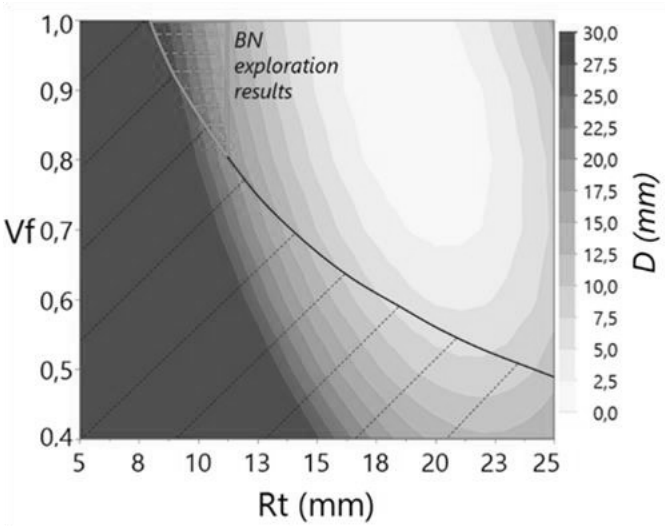

Figure 30: BN simulation used to perform design space exploration

In the detailed design phase, the scenarios from the BN model are taken into consideration, and additional design alternatives are explored with higher safety factor (Sf).

Next, desirability function approach is used to transform a multi-response problem into a single response problem. To simultaneously optimize several responses, each of these disciplinary desirability scores is combined using the geometric mean that leads to the overall desirability score for each design solution. The simulation and optimization during the exploitation phase are based on a gradient descent algorithm as the design variables are continuous. The choice of desirability functions and weighting factor depends on the priorities of the decision-maker. This allows integrating prior knowledge or preferences. The initial exploration was assisted at the embodiment design with probabilistic reasoning based on a Bayesian network (BN). The detail design stage showed how to optimize all three objective functions using a desirability function and gradient descent optimization algorithm to isolate non-dominated solutions. The resulting PSPP-MDO problem formulation was used to generate feasible solutions representing the

best trade-off in the Pareto Front (PF) that satisfy disciplinary constraints and optimize objective functions during the product design of a prosthetic socket.

Multi-objective optimization case study involving design and manufacturing of components of a high-field superconducting magnet was investigated in Publication VI. The work defined two objective functions for the optimization problem: (1) minimizing stress developed in the components and (2) minimizing cost of manufacturing. These objective functions where subjected to three design constraints. Genetic algorithm-based solver (gamultiobj in Matlab) was used to solve the multi-objective optimization formulation. The novelty of the modelling approach proposed in the publication is the use of design structure matrix, modified page-rank algorithm, and graph centrality scores to sort the system variables in two categories: variables having high impact and variables of low impact on the objective. The low impact variables were excluded from the optimization process by fixing their values, while the variables of high importance were considered in the optimization algorithm. The two-step optimization process reduced the effective number of variables that had to be optimized to get minimum manufacturing cost. The reduced variable list reduces the computation time during optimization and hence enables cheaper and faster optimization.

4.4 Contributions of the research work

The contributions of the research include the following:

1. Data describing the mechanical, thermal, and electrical properties of metal alloys (i.e., aluminium, copper, and steels) fabricated using additive manufacturing (i.e., WAAM and SLM) were measured and obtained in room temperature and cryogenic environments. This data supports product and process performance modelling. For performing these measurements, modifications to existing testing equipment and procedures had to be undertaken.

2. Understanding the changes in the material properties of AM-fabricated parts across operational temperature ranges is crucial for their qualification for niche applications (e.g., aerospace and applied superconductivity). A hybrid

modelling methodology that integrates information related to the process-structure-property relationships and the performance of product and material systems was developed. This methodology enables the development of probabilistic metamodels for manufacturing process simulation and analysis.

3. The models developed as part of this work are composable and can be adapted for use in other manufacturing processes. Through the various case studies, the robustness of the models in providing manufacturing decision support, sustainability performance evaluation, and process optimization were explored.

4. Cost models developed as part of the dissertation work were adopted for industry partners to evaluate cost of manufacturing of products using additive manufacturing.

5 CONCLUSIONS

This dissertation work helps to answer the research questions posed in Chapter 1, and has been reported in seven publications, as follows:

1. What process-structure-property and performance relationships are crucial for modelling and simulation of manufacturing processes? (Publications I, II, and VII)
2. How can different forms of knowledge be integrated through metamodelling for additive manufacturing processes? (Publications I, III, IV, V, and VI)
3. How can metamodel-based simulation aid in design space exploration, process parameter optimization, product quality enhancement, and material property tailoring? (Publications II-VII)

In Publications I, II, and VII (Research Question 1), the key interactions between process parameters, process physics, and material properties were discovered and modelled through the integration of experimental studies and graph-based probabilistic modelling, as well as multidisciplinary optimization (MDO). As reported in prior research, experimental work herein revealed microstructural variations in grain sizes and phase constituents along the build direction due to the layer-by-layer WAAM process, which influence the mechanical properties of the final part. Similarly, inclusions and defects arising from the SLM process were found to significantly impact the mechanical and electrical properties of the printed parts. These findings emphasize the need for control and monitoring of material heating and cooling cycles throughout the process; offline process control was demonstrated using Bayesian network modelling. Building upon this work, an MDO approach was applied to model the interactions between process parameters, process physics, and material properties for the binder jetting process.

Publications I, III, IV, V, and VI (Research Question 2) focused on knowledge integration and development of composable metamodels. Experimental research conducted in Publication I was instrumental in collecting data and process

knowledge related to the WAAM process. The impact of process parameter settings on part geometry, microstructure evolution, and mechanical properties was mapped for follow-on model development. While Publication III contributed towards a methodology for developing dimensionless metrics used in part manufacturability evaluations for the LPBF process. These dimensionless metrics encode knowledge related to influencing factors, while facilitating aggregation with other metrics. These metrics are a reduced representation of high dimensional relationships and can be represented in Cartesian coordinate system. In addition, the case study results revealed the possibility cluster ordering for the different metrics based on their spatial arrangement in the Cartesian system. Publication IV and V integrated different forms of knowledge into metamodels for manufacturing decision-making. In Publication IV, a probabilistic model was developed to perform what-if scenario analysis by changing process parameters, geometric feature dimensions, and material properties to estimate the defect (part deformation) induced in a part printed using LPBF. The analytic hierarchy process was used to aggregate expert knowledge about the process into the model. Publication V developed a probabilistic simulation model to relate manufacturing decisions and their impact on product sustainability performance. The presented approach successfully integrated various forms of knowledge (e.g., data, analytical and empirical relationships, and expert knowledge) in a unified simulation model.

Publications II-VII (Research Question 3) examine the application of the developed metamodelling approach for performing design space exploration, process parameter optimization, product quality improvement, and product sustainability performance assessment through several case studies. Publication II, IV, V, and VII explored the development of probabilistic simulation models. The work entailed aggregation of different forms of knowledge in a unified graph-model. Publication III provided a new perspective for development of product design evaluation metrics with a focus on manufacturability aspect. The method established in this publication can help advance design for manufacturing goals. Publication VI and VII addressed multi-objective optimization problems in manufacturing. The methods developed made the optimization process efficient and targeted. These studies elucidate the adaptability and composability of metamodels for a variety of applications.

The foregoing dissertation research was faced with a number of barriers that led to natural limitations of the work. To support future research, several prospective topics have been envisioned based upon these limitations, as follows:

1. Unit manufacturing process (UMP) models have been developed for several manufacturing processes. These models can support information modelling and material flow simulations for manufacturing assembly lines. Integration of UMP models in the machine learning based metamodels will allow for development of factory-level virtual process monitoring capabilities.
2. Real-time monitoring and control of AM processes requires models that can manage large volumes of information flow, process the information quickly, and provide immediate corrective actions. This has been a major limitation of existing model-based process control. Identification of a limited set of key process indicators that need to be monitored and development of modular metamodels with varying levels of abstraction can provide faster response times, which can enable real-time process control.

REFERENCES

A. Simon, H., & Iwasaki, Y. (1988). Causal ordering, comparative statics, and near decomposability. *Journal of Econometrics*, *39*(1), 149–173. https://doi.org/10.1016/0304-4076(88)90043-7

Al-Ahmari, A., Ashfaq, M., Alfaify, A., Abdo, B., Alomar, A., & Dawud, A. (2016). Predicting surface quality of γ-TiAl produced by additive manufacturing process using response surface method. *Journal of Mechanical Science and Technology*, *30*(1), 345–352. https://doi.org/10.1007/s12206-015-1239-y

Alloghani, M., Al-Jumeily, D., Mustafina, J., Hussain, A., & Aljaaf, A. J. (2020). A Systematic Review on Supervised and Unsupervised Machine Learning Algorithms for Data Science. In M. W. Berry, A. Mohamed, & B. W. Yap (Eds.), *Supervised and Unsupervised Learning for Data Science* (pp. 3–21). Springer International Publishing. https://doi.org/10.1007/978-3-030-22475-2_1

Almeida, P., & Williams, S. (2010). Innovative process model of Ti–6Al–4V additive layer manufacturing using cold metal transfer (CMT). *Proceedings of the Twenty-First Annual International Solid Freeform Fabrication Symposium, University of Texas at Austin, Austin, TX, USA*.

Aminzadeh, M., & Kurfess, T. R. (2019). Online quality inspection using Bayesian classification in powder-bed additive manufacturing from high-resolution visual camera images. *Journal of Intelligent Manufacturing*, *30*(6), 2505–2523. https://doi.org/10.1007/s10845-018-1412-0

ASTM. (2021, November 17). *Standard Test Methods for Determining Average Grain Size*. https://www.astm.org/e0112-13r21.html

Bartolomé, E., Bozzo, B., Sevilla, P., Martínez-Pasarell, O., Puig, T., & Granados, X. (2017). ABS 3D printed solutions for cryogenic applications. *Cryogenics*, *82*, 30–37. https://doi.org/10.1016/j.cryogenics.2017.01.005

Bhadeshia, H. K. D. H., & Christian, J. (1990). Bainite in steels. *Metallurgical Transactions A*, *21*(3), 767–797.

Bi, K., Lin, D., Liao, Y., Wu, C.-H., & Parandoush, P. (2021). Additive manufacturing embraces big data. *Progress in Additive Manufacturing*, *6*(2), 181–197. https://doi.org/10.1007/s40964-021-00172-8

Bidulský, R., Bidulská, J., Gobber, F. S., Kvačkaj, T., Petroušek, P., Actis-Grande, M., Weiss, K.-P., & Manfredi, D. (2020). Case Study of the Tensile Fracture Investigation of Additive Manufactured Austenitic Stainless Steels Treated at Cryogenic Conditions. *Materials*, *13*(15), 3328. https://doi.org/10.3390/ma13153328

Blakey-Milner, B., Gradl, P., Snedden, G., Brooks, M., Pitot, J., Lopez, E., Leary, M., Berto, F., & du Plessis, A. (2021). Metal additive manufacturing in aerospace: A review. *Materials & Design*, *209*, 110008. https://doi.org/10.1016/j.matdes.2021.110008

Bowes, R. G. (2008). Classic contributions: Cryogenic treatment Theory and practice of sub-zero treatment of metals. *International Heat Treatment and Surface Engineering*, *2*(2), 76–79. https://doi.org/10.1179/174951508X358473

Bruzzone, P., Fietz, W. H., Minervini, J. V., Novikov, M., Yanagi, N., Zhai, Y., & Zheng, J. (2018). High temperature superconductors for fusion magnets. *Nuclear Fusion*, *58*(10), 103001. https://doi.org/10.1088/1741-4326/aad835

Bykovsky, N., Uglietti, D., Wesche, R., & Bruzzone, P. (2015). Strain Management in HTS High Current Cables. *IEEE Transactions on Applied Superconductivity*, *25*(3), 1–4. https://doi.org/10.1109/TASC.2014.2360041

Cao, L., Li, J., Hu, J., Liu, H., Wu, Y., & Zhou, Q. (2021). Optimization of surface roughness and dimensional accuracy in LPBF additive manufacturing. *Optics & Laser Technology*, *142*, 107246. https://doi.org/10.1016/j.optlastec.2021.107246

Cao, W. (2011). High-Temperature Superconducting Wind Turbine Generators. In I. H. Al-Bahadly (Ed.), *Wind Turbines*. InTech. https://doi.org/10.5772/14660

Chakraborti, A., Nagarajan, H. P. N., Panicker, S., Mokhtarian, H., Coatanéa, E., & Koskinen, K. T. (2019). A Dimension Reduction Method for Efficient Optimization of Manufacturing Performance. *Procedia Manufacturing*, *38*, 556–563. https://doi.org/10.1016/j.promfg.2020.01.070

Chaudhuri, S., Dayal, U., & Narasayya, V. (2011). An overview of business intelligence technology. *Communications of the ACM*, *54*(8), 88–98.

Chen, D., Li, J., Yuan, Y., Gao, C., Cui, Y., Li, S., Liu, X., Wang, H., Peng, C., & Wu, Z. (2021). A Review of the Polymer for Cryogenic Application: Methods, Mechanisms and Perspectives. *Polymers*, *13*(3), 320. https://doi.org/10.3390/polym13030320

Chen, M., Donzel, L., Lakner, M., & Paul, W. (2004). High temperature superconductors for power applications. *Journal of the European Ceramic Society*, *24*(6), 1815–1822. https://doi.org/10.1016/S0955-2219(03)00443-6

Chen, R., Lu, Y., Witherell, P., Simpson, T. W., Kumara, S., & Yang, H. (2021). Ontology-Driven Learning of Bayesian Network for Causal Inference and Quality Assurance in Additive Manufacturing. *IEEE Robotics and Automation Letters*, *6*(3), 6032–6038. https://doi.org/10.1109/LRA.2021.3090020

Cheng, B., Shrestha, S., & Chou, K. (2016). Stress and deformation evaluations of scanning strategy effect in selective laser melting. *Additive Manufacturing*, *12*, 240–251. https://doi.org/10.1016/j.addma.2016.05.007

Coatanéa, E., Nagarajan, H. P. N., Panicker, S., Prod'hon, R., Mokhtarian, H., Chakraborti, A., Paris, H., Ituarte, I. F., & Haapala, K. R. (2020). Systematic manufacturability evaluation using dimensionless metrics and singular value decomposition: A case study for additive manufacturing. *The International Journal of Advanced Manufacturing Technology*. https://doi.org/10.1007/s00170-020-06158-0

Colosimo, B. M., Huang, Q., Dasgupta, T., & Tsung, F. (2018). Opportunities and challenges of quality engineering for additive manufacturing. *Journal of Quality Technology*, *50*(3), 233–252. https://doi.org/10.1080/00224065.2018.1487726

Costa, L., Vilar, R., Reti, T., & Deus, A. M. (2005). Rapid tooling by laser powder deposition: Process simulation using finite element analysis. *Acta Materialia*, *53*(14), 3987–3999. https://doi.org/10.1016/j.actamat.2005.05.003

Craeghs, T., Clijsters, S., Kruth, Jean.-P., Bechmann, F., & Ebert, Marie.-C. (2012). Detection of Process Failures in Layerwise Laser Melting with Optical Process Monitoring. *Physics Procedia*, *39*, 753–759. https://doi.org/10.1016/j.phpro.2012.10.097

Das, P., Chandran, R., Samant, R., & Anand, S. (2015). Optimum part build orientation in additive manufacturing for minimizing part errors and support structures. *Procedia Manufacturing*, *1*, 343–354.

Das, S., & Sutradhar, A. (2020). Multi-physics topology optimization of functionally graded controllable porous structures: Application to heat dissipating problems. *Materials & Design*, *193*, 108775. https://doi.org/10.1016/j.matdes.2020.108775

de Kleer, J., & Brown, J. S. (1986). Theories of causal ordering. *Artificial Intelligence*, *29*(1), 33–61. https://doi.org/10.1016/0004-3702(86)90090-1

Denlinger, E. R., Heigel, J. C., & Michaleris, P. (2015). Residual stress and distortion modeling of electron beam direct manufacturing Ti-6Al-4V. *Proceedings of the Institution of Mechanical Engineers, Part B: Journal of Engineering Manufacture*, *229*(10), 1803–1813.

Doukas, D. I. (2019). Superconducting Transmission Systems: Review, Classification, and Technology Readiness Assessment. *IEEE Transactions on Applied Superconductivity*, *29*(5), 1–5. https://doi.org/10.1109/TASC.2019.2895395

Durrell, J. H., Ainslie, M. D., Zhou, D., Vanderbemden, P., Bradshaw, T., Speller, S., Filipenko, M., & Cardwell, D. A. (2018). Bulk superconductors: A roadmap to applications. *Superconductor Science and Technology*, *31*(10), 103501. https://doi.org/10.1088/1361-6668/aad7ce

Eberhardt, F. (2017). Introduction to the foundations of causal discovery. *International Journal of Data Science and Analytics*, *3*(2), 81–91. https://doi.org/10.1007/s41060-016-0038-6

Eom, S., & Kim, E. (2006). A survey of decision support system applications (1995–2001). *Journal of the Operational Research Society*, *57*(11), 1264–1278. https://doi.org/10.1057/palgrave.jors.2602140

EOS. (2022). *Material Datasheet Copper CuCP*. https://www.eos.info/03_system-related-assets/material-related-contents/metal-materials-and-examples/metal-material-datasheet/copper/material_datasheet_eos-_copper_cucp_en_web.pdf

Espalin, D., Muse, D. W., MacDonald, E., & Wicker, R. B. (2014). 3D Printing multifunctionality: Structures with electronics. *The International Journal of Advanced Manufacturing Technology*, *72*(5), 963–978. https://doi.org/10.1007/s00170-014-5717-7

Filippo, J. M.-D., Delgado, M., Brie, C., & Paynter, H. M. (1991). A survey of bond graphs: Theory, applications and programs. *Journal of the Franklin Institute*, *328*(5), 565–606. https://doi.org/10.1016/0016-0032(91)90044-4

Firouzdor, V., Nejati, E., & Khomamizadeh, F. (2008). Effect of deep cryogenic treatment on wear resistance and tool life of M2 HSS drill. *Journal of Materials Processing Technology*, *206*(1), 467–472. https://doi.org/10.1016/j.jmatprotec.2007.12.072

Fu, C. H., & Guo, Y. B. (2014). Three-Dimensional Temperature Gradient Mechanism in Selective Laser Melting of Ti-6Al-4V. *Journal of Manufacturing Science and Engineering, Transactions of the ASME*, *136*(6). Scopus. https://doi.org/10.1115/1.4028539

Garg, A., Lam, J. S. L., & Savalani, M. M. (2015). A new computational intelligence approach in formulation of functional relationship of open porosity of the additive manufacturing process. *The International Journal of Advanced Manufacturing Technology*, *80*(1), 555–565. https://doi.org/10.1007/s00170-015-6989-2

Ge, J., Ma, T., Han, W., Yuan, T., Jin, T., Fu, H., Xiao, R., Lei, Y., & Lin, J. (2019). Thermal-induced microstructural evolution and defect distribution of wire-arc additive manufacturing 2Cr13 part: Numerical simulation and experimental characterization. *Applied Thermal Engineering*, *163*, 114335. https://doi.org/10.1016/j.applthermaleng.2019.114335

Glymour, C., Zhang, K., & Spirtes, P. (2019). Review of Causal Discovery Methods Based on Graphical Models. *Frontiers in Genetics*, *10*. https://www.frontiersin.org/article/10.3389/fgene.2019.00524

Goguelin, S., Dhokia, V., & Flynn, J. M. (2021). Bayesian optimisation of part orientation in additive manufacturing. *International Journal of Computer Integrated Manufacturing*, *34*(12), 1263–1284. https://doi.org/10.1080/0951192X.2021.1972466

Goldak, J., Chakravarti, A., & Bibby, M. (1984). A new finite element model for welding heat sources. *Metallurgical Transactions B*, *15*(2), 299–305. https://doi.org/10.1007/BF02667333

Gordon, J. V., Haden, C. V., Nied, H. F., Vinci, R. P., & Harlow, D. G. (2018). Fatigue crack growth anisotropy, texture and residual stress in austenitic steel made by wire and arc additive manufacturing. *Materials Science and Engineering: A*, *724*, 431–438. https://doi.org/10.1016/j.msea.2018.03.075

Goudet, O., Kalainathan, D., Caillou, P., Guyon, I., Lopez-Paz, D., & Sebag, M. (2018). Learning Functional Causal Models with Generative Neural Networks. In H. J. Escalante, S. Escalera, I. Guyon, X. Baró, Y. Güçlütürk, U. Güçlü, & M. van Gerven (Eds.), *Explainable and Interpretable Models in Computer Vision and Machine Learning* (pp. 39–80). Springer International Publishing. https://doi.org/10.1007/978-3-319-98131-4_3

Graf, M., Hälsig, A., Höfer, K., Awiszus, B., & Mayr, P. (2018). Thermo-Mechanical Modelling of Wire-Arc Additive Manufacturing (WAAM) of Semi-Finished Products. *Metals*, *8*(12), Article 12. https://doi.org/10.3390/met8121009

Gu, D., Shi, X., Poprawe, R., Bourell, D. L., Setchi, R., & Zhu, J. (2021). Material-structure-performance integrated laser-metal additive manufacturing. *Science*, *372*(6545), eabg1487. https://doi.org/10.1126/science.abg1487

Gubser, D. U. (2003). Superconducting motors and generators for naval applications. *Physica C: Superconductivity*, *392–396*, 1192–1195. https://doi.org/10.1016/S0921-4534(03)01124-9

Guschlbauer, R., Momeni, S., Osmanlic, F., & Körner, C. (2018). Process development of 99.95% pure copper processed via selective electron beam melting and its mechanical and physical properties. *Materials Characterization*, *143*, 163–170. https://doi.org/10.1016/j.matchar.2018.04.009

Hartwig, G. (1995). *Polymer Properties at Room and Cryogenic Temperatures*. Springer Science & Business Media.

Hartwig, Z. S., Vieira, R. F., Sorbom, B. N., Badcock, R. A., Bajko, M., Beck, W. K., Castaldo, B., Craighill, C. L., Davies, M., Estrada, J., Fry, V., Golfinopoulos, T., Hubbard, A. E., Irby, J. H., Kuznetsov, S., Lammi, C. J., Michael, P. C., Mouratidis, T., Murray, R. A., … Zhou, L. (2020). VIPER: An industrially scalable high-current high-temperature superconductor cable. *Superconductor Science and Technology*, *33*(11), 11LT01. https://doi.org/10.1088/1361-6668/abb8c0

Haruna, A., & Jiang, P. (2022). Adaptability analysis of design for additive manufacturing by using fuzzy Bayesian network approach. *Advanced Engineering Informatics*, *52*, 101613. https://doi.org/10.1016/j.aei.2022.101613

Hertlein, N., Deshpande, S., Venugopal, V., Kumar, M., & Anand, S. (2020). Prediction of selective laser melting part quality using hybrid Bayesian network. *Additive Manufacturing*, *32*, 101089. https://doi.org/10.1016/j.addma.2020.101089

Hilletofth, P., Hilmola, O.-P., Wang, Y., Rouzafzoon, J., & Helo, P. (2016). Developing service supply chains by using agent based simulation. *Industrial Management & Data Systems*.

Hiltunen, I. (2010). *Tools for cryogenic design of superconducting induction heater* [Tampere University of Technology]. https://trepo.tuni.fi/handle/10024/114926

Hiltunen, I., Jarvela, J., Lehtonen, J., Mikkonen, R., Stenvall, A., & Viljamaa, J. (2009). Transverse Thermal Conductivity in an Epoxy Impregnated $\rm MgB_2$ Coil. *IEEE Transactions on Applied Superconductivity*, *19*(3), 2407–2410. https://doi.org/10.1109/TASC.2009.2018045

Hu, Z., & Mahadevan, S. (2017). Uncertainty quantification in prediction of material properties during additive manufacturing. *Scripta Materialia*, *135*, 135–140. https://doi.org/10.1016/j.scriptamat.2016.10.014

Hull, J. R., & Murakami, M. (2004). Applications of bulk high-temperature Superconductors. *Proceedings of the IEEE*, *92*(10), 1705–1718. https://doi.org/10.1109/JPROC.2004.833796

Irwin, J., & Michaleris, P. (2016). A line heat input model for additive manufacturing. *Journal of Manufacturing Science and Engineering*, *138*(11), 111004.

ISO/TC 261, & ASTM Committee F42. (2021). *ISO/ASTM 52900:2021(en), Additive manufacturing—General principles—Fundamentals and vocabulary*. ISO/ASTM. https://www.iso.org/obp/ui/#iso:std:iso-astm:52900:ed-2:v1:en

Iwasa, Y. (2006). HTS and NMR/MRI magnets: Unique features, opportunities, and challenges. *Physica C: Superconductivity and Its Applications*, *445–448*, 1088–1094. https://doi.org/10.1016/j.physc.2006.05.040

Iwasaki, Y., & Simon, H. A. (1994). Causality and model abstraction. *Artificial Intelligence*, *67*(1), 143–194. https://doi.org/10.1016/0004-3702(94)90014-0

Jadhav, S. D., Dadbakhsh, S., Goossens, L., Kruth, J.-P., Van Humbeeck, J., & Vanmeensel, K. (2019). Influence of selective laser melting process parameters on texture evolution in pure copper. *Journal of Materials Processing Technology*, *270*, 47–58. https://doi.org/10.1016/j.jmatprotec.2019.02.022

Jang, C., Cho, P.-Y., Kim, M., Oh, S.-J., & Yang, J.-S. (2010). Effects of microstructure and residual stress on fatigue crack growth of stainless steel narrow gap welds. *Materials & Design*, *31*(4), 1862–1870. https://doi.org/10.1016/j.matdes.2009.10.062

Jawahir, I. S., Attia, H., Biermann, D., Duflou, J., Klocke, F., Meyer, D., Newman, S. T., Pusavec, F., Putz, M., Rech, J., Schulze, V., & Umbrello, D. (2016). Cryogenic manufacturing processes. *CIRP Annals - Manufacturing Technology*, *65*(2), 713–736. https://doi.org/10.1016/j.cirp.2016.06.007

Jia, H., Sun, H., Wang, H., Wu, Y., & Wang, H. (2021). Scanning strategy in selective laser melting (SLM): A review. *The International Journal of Advanced Manufacturing Technology*, *113*(9), 2413–2435. https://doi.org/10.1007/s00170-021-06810-3

Jing, L., & Ma, J. (2020, November 3). *Additive Manufacturing Adaptiveness Analysis Using Fuzzy Bayesian Network*. ASME 2020 International Design Engineering Technical Conferences and Computers and Information in Engineering Conference. https://doi.org/10.1115/DETC2020-22535

Kaisler, S., Armour, F., Espinosa, J. A., & Money, W. (2013). *Big data: Issues and challenges moving forward*. 995–1004.

Kalia, S., & Fu, S.-Y. (Eds.). (2013). *Polymers at Cryogenic Temperatures*. Springer Berlin Heidelberg. https://doi.org/10.1007/978-3-642-35335-2

Karthik, G. M., Kim, E. S., Sathiyamoorthi, P., Zargaran, A., Jeong, S. G., Xiong, R., Kang, S. H., Cho, J.-W., & Kim, H. S. (2021). Delayed deformation-induced martensite transformation and enhanced cryogenic tensile properties in laser additive manufactured 316L austenitic stainless steel. *Additive Manufacturing*, *47*, 102314. https://doi.org/10.1016/j.addma.2021.102314

Kelly, S. M., & Kampe, S. L. (2004). Microstructural evolution in laser-deposited multilayer Ti-6Al-4V builds: Part II. Thermal modeling. *Metallurgical and Materials Transactions A*, *35*(6), 1869–1879. https://doi.org/10.1007/s11661-004-0095-7

Khan, S. G., Herrmann, G., Lewis, F. L., Pipe, T., & Melhuish, C. (2012). Reinforcement learning and optimal adaptive control: An overview and implementation examples. *Annual Reviews in Control*, *36*(1), 42–59. https://doi.org/10.1016/j.arcontrol.2012.03.004

Khanzadeh, M., Rao, P., Jafari-Marandi, R., Smith, B. K., Tschopp, M. A., & Bian, L. (2017). Quantifying Geometric Accuracy With Unsupervised Machine Learning: Using Self-Organizing Map on Fused Filament Fabrication Additive Manufacturing Parts. *Journal of Manufacturing Science and Engineering*, *140*(3). https://doi.org/10.1115/1.4038598

Kok, Y., Tan, X. P., Wang, P., Nai, M. L. S., Loh, N. H., Liu, E., & Tor, S. B. (2018). Anisotropy and heterogeneity of microstructure and mechanical properties in metal additive manufacturing: A critical review. *Materials & Design*, *139*, 565–586. https://doi.org/10.1016/j.matdes.2017.11.021

Le, V. T., & Mai, D. S. (2020). Microstructural and mechanical characteristics of 308L stainless steel manufactured by gas metal arc welding-based additive manufacturing. *Materials Letters*, *271*, 127791. https://doi.org/10.1016/j.matlet.2020.127791

Le, V. T., Mai, D. S., Doan, T. K., & Paris, H. (2021). Wire and arc additive manufacturing of 308L stainless steel components: Optimization of processing parameters and material properties. *Engineering Science and Technology, an International Journal*, *24*(4), 1015–1026. https://doi.org/10.1016/j.jestch.2021.01.009

Lewandowski, J. J., & Seifi, M. (2016). Metal Additive Manufacturing: A Review of Mechanical Properties. *Annual Review of Materials Research*, *46*(1), 151–186. https://doi.org/10.1146/annurev-matsci-070115-032024

Li, B., Wang, C., Wei, Z., Xin, Y., Li, B., & He, J. (2018). Technical Requirements of the DC Superconducting Fault Current Limiter. *IEEE Transactions on Applied Superconductivity*, *28*(4), 1–5. https://doi.org/10.1109/TASC.2018.2811961

Li, C., Ren, J., & Wang, H. (2016). A system dynamics simulation model of chemical supply chain transportation risk management systems. *Computers & Chemical Engineering*, *89*, 71–83.

Li, J., Hu, J., Cao, L., Wang, S., Liu, H., & Zhou, Q. (2021). Multi-objective process parameters optimization of SLM using the ensemble of metamodels. *Journal of Manufacturing Processes*, *68*, 198–209. https://doi.org/10.1016/j.jmapro.2021.05.038

Li, P., Warner, D. H., Fatemi, A., & Phan, N. (2016). Critical assessment of the fatigue performance of additively manufactured Ti–6Al–4V and perspective for future research. *International Journal of Fatigue*, *85*, 130–143. https://doi.org/10.1016/j.ijfatigue.2015.12.003

Lovatt, A. M., & Shercliff, H. R. (1998). Manufacturing process selection in engineering design. Part 1: The role of process selection. *Materials & Design*, *19*(5–6), 205–215. https://doi.org/10.1016/S0261-3069(98)00038-7

Lu, X., Zhou, Y. F., Xing, X. L., Shao, L. Y., Yang, Q. X., & Gao, S. Y. (2017). Open-source wire and arc additive manufacturing system: Formability, microstructures, and mechanical properties. *The International Journal of Advanced Manufacturing Technology*, *93*(5), 2145–2154. https://doi.org/10.1007/s00170-017-0636-z

Luo, Z., & Zhao, Y. (2018). A survey of finite element analysis of temperature and thermal stress fields in powder bed fusion Additive Manufacturing. *Additive Manufacturing*, *21*, 318–332. https://doi.org/10.1016/j.addma.2018.03.022

Lvovsky, Y., Stautner, E. W., & Zhang, T. (2013). Novel technologies and configurations of superconducting magnets for MRI. *Superconductor Science and Technology*, *26*(9), 093001. https://doi.org/10.1088/0953-2048/26/9/093001

Maconachie, T., Leary, M., Lozanovski, B., Zhang, X., Qian, M., Faruque, O., & Brandt, M. (2019). SLM lattice structures: Properties, performance, applications and challenges. *Materials & Design*, *183*, 108137. https://doi.org/10.1016/j.matdes.2019.108137

Marchionini, B. G., Yamada, Y., Martini, L., & Ohsaki, H. (2017). High-Temperature Superconductivity: A Roadmap for Electric Power Sector Applications, 2015–2030. *IEEE Transactions on Applied Superconductivity*, *27*(4), 1–7. https://doi.org/10.1109/TASC.2017.2671680

Martina, F., Colegrove, P. A., Williams, S. W., & Meyer, J. (2015). Microstructure of Interpass Rolled Wire + Arc Additive Manufacturing Ti-6Al-4V Components. *Metallurgical and Materials Transactions A*, *46*(12), 6103–6118. https://doi.org/10.1007/s11661-015-3172-1

Mazzucato, F., Avram, O., Valente, A., & Carpanzano, E. (2019). Recent Advances Toward the Industrialization of Metal Additive Manufacturing. In *Systems Engineering in the Fourth Industrial Revolution* (pp. 273–319). John Wiley & Sons, Ltd. https://doi.org/10.1002/9781119513957.ch12

Mezrag, B., Deschaux-Beaume, F., & Benachour, M. (2015). Control of mass and heat transfer for steel/aluminium joining using cold metal transfer process. *Science and Technology of Welding and Joining*, *20*(3), 189–198.

Michaleris, P. (2014). Modeling metal deposition in heat transfer analyses of additive manufacturing processes. *Finite Elements in Analysis and Design*, *86*, 51–60. https://doi.org/10.1016/j.finel.2014.04.003

Mirzendehdel, A. M., & Suresh, K. (2015). A Pareto-optimal approach to multimaterial topology optimization. *Journal of Mechanical Design*, *137*(10).

Mokhtarian, H., Coatanéa, E., Paris, H., Ritola, T., Ellman, A., Vihinen, J., Koskinen, K., & Ikkala, K. (2016, December 5). *A Network Based Modelling Approach Using the Dimensional Analysis Conceptual Modeling (DACM) Framework for Additive Manufacturing Technologies*. ASME 2016 International Design Engineering Technical Conferences and Computers and Information in Engineering Conference. https://doi.org/10.1115/DETC2016-60473

Mokhtarian, H., Hamedi, A., Nagarajan, H. P. N., Panicker, S., Coatanéa, E., & Haapala, K. (2019). Probabilistic Modelling of Defects in Additive Manufacturing: A Case Study in Powder Bed Fusion Technology. *Procedia CIRP*, *81*, 956–961. https://doi.org/10.1016/j.procir.2019.03.234

Montevecchi, F., Venturini, G., Grossi, N., Scippa, A., & Campatelli, G. (2018). Idle time selection for wire-arc additive manufacturing: A finite element-based technique. *Additive Manufacturing*, *21*, 479–486. https://doi.org/10.1016/j.addma.2018.01.007

Montevecchi, F., Venturini, G., Scippa, A., & Campatelli, G. (2016). Finite Element Modelling of Wire-arc-additive-manufacturing Process. *Procedia CIRP*, *55*, 109–114. https://doi.org/10.1016/j.procir.2016.08.024

Mukherjee, P., & Rao, V. V. (2019). Design and development of high temperature superconducting magnetic energy storage for power applications—A review. *Physica C: Superconductivity and Its Applications*, *563*, 67–73. https://doi.org/10.1016/j.physc.2019.05.001

Nagarajan, H. P. N., Panicker, S., Mokhtarian, H., Coatanéa, E., & Haapala, K. R. (2020). Improving worker health and safety in wire arc additive manufacturing: A graph-based approach. *Procedia CIRP*, *90*, 461–466. https://doi.org/10.1016/j.procir.2020.01.116

Nagarajan, H. P. N., Panicker, S., Mokhtarian, H., Remy-Lorit, T., Coatanéa, E., Prod'hon, R., Jafarian, H., Haapala, K. R., & Chakraborti, A. (2019). Graph-Based Metamodeling for Characterizing Cold Metal Transfer Process Performance. *Smart and Sustainable Manufacturing Systems*, *3*(2), 20190026. https://doi.org/10.1520/SSMS20190026

Nannapaneni, S., Mahadevan, S., & Rachuri, S. (2016). Performance evaluation of a manufacturing process under uncertainty using Bayesian networks. *Journal of Cleaner Production*, *113*, 947–959. https://doi.org/10.1016/j.jclepro.2015.12.003

Niyaghi, F., Haapala, K. R., Harper, S. L., & Weismiller, M. C. (2014). Stability and Biological Responses of Zinc Oxide Metalworking Nanofluids (ZnO MWnFTM) using Dynamic Light Scattering and Zebrafish Assays. *Tribology Transactions*, *57*(4), 730–739. https://doi.org/10.1080/10402004.2014.906695

Pahl, G., Beitz, W., Feldhusen, J., & Grote, K. (2007). Engineering Design: A Systematic Approach Third Edition. *Berlin, Springer Science+ Business Media Deutschland GmbH, 2007. 632*.

Panicker, S., Nagarajan, H. P. N., Mokhtarian, H., Hamedi, A., Chakraborti, A., Coatanéa, E., Haapala, K. R., & Koskinen, K. (2019). Tracing the Interrelationship between Key Performance Indicators and Production Cost using Bayesian Networks. *Procedia CIRP*, *81*, 500–505. https://doi.org/10.1016/j.procir.2019.03.136

Panicker, S., Nagarajan, H. P. N., Tuominen, J., Patnamsetty, M., Coatanéa, E., & Haapala, K. R. (2022). Investigation of thermal influence on weld microstructure and mechanical properties in wire and arc additive manufacturing of steels. *Materials Science and Engineering: A*, *853*, 143690. https://doi.org/10.1016/j.msea.2022.143690

Paredes, M., Grolleau, V., & Wierzbicki, T. (2020). On ductile fracture of 316L stainless steels at room and cryogenic temperature level: An engineering approach to determine material parameters. *Materialia*, *10*, 100624. https://doi.org/10.1016/j.mtla.2020.100624

Paul, S., & Chattopadhyay, A. B. (1995). Effects of cryogenic cooling by liquid nitrogen jet on forces, temperature and surface residual stresses in grinding steels. *Cryogenics*, *35*(8), 515–523. https://doi.org/10.1016/0011-2275(95)98219-Q

Paul, S., & Chattopadhyay, A. B. (2006). Environmentally Conscious Machining and Grinding with Cryogenic Cooling. *Machining Science and Technology*, *10*(1), 87–131. https://doi.org/10.1080/10910340500534316

Pearl, J. (2000). *Causality: Models, reasoning and inference* (Vol. 29). Springer.

Pérez, M., Carou, D., Rubio, E. M., & Teti, R. (2020). Current advances in additive manufacturing. *Procedia CIRP*, *88*, 439–444. https://doi.org/10.1016/j.procir.2020.05.076

Petersen, M. L., & van der Laan, M. J. (2014). Causal models and learning from data: Integrating causal modeling and statistical estimation. *Epidemiology (Cambridge, Mass.)*, *25*(3), 418–426. https://doi.org/10.1097/EDE.0000000000000078

Pillai, D. D. (1990). Developing a decision support system for optimizing automated wafer fabrication. *IEEE Transactions on Components, Hybrids, and Manufacturing Technology*, *13*(1), 94–102.

Plocher, J., & Panesar, A. (2019). Review on design and structural optimisation in additive manufacturing: Towards next-generation lightweight structures. *Materials & Design*, *183*, 108164. https://doi.org/10.1016/j.matdes.2019.108164

Popov, D., Fikiin, K., Stankov, B., Alvarez, G., Youbi-Idrissi, M., Damas, A., Evans, J., & Brown, T. (2019). Cryogenic heat exchangers for process cooling and renewable energy storage: A review. *Applied Thermal Engineering*, *153*, 275–290. https://doi.org/10.1016/j.applthermaleng.2019.02.106

Power, D. J. (2001). Supporting decision-makers: An expanded framework. *Proceedings of Informing Science and IT Education*, 1901–1915.

Qian, L., Mei, J., Liang, J., & Wu, X. (2005). Influence of position and laser power on thermal history and microstructure of direct laser fabricated Ti–6Al–4V samples. *Materials Science and Technology*, *21*(5), 597–605. https://doi.org/10.1179/174328405X21003

Qiu, C., Adkins, N. J. E., & Attallah, M. M. (2016). Selective laser melting of Invar 36: Microstructure and properties. *Acta Materialia*, *103*, 382–395. https://doi.org/10.1016/j.actamat.2015.10.020

Raina, R., Battle, A., Lee, H., Packer, B., & Ng, A. Y. (2007). Self-taught learning: Transfer learning from unlabeled data. *Proceedings of the 24th International Conference on Machine Learning*, 759–766. https://doi.org/10.1145/1273496.1273592

Ray, K. K., & Das, D. (2017). Improved wear resistance of steels by cryotreatment: The current state of understanding. *Materials Science and Technology*, *33*(3), 340–354. https://doi.org/10.1080/02670836.2016.1206292

Rehman, W., farhan, M., & Rehman, F. (2020, August 4). A Review of Cryogenics Applications for Power and Energy. *ASME 2020 Power Conference*. ASME 2020 Power Conference collocated with the 2020 International Conference on Nuclear Engineering, Virtual, Online. https://doi.org/10.1115/POWER2020-16911

Reichardt, A., Shapiro, A. A., Otis, R., Dillon, R. P., Borgonia, J. P., McEnerney, B. W., Hosemann, P., & Beese, A. M. (2021). Advances in additive manufacturing of metal-based functionally graded materials. *International Materials Reviews*, *66*(1), 1–29. https://doi.org/10.1080/09506608.2019.1709354

Rodrigues, T. A., Duarte, V., Avila, J. A., Santos, T. G., Miranda, R. M., & Oliveira, J. P. (2019). Wire and arc additive manufacturing of HSLA steel: Effect of thermal cycles on microstructure and mechanical properties. *Additive Manufacturing*, *27*, 440–450. https://doi.org/10.1016/j.addma.2019.03.029

Rodrigues, T. A., Duarte, V., Miranda, R., Santos, T. G., & Oliveira, J. (2019). Current status and perspectives on wire and arc additive manufacturing (WAAM). *Materials*, *12*(7), 1121.

Rodriguez, E., Medina, F., Espalin, D., Terrazas, C., Muse, D., Henry, C., MacDonald, E., & Wicker, R. B. (2012). *Integration of a Thermal Imaging Feedback Control System in Electron Beam Melting*. https://doi.org/10.26153/TSW/15402

Roh, B.-M., Kumara, S. R. T., Simpson, T. W., Michaleris, P., Witherell, P., & Assouroko, I. (2016, December 5). *Ontology-Based Laser and Thermal Metamodels for Metal-Based Additive Manufacturing*. ASME 2016 International Design Engineering Technical Conferences and Computers and Information in Engineering Conference. https://doi.org/10.1115/DETC2016-60233

Russenschuck, S. (2010). Appendix A: Material Property Data for Quench Simulations. In *Field Computation for Accelerator Magnets* (pp. 703–715). John Wiley & Sons, Ltd. https://doi.org/10.1002/9783527635467.app1

Saaty, T. L. (1980). *The analytic hierarchy process: Planning, priority setting, resource allocation*. McGraw-Hill International Book Co.

Salman, O. O., Brenne, F., Niendorf, T., Eckert, J., Prashanth, K. G., He, T., & Scudino, S. (2019). Impact of the scanning strategy on the mechanical behavior of 316L steel synthesized by selective laser melting. *Journal of Manufacturing Processes*, *45*, 255–261. https://doi.org/10.1016/j.jmapro.2019.07.010

Seifi, M., Gorelik, M., Waller, J., Hrabe, N., Shamsaei, N., Daniewicz, S., & Lewandowski, J. J. (2017). Progress Towards Metal Additive Manufacturing Standardization to

Support Qualification and Certification. *JOM*, *69*(3), 439–455. https://doi.org/10.1007/s11837-017-2265-2

Silbernagel, C., Gargalis, L., Ashcroft, I., Hague, R., Galea, M., & Dickens, P. (2019). Electrical resistivity of pure copper processed by medium-powered laser powder bed fusion additive manufacturing for use in electromagnetic applications. *Additive Manufacturing*, *29*, 100831. https://doi.org/10.1016/j.addma.2019.100831

Singla, A. K., Singh, J., & Sharma, V. S. (2018). Processing of materials at cryogenic temperature and its implications in manufacturing: A review. *Materials and Manufacturing Processes*, *33*(15), 1603–1640. https://doi.org/10.1080/10426914.2018.1424908

SLM Solutions. (2019). *Material Datasheet Fe-Alloy Invar36*. https://www.slm-solutions.com/fileadmin/Content/Powder/MDS/MDS_Fe-Alloy_Invar36_0219_EN.pdf

Song, C., Liu, Q., Deng, S., Li, H., & Kitamura, Y. (2019). Cryogenic-based CO2 capture technologies: State-of-the-art developments and current challenges. *Renewable and Sustainable Energy Reviews*, *101*, 265–278. https://doi.org/10.1016/j.rser.2018.11.018

Song, Y., Sun, Q., Guo, K., Wang, X., Liu, J., & Sun, J. (2020). Effect of scanning strategies on the microstructure and mechanical behavior of 316L stainless steel fabricated by selective laser melting. *Materials Science and Engineering: A*, *793*, 139879. https://doi.org/10.1016/j.msea.2020.139879

Spirtes, P., Glymour, C. N., Scheines, R., & Heckerman, D. (2000). *Causation, prediction, and search*. MIT press.

Stautner, W., Vanapalli, S., Weiss, K.-P., Chen, R., Amm, K., Budesheim, E., & Ricci, J. (2017). The scope of additive manufacturing in cryogenics, component design, and applications. *IOP Conference Series: Materials Science and Engineering*, *278*, 012134. https://doi.org/10.1088/1757-899X/278/1/012134

Steel, D. (2005). Indeterminism and the Causal Markov Condition. *The British Journal for the Philosophy of Science*, *56*(1), 3–26. https://doi.org/10.1093/phisci/axi101

Sun, L., Jiang, F., Huang, R., Yuan, D., Guo, C., & Wang, J. (2020). Microstructure and Mechanical Properties of Low-Carbon High-Strength Steel Fabricated by Wire and Arc Additive Manufacturing. *Metals*, *10*(2), Article 2. https://doi.org/10.3390/met10020216

Tan, X., Kok, Y., Toh, W. Q., Tan, Y. J., Descoins, M., Mangelinck, D., Tor, S. B., Leong, K. F., & Chua, C. K. (2016). Revealing martensitic transformation and α/β interface evolution in electron beam melting three-dimensional-printed Ti-6Al-4V. *Scientific Reports*, *6*(1), Article 1. https://doi.org/10.1038/srep26039

Tian, Y., Tomus, D., Rometsch, P., & Wu, X. (2017). Influences of processing parameters on surface roughness of Hastelloy X produced by selective laser melting. *Additive Manufacturing*, *13*, 103–112. https://doi.org/10.1016/j.addma.2016.10.010

Todai, M., Nakano, T., Liu, T., Yasuda, H. Y., Hagihara, K., Cho, K., Ueda, M., & Takeyama, M. (2017). Effect of building direction on the microstructure and tensile properties of Ti-48Al-2Cr-2Nb alloy additively manufactured by electron beam melting. *Additive Manufacturing*, *13*, 61–70. https://doi.org/10.1016/j.addma.2016.11.001

Tran, T. Q., Chinnappan, A., Lee, J. K. Y., Loc, N. H., Tran, L. T., Wang, G., Kumar, V. V., Jayathilaka, W. a. D. M., Ji, D., Doddamani, M., & Ramakrishna, S. (2019). 3D Printing of Highly Pure Copper. *Metals*, *9*(7), 756. https://doi.org/10.3390/met9070756

Uglietti, D. (2019). A review of commercial high temperature superconducting materials for large magnets: From wires and tapes to cables and conductors. *Superconductor Science and Technology*, *32*(5), 053001. https://doi.org/10.1088/1361-6668/ab06a2

Vaghela, H., Lakhera, V. J., & Sarkar, B. (2021). Forced flow cryogenic cooling in fusion devices: A review. *Heliyon*, *7*(1), e06053. https://doi.org/10.1016/j.heliyon.2021.e06053

Välimäki, E. (2017). *Modelling, simulation and validation of CMT process: An application for additive manufacturing*.

Van Nugteren, J. (2016). *High Temperature Superconductor Accelerator Magnets* [University of Twente]. https://cds.cern.ch/record/2228249

Velaga, S. K., & Ravisankar, A. (2017). Finite element based parametric study on the characterization of weld process moving heat source parameters in austenitic stainless steel. *International Journal of Pressure Vessels and Piping*, *157*, 63–73. https://doi.org/10.1016/j.ijpvp.2017.09.001

Vilalta, R., & Drissi, Y. (2002). A Perspective View and Survey of Meta-Learning. *Artificial Intelligence Review*, *18*(2), 77–95. https://doi.org/10.1023/A:1019956318069

Vuković, M., & Thalmann, S. (2022). Causal Discovery in Manufacturing: A Structured Literature Review. *Journal of Manufacturing and Materials Processing*, *6*(1), Article 1. https://doi.org/10.3390/jmmp6010010

Vyas, H., Mehta, K. P., Badheka, V., & Doshi, B. (2020). Pipe-to-pipe friction welding of dissimilar Al-SS joints for cryogenic applications. *Journal of the Brazilian Society of Mechanical Sciences and Engineering*, *42*(2), 96. https://doi.org/10.1007/s40430-020-2181-1

Wang, C., Tan, X. P., Tor, S. B., & Lim, C. S. (2020). Machine learning in additive manufacturing: State-of-the-art and perspectives. *Additive Manufacturing*, *36*, 101538. https://doi.org/10.1016/j.addma.2020.101538

Wang, X. L., Tsai, Y. T., Yang, J. R., Wang, Z. Q., Li, X. C., Shang, C. J., & Misra, R. D. K. (2017). Effect of interpass temperature on the microstructure and mechanical properties of multi-pass weld metal in a 550-MPa-grade offshore engineering steel. *Welding in the World*, *61*(6), 1155–1168. https://doi.org/10.1007/s40194-017-0498-x

Wang, Y., Zhong, R. Y., & Xu, X. (2018). A decision support system for additive manufacturing process selection using a hybrid multiple criteria decision-making method. *Rapid Prototyping Journal*, *24*(9), 1544–1553. https://doi.org/10.1108/RPJ-01-2018-0002

Wang, Z. Y., & Rajurkar, K. P. (2000). Cryogenic Machining of Hard-to-Cut Materials. *Wear*, *239*(2), 168–175. https://doi.org/16/S0043-1648(99)00361-0

Witherell, P., Feng, S., Simpson, T. W., Saint John, D. B., Michaleris, P., Liu, Z.-K., Chen, L.-Q., & Martukanitz, R. (2014). Toward Metamodels for Composable and

Reusable Additive Manufacturing Process Models. *Journal of Manufacturing Science and Engineering*, *136*(6). https://doi.org/10.1115/1.4028533

Wu, Q., Mukherjee, T., De, A., & DebRoy, T. (2020). Residual stresses in wire-arc additive manufacturing – Hierarchy of influential variables. *Additive Manufacturing*, *35*, 101355. https://doi.org/10.1016/j.addma.2020.101355

Xin, B., Zhou, X., Cheng, G., Yao, J., & Gong, Y. (2020). Microstructure and mechanical properties of thin-wall structure by hybrid laser metal deposition and laser remelting process. *Optics & Laser Technology*, *127*, 106087. https://doi.org/10.1016/j.optlastec.2020.106087

Yakout, M., Elbestawi, M. A., & Veldhuis, S. C. (2019). Density and mechanical properties in selective laser melting of Invar 36 and stainless steel 316L. *Journal of Materials Processing Technology*, *266*, 397–420. https://doi.org/10.1016/j.jmatprotec.2018.11.006

Yakout, M., Phillips, I., Elbestawi, M. A., & Fang, Q. (2021). In-situ monitoring and detection of spatter agglomeration and delamination during laser-based powder bed fusion of Invar 36. *Optics & Laser Technology*, *136*, 106741. https://doi.org/10.1016/j.optlastec.2020.106741

Yan, X., Chang, C., Dong, D., Gao, S., Ma, W., Liu, M., Liao, H., & Yin, S. (2020). Microstructure and mechanical properties of pure copper manufactured by selective laser melting. *Materials Science and Engineering: A*, *789*, 139615. https://doi.org/10.1016/j.msea.2020.139615

Yang, X., Ma, W., Ren, Y., Liu, S., Wang, Y., Wang, W., & Tang, H. (2021). Subgrain microstructures and tensile properties of 316L stainless steel manufactured by selective laser melting. *Journal of Iron and Steel Research International*, *28*(9), 1159–1167. https://doi.org/10.1007/s42243-021-00561-x

Yang, Z., Eddy, D., Krishnamurty, S., Grosse, I., Denno, P., & Lopez, F. (2016, December 5). *Investigating Predictive Metamodeling for Additive Manufacturing*. ASME 2016 International Design Engineering Technical Conferences and Computers and Information in Engineering Conference. https://doi.org/10.1115/DETC2016-60506

Yazdani-Asrami, M., Zhang, M., & Yuan, W. (2021). Challenges for developing high temperature superconducting ring magnets for rotating electric machine applications in future electric aircrafts. *Journal of Magnetism and Magnetic Materials*, *522*, 167543. https://doi.org/10.1016/j.jmmm.2020.167543

Ye, J., Mahmoudi, M., Karayagiz, K., Johnson, L., Seede, R., Karaman, I., Arroyave, R., & Elwany, A. (2021). Bayesian Calibration of Multiple Coupled Simulation Models for Metal Additive Manufacturing: A Bayesian Network Approach. *ASCE-ASME J Risk and Uncert in Engrg Sys Part B Mech Engrg*, *8*(1). https://doi.org/10.1115/1.4052270

Zaeh, M. F., & Branner, G. (2010a). Investigations on residual stresses and deformations in selective laser melting. *Production Engineering*, *4*(1), 35–45. https://doi.org/10.1007/s11740-009-0192-y

Zaeh, M. F., & Branner, G. (2010b). Investigations on residual stresses and deformations in selective laser melting. *Production Engineering*, *4*(1), 35–45. https://doi.org/10.1007/s11740-009-0192-y

Zhang, B., Li, Y., & Bai, Q. (2017). Defect Formation Mechanisms in Selective Laser Melting: A Review. *Chinese Journal of Mechanical Engineering*, *30*(3), 515–527. https://doi.org/10.1007/s10033-017-0121-5

Zhang, D. Q., Cai, Q. Z., Liu, J. H., Zhang, L., & Li, R. D. (2010). Select laser melting of W–Ni–Fe powders: Simulation and experimental study. *The International Journal of Advanced Manufacturing Technology*, *51*(5), 649–658. https://doi.org/10.1007/s00170-010-2641-3

Zhang, F., Johnson, D., Johnson, M., Watkins, D., Froese, R., & Wang, J. (2016). Decision support system integrating GIS with simulation and optimisation for a biofuel supply chain. *Renewable Energy*, *85*, 740–748. https://doi.org/10.1016/j.renene.2015.07.041

Zhang, L. (2014). *A framework to model big data driven complex cyber physical control systems*. 283–288.

Zhang, S., Zhu, H., Hu, Z., Zeng, X., & Zhong, F. (2019). Selective Laser Melting of Cu10Zn alloy powder using high laser power. *Powder Technology*, *342*, 613–620. https://doi.org/10.1016/j.powtec.2018.10.002

Zhou, F., Yang, B., Li, L., & Chen, Z. (2008). Overview of the New Types of Intelligent Decision Support System. *2008 3rd International Conference on Innovative Computing Information and Control*, 267–267. https://doi.org/10.1109/ICICIC.2008.412

PUBLICATIONS

PUBLICATION I

Investigation of thermal influence on weld microstructure and mechanical properties in wire and arc additive manufacturing of steels

Suraj Panicker, Hari P.N. Nagarajan, Jari Tuominen, Madan Patnamsetty, Eric Coatanéa, and Karl R. Haapala

Materials Science & Engineering A, vol. 853 (2022)

https://doi.org/10.1016/j.msea.2022.143690

Materials Science & Engineering A 853 (2022) 143690

Contents lists available at ScienceDirect

Materials Science & Engineering A

journal homepage: www.elsevier.com/locate/msea

Investigation of thermal influence on weld microstructure and mechanical properties in wire and arc additive manufacturing of steels

Suraj Panicker [a,*], Hari P.N. Nagarajan [a], Jari Tuominen [b], Madan Patnamsetty [b], Eric Coatanéa [a], Karl R. Haapala [c]

[a] Faculty of Engineering and Natural Sciences, Automation Technology and Mechanical Engineering, Tampere University, Tampere, 33720, Finland
[b] Faculty of Engineering and Natural Sciences, Materials Science and Environmental Engineering, Tampere University, Tampere, 33720, Finland
[c] School of Mechanical, Industrial, and Manufacturing Engineering, Oregon State University, Corvallis, OR, 97331, USA

ARTICLE INFO

Keywords:
Wire and arc additive manufacturing
Microstructure characterization
Mechanical properties
Steels

ABSTRACT

Alloy steels are commonly used in many industrial and consumer products to take advantage of their strength, ductility, and toughness properties. In addition, their machinability and weldability performance make alloy steels suitable for a range of manufacturing operations. The advent of additive manufacturing technologies, such as wire and arc additive manufacturing (WAAM), has enabled welding of alloy steels into complex and customized near net-shape products. However, the functional reliability of as-built WAAM products is often uncertain due to a lack of understanding of the effects of process parameters on the material microstructure and mechanical properties that develop during welding, primarily driven by thermal phenomena. This study investigated the influence of thermal phenomena in WAAM on the microstructure and mechanical properties of two alloy steels (G4Si1, a mild steel, and AM70, a high-strength, low-alloy steel). The interrelationships between process parameters, heating and cooling cycles of the welded part, and the resultant microstructure and mechanical properties were characterized. The welded part experienced multiple reheating cycles, a consequence of the layer-by-layer manufacturing approach. Thus, high temperature gradients at the start of the weld formed fine grain structure, while coarser grains were formed as the height of the part increases and the temperature gradient decreased. Microstructural analysis identified the presence of acicular ferrite and equiaxed ferrite structures in G4Si1 welds, as well as a small volume fraction of pearlite along the ferrite grain boundaries. Analysis of AM70 welds found acicular ferrite, martensite, and bainite structures. Mechanical testing for both materials found that the hardness of the material decreased with the increase in the height of the welded part as a result of the decrease in the temperature gradient and cooling rate. In addition, higher hardness and yield strength, and lower elongation at failure was observed for parts printed using process parameters with lower energy input. The findings from this work can support automated process parameter tuning to control thermal phenomena during welding and, in turn, control the microstructure and mechanical properties of printed parts.

1. Introduction

Directed energy deposition (DED) is a class of additive manufacturing technologies that fuse together powder or wire/filament material layer by layer as it is deposited using a heat source such as a laser, electron beam, or electric/plasma arc [1]. In particular, wire and arc additive manufacturing using cold metal transfer (WAAM-CMT) process, with its flexible material deposition rates (1–5 kg/h) and its ability to accommodate metallic materials with poor weldability, has enabled the timely and cost-effective production of large-scale metal products without the need for costly manufacturing setups [2,3]. WAAM is an emerging DED process technology used to manufacture large metal components [3]. Specifically, welding of alloy steels has become more widespread with the use of WAAM [4]. With the increased development of functional steel components using additive manufacturing, it is important to understand the influence of process parameters on the evolution of microstructure and the resulting mechanical properties [5]. Broad research around WAAM is focused on qualification efforts for dimensional quality, mechanical strength, and welding path planning for different metal wire feedstocks, as summarized by Rodrigues et al.

* Corresponding author.
E-mail address: suraj.panicker@tuni.fi (S. Panicker).

https://doi.org/10.1016/j.msea.2022.143690
Received 22 March 2022; Received in revised form 14 July 2022; Accepted 23 July 2022
Available online 9 August 2022

[6] in their state-of-the-art review. They discussed the different types of welding technologies used in WAAM, common defects in WAAM printed parts, and stress relief strategies to improve mechanical strength. They found that residual stress buildup due to inhomogeneous heat distribution was a common occurrence in WAAM. Employing stress relief strategies such as cold interlayer rolling, machine hammer peening, or laser peening was found to help achieve grain growth refinement, providing better control of mechanical properties, path width, and surface finish.

In addition, Rodrigues and co-workers [6] found that interlayer temperature, or interpass temperature, had a high influence on final printed part quality and microstructure. A higher interpass temperature generally provides finer grain structure and improved toughness for high-strength steel. However, this characteristic reverses as interpass temperature exceeds 260 °C; increasing the interpass temperature beyond this limit causes the weld pool to puddle and collapse, affecting the quality of the part [7]. The wait time for cooling to the required interpass temperature is influenced by the cooling rate of the layer, which varies as a function of energy density and product height. Increasing part height influences conduction, convection, and radiation and, in turn, causes a reduction in the cooling rate of subsequent weld layers. Thus, controlling the thermal cycles during the process to maintain stable interpass temperatures is essential for achieving high quality welds (and parts). While their in-depth review provides an overview of WAAM part quality, Rodrigues and co-workers in Ref. [6] did not provide information on the microstructure and mechanical properties of alloys used in WAAM. Thus, several studies are detailed below that are relevant to the experimental work presented in this manuscript. These studies examine the microstructure and mechanical properties of similar steel alloys printed using a range of WAAM technologies.

Sun et al. [8] investigated the microstructure and mechanical properties of low-carbon, high-strength steel fabricated using WAAM. A 907-steel alloy plate substrate and an A-Fe-W-86 welding alloy wire feedstock were used. They found the microhardness values varied from 290 HV to 260 HV along the build direction of the welded part. In addition, the average UTS of longitudinal specimens (976.53 MPa) was significantly lower than transverse specimens (1017.8 MPa), confirming anisotropic behavior. The inclusion of more interlayer zones in the microstructure resulted in higher stress concentrations in the longitudinal specimens. Electron back-scatter diffraction (EBSD) revealed a higher Taylor factor (0.907) for interlayer zones compared to the deposited weld (0.865), which indicates the presence of non-uniform deformation and local stress concentrations in the interlayer zones. Phase transformation analysis revealed that the bottom zone of the printed part was comprised of tempered bainite and sorbite, while the middle zone was comprised of tempered bainite and the top zone was comprised of tempered bainite, tempered sorbite, and ferrite. The order of occurrence of the phases also corresponded with the microhardness results, where hardness decreased along the build direction. Additionally, two crucial control parameters were found to influence the microstructure formation: temperature gradient (G) and solidification velocity (SV). Based on solidification theory, the G/SV ratio determines the microstructure formation. When G/SV is extremely high (approaching infinity), planar grains form, when G/SV is relatively high, columnar grains form, and when G/SV is small, equiaxed grains form.

Lu et al. [9] investigated the microstructure and mechanical properties of copper-coated mild steel welding wire (0.8 mm diameter) deposited on an ASTM 1045 steel substrate using an open-source GMAW-AM process. In their study, forced cooling of the weld zone facilitated a successful deposition of a thin-walled structure with 150 layers. The YS and UTS values of horizontal specimens (519.5 ± 8.3 MPa and 693.5 ± 8.5 MPa) were higher than for specimens from the vertical build direction (461.5 ± 6.3 MPa and 618.5 ± 10.8 MPa). Elongation along the horizontal and vertical directions were found to be 36.8 ± 0.2% and 28.2 ± 0.5%, respectively. The microstructural evolution shows the presence of primary austenite dendrites along the building direction. In addition, acicular ferrite and reticular ferrite intergranular structures were observed in the bottom zone, due to continued air cooling and conduction.

While the prior study focused on mild steel, Rodrigues et al. [10] investigated the thermal influence of WAAM on microstructure and mechanical properties of high-strength, low-alloy steel using a commercial-grade wire electrode (AWS A5.28 ER110S-G) deposited onto a mild steel substrate. Two samples were printed at two levels of heat input (P1 at 511 J/mm and P2 at 221 J/mm). The voltage (21 V), current (95 A), and wire feed rate (3 m/min) were maintained constant for both samples, while travel speed and shielding gas flowrate was maintained at two different levels for the experiments. Sample P1 used a travel speed of 3.9 mm/s and a shielding gas flowrate of 8 L/min, while sample P2 used 9 mm/s and 16 L/min, respectively.

The microstructural analysis in the above study found that ferrite, bainite, martensite, and retained austenite were present for both levels of heat input. Further, it was reported that heat input directly affected the cooling rates, interlayer temperatures, and residence times in the 800 °C–500 °C cooling interval. These findings align with well-established knowledge that cooling rate has a significant impact on the microstructure obtained for steels [11]. Two primary cooling intervals (1300 °C–800 °C and 800 °C–500 °C) are known to promote phase transformations and grain growth development. Austenite grain growth occurs in the 1300 °C–800 °C range, while in the 800 °C–500 °C range, a phase transformation from austenite to distinct ferrite morphologies and bainite can be observed. Oxide inclusions, weld metal hardenability, and cooling conditions are known to be associated with acicular ferrite formation. Also, cooldown to room temperature can cause full or partial transformation of the remaining austenite to martensite, depending on the carbon content of the weld.

In the experiments reported by Rodrigues et al. [10], martensite-austenite (MA) microstructures were observed for cooling rates in the range of 10–40 °C/s. Bainite formed under intermediate cooling rates (between martensite and pearlite phases), and its presence increased the UTS of the printed parts. The presence of bainite has been reported to play a critical role in crack initiation and propagation [12]. Rodrigues and co-workers found that the welds deposited with the higher heat input had a smoother, less bumpy top surface, which was credited to improving the weldability of subsequent layers. For both heat input levels, it was observed that overall part temperature increased with part height, while cooling rates and temperature gradients decreased through the weld. For the higher heat input level, higher residence times were observed in the 800 °C–500 °C temperature range at higher layer numbers (as part height increases). Despite using different heat inputs for the two samples, no significant difference was observed in the microstructure of the parts. Both samples had the same phase constituents (i.e., ferrite, bainite, and MA). Uniaxial tensile tests and Charpy impact tests found the mechanical properties in the build and travel directions to be similar, exhibiting isotropic behavior. Sample P1 (higher heat input) was found to have slightly higher UTS (by ~50 MPa) than sample P2 (lower heat input). Consequently, for sample P2, lower and more uniform microhardness values were measured along the part height compared to sample P1.

The above studies have characterized the microstructure and mechanical properties of metal alloys printed using WAAM and found that the thermal cycles of the layer-by-layer fabrication process influence the microstructural evolution of the part material. Specifically, controlling the cooling rates and maintaining stable interpass temperatures in the build can aid in controlling microstructure phase evolution, hence improving the mechanical properties of the final part. Process parameters directly influence welding energy density and part temperature gradients, which in turn affect cooling rates of printed parts. Thus, characterizing the influence of WAAM process parameters on part microstructures and mechanical properties can support qualification efforts for different metal alloys, and enable product quality improvement

and repeatability in production. Towards that goal, this research investigates the influence of two sets of process parameters on thermal cycles during WAAM as well as the resultant microstructures and mechanical properties for two alloy steels: G4Si1, a mild steel, and AM 70, a high-strength, low-alloy steel. This research adds to the state of the art by qualifying the WAAM-CMT process for two alloy steel wires and enables the development of material models for simulation and optimization purposes. The remainder of the manuscript is organized as follows: Section 2 describes the experimental study undertaken, and Section 3 presents the experimental study results characterizing the interconnections of WAAM process parameters and thermal and mechanical properties. Section 4 provides a discussion on the mechanisms influencing the microstructure of WAAM printed components, and Section 5 discusses the findings and opportunities for future work.

2. Materials and methods

2.1. Materials and equipment

For the WAAM-CMT experimental work, G4Si1 and AM70 alloy steel wire feedstock (1.2 mm diameter) is used; their chemical compositions are presented in Table 1. An S355 mild steel plate (300 × 200 × 20 mm) was used as a substrate for the fabrication of a thin wall. The WAAM-CMT setup (Fig. 1) consists of a welding unit (Fronius CMT Advanced 4000), a 6-axis industrial robot with a 3-axis worktable (ABB 4600 40/2.55), a wire feeder, and an inert gas supply. The welding torch is mounted on the industrial robot arm such that the travel direction is in the X axis, build direction is in the Z axis, and traverse direction is in the Y axis.

The robot path program was generated using Robot Studio 6. An infrared pyrometer (Micro Epsilon w/max temperature 1000 °C) in tandem with temperature measurement software (Compact Connect v1.9) was used to measure and record the temperature of the weld during fabrication. In addition, a contact-type digital thermal probe (Center 314 humidity temperature meter with a K-Type thermocouple) was used to monitor the interpass temperature between consecutive weld passes.

Welding was performed with CMT technology, which alters arc length and thermal input during welding by controlling material transfer (droplet removal) to the melt pool through a short-circuiting phase [15]. During this phase, the wire feeder dips the molten droplet into the weld pool and retracts the wire at a specific frequency (50–120 Hz) to detach the droplet through surface tension. The controlled wire oscillating motion in the nozzle is carried out at zero current, lowering heat input to the weld. The fast-retracting motion results in near spatter-free droplet transfer. Further, the lowering of heat input enables the fabrication of thin-walled structures (a few millimeters in thickness).

2.2. Product and process parameters

A schematic of the thin wall structure built using WAAM-CMT is shown in Fig. 2. The steel baseplate was sandblasted and cleaned with ethanol before the first print and cleaned using a wire brush for each subsequent wall to remove residual spatter from the print area. Wire feed rate (WFR) and interpass temperature (T_0) parameters were chosen for Material 1 (G4Si1) and Material 2 (AM70) to achieve low-heat input and high-heat input levels, resulting in four printed wall structures. The travel speed and shielding gas flow rate were kept constant at 10 mm/s and 15 L/min, respectively, for all experiments. The process parameters chosen for the experiments are shown in Table 2. A WFR of 6 m/min was used in printing the first layer to avoid incomplete deposition of subsequent layers.

This higher WFR provides a thicker base layer and preheats the baseplate, resulting in better bonding between subsequent layers. A two-directional travel strategy was implemented for the weld nozzle during deposition to aid in maintaining a constant printed wall height along its length. Samples were taken from the deposited walls to investigate the microstructure evolution (optical microscopy specimens) and mechanical properties (tensile and microhardness specimens) under the different weld conditions explored, as shown in the figure.

Table 1
Wire feedstock chemical composition [13,14].

Elements	G4Si1 (wt. %)	AM70 (wt. %)
C	0.090%	0.08%
Mn	1.670%	1.700%
Si	0.87%	0.60%
S	0.006–0.010%	0.000%
P	0.004–0.010%	0.000%
Cr	0.000%	0.200%
Mo	0.000%	0.500%
Ni	0.000%	1.500%
Fe	98.133–98.143%	95.42%

2.3. Thermal profile during welding

As discussed in Section 1, the thermal profile during welding influences solid state transformations and grain formation during cooling, which affect the microstructure and mechanical properties of the welded part. The ratio of wire feed rate to travel speed influences the amount of heat input to the weld, with higher wire feed rates increasing heat input for a fixed travel speed. Thus, WFR was varied for the different wall specimens to investigate the effect of heat input on the weld microstructure.

A wait time was introduced before depositing each layer to allow the previously deposited layer to cool to the desired interpass temperature (150 °C or 250 °C). The interpass temperature was measured at the middle of each layer before depositing the next layer, as shown in Fig. 2 using the contact-type digital thermal probe. From literature [16], it is seen that the thermal profile of a layer changes as new material is deposited, impacting microstructure evolution. Initially, the heat input to the weld is dissipated by conduction to the baseplate, forced convection through the shielding gas, and radiation to the surroundings. The increase in the number of layers affects the heat accumulation in the part, resulting in varying thermal cycles in the deposited layers. Thus, the pyrometer was used to measure the thermal profile of every 10^{th} layer of material deposited. This data is used to characterize the effect of successive heating and cooling of one weld layer on associated microstructure evolution and mechanical properties.

2.4. Mechanical characterization

A total of four walls were printed for the different process parameter settings. The walls printed using the higher energy input setting (M1E2 and M2E2) resulted in thicker walls (~1–2 mm thicker) than their lower energy counterparts. Thus, post-process machining (face milling) was performed to ensure uniform thickness (~2.5 mm) for all walls. Following the initial machining, hardness test specimens were cut along the build direction from the bottom, middle, and top of each wall using a CNC mill (Fig. 2). For the tensile tests, specimens were cut along the build direction (wall height) and along the travel direction (wall length). Microhardness tests were performed in accordance with ASTM test standard E92-17 using a Vickers microhardness tester (Matsuzawa MMT-X7) with a test load of 9.8 N and dwell time of 10 s. Tensile properties (i.e., YS, UTS, and percent elongation) were investigated according to EN ISO 6892-1:2019 (Annex B) with tests conducted using an Instron 8800. A crosshead speed of 0.01 mm/s and an initial strain rate of 0.00025/s were set, based on the test standard.

2.5. Microstructure characterization

Five samples for optical measurement (metallographic analysis)

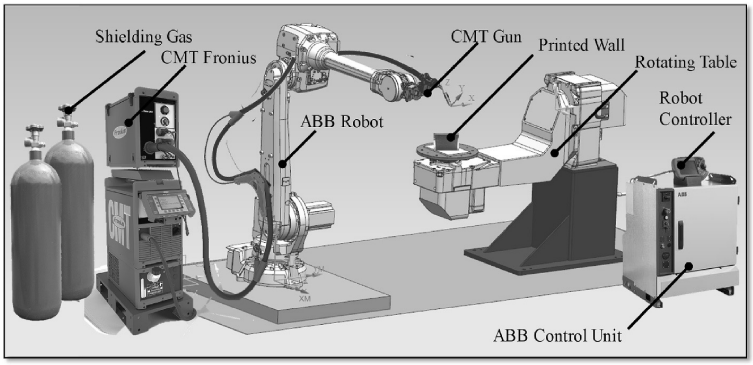

Fig. 1. WAAM equipment setup.

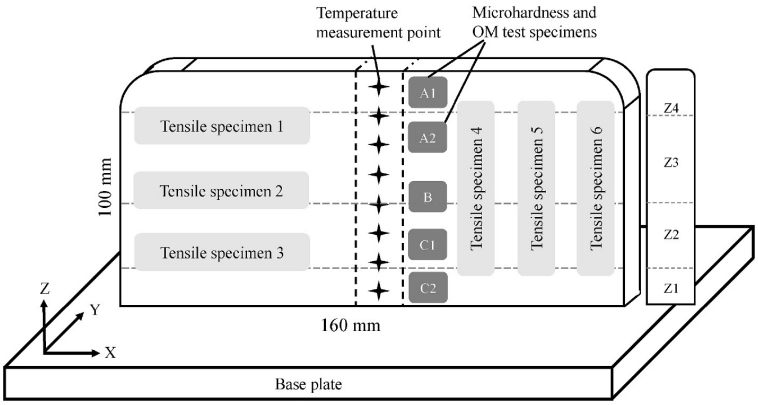

Fig. 2. Schematic of the deposited wall with locations of temperature measurement and mechanical samples marked along build direction.

Table 2
Description of experimental setup and process parameters.

Study Material and Equipment	Material 1	Material 2
Base Plate Size (Material)	300*200*20 mm (S355 steel)	
Wire Material (Diameter)	G4Si1 (1.2 mm)	AM70 (1.2 mm)
Wall Length	160 mm	
Wall Height	100 mm	
Robot	ABB 4600 40/2.55	
Shielding Gas Type (Composition)	Mison 8 (Ar + 8% CO_2 + 0.03% NO)	
Study Parameter		
F - Ignition Time	0.2 s	
F - Ignition Current	80%	
Wire Feed Rate (Level)	2 m/min (M1E1), 4 m/min (M1E2)	3 m/min (M2E1), 6 m/min (M2E2)
Interpass Temperature (Level)	150 °C (M1E1), 250 °C (M1E2)	150 °C (M2E1), 250 °C (M2E2)
Step Height	1.2 mm (M1E1), 1.5 mm (M1E2)	1.5 mm (M2E1 and M2E2)
F - Travel Speed	10 mm/s	
F - Shielding Gas Flow Rate	15 L/min	
F - Arc Ending Time	0.2 s	
F - Arc Ending Current	80%	
F - Wire Stick Out	15 mm	

Note: **F**- Fixed Parameter.

were selected at different heights along the build direction of each wall with a sample cross section length of 15 mm. These specimens were mechanically polished and etched using 4% Nital solution. The microstructures of the prepared specimens were observed and recorded using a Leica DMi8 optical microscope. The microstructural images obtained for G4Si1 were used to estimate grain size in Leica Application Suite X (LAS X version 5) software following the ASTM E112 standard using the Jeffries planimetric method [17]. Image analysis for grain size estimation was not conducted using LAS X for AM70 due to lack of equiaxed grains in the specimen. Instead, grain size estimation for AM70 was performed manually following the Jeffries planimetric method.

Electron back-scatter diffraction (EBSD) was used to analyze the prior austenite grain structure of the evaluated metallographic specimens for AM70. EBSD was not conducted for G4Si1 due to the lack of prior austenite grains in the microstructure. Following OM, the metallographic samples were polished further using a 0.02 μm colloidal silica suspension to enable EBSD analysis. Data acquisition for EBSD was done using a Zeiss Ultra Plus field emission scanning electron microscope (FESEM) equipped with a Symmetry® EBSD detector (Oxford Instruments). Data was acquired with a step size of 0.7 μm over a 300 μm × 1500 μm area using an acceleration voltage of 20 kV. The collected data was analyzed using Channel 5 EBSD software. The grain boundaries were categorized based on a minimum cut-off misorientation angle of 15°, and only the grains above 10 pixels (at 2048 × 1536 resolution) were considered for noise reduction.

3. Results and analysis

The wall temperature data, hardness and tensile strength properties, and microstructure images were used to characterize the effect of different process parameters (i.e., filler wire material, WFR, TS, and T_0) on the weld properties.

3.1. Thermal analysis

Using the collected temperature data, four zones of interest from the bottom to the top of the wall, labeled Z1, Z2, Z3, and Z4 in Fig. 2 were identified. The cooling rate of the weld tends to decrease moving from zone Z1 to Z4. This trend has the effect of increasing the wait time to reach the specified interpass temperature between successive depositions. It was observed that the cooling rate reaches a steady state value as the height of the part and number of layers deposited increases; this value appears to be dependent on the material type and energy input. This phenomenon was not examined further in this study.

At the bottom of the wall (Z1), for one to ten layers (up to ~10–15 mm wall height), the weld experiences the fastest cooling rate, with wait times between subsequent weld passes of 10–15 s. In the lower middle section of the wall (Z2), for ten to thirty layers (~15–45 mm wall height), the weld experiences a much slower cooling rate, with wait times of 20–48s per layer, increasing with layer number. At the start of the upper middle section of the wall (Z3, >45 mm), the cooling rate sees a slight decrease from zone Z2. However, the rate of decrease of cooling rate is comparatively slower for zone Z3 than Z2. For example, in the wall printed using parameter set M1E1, the average interpass wait time at layer 10 (~12 mm) was found to be 12s, while at layers 20 (~ 24 mm) and 30 (~ 36 mm) the wait time increased to 26s and 48s between deposition, respectively. We can see that the cooling rate reduces ~50% between layers 10–20, and ~75% between layers 10–30. However, in zone Z3 of this wall (M1E1), the average wait time at layers 40, 50, and 60 were found to be 58s, 62s, and 64s, respectively.

From this data, it is evident that the rate of decrease in the cooling rate is not uniform as the height of the part increases. The decrease in cooling rate appears to reach a steady state in zone Z3, which was also observed for other prints in this study and is maintained through printing of zone Z4. A key difference in thermal phenomena between zones Z3-Z4 is a decrease in the number of heating and cooling cycles that each subsequent layer undergoes in this metal additive process.

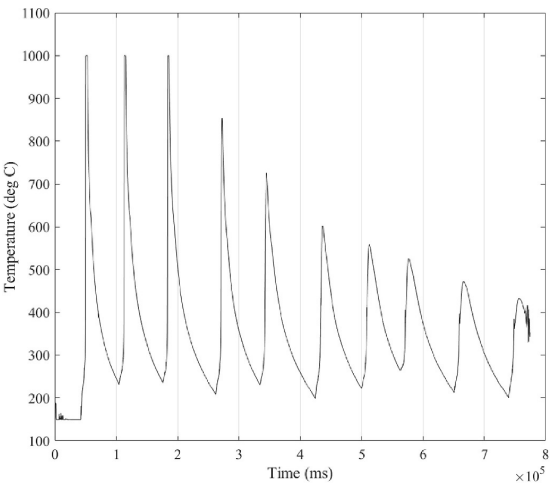

Fig. 3. Temperature profile of layer 40 (M1E1) extracted from infrared pyrometer showing reheating and cooling cycles.

Fig. 3 presents the temperature profile for the 40th layer (M1E1) to show the reheating and cooling cycles undergone by a single layer. In WAAM, arc energy is used to melt the filler material and substrate to temperatures above 1000 °C. Thus, as a new layer is deposited, a number of previously deposited layers undergo conductive heating to temperatures above 1000 °C. This successive heating and cooling of the part highly influences the resultant material microstructure (e.g., grain sizes and shape, and microstructural phase constituents) and its mechanical properties.

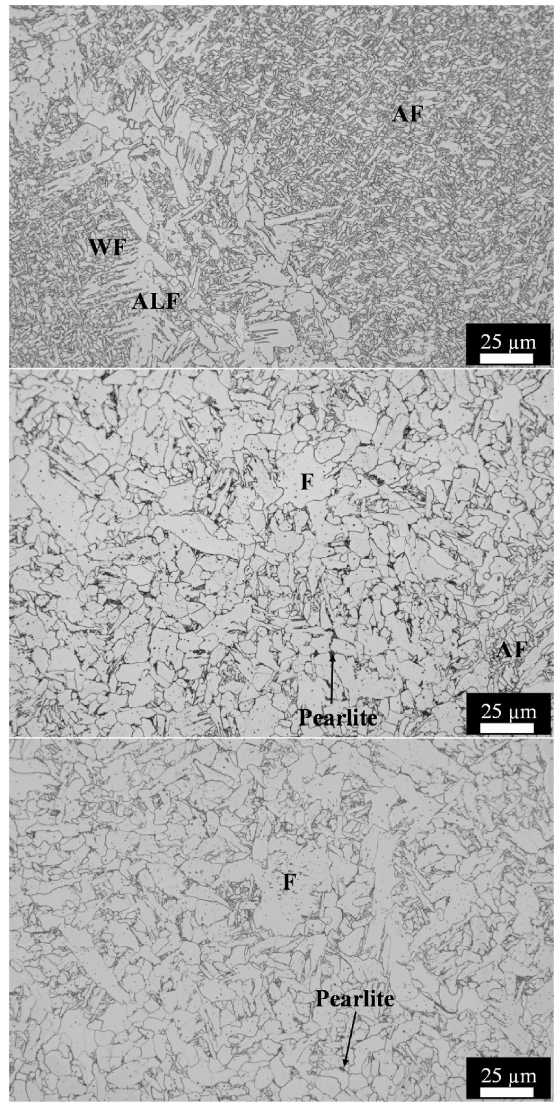

Fig. 4a. Optical micrographs (25 µm scale) of WAAM built parts using G4Si1 welding wire for M1E1. Micrographs reported along wall height from top to bottom (sample A1, A2, and B). Phases identified: AF – Acicular ferrite, ALF – Allotriomorphic ferrite, WF – Widmanstätten ferrite, and F – Equiaxed ferrite.

3.2. Microstructure and mechanical properties

Image analysis was used to identify the material grain sizes and microstructure phase constituents of the printed specimens. Fig. 4a–d shows the microstructural variation along the height of the WAAM-built walls for the two parameter sets (M1E1 and M1E2) using G4Si1. As shown in Fig. 2, sample A1 was taken from zone Z4 and sample A2 from zone Z3, sample B overlaps zones Z2 and Z3, sample C1 was taken from zone Z2, and sample C2 was taken from zone Z1 adjacent to the base plate. For the G4Si1 alloy, both welded walls exhibit distinctive microstructural (grain size) variations resulting from layer-by-layer deposition. For M1E1, sample C2 (Fig. 4b) experiences the highest cooling rate due to the large temperature difference between the new weld layers and the non-preheated baseplate, resulting in faster heat dissipation from the weld. In addition, a higher WFR for the first layer results in a higher heat input and contributes to the temperature difference between the base plate and the weld. This thermal phenomenon results in small grain sizes (2.46 ± 1.95 μm) in zone Z1 with the microstructure largely composed of bainite and acicular ferrite with traces of Widmanstätten and allotriomorphic ferrite. The hardness at the bottom of the wall was measured to be 248.25 ± 28.27 HV1. The large variability in the hardness at this location is due to the rapidly changing cooling rate at the bottom of the wall. As the height of the wall increases to the lower middle zone Z2, the cooling rate decreases to less than half of the cooling rate at the bottom of the wall. The microstructure of sample C1 (Fig. 4b) consists of equiaxed ferrite, allotriomorphic ferrite, and with small regions exhibiting bainite, pearlite islands, and remnant acicular ferrite with average grain size of 2.96 ± 3.15 μm and hardness of 173.55 ± 4.10 HV1. Sample B (Fig. 4a) is largely comprised of equiaxed ferritic grains with trace amounts of pearlite at the grain boundaries. The average grain size and hardness at this location were found to be 4.03 ± 4.30 μm and 168.60 ± 4.85 HV1, respectively. Sample A2 (Fig. 4a) was similar in microstructure to sample B, with remnant acicular ferrite grains also observed, indicating a lack of transformation time during welding.

The average grain size and hardness at this location were found to be 5.39 ± 4.21 μm and 168.65 ± 5.39 HV1, respectively. Sample A1 (Fig. 4a), taken from zone Z4 of the weld, was largely comprised of acicular ferrite with allotriomorphic ferrite found along the prior austenitic grain boundaries.

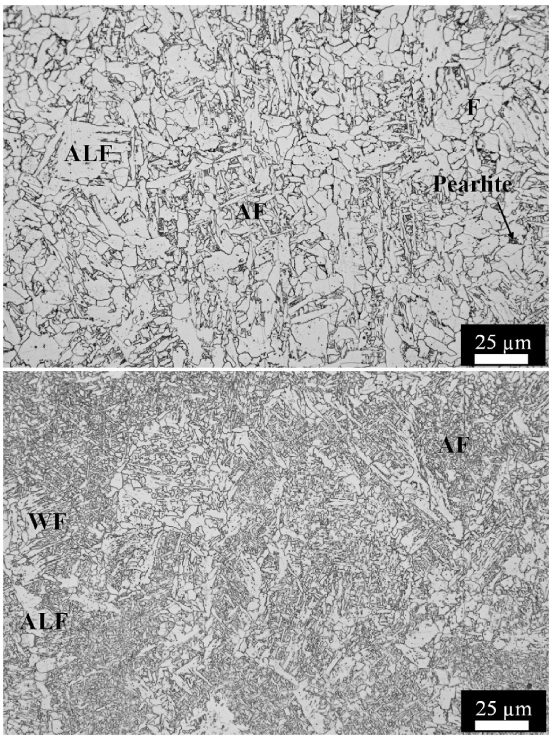

Fig. 4b. Optical micrographs (25 μm scale) of WAAM built parts using G4Si1 welding wire for M1E1. Micrographs reported along wall height from top to bottom (sample C1 and C2). Phases identified: AF – Acicular ferrite, ALF – Allotriomorphic ferrite, WF – Widmanstätten ferrite, and F – Equiaxed ferrite.

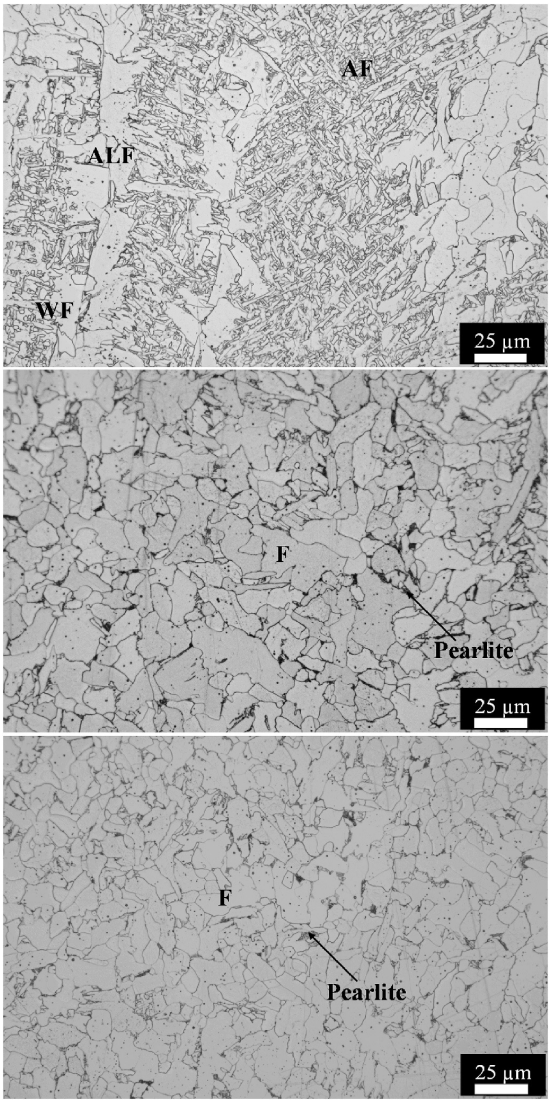

Fig. 4c. Optical micrographs (25 μm scale) of WAAM built parts using G4Si1 welding wire for M1E2. Micrographs reported along wall height from top to bottom (samples A1, A2, and B). Phases identified: AF – Acicular ferrite, ALF – Allotriomorphic ferrite, WF – Widmanstätten ferrite, and F – Equiaxed ferrite.

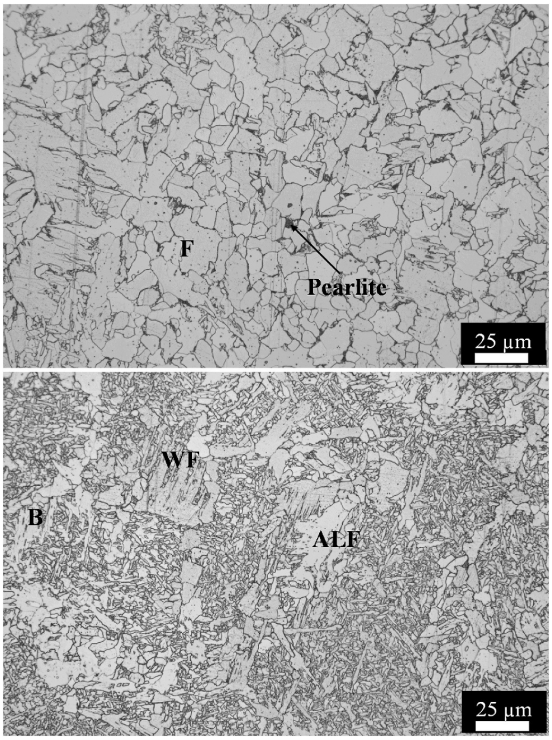

Fig. 4d. Optical micrographs (25 µm scale) of WAAM built parts using G4Si1 welding wire for M1E2. Micrographs reported along wall height from top to bottom (sample C1 and C2). Phases identified: AF – Acicular ferrite, ALF – Allotriomorphic ferrite, WF – Widmanstätten ferrite, and F – Equiaxed ferrite.

In addition, Widmanstätten ferritic grains were observed at the grain boundaries of allotriomorphic ferrite as shown in Fig. 4b. The grains in this region have an average hardness value of 191.90 ± 9.45 HV1 and average grain size of 3.21 ± 2.90 µm.

The hardness of the material increases (~20 HV1) as we move from zone Z3 to zone Z4. The increase in hardness at the top of the wall (sample A1) can be associated with the variation in constituent phases and smaller grain sizes compared to sample A2. In addition, the top of the wall experiences fewer reheating and cooling cycles, limiting recrystallization and the number of phase transformations in the region. From the microstructure and hardness characterization for experimental wall M1E1, it was seen that the material becomes softer as we move from zone Z1 to zone Z3, with an increase in average grain size. The microstructure phase analysis (Fig. 4c and d) for wall M1E2 showed a similar phase structure to that of M1E1, but with increased ferritic grain sizes. It was seen that the higher energy printing parameters (M1E2) resulted in a wall with lower hardness than M1E1. Though the trends for cooling rate, hardness, and grain size for M1E2 were similar to M1E1, microstructure analysis found a small fraction of bainitic structures in the C2 (Fig. 4d) sample close to the base plate. The resulting microstructure phases, grain sizes, and mechanical properties for the experiments are presented in Table 3.

Similar to G4Si1, the walls printed using AM70 steel alloy exhibit distinctive microstructural variations as a result of layer-by-layer deposition (Fig. 5a–d). The walls produced using AM70 (M2E1 and M2E2), resulted in a fine-grained steel consisting of ferrite, martensite, and bainite, along with trace amounts of oxide inclusions. The grain sizes of walls printed using AM70 were smaller than their G4Si1

Table 3
Microstructure and mechanical property results for G4Si1 and AM70 deposits.

Tested Sample	HV1	Grain Size (µm)	YS (MPa)	UTS (MPa)	% e	Phase
M1E1-A1	191.90 ± 9.45	3.21 ± 2.90	447.20 ± 0.78	628.35 ± 17.78	31%	Acicular ferrite with traces of Widmanstätten and allotriomorphic ferrite
M1E1-A2	168.65 ± 5.39	4.21 ± 3.92				Equiaxed ferrite, remanent acicular ferrite, traces of pearlite and bainite
M1E1-B	168.60 ± 4.85	4.03 ± 4.30				Equiaxed ferrite and traces of pearlite
M1E1-C1	173.55 ± 4.10	5.61 ± 3.15				Equiaxed ferrite and pearlite, allotriomorphic ferrite, remanent acicular ferrite, and traces of bainite
M1E1-C2	248.25 ± 28.27	2.46 ± 1.95				Acicular ferrite and traces of Widmanstätten, allotriomorphic ferrite and bainite
M1E2-A1	165.25 ± 11.92	4.55 ± 4.83	395.55 ± 1.62	605.00 ± 10.60	41%	Acicular ferrite with traces of Widmanstätten and allotriomorphic ferrite
M1E2-A2	155.10 ± 3.26	5.40 ± 4.78				Equiaxed ferrite, remanent acicular ferrite, traces of pearlite and bainite
M1E2-B	155.15 ± 2.16	5.38 ± 4.58				Equiaxed ferrite with trace amounts of pearlite
M1E2-C1	170.45 ± 6.00	3.92 ± 2.34				Equiaxed ferrite and pearlite, allotriomorphic ferrite, remanent acicular ferrite, and traces of bainite
M1E2-C2	190.5 ± 10.63	2.79 ± 2.07				Bainite, acicular ferrite and traces of Widmanstätten and allotriomorphic ferrite
M2E1-A1	311.00 ± 26.18	2[a]	771.82 ± 0.84	932.96 ± 28.67	25%	Acicular ferrite and bainite
M2E1-A2	271.55 ± 7.58					Bainite and acicular ferrite
M2E1-B	271.45 ± 9.56					Bainite, acicular ferrite, and martensite
M2E1-C1	286.90 ± 11.03					Bainite and acicular ferrite
M2E1-C2	339.17 ± 15.34					Bainite and martensite
M2E2-A1	305.30 ± 9.30	2-3[a]	707.58 ± 3.53	943.34 ± 9.98	28%	Acicular ferrite and bainite

(*continued on next page*)

Table 3 (*continued*)

Tested Sample	HV1	Grain Size (μm)	YS (MPa)	UTS (MPa)	% e	Phase
M2E2-A2	266.50 ± 10.62					Bainite and acicular ferrite
M2E2-B	244.95 ± 7.96					Bainite, acicular ferrite, and martensite
M2E2-C1	281.95 ± 12.45					Bainite and acicular ferrite
M2E2-C2	346.25 ± 24.07					Bainite and martensite

[a] Obtained using manual measurement following ASTM E112.

counterparts, averaging at 2–3 μm throughout the part.

AM70 material showed overall higher hardness and strength compared to G4Si1. For sample C2 (Fig. 5b) in M2E1, the microstructure was largely composed of bainite and martensite. The hardness at the bottom of the wall was measured to be 339.17 ± 15.34 HV1. The large variability in the hardness at this location is due to the rapidly changing cooling rate at the bottom of the wall.

As the height of the wall increases to zone Z2, the microstructure of sample C1 (Fig. 5b) is similar to that of C2, comprised of bainite and acicular ferrite in a weave basket pattern with average hardness of 286.90 ± 11.03 HV1. Sample B (Fig. 5a) taken at the intersection of zones Z2 and Z3 is largely comprised of lower bainite, upper bainite, acicular ferrite, and martensite with an average hardness of 271.45 ± 9.56 HV1. Sample A2 (Fig. 5a) was comprised of bainite and acicular ferrite, exhibiting an average hardness of 271.55 ± 7.58 HV1. Sample A1 (Fig. 5a) was found to be largely comprised of acicular ferrite and bainite. The hardness in this region was 311.00 ± 26.18 HV1. The increase in hardness at the top of the wall can be associated with fewer heating and cooling cycles resulting in more harder phases in the microstructure, as observed in the experiments using G4Si1 steel alloy.

The microstructure analysis for M2E2 (Fig. 5c and d) showed a similar phase structure to M2E1. It was seen that the higher energy printing parameters (M2E2) resulted in a wall with lower hardness than M2E1. The trends for cooling rate, hardness, and grain size were observed to be the same for M2E1 and M2E2. The only difference in microstructural phases was seen in prior austenite grains observed through EBSD analysis. It was observed that prior austenite grains were polygonal with parameter set M2E1, while prior austenite grains were columnar using parameter set M2E2, as shown in Fig. 6a and b, respectively.

The higher energy parameter set (M2E2) normalized the columnar grains and increased the sub-grain size. The variation of hardness along the build direction for both materials (all parameter combinations) is shown in Fig. 7. From the figure, it is seen that the hardness is uniform through the part, with a slight increase at the bottom and top of the printed walls.

Following the optical microscopy of the hardness samples, tensile specimens cut along the build direction (vertical) and nozzle travel direction (horizontal) were tested. For both materials, the strength did not vary with orientation of the tensile specimen (horizontal and vertical) implying that mechanical properties favor isotropy in WAAM-CMT. The wall with parameter combination M1E1 showed higher YS (447.20 MPa), UTS (628.35 MPa), and lower elongation at failure (31%) than the wall built using parameter set M1E2 (395.55 MPa, 605 MPa, and 41%, respectively). The samples from wall M1E2 experienced greater elongation (~5% higher strain) than M1E1. The M1E2 specimens experienced higher heat input per layer and a slower cooling rate than M1E1, resulting in specimens with lower hardness and higher ductility, but with slightly lower strength. The difference in average UTS between the

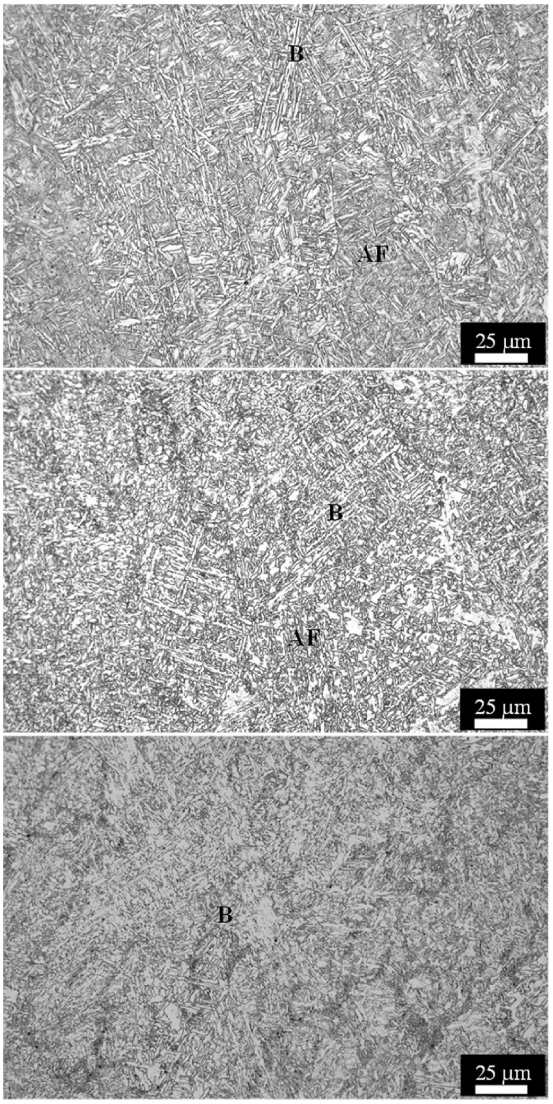

Fig. 5a. Optical micrographs (25 μm scale) of WAAM built parts using AM70 welding wire for M2E1. Micrographs reported along wall height from top to bottom (samples A1, A2, and B). Phases identified: AF – Acicular ferrite, and B – Bainite.

two parameter sets (M1E1 and M1E2) was found to be 15 MPa.

The measured YS, UTS, and % elongation values for parameter sets M1E1 and M1E2 are reported in Table 3, and the true stress strain curves for the two parameter sets tested for material G4Si1 in shown in Fig. 8. For the AM70 alloy, specimens from the lower weld energy parameter set M2E1 exhibited higher YS (771.82 MPa), lower UTS (932.96 MPa), and lower elongation (25%) than the wall using parameter set M2E2 (707.58 MPa, 943.34 MPa, and 28%, respectively).

The measured YS, UTS, and % elongation values for parameter sets M2E1 and M2E2 are shown in Table 3, and the true stress strain curves for the two parameter sets tested for material AM70 in shown in Fig. 8. The findings indicate that lower energy input results in higher YS and

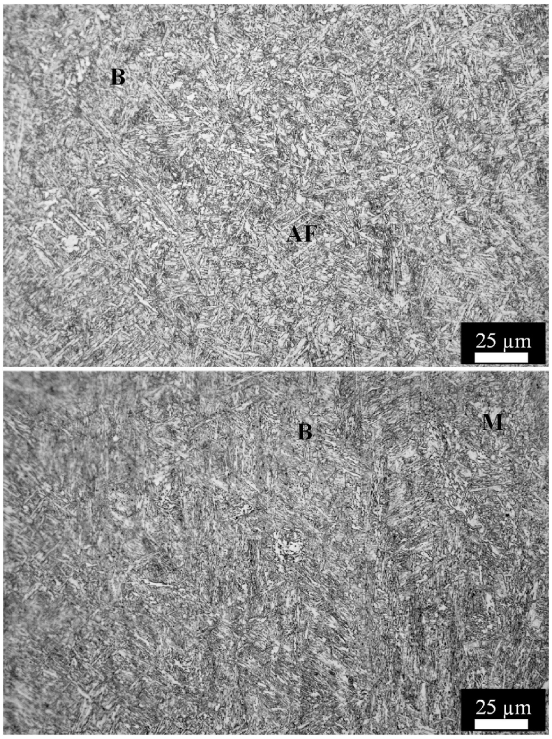

Fig. 5b. Optical micrographs (25 µm scale) of WAAM built parts using AM70 welding wire for M2E1. Micrographs reported along wall height from top to bottom (samples C1 and C2). Phases identified: AF – Acicular ferrite, B – Bainite, and M – Martensite.

UTS for both materials. However, the ductility of both materials increased when printing using the higher energy input parameters.

4. Discussion and validation

Microstructural characterization for the two steel alloys (G4Si1 and AM70) showed presence of acicular ferrite, bainite, equiaxed ferrite, Widmanstätten ferrite, allotriomorphic ferrite phases, and pearlite. In addition, martensite was also formed in the AM70 welds. The fraction of each of these microstructure phases identified influences the mechanical properties observed during testing of the welds. Acicular ferrite is a desired phase in inoculated steels due to its influence on the overall toughness of the material. Acicular ferrite grains are usually formed at intragranular nucleation sites formed at inclusions. Similar to bainite, which nucleates at austenite grain boundaries and grow inwards as sheaves or plates, transformation to acicular ferrite occurs below the bainite start temperature. The growth of acicular ferrite phase over bainite may be favored based on the prior austenite grain size and inclusion density in the alloy used for printing [18]. In addition, the presence of Widmanstätten ferrite and allotriomorphic ferrite along prior austenite grain boundaries have been seen to favor acicular ferrite growth over bainite. The increased amount of acicular ferrite grains may be favored in applications where higher ductility is warranted. Similar to acicular ferrite, the presence of bainite may also bring good strength to ductility performance but with higher hardness. Widmanstätten ferrite structures generally possess higher hardness due to a higher phase boundary area where dislocations at short distances may be hindered resulting in an increase in the hardness. In addition, microcracks

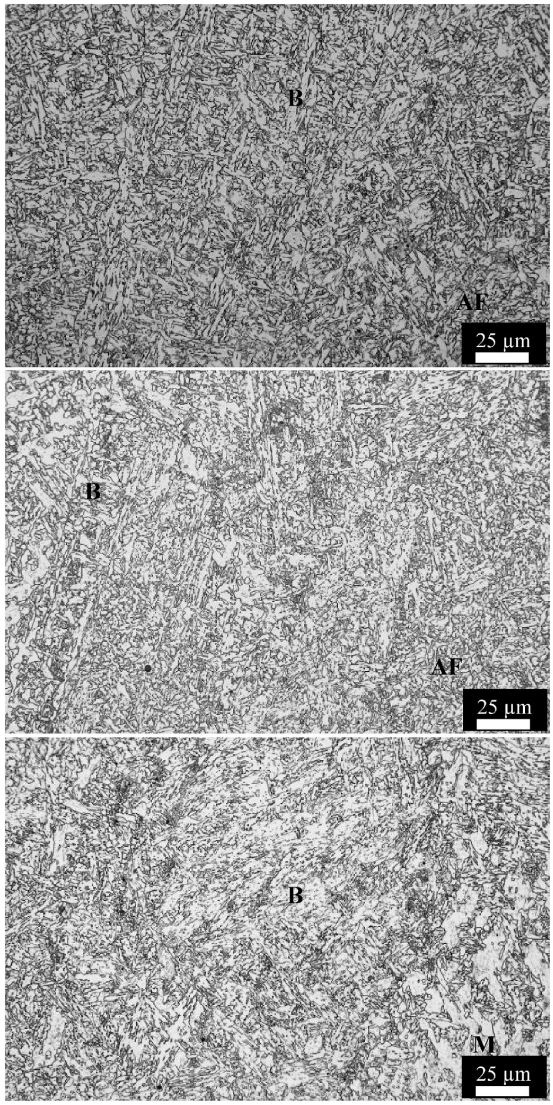

Fig. 5c. Optical micrographs (25 µm scale) of WAAM built parts using AM70 welding wire for M2E2. Micrographs reported along wall height from top to bottom (samples A1, A2, and B). Phases identified: AF – Acicular ferrite, B – Bainite, and M – Martensite.

are common in Widmanstätten ferrite which can limit the impact strength of the material and thus, only preferable in select applications. A high cooling rate can result in an increase in Widmanstätten ferrite since it provides less time for ferrite nucleation sites. Pearlite on the other hand forms when the material is slowly cooled from the austenitizing temperature for steels. Pearlites are generally lamellar with alternating layers of ferrite and cementite and are formed in steels with lower than eutectoid carbon content (~ 0.75–0.85 wt % of carbon). The presence of pearlite can increase hardness, strength, and ductility of steels, but can have a detrimental effect on the toughness properties of the material. Finally, martensite structures are generally the hardest and strongest phase in steel alloys but also constitute the most brittle

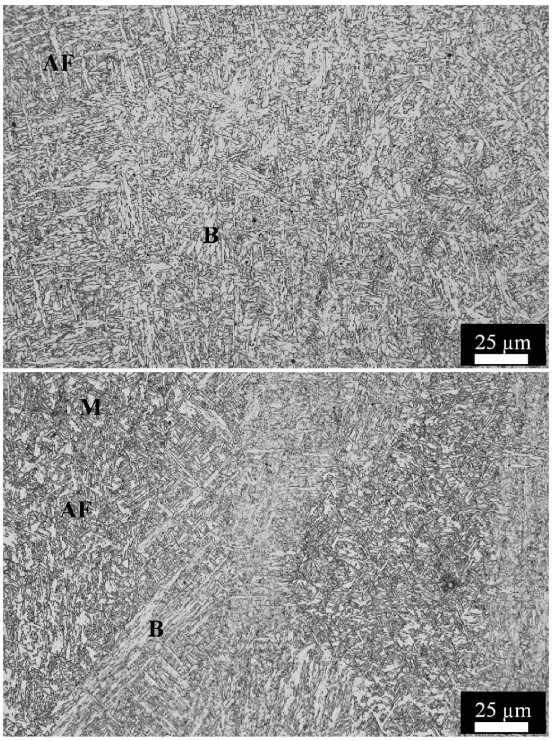

Fig. 5d. Optical micrographs (25 µm scale) of WAAM built parts using AM70 welding wire for M2E2. Micrographs reported along wall height from top to bottom (samples C1 and C2). Phases identified: AF – Acicular ferrite, B – Bainite, and M – Martensite.

structure [18].

The SEM micrographs for G4Si1 welds (both process parameter settings) indicated the presence of allotriomorphic ferrite and Widmanstätten ferrite phases along the prior austenite grain boundaries at the bottom (Zone Z4) and top (Zone Z1) zones of the part as shown in Fig. 9a. Thus, G4Si1 welds exhibited a higher percentage of acicular ferrite phase in their microstructure than bainite. Additionally, the higher energy input parameters (M1E2) resulted in an increase in the percentage of equiaxed ferrite, acicular ferrite, and pearlite phases and also increased the grain sizes in the microstructure (Fig. 9b). The combination of the phases as well as the larger grain sizes resulted in decreasing the hardness, while increasing the ductility of the high energy input G4Si1 welds without a considerable loss in strength (UTS for M1E2 was 23 MPa less than M1E1). On the other hand, AM70 is a bainitic steel with chromium, manganese, and molybdenum concentrations which may lower the formation of allotriomorphic ferrite in the final microstructure [18]. Hence, the resulting microstructure saw a decrease in the presence of acicular ferrite.

However, it is important to note that, the concentration of acicular ferrite in AM70 was significantly higher than the G4Si1 welds. All four temperature zones in AM70 samples exhibited largely bainitic grains (mean grain size of 2–3 µm) with smaller regions of acicular and martensitic phases.

Martensitic laths were identified in the microstructure of AM70 deposits at the top of the wall and near the base plate (A1 and C2 zones) as shown in Fig. 10. The formation of martensitic laths along the prior austenite grain boundaries can be attributed to the high cooling rates near the base plate and lack of remelting (due to addition of layers of top) at the top of the wall. Acicular ferrite phases can be linked to the

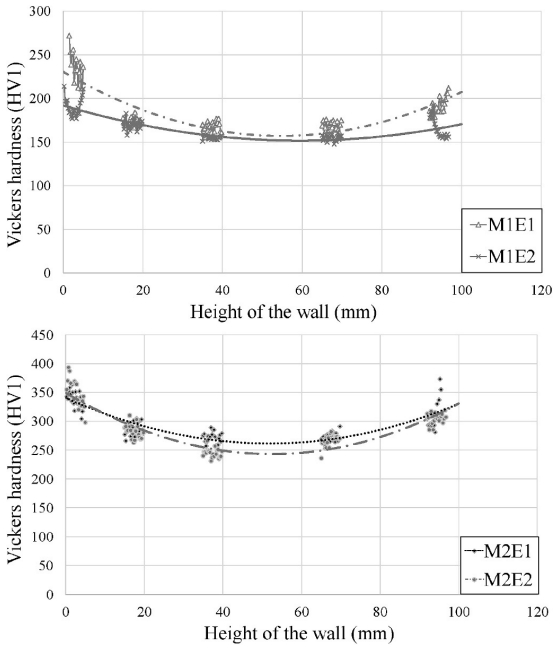

Fig. 7. Microhardness values for G4Si1 (top) and AM70 (bottom) deposits measured along build direction.

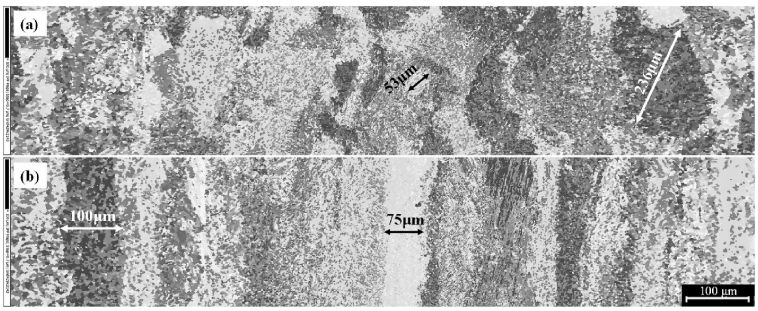

Fig. 6. EBSD scans of AM70 welds with parameter set a) M2E1 and b) M2E2.

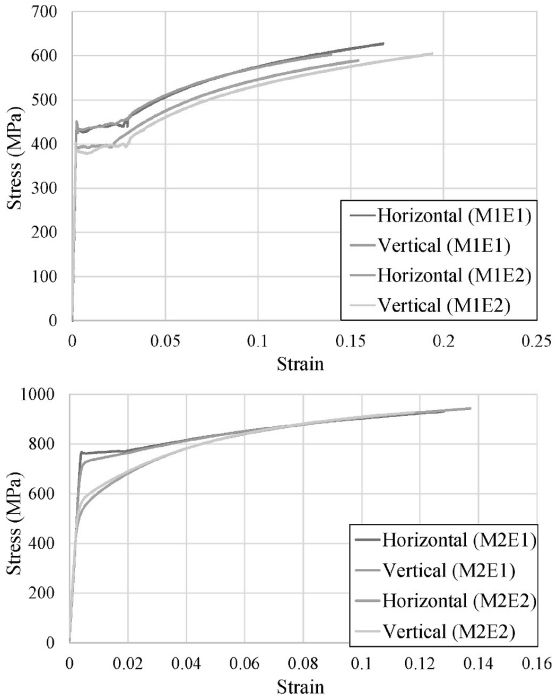

Fig. 8. Stress-strain curve for G4Si1 deposits (top) and AM70 deposits (bottom) characterized in the build (vertical) and travel (horizontal) direction.

presence of microscopic inclusions as seen in the micrographs of AM70 welds (Fig. 4). Similar to G4Si1, the AM70 micrographs show an increase in the fraction of acicular ferrite phase when using higher energy input parameters (M2E2) compared to M2E1, which slightly increased ductility and strength.

This performance improvement can be associated with the largely bainitic microstructure of AM70 welds. Specimens for both process parameter settings (M2E1 and M2E2) resulted in similar UTS (~930 MPa for M2E1 and ~940 MPa for M2E2). However, despite having similar UTS, the YS for M2E1 and M2E2 have a difference of 70 MPa (~10%), indicating that M2E1 is more brittle. The microstructural phases obtained for AM70 are in accordance with prior research investigating HSLA steels, where in the major constituents were ferrite and bainite phases [10,19]. Further, the small grain size and presence of bainite (Fig. 11) and acicular ferrite throughout the sample contributed to higher hardness, UTS, and YS, but lower ductility than G4Si1 samples. The relative lower ductility of AM70 may be associated with the large number of fine inclusions found throughout the welded microstructure which can aggravate microcracks and their propagation in the weld. The hardness and strength of fully bainitic microstructures decrease during tempering; this change is more evident in high strength steels. The repeated heating and cooling cycles in the WAAM process results in a non-uniform tempering of the printed part. Consequently, a clear variation in the microstructure and mechanical properties can be seen due to the layer-by-layer building approach. For printing WAAM parts with uniform microstructure, reducing or eliminating the need for stress relief heat treatment requires understanding the variation in microstructure caused by process-related thermal phenomena. Capturing data related to changes in cooling rates and wait times as a function of part height can help create computational models which can enable process tuning and optimization.

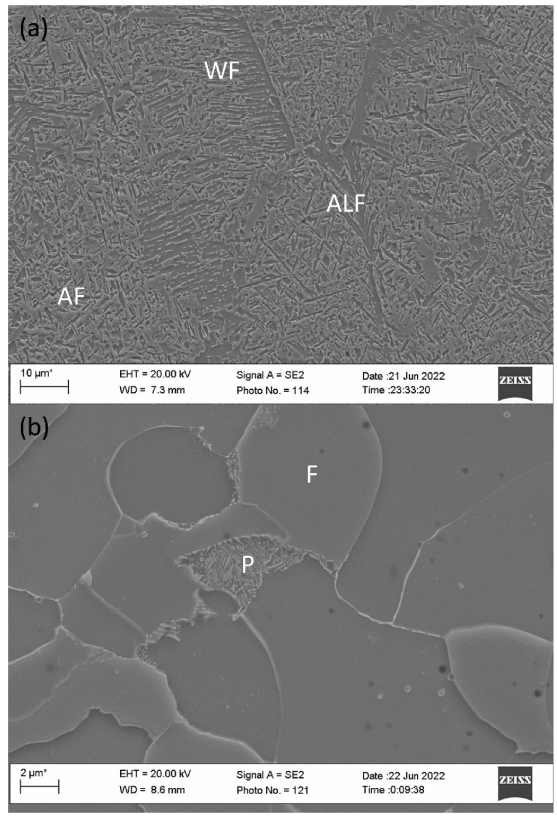

Fig. 9. SEM micrographs of G4Si1 deposits for M1E1 (top) and M1E2 (bottom); (a) AF- acicular ferrite, WF- Widmanstätten ferrite, and ALF- allotriomorphic ferrite, (b) P- pearlite and F- equiaxed ferrite.

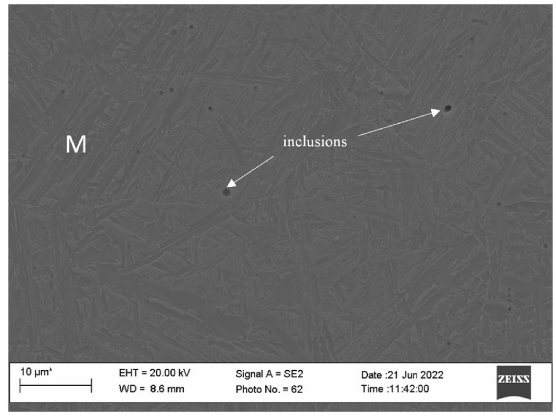

Fig. 10. SEM micrographs of AM70 deposits for M2E1 with martensite (M) laths.

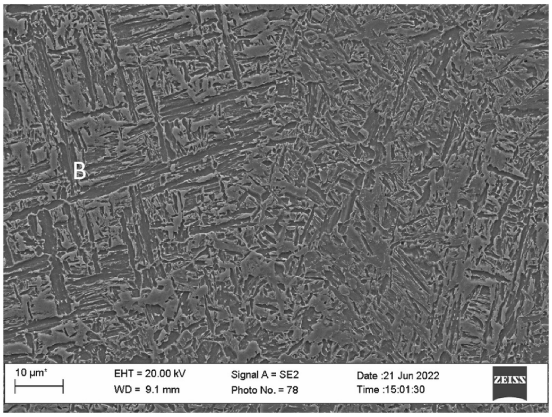

Fig. 11. SEM micrographs of AM70 deposits for M2E1 with bainite (B).

5. Conclusions and future work

Thin walls (160 × 100 × 5 mm) of mild steel (G4Si1) and high-strength, low-alloy steel (AM70) were fabricated using WAAM-CMT. A fixed travel speed and two different sets of wire feed rates and interpass temperatures were employed, resulting in four walls for subsequent microstructural analysis and mechanical testing. Microstructural evolution (using an optical microscope, SEM, and EBSD scans) and mechanical properties (i.e., YS, UTS, and %e) were investigated (in the horizontal and vertical directions of material deposition) to better understand the associated influence of thermal cycles of layer-by-layer deposition.

From these investigations, the following observations were made:

- Based on observed phenomena, four different temperature zones were identified, which are characterized by differences in cooling rate, wait time between layers, and number of reheating cycles.
- Cooling rate decreases as the height of the part increases until it reaches a steady state value. The decrease in cooling rate leads to an increase in wait time between layers as the height of the part increases.
- Lower heat input resulted in higher YS and UTS and lower uniform strain.
  - o YS and UTS increased by 13% and 3.8%, respectively, in G4Si1 steel deposits with the lower energy input parameters (M1E1) than with higher energy input parameters (M1E2).
  - o YS increased by 9% in AM70 steel deposits with the lower energy input parameters (M2E1) than with higher energy input parameters (M2E2). However, in case of UTS the lower energy input parameters (M2E1) saw a 1% decrease compared to high energy input parameter (M2E2).
  - o Percentage elongation at failure was 10% and 3% lower in G4Si1 and AM70 deposits respectively, for printing with lower energy input parameters (M1E1 and M2E1) than with higher energy input parameters (M1E2 and M2E2).
- Higher energy input parameters resulted in increased ductility and reduced hardness for both materials.
- Owing to a lack of significant anisotropy in G4Si1 deposits due to an equiaxed grain structure, the mechanical properties in the travel direction showed negligibly higher UTS (0.38%) than the samples taken in the build direction. A similar trend was observed for AM70 (increases of 2.7% and 0.24% in YS and UTS, respectively).
- Even though energy input varied for both materials for the different parameter sets, no significant microstructural changes were observed across the parameter sets for G4Si1, though energy input variation had a significant influence on the material microstructure for AM70. Prior austenite grains were equiaxed/polygonal for M2E1, while they were columnar for M2E2. Higher heat input settings normalized the columnar grains, increasing the sub-grain size. The observed microstructures for M2E1 and M2E2 were comprised of similar phases (i.e., ferrite + bainite + martensite + inclusions).
- Smaller grain sizes due to higher solidification rates and limited grain growth in lower energy input parameter sets (M1E1 and M2E1) resulted in higher YS and hardness in both alloys. Since grain boundaries play an essential role in resisting dislocation movement in polycrystalline materials, the observed mechanical property trends are attributed to the presence of more grain boundaries in samples printed using lower energy input parameters.

The work herein will support development of models capable of characterizing the process parameter-process physics-property relationships for a family of steels. Specifically, graph-based modeling and machine learning approaches are being investigated to combine knowledge from different domains into one integrated system model.

CRediT authorship contribution statement

Suraj Panicker: Conceptualization, Methodology, Software, Validation, Formal analysis, Investigation, Writing – original draft, Writing – review & editing. **Hari P.N. Nagarajan:** Methodology, Validation, Formal analysis, Investigation, Data curation, Writing – original draft, Writing – review & editing, Visualization. **Jari Tuominen:** Validation, Formal analysis, Investigation, Resources, Writing – review & editing. **Madan Patnamsetty:** Validation, Formal analysis, Investigation, Writing – review & editing. **Eric Coatanéa:** Writing – review & editing, Supervision, Project administration. **Karl R. Haapala:** Writing – review & editing, Visualization, Supervision.

Declaration of competing interest

The authors declare that they have no known competing financial interests or personal relationships that could have appeared to influence the work reported in this paper.

Data availability

Data will be made available on request.

Acknowledgements

The authors acknowledge the support from Jaakko Kotiranta and Merja Ritola from the Automation Technology and Mechanical Engineering Lab at Tampere University for their assistance in the machining and preparation of metallographic and mechanical specimens for material testing.

References

[1] F42 Committee, Standard Guide for Directed Energy Deposition of Metals, ASTM International, Sep. 2016, https://doi.org/10.1520/F3187-16.
[2] D. Ding, Z. Pan, D. Cuiuri, H. Li, Wire-feed additive manufacturing of metal components: technologies, developments and future interests, Int. J. Adv. Manuf. Technol. 81 (1–4) (Oct. 2015) 465–481, https://doi.org/10.1007/s00170-015-7077-3.
[3] B. Wu, et al., A review of the wire arc additive manufacturing of metals: properties, defects and quality improvement, J. Manuf. Process. 35 (Oct. 2018) 127–139, https://doi.org/10.1016/j.jmapro.2018.08.001.
[4] W. Jin, C. Zhang, S. Jin, Y. Tian, D. Wellmann, W. Liu, Wire arc additive manufacturing of stainless steels: a review, Appl. Sci. 10 (5) (Jan. 2020), https://doi.org/10.3390/app10051563. Art. no. 5.
[5] M.R. Jandaghi, A. Saboori, L. Iuliano, M. Pavese, On the effect of rapid annealing on the microstructure and mechanical behavior of additively manufactured stainless steel by Laser Powder Bed Fusion, Mater. Sci. Eng. A 828 (Nov. 2021) 142109, https://doi.org/10.1016/j.msea.2021.142109.

[6] T.A. Rodrigues, V. Duarte, R. Miranda, T.G. Santos, J. Oliveira, Current status and perspectives on wire and arc additive manufacturing (WAAM), Materials 12 (7) (2019) 1121.
[7] X.L. Wang, et al., Effect of interpass temperature on the microstructure and mechanical properties of multi-pass weld metal in a 550-MPa-grade offshore engineering steel, Weld. World 61 (6) (Nov. 2017) 1155–1168, https://doi.org/10.1007/s40194-017-0498-x.
[8] L. Sun, F. Jiang, R. Huang, D. Yuan, C. Guo, J. Wang, Microstructure and mechanical properties of low-carbon high-strength steel fabricated by wire and arc additive manufacturing, Metals 10 (2) (Feb. 2020), https://doi.org/10.3390/met10020216. Art. no. 2.
[9] X. Lu, Y.F. Zhou, X.L. Xing, L.Y. Shao, Q.X. Yang, S.Y. Gao, Open-source wire and arc additive manufacturing system: formability, microstructures, and mechanical properties, Int. J. Adv. Manuf. Technol. 93 (5) (Nov. 2017) 2145–2154, https://doi.org/10.1007/s00170-017-0636-z.
[10] T.A. Rodrigues, V. Duarte, J.A. Avila, T.G. Santos, R.M. Miranda, J.P. Oliveira, Wire and arc additive manufacturing of HSLA steel: effect of thermal cycles on microstructure and mechanical properties, Addit. Manuf. 27 (May 2019) 440–450, https://doi.org/10.1016/j.addma.2019.03.029.
[11] V.N. Lazić, et al., Theoretical-experimental determining of cooling time (t8/5) in hard facing of steels for forging dies, Therm. Sci. 14 (1) (2010) 235–246.
[12] A. Lambert-Perlade, T. Sturel, A.F. Gourgues, J. Besson, A. Pineau, Mechanisms and modeling of cleavage fracture in simulated heat-affected zone microstructures of a high-strength low alloy steel, Metall. Mater. Trans. A 35 (3) (Mar. 2004) 1039–1053, https://doi.org/10.1007/s11661-004-0030-y.
[13] Lincoln Electric, "G4Si1, Mild Steel, Material Safety Data Sheet." https://www.lincolnelectric.com/assets/global/Products/Consumable_MIGGMAWWires-SuperArc-SuperArcG4Si1/c41025.pdf.
[14] Böhler, "3D PrintAM70, low-alloyed, high strength steel, Material Safety Data Sheet." https://www.vabw-service.com/documents/boehler/datenblaetter/en/L1_34551_en_3Dprint_AM_70_1H43C006_3367515_EN%20(1).pdf?cache=1639059520.
[15] B. Mezrag, F. Deschaux-Beaume, M. Benachour, Control of mass and heat transfer for steel/aluminium joining using cold metal transfer process, Sci. Technol. Weld. Join. 20 (3) (2015) 189–198.
[16] S. Ríos, P.A. Colegrove, F. Martina, S.W. Williams, Analytical process model for wire+ arc additive manufacturing, Addit. Manuf. 21 (2018) 651–657.
[17] "Standard Test Methods for Determining Average Grain Size." https://www.astm.org/e0112-96e02.html (accessed Mar. 01, 2022).
[18] H.K.D.H. Bhadeshia, J. Christian, Bainite in steels, Metall. Trans. A 21 (3) (1990) 767–797.
[19] P. Dirisu, S. Ganguly, A. Mehmanparast, F. Martina, S. Williams, Analysis of fracture toughness properties of wire+ arc additive manufactured high strength low alloy structural steel components, Mater. Sci. Eng. A 765 (2019), 138285.

PUBLICATION II

Graph-based Meta-Modeling for Characterizing Cold Metal Transfer (CMT) Process Performance

Hari P.N. Nagarajan, Suraj Panicker, Hossein Mokhtarian, Théo Remy-Lorit, Eric Coatanéa, Ananda Chakraborti, Romaric Prod'hon, Hesam Jafarian, and Karl R. Haapala

ASTM Smart and Sustainable Manufacturing, vol. 3, issue 2 (2019)

10.1520/SSMS20190026

PUBLICATION III

Systematic manufacturability evaluation using dimensionless metrics and singular value decomposition: a case study for additive manufacturing

Eric Coatanéa, Hari P.N. Nagarajan, Suraj Panicker, Romaric Prod'hon, Hossein Mokhtarian, , Ananda Chakraborti, Henri Paris , Inigo Flores Ituarte , and Karl R. Haapala

The International Journal of Advanced Manufacturing Technology, vol. 115 (2021)
https://doi.org/10.1007/s00170-020-06158-0

The International Journal of Advanced Manufacturing Technology (2021) 115:715–731
https://doi.org/10.1007/s00170-020-06158-0

ORIGINAL ARTICLE

Systematic manufacturability evaluation using dimensionless metrics and singular value decomposition: a case study for additive manufacturing

Eric Coatanéa[1] · Hari P. N. Nagarajan[1] · Suraj Panicker[1] · Romaric Prod'hon[1] · Hossein Mokhtarian[1] · Ananda Chakraborti[1] · Henri Paris[2] · Iñigo Flores Ituarte[1,3] · Karl R. Haapala[4]

Received: 17 August 2020 / Accepted: 24 September 2020 / Published online: 27 October 2020

Abstract
Additive manufacturing has been presented as a novel and competitive method to achieve unprecedented part shapes and material complexities. Though this holds true in niche markets, the economic viability of additive manufacturing for large-scale industrial production is still in question. Companies often struggle to justify their investment in additive manufacturing due to challenges in the integration of such technologies into mainstream production. First, most additive technologies exhibit a relatively low production rate when compared with traditional production processes. Second, there is a lack of robust design for additive manufacturing methods and tools that enable the leveraging of the attendant unique capabilities, including the ability to form organic part geometries and automated part consolidations. Third, there is a dearth of systematic part screening methods to evaluate manufacturability in additive manufacturing. To tackle the challenge of manufacturability evaluation, the present work proposes a novel approach derived from latent semantic analysis and dimensional analysis to evaluate parts and their production for a variety of selected metrics. The selected metrics serve as descriptors of design features and manufacturing functions, which are developed using functional modeling and dimensional analysis theory. Singular-value decomposition and Euclidean distance measurement techniques are used to determine the relative manufacturability for a set of parts for a specified manufacturing process technology. The utility of the method is demonstrated for laser powder bed fusion technology. While demonstrated for additive manufacturing here, the developed approach can be expanded for any given set of manufacturing processes. Expansion of this systemic manufacturability analysis method can support part design decision-making, process selection, and design and manufacturing optimization.

Keywords Manufacturing process selection · Part consolidation · Latent semantic analysis · Machine learning · Additive manufacturing

1 Introduction

Additive manufacturing (AM) is presented in literature as a strong competitor of traditional manufacturing methods [1]. The growth in popularity of AM is related to the advantages it provides in terms of material and design freedom to produce unprecedented shapes with high geometric complexity. However, successful adoption and integration of AM into production environments has been challenging for businesses. Often, the full potential of AM technologies is not leveraged, and direct application of AM for products with existing traditional manufacturing solutions is not economically viable [2]. Thus, industries must focus on designing and developing products that are suited for AM rather than using the technology as a direct replacement of traditional manufacturing processes [3].

✉ Eric Coatanéa
eric.coatanea@tuni.fi

[1] Faculty of Engineering and Natural Sciences, Tampere University, 33720 Tampere, Finland

[2] Université de Grenoble Alpes, CNRS, G-SCOP, F-38000 Grenoble, France

[3] Department of Mechanical Engineering, Technical University of Denmark, Building 425, Lyngby, Denmark

[4] School of Mechanical, Industrial and Manufacturing Engineering, Oregon State University, Corvallis, OR 97331, USA

A decision support system (DSS) can aid in finding potential candidate products for AM through systematic evaluation of alternatives. However, the priorities of most DSS solutions revolve around productivity and economics and seldom integrate design for manufacturing and assembly assessments. Recently, research effort has been directed towards building integrated DSS solutions capable of evaluating the technical and economic aspects of production [3, 4]. Nevertheless, such solutions are still in their infancy and require a significant amount of human interaction. In addition, the design freedom in AM can be leveraged by redesign for consolidation of parts into sub-assemblies; evaluating the relative performance of such part consolidations is challenging, however, due to a lack of metrics and systematic evaluation techniques. Pradel et al. [2] developed a design framework for mapping design and manufacturing knowledge in the context of design for additive manufacturing (DFAM). The study reviewed the current state of the art in DFAM and highlighted several limitations and future directions for research in the field. An important takeaway from the study was the need for easy-to-use and reliable tools which can aid the user to identify when AM can function as a competitive alternative for traditional manufacturing. The authors emphasize that such tools must provide a comprehensive survey of available AM technologies and allow for rapid identification of potential processes based on evaluation of product or part over a wide range of design, production, and economic metrics. Thus, in this research, a novel evaluation approach derived from singular value decomposition (SVD) and its application in the latent semantic analysis (LSA) method is developed herein to evaluate parts and their production for a variety of selected metrics. The developed approach serves to achieve two distinct objectives. First, the approach supports fast clustering of parts from a database for specific manufacturing processes, which enables evaluation of their manufacturability based on a set of design and manufacturing metrics. Metric values for part design alternatives and an "ideal" part are computed and compared using a mapping approach based on Euclidean distances between the evaluated parts. Second, the potential for consolidation of parts into sub-assemblies is evaluated using the additive property of part features and metrics provided by the SVD approach. The developed methodology aims to provide users with an evaluation approach which is automatic and allows for rapid identification of potential processes for different designs. However, the current approach does not provide any design guidelines for AM, rather it aims to provide designers with a generalized framework for development of dimensionless metrics which are scale independent and invariant as well as providing a mathematical mechanism for performing fast manufacturability evaluations.

The remainder of the manuscript is organized into five sections. Section 2 discusses relevant background information. Section 3 presents the methodology as follows. First, metrics are formalized using a combination of taxonomies organized around functions, organs, and variables, and the approach to build metrics as a combination of variables is selected. Second, the use of SVD is presented for part design and manufacturing evaluation. Sections 4 and 5 then demonstrate the usability of the developed approach using an AM case study. Finally, the findings of the presented work and potential for future developments are discussed in Section 6.

2 Background

DSS solutions for complex decision-making and problem-solving became widespread in the 1970s with the growth of computer technology. Over the past several decades, the utility of DSS has improved, and, with manufacturing moving towards more automated processes, solutions have been developed leading to intelligent decision support systems (IDSS) and cyber-physical production systems (CPPS). DSS can serve as passive, active, or cooperative systems depending upon their functionality. The available literature categorizes DSS into five types, namely, model-driven, data-driven, knowledge-driven, document-driven, and communication-driven systems [5]. In this current research, a combination of model-driven, data-driven, and knowledge-driven approaches is used to evaluate part manufacturability.

A model-driven DSS is typically not data intensive, rather it uses analytical models, simulation tools, and optimization methods to generate multiple experiments depicting the effects of alternative decisions. Monte Carlo simulation, discrete event simulation, probabilistic forecasting, agent-based and multi-agent simulation, system dynamics, and visual simulation are some of the common simulation methods used in model-driven DSS [6–8]. Data-driven DSS, on the other hand, utilizes structured data (e.g., machine learning using neural networks), such as internal and external company data, time-series data, and real-time data [9]. Business intelligence systems or online analytical processing (OLAP) are examples of data-driven DSS that enables better decision support by formulating decisions through triggering, manipulating, and/or analyzing data. However, accurate and structured data are a key requirement in developing data-driven solutions, and, thus, efficient data processing could enable fast and accurate decision-making [10, 11]. Knowledge-based DSS methods of today (e.g., fuzzy logic, Bayesian networks, and genetic algorithms) have evolved from their predecessors, known as rule-based expert systems. Such rule-based expert systems use heuristics to solve problems with the help of human expert knowledge stored in databases. In the age of big data, the challenges pertaining to the properties of data (i.e., volume, variety, velocity, veracity, validity, and value) need to be addressed to improve the process of decision-making [12–15].

Decision support for manufacturing process selection has been of key interest for the AM research community. Such systems require evaluation of design and manufacturing capability

to choose the right process for a specific design or vice versa. Selection criteria for design elements are often objective and can be expressed in the mathematical form to be either maximized or minimized. However, tradeoffs involving conflicting selection criteria may introduce a certain level of subjectivity which, when combined with the existing complexity of the evaluated problem, makes the selection process difficult. In addition, material selection, process selection, and shape selection for AM should not be considered independent, mutually exclusive entities, rather they must be addressed with a focus on overlaps and interrelationships [2, 16]. Wang et al. [17] developed a DSS for AM process selection using a hybrid multi-criteria decision-making method, the analytic hierarchy process (AHP) combined with a technique for order preference by similarity. Their method was used to obtain an ideal solution to explore and refine the solution space and to rank suitable alternatives. Technical and economic aspects of the processes are taken into account; however, the method requires development of probabilistic models for representing each process and its capabilities for initial sampling based on customer preferences obtained through the AHP. Such an approach implies the need for large amounts of data relating to each technical or economic aspect of interest for training. Modeling each process with less data is challenging, especially in AM where parameters often reflect a non-linear relationship, requiring more intensive training to track them [18].

For humans, learning new concepts and skills is usually fast and efficient with only a few training examples. For example, people who know how to use a lathe are likely to quickly learn how to use a milling machine with little or no demonstration. In contrast, training a machine learning (ML) model for a similar situation would require a large number of training samples and is not likely to become an expert system capable of independent operation. Further, the training performed for the lathe will not be transferrable to the milling machine. The lack of interoperability is a fundamental problem of current ML approaches limiting their application to large-scale real problems [19]. In order to effectively use ML models in a particular design or manufacturing domain, it is important to evaluate the capability of current approaches based on their ability to quickly learn new concepts and skills with few training samples. Approaches that will enable the generalization of ML models for related application domains need to be developed.

Automated approaches are becoming increasingly popular for modeling AM processes, but the objectives for the use of ML methods are often unclear. The fundamental question remains: *What is the real added value of the application of ML in AM process modeling?* When comparing ML models with analytical modeling strategies, one fundamental difference is the ability of ML models to improve continuously and automatically over time. In this respect, other models are rigid and not updated dynamically during use. The second fundamental element to consider with modeling is the complexity of the modeling problem, which is strongly correlated with the required size of the datasets needed to generate the models. Based on these two fundamental aspects of ML, a primary goal of the research herein is to provide an approach capable of integrating new knowledge over time to modify predictions or update clustering when new data is included or when data is removed. Thus, the proposed approach can be coined as a type of machine learning method. As a second key goal, the ML approach should be capable of providing adequate evaluations using very small datasets.

To achieve these two goals, three fundamental approaches from meta-learning, a branch of ML dealing with improving learning and learning processes, are adopted. Meta-learning proposes metric-based, model-based, and optimization-based approaches to improve training of ML models. First, a metric-based approach is established here using dimensional analysis theory (DAT) and the Vashy-Buckingham theorem. The approach has been applied to manufacturing in general and is applicable to other engineering domains at large. Second, model-based and optimization-based approaches are then combined using SVD to perform part evaluation. This combination will also be studied further in future papers. This paper presents only one limited aspect of the combination between model-based and optimization-based approaches.

3 Methodology

As introduced above, the methodology followed in this research develops an ML approach for evaluating parts for manufacturability and presents some fundamental aspects of the approach suitable for part consolidation. The step-by-step implementation of the methodology is shown in Fig. 1. The methodology first uses the dimensional analysis conceptual modeling (DACM) framework to describe the function and define the organs and variables associated with the function. A group of dimensionless metrics are then formulated and computed for the part to be evaluated. Next, SVD and Euclidean distance measurement techniques are used to cluster part designs and compute distances between the evaluated parts and "ideal" parts for different manufacturing process technologies.

Steps I–V in Fig. 1 follow the hypothesis that functions can be efficiently described using a group of dimensionless variables and, subsequently, describe subsystems and systems. Such dimensionless variables can serve as metrics for assessing design and manufacturing information. The methodology starts by describing a set of functions representing the different activities of a system (step I). A function can be described using an action verb. In a graphical context, a function can be represented as a box with inputs and outputs; this is the traditional Pahl and Beitz model [18].

Figure 2 shows a modified generic model of a function and the associated variables. A generic model of a function was initially proposed in bond graph theory [20, 21] but later modified in the dimensional analysis conceptual modeling (DACM)

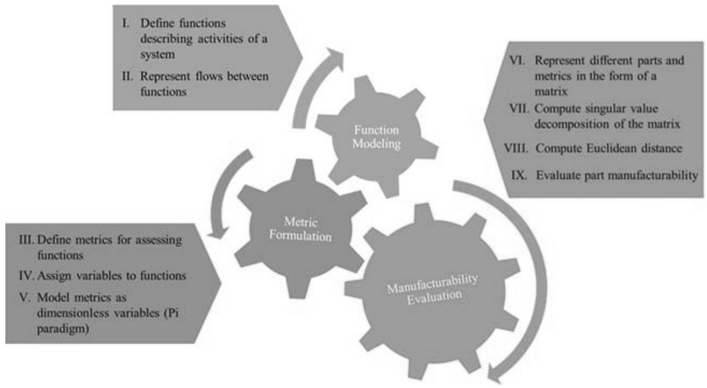

Fig. 1 Methodology for evaluating part manufacturability and part consolidation

framework by Coatanéa et al. [22]. In Fig. 2, a function is represented using three categories of variables, namely, power variables, state variables, and connecting variables. The power variables represent effort (in the form of force, pressure, temperature, and chemical potential) and flow (in the form of velocity, volumetric flow, volumetric velocity, and entropy flow), while state variables represent displacement and momentum. Generic categories of variables for different energy domains are shown in Table 1. The generic classification model was expanded by Coatanéa et al. [22] by introducing a supplementary category of variables called connecting variables, for describing the connections that exist between power variables (i.e., effort and flow) and state variables (i.e., displacement and momentum).

Connecting variables can describe the geometry of a part as well as material-related properties.

Functions can be classified using the terms employed by the DACM framework. The equivalence of functional terms used in DACM to the notation of other functional modeling approaches is shown in Fig. 3. After classification, the functional terms are associated with organs, such as in bond graph theory, to represent the function as an input-output relationship of generic variables [23]. Organs represent an intermediate layer of detail between the abstract concept of a function and a physical component or subsystem required to implement a function. The mapping between functions and organs is shown in Table 2.

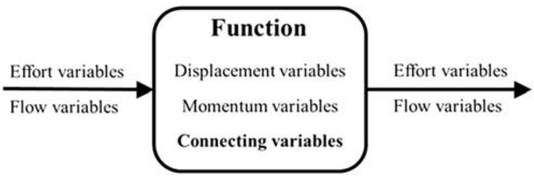

Fig. 2 Modified generic graphical model of a function with new variable category

Following the description of functions, dimensionless variables can be computed to define metrics. Metrics are measures used to track or assess the status of a system or activity. In this research, metrics are used to assess the performance of the different functions of the system. To illustrate how metrics can be used to assess the nature of surfaces, an example case for machining a cube is considered. Machining requires an operator to locate and to clamp a workpiece. We can assume that the functions (locating and clamping) are more easily achieved if the shape of the blank workpiece is known. Hence, the fulfillment of these functions can be analyzed by defining a metric representing the shape of the workpiece. We can conceptualize the shape of the workpiece with the help of a dimensionless Pi (π) number.

Assuming the face of the workpiece to be located and clamped is circular with a diameter D, the Pi number could be calculated using either Eq. 1 (surface area) or Eq. 2 (circumference).

$$S = \frac{\pi D^2}{4} \tag{1}$$

$$C = \pi D \tag{2}$$

Rearranging Eqs. 1 and 2, we obtain:

$$\pi = \frac{4S}{D^2} = 3.1416 \tag{3}$$

$$\pi = \frac{C}{D} = 3.1416 \tag{4}$$

We see that both equations provide the same value for π (3.1416). This specific value of Pi is associated with the shape of the geometric form considered, in this case a circle.

The concept of reordering the elements in the equations to find the value of Pi can be performed using the Vashy-Buckingham theorem in DAT [28]. The theorem allows the creation of a set of dimensionless numbers, where, if a

Table 1 Generic categories of variables for different energy domains

	Effort e (dimension)	Flow f (dimension)	Generalized momentum p (dimension)	Generalized displacement q (dimension)
Translation	Force F (N)	Velocity v (m s^{-1})	Momentum p (N.s)	Displacement x (m)
Rotation	Torque T (N.m)	Torque velocity Ω (rad s^{-1})	Angular momentum b (N.ms)	Angle φ (rad)
Hydraulic	Total pressure p ($N.m^{-2}$)	Volumetric flow φv ($m^3 s^{-1}$)	Pressure momentum Γ ($N.m^{-2}s$)	Volume V (m^3)
Acoustic	Pressure p ($N.m^{-2}$)	Volumetric velocity φv ($m^3 s^{-1}$)	Momentum Γ ($N.m^{-2}s$)	Volume V (m^3)
Electric	Voltage u (V)	Current i (A)	Flux linkage φ (Vs)	Charge q (C)
Chemical	Chemical potential μ (J mol^{-1})	Molar flow N' (mol s^{-1})		Molar mass N (mol)
Thermal	Temperature T (K)	Entropy flow S' (J s^{-1} K^{-1})		Entropy S ($J.K^{-1}$)

physical phenomenon is represented such that q_1, a dependent variable, is influenced by a set of independent variables, then

$$q_1 = f(q_2, q_3, \ldots, q_n) \tag{5}$$

where q_i are the n physical variables, which are expressed in terms of h independent physical quantities. Equation 5 can be rewritten as (Eq. 6):

$$\pi_1 = f(\pi_2, \pi_3, \ldots, \pi_j) \tag{6}$$

where π_i are dimensionless parameters constructed from q_i such that $j = (n - h)$ dimensionless equations (Pi numbers herein) exist of the form (Eq. 7):

$$\pi_i = q_1^{\alpha}.q_2^{\beta}.q_3^{\gamma}..q_n^{\delta} \tag{7}$$

where the exponents are rational numbers. To calculate the values of the dimensionless Pi numbers, one variable (q_i) is selected as the performance variable (i.e., dependent variable) whose exponent is 1, while the other variables are classified as repeating variables.

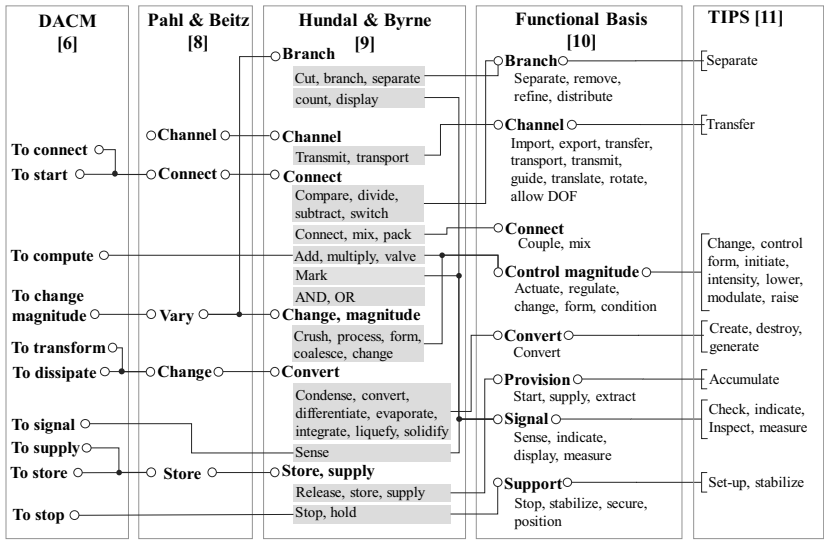

Fig. 3 Comparison of different notations used in functional modeling [22, 24–27]

Table 2 Function-to-organ mapping

Elementary functions	Associated organs	Number of possible organ connections (N)
To supply	Source of effort	1
	Source of flow	1
	Sink	1
To transform/to change magnitude	Transformer	2
	Gyrator	2
To transform/to dissipate	Resistor	1
To transform/to store	Inertia	1
	Capacitor	1
To connect	Flow junction	$N \geq 1$
	Effort junction	$N \geq 1$
To start/to stop	Switch	$N \geq 1$
To compute	AND	2
	OR	2
	NOR	2
	NAND	2
	Add	$N \geq 1$
	Subtract	2
	Multiply	2
	Divide	2
To signal	Sense	1
	Display	$N \geq 1$

Similarly, considering the face of the workpiece to be located and clamped to be a rectangular shape involving three describing variables (length, l, and width, w, measured in meters, m, and surface area, S, measured in square meters, m^2). If S is selected as the performance variable, the Pi number can be calculated as shown in Eq. 8:

$$\pi = \frac{S}{l.w} \tag{8}$$

In this case, $\pi = 1$ is a constant value classifying the shape as being rectangular. It is important to note that the value of π is independent from the scale and dimension of the rectangular shape, since S is dependent on l and w.

Thus, using DAT and the Vashy-Buckingham theorem, a generic method can be followed to combine parameters and form metrics measuring certain aspects of a designed part. Pi numbers have a broad usage in engineering; in this research, we demonstrate that they can be used as descriptors of functions. This hypothesis is supported in literature [29], where it is shown that combination of parameters supports the creation of parsimonious metrics. Such parsimonious metrics have proven to be efficient in assessing model performance.

Hence, the hypothesis in this research is similar, where the parsimonious principle applies to the description of functions. Revisiting the example of machining the cube, the goal is to evaluate the "locating" and "clamping" functions for a part in a material removal process. The evaluation of the functions requires considering the efficiency and ease with which both functions are performed. Thus, using the metric values, we can evaluate how "distant" a specific part is from an ideal part—a part for which the two functions (locating and clamping) are most optimally performed (e.g., when the shape is circular or prismatic and locating and clamping can be performed using a three- or six-jaw chuck or a vise). In this research, ideal parts are used to represent different manufacturing process technologies following the TRIZ concept of ideality [27]. In addition, metrics can be computed based on other functional requirements, such as shape complexity, macro- and micro-level precision, volume of material removed or added, and material complexity.

Through the previous examples, a generic method grounded in functional modeling and DAT can be conceptualized for the development of metrics. Though dimensional analysis has been widely used in engineering, the current application of this mathematical approach establishes a mechanism to select the appropriate combination of variables for an engineering application using the DACM framework. The lack of such mechanism to select the right performance and repeating variables for the study in traditional DAT implies that the domain knowledge associated with the study is absent. The DACM framework applied in this research bridges this gap by providing a functional basis through which performance and repeating variables can be assigned. Thus, the Pi numbers computed using this approach do not serve solely as combinations of

variables to ensure dimensional homogeneity but also as metrics which describe specific functions associated with a technical system or part. The presented approach establishes a formal association between Pi numbers, a type of structural description metric, and functional modeling using the principle of composability (Fig. 4). In practice, a function is implemented using components. The components are modeled using variables and equations. Pi numbers are a generic form of power laws present ubiquitously in nature and used in order to model a function via key performances (i.e., key performance indicators), repeating variables (i.e., independent variables), and the equations combining them. Pi numbers are scale, metric, aggregation, and composition invariant. They form an ideal tool to represent manufacturing metrics when parts with different scales, metrics, and compositions need to be compared.

Metrics have long been used as a means of evaluating functions. Nevertheless, the use of dimensionless numbers as performance indicators is a generalization enabling the creation of generic metrics that can apply to a broader spectrum of functional use cases. The concept for the use of metrics to represent functions is next explained using an additive manufacturing example.

In laser or electron beam powder bed technologies, the build volume rate V (mm^3/s) is a key performance indicator for assessing building time and, consequently, production rate and cost [30]. V is dependent on the layer thickness D_S (μm), the scan speed V_{scan} (mm/s), and the scan line distance between parallel laser tracks Δy_s (μm). Other important variables affecting the overall product cost are height of the part H (mm), part orientation, part surface area S_P (mm^2), and total printing time t_B (s). A printing process is equivalent to the superfunction/organ D in Fig. 4, wherein multiple low-level functions are integrated to form a high-level function (to print). The level of granularity of function descriptions focuses on the key outputs of the manufacturing machine sub-functions, namely, to create a layer of powder and to move the laser or electron beam with respect to the powder layer. Parameters related to the different functions as well as those

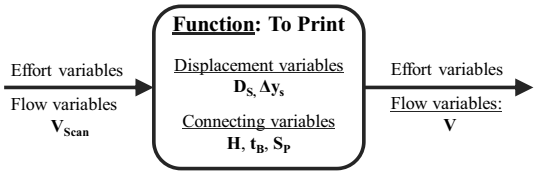

Fig. 5 Functional model for the "to print" superfunction in powder bed printing technology

that specify part properties and part position on the printing table are considered. Figure 5 shows the high-level functional model for the superfunction "to print" for powder bed printing technology. Variables are represented as their generic categories following Table 1.

The two performance variables (i.e., variables used to assess the performance of the printing process) here are V, the expected build volume rate, and t_B, the total printing time. The expected build volume rate accounts for the specific performance of the laser or electron beam when taking into account laser beam diameter, line spacing between laser scans, and the height of the powder layer. The total printing time evaluates the total duration of the printing process, which is dependent on the part geometry. The dependent variables (performance variables) and the independent variables can be represented in the form of vectors. Table 3 presents the decomposition for the first performance variable V. Using the formula $[C] = [A]^{-1}.[B]$, the exponents ($[C]$) of the influencing variables in matrix A can be computed to ensure dimensional homogeneity. The base dimensions of the variables in this case are represented as the length of the part layers in each ordinal direction (L_x and L_z) and time (T). Here, time (T) is one of the seven base dimensions of the international system of units. In addition, matrix A is square due to wise decomposition of the base dimensions. Obtaining a square matrix A is needed to compute the matrix inverse, $[A]^{-1}$.

Matrix A can be represented as a square matrix by modifying the number of base dimensions by either adding, suppressing, or combining variables in columns. Szirtes [31] presents heuristic rules to follow when performing such

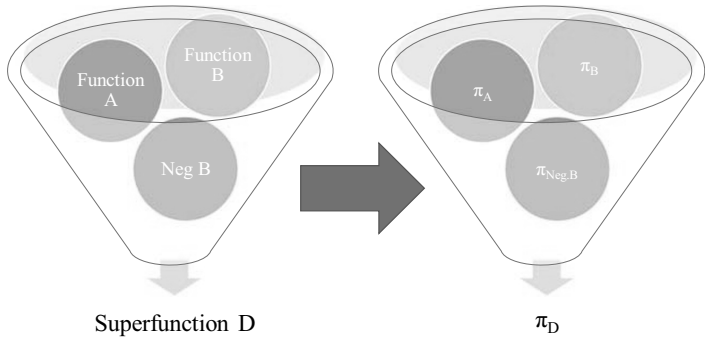

Fig. 4 Composability of functions and dimensionless metrics

Table 3 Decomposition of performance variable V using DAT

π_V		Independent variables [A]			Dependent variable [B]
		V_{scan}	D_s	Δy_s	V
Base dimension	L_z	0	1	0	1
	L_x	1	0	1	2
	T	−1	0	0	−1

transformations. Using the proposed approach, Pi numbers are developed for the two performance variables, V and t_B, selected above. Thus, the performance variables are represented in the form of dimensionless variables as presented in Eqs. 9 and 10:

$$\pi_V = \frac{V}{V_{Scan}.D_S.\Delta y_S} \tag{9}$$

$$\pi_{t_b} = \frac{t_B.V_{Scan}.D_S.\Delta y_S}{H.S_P} \tag{10}$$

Following the development of dimensionless variables as metrics describing functions, steps VI–IX in Fig. 1 are used to define the mathematical mechanisms to support SVD for part evaluation. The different part alternatives and metrics for their characterization are represented in the form of matrix X (Table 4). In addition to the evaluated part alternatives, an ideal part for each manufacturing process technology is also considered in matrix X. The ideal part is one in which the different functions of the manufacturing system are most optimally performed. This implies that the ideal part will have the ideal (maximum, minimum, or limit) value for all metrics assessed.

Matrix X is decomposed using SVD to enable the computation of distances between the evaluated part alternatives and the ideal part for each potential manufacturing process technology. SVD allows the creation of a model of parts and processes, presented in the form of a succession of vectors composed of metrics [32]. SVD is a decomposition technique related to principal component analysis (PCA) and used for classification and ranking of tasks. Applications of SVD have been presented in literature, for example, in aeronautics and in metamodeling [29, 33]. However, prior to this research, the use of the approach as a systematic part screening method has not been reported. In this research, SVD is used for part clustering, which enables the calculation of distances between the evaluated part alternatives and the ideal part for each manufacturing process technology. Matrix X can be decomposed to the form (Eqs. 11 and 12):

Table 4 Part alternatives and metrics forming matrix X

	Metric 1	Metric 2	Metric 3	…	Metric n
Ideal part for process 1 (laser powder bed fusion)					
Part 1					
…					
Part m					

$$[X] = [U].[W].[V]^T \tag{11}$$

$$\begin{bmatrix} X_{11} & X_{12} & X_{13} \\ X_{21} & X_{22} & X_{23} \\ X_{31} & X_{32} & X_{33} \\ X_{41} & X_{42} & X_{43} \end{bmatrix} = \begin{bmatrix} U_{11} & U_{12} & U_{13} \\ U_{21} & U_{22} & U_{23} \\ U_{31} & U_{32} & U_{33} \\ U_{41} & U_{42} & U_{43} \end{bmatrix} . \begin{bmatrix} W_{11} & 0 & 0 \\ 0 & W_{22} & 0 \\ 0 & 0 & W_{33} \end{bmatrix} . \begin{bmatrix} V_{11} & V_{21} & V_{31} \\ V_{21} & V_{22} & V_{32} \\ V_{31} & V_{32} & V_{33} \end{bmatrix}^T \tag{12}$$

In Eq. 12, a compact SVD approach is followed, in which $[X]$ is an $(m \times n)$ matrix, $[U]$ is an $(m \times r)$ matrix, $[W]$ is square diagonal matrix of size $(r \times r)$, where r represents the rank of $[X]$ with $r \leq min\{m, n\}$ and $[V]$ is an $(n \times r)$ matrix. A compact SVD approach implies that no null columns exist in the matrix [W]. The approach is chosen to ensure that the decomposition results in a square diagonal matrix to allow for straightforward inverse matrix operations.

The matrix $[W]$ resulting from the decomposition is arranged in a way that its diagonal elements (i.e., the singular values) are ranked in descending order. This implies that the influence of the $[U]$ rows is also in descending order. The initial $[X]$ can be reconstructed with reasonable accuracy by reducing the number of rows in $[U]$. An interesting property of $[U]$ is that the sum of the variance of each column is one. Thus, all columns have the same deviation. Considering only the singular values in $[W]$, let us assume that the number of selected singular values, k, is two. Then, $[W]$ can be represented as Eq. 13:

$$[W] = \begin{bmatrix} W_{11} & 0 \\ 0 & W_{22} \end{bmatrix} \tag{13}$$

The parts are represented by the terms in the row vectors of the matrix product $[U_k].[W_k]$. Similarly, the metrics are represented by the column vectors of the matrix product $[W_k].[V_k]^T$. The matrix product $[U_k].[W_k]$ creates vectors of dimension k, where the rows represent the parts (and respective manufacturing process technologies) considered in the study. Thus, the SVD approach develops a reduced model linking parts, metrics, and manufacturing processes. The required level of accuracy can be selected by choosing the number of singular values retained in the reduced model. In this research, the variation in the accuracy of models depending on the number of singular values selected is investigated as part of the case study. The use of SVD and of the decomposed products $[U_k].[W_k]$ and $[W_k].[V_k]^T$ provides several advantages. First, it enables computation of distances using the Euclidean distance measurement approach and thus allows screening and ranking of parts in terms

of their manufacturability for each manufacturing process technology evaluated. Ideal parts can be added for consideration of different manufacturing process technologies by computing the limits of each metric. The ideal limit of each metric computed would imply the best performance in a specific function. Subsequent ranking would then allow evaluation of the suitability of multiple manufacturing methods for a given part design or set of design alternatives. Further, SVD enables reconstruction of the design space, which allows for development of aggregated metrics and parts. These advantages are further explored in the case study for an additive manufacturing process technology below.

In order to rank the different parts and evaluate their suitability for certain manufacturing processes, the distance between the ideal part for the given manufacturing process technology and the evaluated parts from a database needs to be computed. Several methods are presented in literature to perform such computation. The two most frequently used approaches, the cosine similarity approach and the Euclidean distance computation approach, are investigated in this research. Cosine similarity is a measure of similarity between two non-zero vectors of an inner product space based on the cosine of the angle between them. Cosine similarity is usually used in positive design space, wherein the outcome is bounded in [0, 1]. It is assumed that the set of metrics developed is also bounded in [0, 1]. Thus, the input data is normalized in order to obtain values in the range of zero (0) to one (1) for computing cosine similarity. For two vectors A and B, the cosine similarity measure can be computed as (Eq. 14):

$$cos(\theta) = \frac{A.B}{\|A\|.\|B\|} = \frac{\sum_{i=1}^{n} A_i.B_i}{\sqrt{\sum_{i=1}^{n} A_i{}^2}\cdot\sqrt{\sum_{i=1}^{n} B_i{}^2}} \tag{14}$$

Cosine similarity is often used as a metric for measuring distance when the magnitude of the vectors does not matter, e.g., in semantic analysis. However, if the magnitude of the vectors is important, then a second approach can be followed by computing a Euclidean distance. The Euclidean distance between an ideal reference part (r), which represents a part containing the ideal features (also implies optimal metric values) for a specified manufacturing process technology, powder bed fusion technology in this case, and a real part to be evaluated (i), can be computed as (Eq. 15):

$$d_{ir} = \sqrt{(x_i - x_r)^2 + (y_i - y_r)^2 + (z_i - z_r)^2 + \ldots + (f_i - f_r)^2} \tag{15}$$

where x, y, z, and f represent the vectors of the product $[U_k]$. $[W_k]$ when assessing part distances (Fig. 7) and vectors of the product $[W_k]$. $[V_k]^T$ when assessing metrics (Fig. 8). In this research, the magnitude of the distance between the points is of importance. Since the reference technologies play the role of ideal targets, distances must be computed between these ideal parts (technologies) and the evaluated alternative parts. The Euclidean distance method is chosen to compute distances and rank parts for a specific manufacturing process technology. Nevertheless, the cosine similarity measure is also used for comparison in the case study. Distance computation and ranking facilitate screening for part manufacturability for a specific technology by comparing metric performance with ideal values.

An important aspect of the current methodology is the development of dimensionless metrics (Pi numbers) which are scale, metric, and composability invariant, by virtue of the Pi laws (i.e., power laws with dimensional homogeneity). The developed metrics enable the computation of Euclidean distances by weighting each metric equally. If not, the Euclidean distance computed would not give equal importance to each metric rather will favor the ones with high variance when measured in the principal component space [33]. The use of the Euclidean distance to perform ranking would not be possible without the invariant nature of the developed metrics. Alternately, Mahalanobis distance could be used for comparing metrics. However, it is important to note that the Mahalanobis distance measurement would require the computation of the variance-covariance matrix of the dataset. The computation of the variance-covariance matrix is difficult when the data is multicollinear and/or when the number of variables exceeds the number of objects in the dataset. A feature reduction would then need to be carried out to accurately calculate the Mahalanobis distance [33]. The current approach provides an advantage over Mahalanobis distance, wherein the developed Pi numbers provide a method to reduce the dimension and complexity of a problem by aggregating metrics.

4 Additive manufacturing case study

The utility of the method developed above for systematic manufacturability evaluation using dimensionless metrics and SVD is demonstrated for an additive manufacturing case study using the laser powder bed fusion (LPBF) process. LPBF technology is considered as a unique manufacturing method in this proof of concept exemplar (no competing manufacturing method is considered here). Nevertheless, through future extension, the approach will enable the integration of several manufacturing processes simultaneously. The capability of the approach to aid manufacturing process selection will be investigated in future research.

In this work, twelve metrics are computed, as presented in Table 5, following the design rules proposed by Zimmer and Adam [34]. The last column of Table 5 is used to compute the position of the ideal part used as the reference for a given manufacturing method. Eight parts exhibiting a range of complexities (e.g., size and number and type of features) were selected to be assessed for the LPBF process (Fig. 6).

Table 5 Metrics for characterizing functions in laser powder bed fusion technology (based on design and manufacturing principles from [30])

Metric #	Metric calculation	Name of the variables (units)	Category [Purpose of the metric]	Ideal objective
Metric 1	$\pi_V = \frac{V}{V_{Scan}.D_S.\Delta y_S}$	V: Expected build volume rate per layer (mm^3/s) V_{Scan}: Scan speed (mm/s) D_S: Layer thickness (mm) Δy_s: Scan line distance between parallel laser tracks (mm)	**Production rate** [Evaluating build time per layer]	$\lim_{Ideal} \pi_V = 1$
Metric 2	$\pi_{Vn} = \frac{V}{V_{Scan}.D_S.\Delta y_S}.n$	$n = \frac{S_{BP}}{S_P}$ with: S_{BP}: Surface area of build plate (cm^2) S_P: Surface area per part layer (cm^2)	**Production rate** [Evaluating building time per layer for n parts]	$\lim_{Ideal} \pi_{Vn} = n$
Metric 3	$\pi_{t_b} = \frac{t_B.V_{Scan}.D_S.\Delta y_S}{H.S_P}$	H: Height of the part (considering the part orientation) (mm) t_B: Total printing time (s) S_P: Surface area per part layer (mm^2) V_{scan}: Scan speed (mm/s) D_S: Layer thickness (mm) Δy_s: Scan line distance between parallel laser tracks (mm)	**Cost** [Total build time of a0 specific part]	$\lim_{Ideal} \pi_{t_B} = 1$
Metrics 4 and 5	$\pi_{R_{IH}} = \frac{R_{IH}}{D_S}$	R_{IH}: Internal radius (horizontal holes) (mm) D_S: Layer thickness (mm)	**Design rule: Internal support structure** [Evaluating the need for support structure in internal round channels] **Design rule: Post-processing** [Evaluating needs for post-processing of holes]	$\lim_{Ideal} \pi_{R_{IH}} < 45$ $\lim_{Ideal} \pi_{R_{IH}} > 10$
Metric 6	$\pi_{R_V} = \frac{D_V}{D_L}$	S: Surface of the contour + Surface internal hole (mm^2) D_L: Laser beam diameter (mm) C_L: Generated laser beam circumference (mm) $D_V = \frac{S}{C_L}$: Length vertical holes (mm)	**Design rule** [Evaluate the minimal size of vertical holes that can be printed]	$\lim_{Ideal} \pi_{R_V} > 0$
Metric 7	$\pi_L = \frac{L}{10.R^{1/2}.L_P^{1/2}}$	L: Length of the holes (mm) L_P: Length of the part (mm) R: Radius of the holes (mm)	**Design rule** [Depowdering feasibility evaluation]	$\lim_{Ideal} \pi_L \leq 1$
Metric 8	$\pi_S = \frac{S}{S_A}$	D_S: Layer thickness (mm) n: Number of layers of the surface printed with δ angle δ: Printing angle with the build plate $S_A = n.\frac{2D_S}{\tan\delta} + S$ S: Total surface printed with angle S_A: Surface printed at 0° or 90°	**Design rule** [Evaluation of the relative printing default for surfaces with printing angle at 0° or 90°]	$\lim_{Ideal} \pi_S = 1$
Metric 9	$\pi_{D_S} = \frac{D_S}{C}$	C: Minimal size of chamfer or radius parallel or perpendicular to the building plate (mm) D_S: Layer thickness (mm)	**Design rule** [Evaluation of the printability and risk of shape deviation]	$\lim_{Ideal} \pi_{D_S} = 0$
Metric 10	$\pi_{V_T} = \frac{V_T}{V_L} V_L$	V_T: Total volume (mm^3) V_L: Lattice volume (mm^3)	**Design rule** [% of lattice structures and thick walls]	$\lim_{Ideal} \pi_{V_T} = 0$
Metric 11	$\pi_{S_T} = \frac{S_T}{S_C + S_P}$	S_T: Total surface of the part (mm^2) S_C: Cylindrical surfaces (mm^2) S_P: Plane surfaces (mm^2)	**Design rule** [Evaluation of clamping capability for post-processing]	$\lim_{Ideal} \pi_{S_T} = 1$
Metric 12	$\pi_{S_O} = \frac{S_O.(L_O/L_H)}{S_T}$	L_O: Overhanging length (mm) L_H: Overhanging height (mm) S_O: Overhanging surface (mm^2) S_T: Total surface of the part (mm^2)	**Design rule** [Evaluation of support for overhanging structures]	$\lim_{Ideal} \pi_{S_O} = 0$

Specific features of Bracket A and Connector D have been isolated in this case study to simplify the evaluation of certain metrics as well as to demonstrate the capability of the proposed method to enable metric or elementary features' and or parts' aggregation through vector representation. Specifically, for Bracket A, the big hole and the small holes have been evaluated separately. Similarly, for Connector D, the helix and holes were evaluated separately. For both parts, the choice to isolate specific features was drawn from design rules for AM [35]. The parts and metrics are combined to form matrix X (Table 6).

Matrix X is decomposed using SVD via a code generated in MATLAB. Before running the SVD decomposition, matrix X is normalized between [− 1, 1] with a maximum standard deviation of 1.

The normalized input matrix [X] is shown in Table 7.

The resulting decomposed matrixes [U], [W], and $[V]^T$ are presented in Eqs. 16, 17, and 18, respectively.

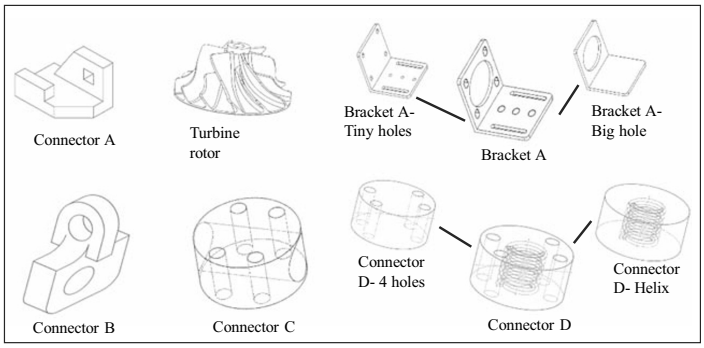

Fig. 6 Case study parts

$$[U] = \begin{bmatrix} -0.90 & -0.09 & -0.21 & -0.12 & -0.10 & 0.03 & -0.04 & -0.01 & -0.33 \\ 0.07 & 0.26 & -0.41 & 0.54 & 0.55 & 0.13 & -0.18 & 0.08 & -0.33 \\ 0.37 & -0.41 & -0.66 & -0.31 & -0.18 & -0.13 & 0.09 & 0.01 & -0.33 \\ 0.10 & 0.64 & -0.03 & 0.18 & -0.61 & -0.19 & 0.16 & -0.09 & -0.33 \\ 0.14 & 0.15 & 0.17 & -0.40 & 0.11 & 0.52 & -0.20 & -0.57 & -0.33 \\ 0.07 & 0.10 & 0.23 & -0.26 & 0.09 & 0.35 & 0.38 & 0.69 & -0.33 \\ 0.08 & 0.01 & 0.29 & -0.21 & 0.07 & -0.48 & -0.67 & 0.26 & -0.33 \\ -0.01 & -0.12 & 0.29 & 0.02 & 0.39 & -0.48 & 0.54 & -0.33 & -0.34 \\ 0.08 & -0.55 & 0.33 & 0.55 & -0.33 & 0.25 & -0.08 & -0.03 & -0.33 \end{bmatrix} \tag{16}$$

$$[W] = \begin{bmatrix} 2.47 & 0.00 & 0.00 & 0.00 & 0.00 & 0.00 & 0.00 & 0.00 & 0.00 \\ 0.00 & 1.47 & 0.00 & 0.00 & 0.00 & 0.00 & 0.00 & 0.00 & 0.00 \\ 0.00 & 0.00 & 1.34 & 0.00 & 0.00 & 0.00 & 0.00 & 0.00 & 0.00 \\ 0.00 & 0.00 & 0.00 & 0.97 & 0.00 & 0.00 & 0.00 & 0.00 & 0.00 \\ 0.00 & 0.00 & 0.00 & 0.00 & 0.85 & 0.00 & 0.00 & 0.00 & 0.00 \\ 0.00 & 0.00 & 0.00 & 0.00 & 0.00 & 0.47 & 0.00 & 0.00 & 0.00 \\ 0.00 & 0.00 & 0.00 & 0.00 & 0.00 & 0.00 & 0.24 & 0.00 & 0.00 \\ 0.00 & 0.00 & 0.00 & 0.00 & 0.00 & 0.00 & 0.00 & 0.20 & 0.00 \\ 0.00 & 0.00 & 0.00 & 0.00 & 0.00 & 0.00 & 0.00 & 0.00 & 0.00 \end{bmatrix} \tag{17}$$

$$[V]^T = \begin{bmatrix} -0.39 & -0.39 & -0.31 & -0.39 & 0.09 & 0.11 & 0.20 & -0.13 & -0.32 & 0.17 & 0.31 & 0.39 \\ -0.06 & -0.06 & 0.28 & -0.02 & 0.56 & -0.43 & -0.28 & 0.03 & -0.30 & -0.46 & 0.14 & 0.06 \\ -0.17 & -0.17 & 0.24 & -0.16 & 0.07 & 0.24 & 0.39 & 0.61 & 0.27 & -0.35 & -0.22 & 0.17 \\ -0.13 & -0.13 & 0.11 & -0.12 & 0.14 & 0.55 & -0.55 & -0.29 & 0.04 & -0.07 & -0.46 & 0.13 \\ -0.12 & -0.12 & 0.12 & -0.18 & -0.54 & -0.38 & 0.17 & -0.44 & 0.00 & -0.40 & -0.32 & 0.12 \\ 0.07 & 0.07 & 0.68 & 0.02 & -0.22 & 0.35 & 0.18 & -0.07 & -0.51 & 0.08 & 0.22 & -0.07 \\ -0.16 & -0.16 & 0.28 & -0.17 & -0.36 & -0.33 & -0.50 & 0.42 & 0.07 & 0.40 & 0.03 & 0.16 \\ -0.08 & -0.07 & 0.45 & -0.06 & 0.36 & -0.15 & 0.25 & -0.38 & 0.52 & 0.39 & 0.05 & 0.08 \\ 0.41 & 0.41 & 0.01 & -0.43 & -0.08 & 0.11 & -0.14 & -0.05 & 0.25 & -0.20 & 0.37 & -0.41 \end{bmatrix} \tag{18}$$

Table 6 Input matrix [*X*] with metric values for ideal part/technology and evaluated parts

	Metric 1 (π_V)	Metric 2 (π_{Vn})	Metric 3 (π_{tB})	Metric 4 (π_{RIH})	Metric 5 (π_{RIH})	Metric 6 (π_{RV})	Metric 7 (π_L)	Metric 8 (π_S)	Metric 9 (π_{DS})	Metric 10 (π_{VT})	Metric 11 (π_{ST})	Metric 12 (π_{SO})
Ideal part for PBF	1	1000	1	10,000	0	0	0	2	1	1	0	0
Connector A	0.9	4.5	0.85	100	0.9	0.01	0	0	0	1	0.15	1
Turbine rotor	0.9	2.7	0.6	0	0	0.02	0.7	0.5	0	1.4	0.4	1
Bracket A (big holes)	0.9	3.6	0.85	900	3.4	0.01	0	2	0	1	0.3	1
Bracket A (tiny holes)	0.9	3.6	0.85	90	0.8	0.01	1	2	0	1	0.3	1
Connector B	0.9	6.3	0.9	150	0.9	0.01	0.9	2	0.3	1.05	0.25	1
Connector C	0.9	5.4	0.78	300	1.2	0.015	1	2	0.5	1	0.2	1
Connector D (4 holes)	0.9	5.4	0.81	40	0	0.015	0.7	2	0.6	1	0.1	1
Connector D (helix)	0.9	5.4	0.8	40	0.22	0.08	0.7	2	0.6	1.2	0.1	1

Several important observations can be made. First, in matrix [*W*] (Eq. 17), the singular values are ranked diagonally in descending order. As a result, the initial matrix [*X*] can be reconstructed by considering only the rows and columns in bold from matrices [*U*], [*W*], and $[V]^T$ in Eqs. 16, 17, and 18, respectively. This means that a complete dataset can be reconstructed with a reduced format of the product of the matrices [*U*], [*W*], and $[V]^T$. For the bolded products in Eqs. 16, 17, 18, the average summed error generated by this reconstruction for [*X*] for the columns (metrics) is 6.66% and for the rows (evaluated parts) is 0.60%. When the number of retained singular values from matrix [*W*] is four, the average summed error drops to 2.66% for the columns and 0.16% for the rows. This important property is used in this paper to represent the position of the parts and metrics in a reduced model. This is explained in Section 3. For the demonstration case herein, two singular values were retained to obtain a reduced model.

The decomposed matrices in Eqs. 16, 17, and 18 are processed to form two sub-products between the three matrices ([*U*], [*W*], and $[V]^T$). The product matrices, [*U*].[*W*] and [*W*].$[V]^T$, are shown in Table 8 and Table 9, respectively. Those two products are fundamental for representing the parts and metrics in a graphical space.

In Tables 8 and 9, the shaded rows and columns represent the vectors of the two retained singular values. In Table 8, each shaded row represents the specific vector of each single part considered in the model. In Table 9, each shaded column represents the specific vector of each metric. The parts and metrics evaluated can also be presented as a 2D graph (Fig. 7) representing the two main axes of the reduced model. In Fig. 7, the ideal part for LPBF serves as a reference for guiding the evaluation of part manufacturability/printability using the technology. From Fig. 7, it can be seen that Connector D with four (4) holes only is closest to the ideal part and, hence, would be the easiest to manufacture using LPBF when compared with the other evaluated parts. In addition, consolidation of parts to form sub-assemblies is investigated by combining two vectors (Connector B + Connector D). Here, the consolidated sub-assembly is evaluated by combining the metric

Table 7 Input matrix [*X*] with normalized metric values for ideal part/technology and evaluated parts

	Metric 1 (π_V)	Metric 2 (π_{Vn})	Metric 3 (π_{tB})	Metric 4 (π_{RIH})	Metric 5 (π_{RIH})	Metric 6 (π_{RV})	Metric 7 (π_L)	Metric 8 (π_S)	Metric 9 (π_{DS})	Metric 10 (π_{VT})	Metric 11 (π_{ST})	Metric 12 (π_{SO})
Ideal part for PBF	0.943	0.943	0.573	0.939	−0.272	−0.284	−0.453	0.176	0.648	−0.183	−0.566	−0.943
Connector A	0.118	−0.118	0.077	−0.128	0.025	−0.133	−0.453	−0.729	−0.324	−0.183	−0.141	0.118
Turbine rotor	−0.118	−0.120	−0.749	−0.139	−0.272	0.017	0.118	−0.503	−0.324	0.831	0.566	0.118
Bracket A (big holes)	−0.118	−0.119	0.077	−0.042	0.850	−0.133	−0.453	0.176	−0.324	−0.183	0.283	0.118
Bracket A (tiny holes)	−0.118	−0.119	0.077	−0.130	−0.008	−0.133	0.363	0.176	−0.324	−0.183	0.283	0.118
Connector B	−0.118	−0.116	0.242	−0.123	0.025	−0.133	0.281	0.176	−0.032	−0.056	0.141	0.118
Connector C	−0.118	−0.117	−0.154	−0.107	0.124	−0.058	0.363	0.176	0.162	−0.183	0.000	0.118
Connector D (4 holes)	−0.118	−0.117	−0.055	−0.135	−0.272	−0.058	0.118	0.176	0.259	−0.183	−0.283	0.118
Connector D (helix)	−0.118	−0.117	−0.088	−0.135	−0.199	0.917	0.118	0.176	0.259	0.324	−0.283	0.118

Table 8 Product $[U].[W]$ with the two singular values of the reduced model in shaded columns

Ideal part for PBF	-2.22	-0.13	-0.28	-0.11	-0.08	0.01	-0.01	0.00	0.00
Connector A	0.18	0.39	-0.54	0.52	0.47	0.06	-0.04	0.02	0.00
Turbine rotor	0.91	-0.60	-0.88	-0.30	-0.16	-0.06	0.02	0.00	0.00
Bracket A (big hole)	0.24	0.94	-0.04	0.18	-0.52	-0.09	0.04	-0.02	0.00
Bracket A (small holes)	0.36	0.23	0.23	-0.38	0.10	0.24	-0.05	-0.12	0.00
Connector B	0.17	0.15	0.30	-0.25	0.08	0.16	0.09	0.14	0.00
Connector C	0.20	0.02	0.39	-0.20	0.06	-0.23	-0.16	0.05	0.00
Connector D (4 holes)	-0.03	-0.18	0.38	0.02	0.33	-0.23	0.13	-0.07	0.00
Connector D (helix)	0.19	-0.80	0.43	0.53	-0.28	0.12	-0.02	-0.01	0.00

values of the individual components through simple vector addition. Additionally, consolidation of metrics can also be performed in a similar fashion.

Next, the Euclidean distances between the ideal part and the assessed parts are computed, and the parts are ranked on their manufacturability (Fig. 8). It is important to note that the ranking is dependent on the number of singular values considered, as shown in Fig. 8. The results of the case study are discussed further in Section 5.

5 Results and discussion

The methodology proposed in this article was demonstrated for ranking a set of parts on their manufacturability using laser powder bed fusion (LPBF) technology. The ranking was carried out for individual parts and a consolidated sub-assembly of two components. The computed ranking of the initial parts and aggregated features and parts were respectively validated graphically (Fig. 7) and using the Euclidean distance for two singular values. The blue-, green-, and orange-shaded ranking scales in Fig. 8 show the ranking when the features of Bracket A (big hole and small holes) and Connector D (4 holes and helix) have been evaluated individually. The ranking is updated when the two features of Bracket A and Connector D are combined. In addition, a consolidated part (Connector B + Connector D) represented as a sub-assembly is added to the evaluation. The updated ranking with feature aggregation and part consolidation is shown in the bottom, gray-shaded ranking scale in Fig. 8.

The Euclidean distance-based approach provided a ranking consistent with the visual evaluation presented in Fig. 7, where Connector D appears closer to the ideal part for LPBF. Cosine similarity-based ranking was also evaluated and presented for comparison. The ranking was updated by considering the combined/aggregated features, which

Table 9 Product $[W].[V]^T$ with the two singular values of the reduced model in shaded rows

Metric 1 (π_V)	Metric 2 (π_{Vn})	Metric 3 (π_{tB})	Metric 4 (π_{RIH})	Metric 5 (π_{RIH})	Metric 6 (π_{RV})	Metric 7 (π_L)	Metric 8 (π_S)	Metric 9 (π_{DS})	Metric 10 (π_{VT})	Metric 11 (π_{ST})	Metric 12 (π_{SO})
-0.96	-0.96	-0.77	-0.95	0.23	0.28	0.48	-0.32	-0.78	0.42	0.77	0.96
-0.09	-0.09	0.41	-0.03	0.83	-0.63	-0.41	0.04	-0.44	-0.68	0.21	0.09
-0.22	-0.22	0.32	-0.22	0.10	0.32	0.52	0.82	0.36	-0.47	-0.30	0.22
-0.13	-0.13	0.11	-0.12	0.14	0.53	-0.53	-0.28	0.04	-0.07	-0.44	0.13
-0.10	-0.10	0.11	-0.15	-0.46	-0.32	0.15	-0.37	0.00	-0.34	-0.27	0.10
0.03	0.03	0.32	0.01	-0.10	0.16	0.08	-0.03	-0.24	0.04	0.10	-0.03
-0.04	-0.04	0.07	-0.04	-0.09	-0.08	-0.12	0.10	0.02	0.10	0.01	0.04
-0.02	-0.01	0.09	-0.01	0.07	-0.03	0.05	-0.08	0.11	0.08	0.01	0.02
0.00	0.00	0.00	0.00	0.00	0.00	0.00	0.00	0.00	0.00	0.00	0.00

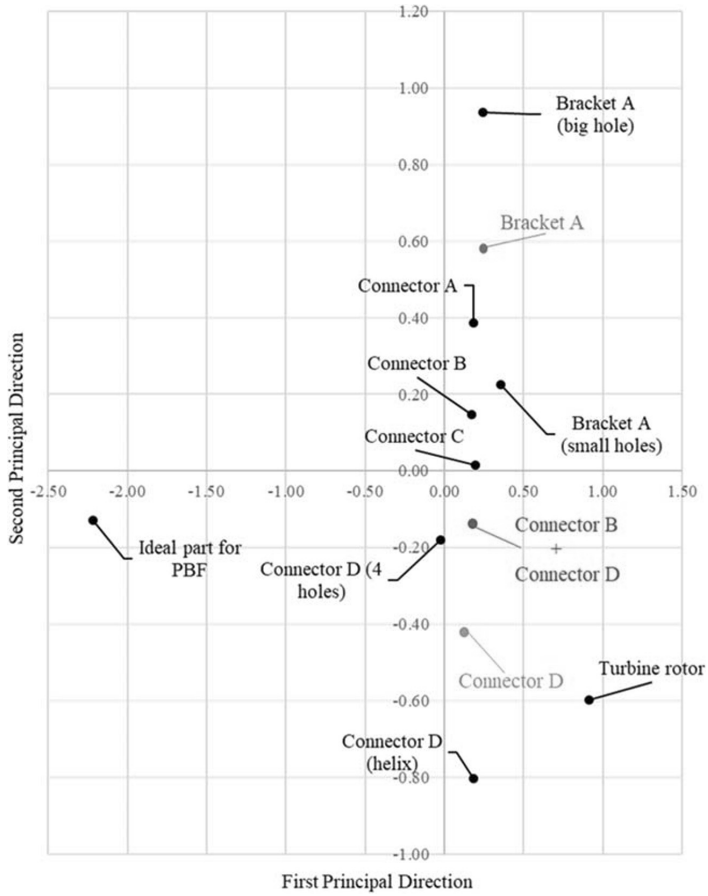

Fig. 7 2D graphical representation of evaluated parts based on computed distances using Euclidean distance measurement (green, red, and blue dots result from aggregation of features and/or parts)

demonstrate how vector representation of the features enables the user to both isolate different features in a part and to compose different features of a part together based on necessity. The combination of features also implies that the individual parts can be combined into sub-assemblies. For example, the sub-assembly (Connector B + Connector D) used in this case study followed the same principle and illustrates the potential to consolidate different parts together to improve the manufacturability for a specific manufacturing process technology. It can be seen that Bracket A (big hole) had an initial ranking (green-shaded scale) of seven and Bracket A (small hole) was ranked sixth (Fig. 8). By virtue of the proposed approach, it was possible to evaluate the effect of combining the two features together (Bracket A) and to compute the resulting ranking of the aggregate features (see Figs. 7 and 8).

As noted above, an important factor in the manufacturability ranking is the number of singular values selected. The global ranking changed for Connectors A, B, C, and D when three singular values were chosen instead of two (Fig. 8). Thus, any model reduction efforts must consider two factors: the average error generated by the reconstruction of a reduced model and the variation in the ranking based on the number of singular values considered.

Another interesting observation is that some metrics appear in clusters when represented in a 2D graph (Fig. 9). For example, Metric 1 (individual part production rate), Metric 2 (batch production rate), and Metric 4 (the need for internal support structures) form a cluster. It is interesting to note that Metric 1 and 2 relate to production time but not initially Metric 4. In addition, Metric 6 (minimum feasible vertical hole size), Metric 7 (difficulty of depowdering), and Metric 10 (internal lattice structures) each indicate part complexity and form a cluster. Metrics 11 and 12, design rules relating to ease of clamping and presence of overhanging features, respectively, appear to be somewhat correlated.

Currently, no specific clustering method has been used here, but methods such as *k*-means could be employed in future studies to further examine clustering and drivers of correlation that can better inform designers and process planners. Metrics clustered together imply the concept of

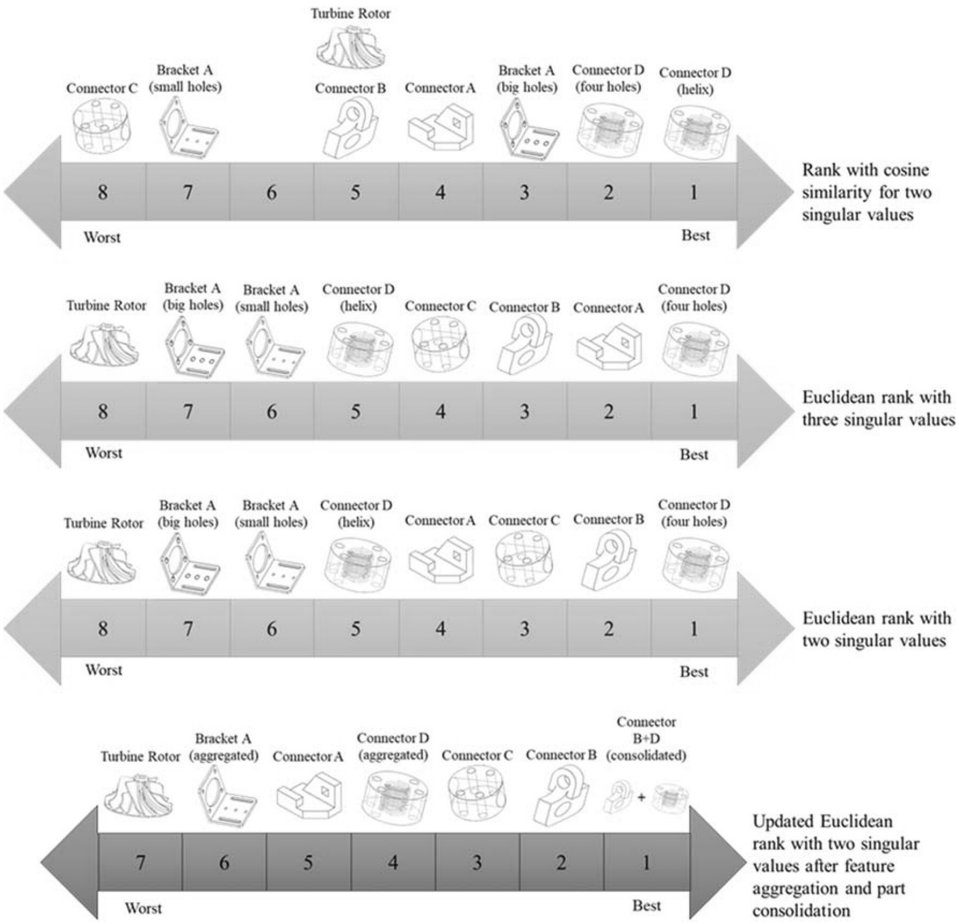

Fig. 8 Ranking of alternatives using cosine similarity and Euclidean distance for different number of singular values

similarity. Hence, metrics initially developed to characterize a specific feature(s) can assist in evaluating other features. For example, Metric 4, initially designed to assess internal support structures that would require additional post-processing, is closely related to Metrics 1 and 2, which are used to evaluate the production rate. Metric 4 combines part and machine properties, while Metric 1 is specifically composed of machine properties. Metric 2 includes the projected surface of parts and combines part and machine properties. The part and machine-related properties considered in the development of the metrics affect the level of closeness of different metrics despite their differences in objectives. Nevertheless, the 2D visualizations in Figs. 7 and 9 represent the design space that enables the combination of metrics and parts to explore and exploit the design space. Using Fig. 9, it can be envisioned that new metrics can be automatically generated to evaluate parts in the design and manufacturing space. This approach to automated metric generation opens opportunities for future research, including the potential creation of new ML approaches for product design and production planning.

6 Conclusions

This research presents a novel and systematic framework based on functional modeling and dimensional analysis theory for the development of parsimonious metrics as descriptors of functions. In addition, the developed metrics are utilized in a mathematical mechanism for evaluating part manufacturability using singular value decomposition. The metrics, developed as part of this study based on key performance indicators and independent variables, allow for evaluation of design features, production types, and product cost. The developed metrics are scale and composition invariant by virtue of the power law form (i.e., Pi number), which enable the computation of the

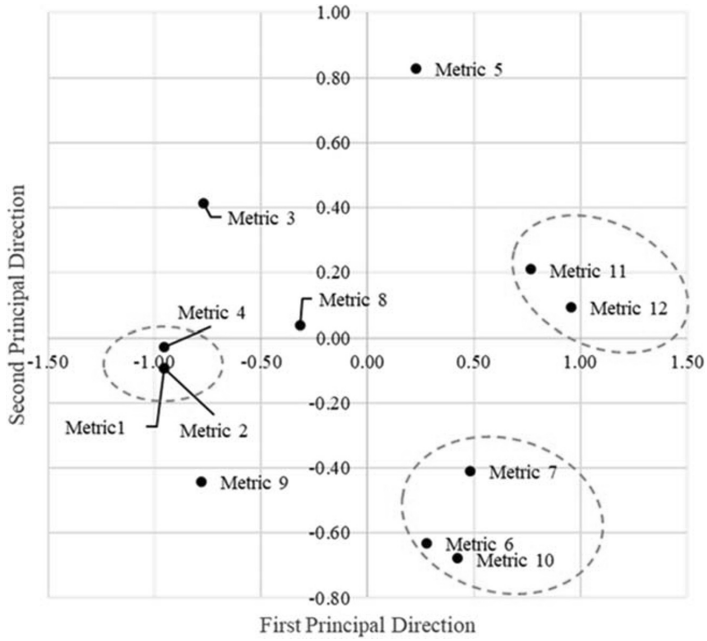

Fig. 9 2D graphical representation of metrics based on computed distances using Euclidean distance measurement (clusters represented as dotted ovals)

Euclidean distance to facilitate the ranking of various part designs based on their ease of manufacturability for different production technologies and part dimensions. The proposed approach improves upon the existing limitations of DAT with the help of the DACM framework to promote a systematic approach for the selection of performance and repeating variables during the development of dimensionless metrics. The combination of functional modeling, DAT, and SVD for the purpose of part manufacturability evaluation has not been considered in the existing literature. The methodology reported herein provides a novel approach to automate product design evaluations and provide feedback to designers during process selection. Readers should keep in mind that automation of the evaluation process is fundamental in this work, which is a key novelty compared with manual (heuristic) guidelines proposed in DfAM methods.

The proposed method evaluates part designs for their "fit" for a variety of potential manufacturing process technologies through the evaluation of their manufacturability with respect to a reference (ideal) part for each process type. The ideal part is developed based on a set of metrics that define the unique attributes of the process. The method developed here and demonstrated for additive manufacturing has the potential to be extended to also consider consolidation of features and parts via the basic mechanisms presented for metric aggregation, i.e., SVD decomposition and the representation of features via vectors of metrics. Part aggregation also requires consideration of multiple other aspects, such as sub-assembly structure, mechanical interface, and the feasibility of assembling the parts in an aggregated sub-assembly. These considerations are not presented herein and form the basis for future work to extend the application of the basic principles and computational approach presented in this article. The principles presented are highly flexible and facilitate feature/part composability and metric ranking. These aspects of the approach have been demonstrated here, together with a concrete implementation of the concept of ideality from TRIZ, which was used in this research for representing the fit of a part for a given manufacturing process technology.

The developed method enables isolated evaluation of individual features comprised in a part but also allows for combining features or parts for aggregate evaluation of complex parts and sub-assemblies. Thus, the method promotes design for manufacturing and assembly through its ability to separate or combine features and parts and perform evaluation of both individual and aggregated features/parts. In addition, the graphical representation of the design space can enable design space exploration to find new combinations of parts and/or new metrics to aid design and manufacturing analysis. An element not studied in this work is the use of the approach as a prediction tool, wherein SVD allows for the computation of metric values for new parts when information about certain metrics are already known. This last element will drive future research efforts for assisting engineers by providing them with emergent design and process

knowledge during product design and process planning, for example, through the use of ML techniques.

References

1. Bandyopadhyay A, Bose S (2019) Additive manufacturing. CRC press publisher, Boca Raton, pp 389
2. Pradel P, Zhu Z, Bibb R, Moultrie J (2018) A framework for mapping design for additive manufacturing knowledge for industrial and product design. J Eng Des 29(6):291–326
3. François M, Segonds F, Rivette M, Turpault S, Peyre P (2019) Design for additive manufacturing (DfAM) methodologies: a proposal to foster the design of microwave waveguide components. Virtual Phys Prototyp 14(2):175–187
4. Yang S, Page T, Zhang Y, Zhao YF (2020) Towards an automated decision support system for the identification of additive manufacturing part candidates. J Intell Manuf. https://doi.org/10.1007/s10845-020-01545-6
5. Felsberger A, Oberegger B, Reiner G (2016) A review of decision support systems for manufacturing systems presented at the SAMI@ iKNOW.
6. Li C, Ren J, Wang H (2016) A system dynamics simulation model of chemical supply chain transportation risk management systems. Comput Chem Eng 89:71–83
7. Hilletofth P, Hilmola O-P, Wang Y, Rouzafzoon J, Helo P (2016) Developing service supply chains by using agent based simulation. Industrial Management & Data Systems
8. Zhang F, Johnson D, Johnson M, Watkins D, Froese R, Wang J (2016) Decision support system integrating GIS with simulation and optimisation for a biofuel supply chain. Renew Energy 85:740–748
9. Power DJ (2001) Supporting decision-makers: an expanded framework. Proceedings of informing science and IT education. pp 1901–1915
10. Chaudhuri S, Dayal U, Narasayya V (2011) An overview of business intelligence technology. Commun ACM 54(8):88–98
11. Pillai DD (1990) Developing a decision support system for optimizing automated wafer fabrication. IEEE Trans Components Hybrids Manuf Technol 13(1):94–102
12. Berman JJ (2013) Principles of big data: preparing, sharing, and analyzing complex information. Morgan Kaufmann Publishers, Burlington
13. Kaisler S, Armour F, Espinosa JA, Money W (2013) Big data: issues and challenges moving forward, presented at the 2013 46th Hawaii International Conference on System Sciences, pp 995–1004
14. Mayer-Schönberger V, Cukier K (2013) Big data: a revolution that will transform how we live, work, and think. Houghton Mifflin Harcourt Publisher, New York
15. Zhang L (2014) A framework to model big data driven complex cyber physical control systems, presented at the 2014 20th International Conference on Automation and Computing. pp 283–288
16. Lovatt AM, Shercliff HR (Dec. 1998) Manufacturing process selection in engineering design. Part 1: the role of process selection. Mater Des 19(5–6):205–215. https://doi.org/10.1016/S0261-3069(98)00038-7
17. Wang Y, Zhong RY, Xu X (2018) A decision support system for additive manufacturing process selection using a hybrid multiple criteria decision-making method. Rapid Prototyp J 58:145–157. https://doi.org/10.1016/j.rcim.2019.03.003
18. Majeed A, Lv J, Peng T (2019) A framework for big data driven process analysis and optimization for additive manufacturing. Rapid Prototyp J 25(2):308–321. https://doi.org/10.1108/RPJ-04-2017-0075
19. Nilsson J (2019) System of systems interoperability machine learning model
20. Borutzky W (2011) Bond graph modelling of engineering systems: Theory, Applications and Software Support, Edition 1, Springer Publisher
21. Shim T (2002) Introduction to physical system modelling using bond graphs
22. Coatanéa E (2005) Conceptual modelling of life cycle design: a modelling and evaluation method based on analogies and dimensionless numbers. Helsinki University of Technology
23. Andreasen MM, Howard TJ, Bruun HPL (2014) Domain theory, its models and concepts. In: Chakrabarti A, Blessing LTM (eds) An anthology of theories and models of design. Springer London, London, pp 173–195
24. Pahl G, Beitz W, Feldhusen J, Grote K-H (2007) Engineering Design: A Systematic Approach, Springer Publisher, New York
25. Hundal M, Byrne J (1990) Computer-aided generation of function block diagrams in a methodical design procedure, Proc of Design Theory and Methodology-DTM. vol. 91, pp 251–257
26. Stone RB, Wood KL (2000) Development of a functional basis for design. J Mech Des 122(4):359–370. https://doi.org/10.1115/1.1289637
27. Altshuller G (2002) 40 principles: TRIZ keys to innovation, vol 1. Technical Innovation Center Publisher, Hagerstown
28. Bridgman P (1922) Dimensional analysis. Philos Mag 2(12):1263–1266
29. Li X, Sudarsanam N, Frey DD (2006) Regularities in data from factorial experiments. Complexity 11(5):32–45. https://doi.org/10.1002/cplx.20123
30. Kretzschmar N, Ituarte IF, Partanen J (2018) A decision support system for the validation of metal powder bed-based additive manufacturing applications. Int J Adv Manuf Technol 96(9–12):3679–3690
31. Szirtes T (2007) Applied dimensional analysis and modeling. Second Edition, Butterworth-Heinemann Publishers, Oxford
32. Mandel J (1982) Use of the singular value decomposition in regression analysis. Am Stat 36(1):15–24
33. Krus P (2016) Models based on singular value decomposition for aircraft design, presented at the FT2016-Aerospace Technology Congress
34. Zimmer D, Adam G (2011) Direct manufacturing design rules, Innovative Developments in Virtual and Physical Prototyping. pp 545–551.
35. Bäßler R (2018) Additive manufacturing of metals–from fundamental technology to rocket nozzles, medical implants, and custom jewelry (book review)

PUBLICATION IV

Probabilistic Modelling of Defects in Additive Manufacturing: A Case Study in Powder Bed Fusion Technology

Hossein Mokhtarian, Azarakhsh Hamedi, Hari P.N. Nagarajan, Suraj Panicker, Eric Coatanéa, and Karl R. Haapala

Procedia CIRP, vol. 81 (2019)
https://doi.org/10.1016/j.procir.2019.03.234

Available online at www.sciencedirect.com

ScienceDirect

Procedia CIRP 81 (2019) 956–961

www.elsevier.com/locate/procedia

52nd CIRP Conference on Manufacturing Systems

Probabilistic Modelling of Defects in Additive Manufacturing: A Case Study in Powder Bed Fusion Technology

Hossein Mokhtarian[a,b,*], Azarakhsh Hamedi[a], Hari P.N. Nagarajan[a], Suraj Panicker[a], Eric Coatanéa[a], Karl Haapala[c]

[a] *Automation Technology and Mechanical Engineering, Tampere University, Finland*
[b] *University Grenoble Alpes, CNRS, G-SCOP Laboratory, Grenoble, France*
[c] *School of Mechanical, Industrial, and Manufacturing Engineering, Oregon State University, Corvallis, Oregon, USA*

* Corresponding author. Tel.: +358-449711254; E-mail address: hossein.mokhtarian@tuni.fi

Abstract

Implementation of additive manufacturing into product manufacturing suffers from the challenge of part defects prediction. Due to interdependencies of design variables and manufacturing parameters in achieving suitable part quality, modelling methods are necessary to provide simulation capabilities for part quality analysis at early stages of product development. A systematic methodology is proposed to extract cause-effect relationships among variables and to transform this causal model into a Bayesian network. The Bayesian network is then used to predict the effect of specific design and manufacturing parameters on part defects and to estimate the needed input parameters backwards, based on acceptable output values.

Keywords: additive manufacturing; powder bed fusion; probabilistic modeling; bayesian network; dimensional analysis conceptual modeling framework

1. Introduction

Additive manufacturing (AM) processes have transitioned from production of prototypes to functional products, serving various industries, such as automotive, aerospace, machinery, electronics, and medical. Specifically, AM of metal products has seen increased adoption as industrial production systems due to the steady decline in the price of machines and materials [1]. However, AM products have been riddled with defects due to the lack of process knowledge and control systems. In addition, the lack of interoperability in machines has made it difficult to create models that can reduce variations in properties and quality across materials and machine types [2]. Thus, product and process qualification efforts are required to improve product quality and meet industry standards. Part-by-part evaluations are time intensive and new research must focus on creating alternatives to existing conventional qualification methods with the use of validated models and probabilistic methods [3].

AM product quality largely depends on the interactions between design geometry, AM technology, and AM specific process parameters. Metal AM processes, such as laser sintering, function as a multi-parameter dependent process, which require an understanding of the process physics to control variations in final product [4]. In selective laser sintering, a laser beam scans over metal powders, melting and forming layers [4]. However, the lack of high-fidelity models for AM processes results in users choosing parameters based on experimental data collection and expertise. Hence, a non-homogenous temperature gradient is often created, which can lead to spheroidization of the liquid melt pool and residual stress formation, causing cracking, warping, and curling defects in the part [5]. These geometric defects are unavoidable without the use of proper process tuning and control strategies.

10.1016/j.procir.2019.03.234

To help prevent such defects, in-situ monitoring and control systems have been proposed in literature [6], [7]. An increase in the number of control variables is required due to the multi-parameter-dependent nature of powder bed AM.

Toward this end, efforts must be focused on early design stage modeling techniques that can evaluate the interactions between geometry and process parameters early in the design process and aid in informed decision making during process parameter tuning. Such models can help fix high-latency variables in the system at values that minimize their impact on product quality, eliminating the need to control them. Towards that goal, a probabilistic modeling method using Bayesian networks is proposed to model defects in AM parts during laser sintering. The developed model characterizes the effect of geometric and manufacturing parameters on part geometry defects. This model will help designers and manufacturers evaluate the probability of occurrence and the magnitude of defects during manufacturing and support effective tuning of parameters to reduce or eliminate such defects. The method is demonstrated for a case study to model the curling defect in an L-shaped block made of titanium alloy, Ti-6Al-4V, using laser sintering.

The remainder of the manuscript is organized as follows. Section 2 provides a background on defect modeling in laser sintering. Section 3 describes the methodology for the additive manufacturing case study. Section 4 discusses the results of the simulation using the developed Bayesian network for the case study. Section 5 presents the conclusions.

2. Background

Defect modeling for laser powder-bed AM processes is necessary to enable simulations, improve product quality, and eliminate or reduce reject/waste. In laser AM, the temperature-rich environment can result in thermal residual stress formation, leading to geometric errors such as distortion, warping, curing, and spalling. These geometric errors can cause unfinished products and premature failure of product [8].

Research in AM defect modeling has investigated several ways to reduce thermally-induced residual stress and its associated geometric tolerance losses. Vasinota et al. [9] performed thermomechanical modeling and simulation of the laser engineered net shaping process with the help of process maps. They found that uniform preheating of the base plate could reduce residual stresses and achieve optimum melt pool length. Similar research have verified that preheating of the base plate is one of most effective means to reducing residual stresses in AM [10], [11]. In addition to preheating, research has focused on optimizing scan patterns and weld deposition paths to reduce residual stress and deflection. Pohl et al. [5] investigated the effect of processing conditions and material on thermal stresses and part deflection during laser sintering. They found that density or strength of laser-sintered products might contradict the goal of reduced thermal stresses. They also found that different scanning patterns, especially direction of line scan and short raster pattern could reduce deflections in the product.

Nickel et al. [12] investigated the effect of deposition patterns on deflection of the part using finite element modeling. Their study showed that deposition patterns had a significant effect on dimensional quality of the part. They found raster patterns with lines perpendicular to the laser beam's long axis yielded low deflections in the part. More recent research has focused on building support structures to prevent residual stress-induced curling and distortion. Calignano [13] investigated the use of supports for overhang features in selective laser sintering. He posited that additional support is required for overhang features to reduce geometric distortions. However, he suggested that it is necessary to use minimal support structure to obtain the best trade-off between time, cost, and accuracy of production.

Cheng and Chou [14] also investigated overhang support patterns to reduce deformation of overhang parts. They developed a thermomechanical model to simulate deformation in overhang structures in electron beam melting. They found that solid support columns could reduce overhang defect. They also reinforced the notion that a trade-off must be met between reducing deformations and reducing the amount of support materials used to maintain low production costs. In the research presented herein, the use of supports and the effect of support geometry on part deformation is evaluated using a Bayesian network model.

3. Case Study and Methodology

Curling is a recurring defect in laser-based metal AM. It predominantly occurs on overhang surfaces that are not supported by enough material from previous layers. Excessive heat energy input (overheating) leads to a cumulative thermal constraint on the part being processed, resulting in an upward deflection of overhanging features. Suppressing the curling defect entails exploring the design space among parameters related to part geometry, part orientation, support structure, and manufacturing process parameters.

The case study presented here aims at developing a probabilistic model to explore the design space of an L-shaped geometry and to characterize the effect of design parameters on the curling defect during early design stage. The case study follows the workflow shown in Fig. 1. The generic workflow includes three main stages: 1) using the dimensional analysis conceptual modeling (DACM) framework to generate a causal graph of the phenomenon and the associated governing equations, 2) translating the causal graph into directed acyclic graphs (DAGs) for Bayesian network model development, and 3) probabilistic modeling of the curling defect in BayesiaLab software. These stages proceed through five steps, as discussed below.

Step 1: The aim of DACM modeling stage is to extract causal rules and establish governing equations among the variables in the problem using the DACM framework [15], [16]. The problem is evaluated from a functional perspective; a systematic approach to extract causal rules and establish governing equations from a functional model is followed. Fig. 2 shows a functional model where the design space is divided into three domains: cyclic functions of the AM process, useful functions of the support structure, and non-desired functions. The support structure comprises two main functions: the function 'to dissipate' heat energy, similar to a heat sink, and

the function ‘to increase inertia’. Heat energy dissipation is defined here by cooling rate (CR), which depends on the geometry of the support and heat transfer variables. Inertia depends on the geometry of the supports and material density. The non-desired functions of the supports characterize the generation of a thermal constraint that results in the bending moment and the function ‘to resist’ the deflection.

Step 2: Once the functional model is established and variables characterizing those functions are assigned, the algorithms developed in DACM lead to systematic extraction of the cause-effect relationships between the variables and to establishing behavioral laws using dimensional analysis (DA) principles. Fig. 3 represents the extracted causal rules between the variables (nodes) in the form of a causal graph, where independent design variables are shown in green, exogenous variables are shown in gray, and performance variables are shown in red. DA uses cause-effect relationships in the form of (1, as well as dimensions of variables to provide the mathematical relationship among variables in the form of (2, where $\{x_{i1}, x_{i2}, \dots, x_{in}\}$ are the influencing (cause) variables, y_i is the performance (effect) variable, and $\{\alpha_{ij} \mid 1 \le j \le n\}$ are the exponents of the variables. DA seeks for finding suitable exponents for the variables to respect the dimensional homogeneity principle [17].

$$y_i = f\left(x_{i1}, x_{i2}, \dots, x_{ij}\right) \quad 1 \le j \le n \tag{1}$$

$$\pi_{y_i} = y_i . x_{i1}^{\alpha_{i1}} . x_{i2}^{\alpha_{i2}} \dots . x_{ij}^{\alpha_{ij}} \tag{2}$$

The DACM framework also enables integration of existing equations directly to the functional model and causal graph. (3 approximates the temperature difference between layers as a function of heating rate (HR), cooling rate (CR), part geometry variables (W, L, and b), and process parameters (d_l, l_t, v, and t_w).

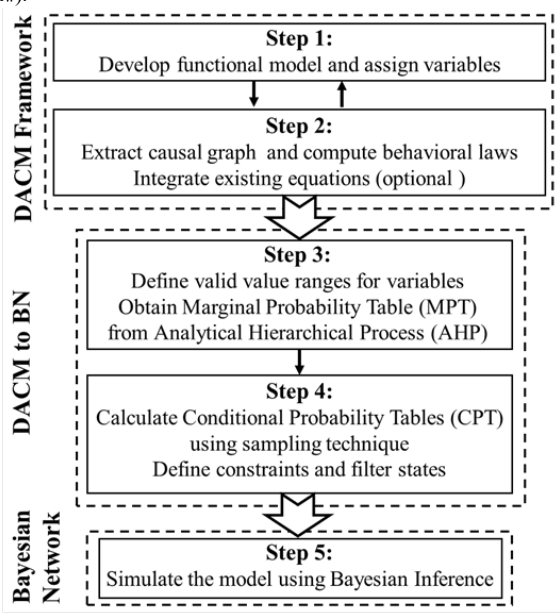

Fig. 1. Methodology workflow.

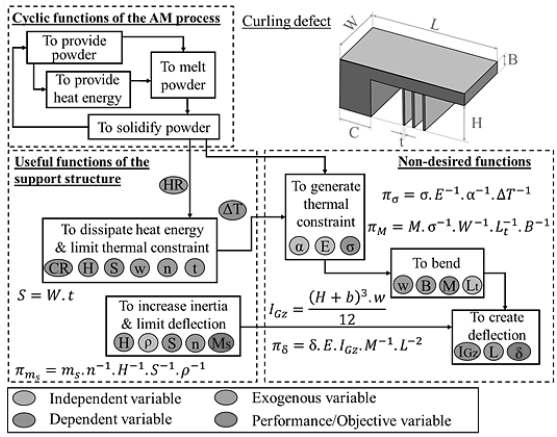

Fig. 2. Functional model for curling defect using DACM Framework.

The equations associated with the functional model shown in Fig. 2 are listed in (3 through (7.

$$\Delta T = \left(\frac{L.W.b}{d_l.l_t.v}\right)\left(HR - CR\right) - \left(\frac{b.t_w}{l_t}\right)\left(CR\right) \tag{3}$$

$$\pi_\sigma = \sigma.E^{-1}.\alpha^{-1}.\Delta T^{-1} \tag{4}$$

$$\pi_M = M.\sigma^{-1}.w^{-1}.L_t^{-1}.b^{-1} \tag{5}$$

$$\pi_\delta = \delta.E.I_{Gz}.M^{-1}.L^{-2} \tag{6}$$

$$\pi_{m_s} = m_s.n^{-1}.H^{-1}.S^{-1}.\rho^{-1} \tag{7}$$

Step 3: This step defines the valid value ranges for the independent variables of the functional model. These ranges are then divided into several intervals, or states. For providing marginal probability tables (MPT) to each interval of the independent variables, it is possible either to assign a random probability of occurrence to each variable interval or to integrate expert knowledge and preferences [18].

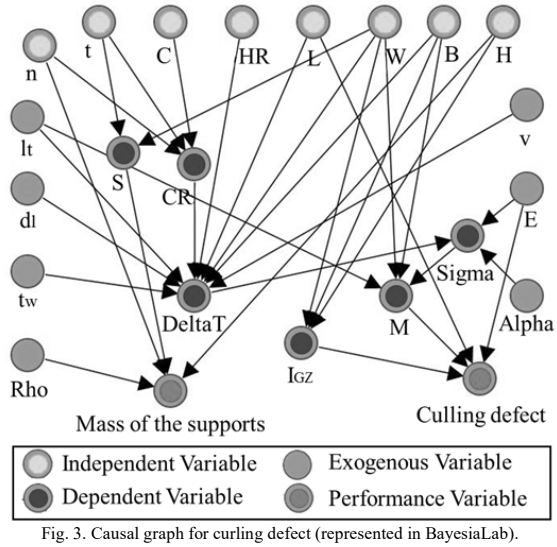

Fig. 3. Causal graph for curling defect (represented in BayesiaLab).

In this study, the analytical hierarchy process (AHP) is used to capture experts' knowledge and preferences in the Bayesian network model [19]. AHP is an efficient tool to deal with complex decision-making problems involving multiple experts and comparisons, since it reduces the complexity of a decision to a series of pairwise comparisons. In this study, experts answered a series of questions by filling AHP tables associated to the required comparisons. The aim was to capture the experts' preferences over different intervals for each independent variable. To enhance this process, AHP tables were transformed into a series of questions. For instance, supposing four intervals (i=4) were defined for the number of supports (n), the questions would be formulated to capture expert preferences over the intervals two-by-two (e.g., interval 1 vs. interval 2), as follows: 'Considering all conditions for printing a desired part, what is your preference of interval 1 compared to interval 2?' The questions were repeated ((i^2-i)/2) times to obtain two-by-two comparisons of all intervals for all independent variables.

Once all preferences were captured from pairwise comparisons, AHP was used to generate a weight for each interval, in a way that the sum of all individual interval weights is equal to one. Hence, the weights generated by AHP are equivalent to the probability of selection of that interval by experts. The process of capturing experts' preferences continues to cover all independent variables. Table 1 provides the list of variables of the case study with their associated units, ranges of values, marginal probabilities, and equations.

Step 4: The causal graph extracted by DACM is a directed acyclic graph (DAG) as an initial Bayesian network prerequisite. However, a few systematic modifications need to be carried out to adapt the DACM causal graph to the Bayesian network model.

First, exogenous variables have a fixed value and do not vary in the system. Therefore, they should be removed from the causal graph. The effect of exogenous variables is not eliminated from the model, since they are considered in the equations as constants. The second modification involves defining the constraints and filter state among variables, which is necessary to avoid impossible combinations of values for independent variables and also to limit the design space. Constraints are defined between parent nodes, and filter states are used as an interval/state within child nodes. The geometric parameters in the case study have been limited using constraints in terms of ratio to avoid the simulation of undesirable geometries. Table 2 represents the acceptable ranges for the design parameters for this case study.

Once the MPTs are established for the independent variables, conditional probability tables (CPTs) are then populated using a sampling technique. The sampling technique starts with calculating the range for the child nodes based on the maximum and minimum value of the parents and the governing equations. The range of values for CPT is then divided into several intervals. The sampling technique continues by taking a number of samples from the parent nodes. The process uses the governing equations for each interval in parent node(s) to calculate the corresponding value in the child node(s). Finally, filtering the impossible values for each child node is essential to avoid propagation of error in the network.

Table 1. List of case study variables with range of values and equations.

Variable (Symbol)	Unit	(Range of values)/Equations **Marginal Probability (%)**		
Part length (L)	mm	(15, 45)	(45, 75)	(75, 120)
		11.11	**66.67**	**22.22**
Part height (H)	mm	(3, 9)	(9, 18)	(18, 36)
		9.53	**24.99**	**65.48**
Part width (W)	mm	(3, 9)	(9, 18)	(18, 36)
		23.85	**62.50**	**13.65**
Part base (C)	mm	(4, 12)	(12, 21)	(21, 33)
		10.95	**30.90**	**58.16**
Part thickness (b)	mm	(2, 6)	(6, 12)	(12, 18)
		19.63	**65.71**	**14.66**
Support thickness (t)	mm	(0.3, 1)	(1, 1.8)	(1.8, 3)
		65.86	**26.28**	**7.86**
Number of supports (n)	---	(1, 5)	(6, 10)	(11, 15) (16, 20)
Cooling rate (CR)	°C/s	(18, 25)		
Heating rate (HR)	°C/s	35		
Elasticity modulus (E)	MPa	$113.8 * 10^3$ [20]		
Thermal expansion (α)	1/K	$8.6 * 10^{-6}$ [20]		
Density (ρ)	g/mm^3	$4.43 * 10^{-3}$ [20]		
Powder layer thickness (l_l)	mm	0.1		
Laser diameter	mm	0.115		
Laser scan velocity (v)	mm/s	1000 [14]		
Temperature difference (ΔT)	K	Calculated by Eq. 3		
Thermal constraint (σ)	MPa	Calculated by Eq. 4		
Thermal constraint moment (M)	N.mm	Calculated by Eq. 5		
Curling defect (δ)	mm	Calculated by Eq. 6		
Total support mass (m_s)	g	Calculated by Eq. 7		

Step 5: Bayesian inference for the case study is implemented in BayesiaLab software. The software uses a sampling technique to calculate all possibilities for the variables in the network. The Bayesian inference mechanism enables simulations to observe the effect of user preferences or evidence across a developed network. The simulation of the developed network is presented in Section 4.

Table 2. Initial and defined acceptable value ranges for geometric constraint ratios to limit the design space.

Constraint Ratio	Initial Range	Acceptable Range
C_1=b/L	(0.016, 1.2)	(0.1, 0.2)
C_2=W/L	(0.025, 2.4)	(0.16, 0.5)
C_3=C/L	(0.033, 2.2)	(0.25, 0.5)
C_4=H/L	(0.025, 2.4)	(0.2, 1)
C_5=n.t/L	(0.0025, 4.0)	(0.0025, 0.5)

4. Results and Discussion

With the aid of the Bayesian inference mechanism, the designer can use the developed model in two directions: (1) for predicting the effect of specific design and manufacturing parameters on defects (forward simulation) and (2) for diagnosing the independent variables' most probable value for particular results in performance (backward simulation). Designers are able to visualize the cascading impacts of choices for design variables in real time. This enables the designer to utilize expert knowledge embedded in the model and make a better-informed decision early in the design process.

4.1. Forward simulation

Fig. 4 shows the effect of the design variables on the resulting curling defect for manufacturing of the L-shaped part. During simulation, the values for part height (H, 9-18 mm), width (W, 9–18 mm), length (L, 45-75 mm), and thickness (b, 12-18 mm) are set as evidence for the Bayesian network model.

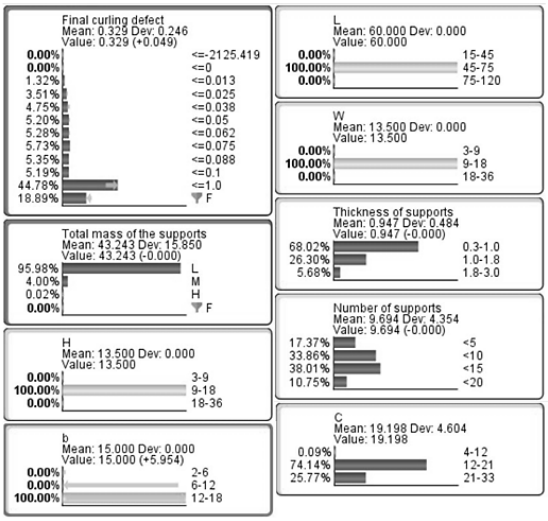

Fig. 4. Predicted effect of part geometric dimensional features on the probability of curling defects for medium-sized parts (45 < L < 75).

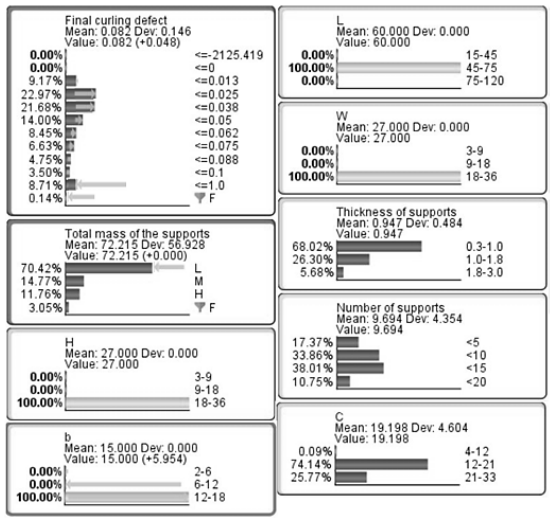

Fig. 6. Predicted effect of part width and part height on the probability of curling defects for medium-sized parts (45 < L < 75) compared to Figure 4.

For these part dimensions, it is seen that the probability of curling increases in the high value state of the variable (curling <=1.0) to 44.78%. In order to reduce the value of curling defect, the influence of two design variables, part height and part width are investigated. The individual effects of width and height on the curling defect are shown in Figure 5. It is seen that increasing part width is predicted to result in an increased curling defect. Lower range values for part height (3-18 mm) are predicted to increase the magnitude of curling, while high range values (18–36 mm) would reduce the curling defect, due to its non-linear relationship with part curling defect. The non-linearity arises due to the design constraints imposed during modelling. The values for curling defect in Figure 5 are calculated using Eqs. 3-7. The knowledge from Figure 5 can be used to set evidence to the Bayesian Network model and/or inversely to validate the results of the Bayesian inference.

The results obtained from Figure 5 are compared with the result of the Bayesian Network. In Fig. 6, new evidence for part width (W, 18–36 mm) and part height (H, 18-36 mm) are presented to characterize the effect of these changes on the curling defect.

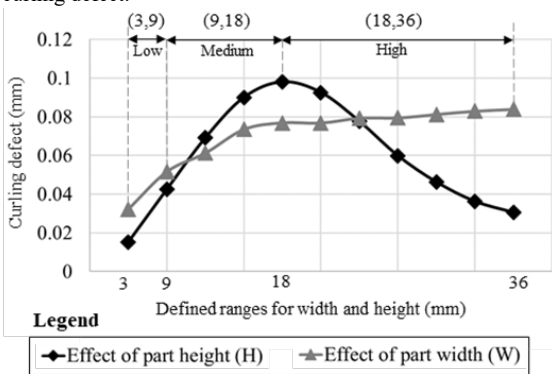

Fig. 5. Effect of part height and part width on the curling defect.

It is seen that the changes reduced value for curling defect. The probability that the curling defect lies in low value states of the variable (<=0.025, <=0.038, and <=0.05) increased to 22.97%, 21.68%, and 14%, respectively, representing significant decrease in the value of curling defect from the range (0.1 mm - 1 mm) to range (0.013 mm to 0.038 mm). It is to be noted that the Bayesian Network results also highlight the relative importance of design variables on the curling defect. The increase in width increases the curling defect as seen in Figure 5 however, the influence of height on curling defect overshadows the influence of width as seen in Figure 6.

4.2. Backward simulation

During backward simulation, the curling defect was set to be in a low state (<=0.013) and the total mass of supports was set in the low range (<=80 g) for small parts (15< L<45). The effect of this evidence is shown in Fig. 7, where the most probable states for the part and support dimensions are found for the set evidences for length of part, curling defect, and the total mass of supports. For low curling defect and low total mass of supports, the model predicts that part height must be in the high value state (0.3-1.0 mm, with a probability of 72.47%), part thickness in the low value state (2-6 mm, with a probability of 71.31%), part width in medium value state (9-18 mm, with a probability of 74.21%), and the number of supports must be less than or equal to five (with a probability of 57.78%).

5. Conclusion

Bayesian network based defect modelling is beneficial for characterizing complex systems such as the design and production of metal parts through additive manufacturing. The foregoing research develops and demonstrates an approach to generate and explore a Bayesian network model characterizing the influence of design and manufacturing parameters on the

curling defect in laser-based additive manufacturing for an L-shaped part.

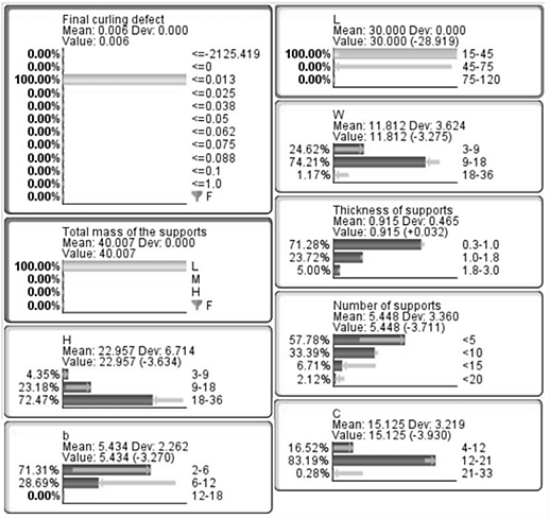

Fig. 7. Backward simulation to minimize curling defect and supports' mass for small-sized parts (15< L <45).

The methodology developed herein is generic and could be expanded to include other geometric defects resulting from non-homogenous temperature gradient in laser additive manufacturing. The Bayesian network allows for two-way monitoring of the modelled system. First, the model estimates the values for targets based on fixed design parameters. Second, it allows the user to set evidence for known targets and then uses the model to backtrack and identify the most probable value ranges for the part geometric dimensions to attain those targets. The simulation of the model helps designers make conscious decisions about changes in product geometry early in the design stage. Such evaluations will eliminate steep costs associated with making design changes late in the production process.

In addition, the results of this study must be used as prior knowledge to calibrate the model with experimental data. For instance, the curling defect is a recursive phenomenon, thus the equations used to model the curling defect uses recursive computation. The model in this research uses approximation to avoid loops in the Bayesian network. Hence, to improve accuracy of the model, future work will focus on training the Bayesian network using data generated through constraint programming for the same governing equations.

References

[1] D. S. Thomas and S. W. Gilbert, "Costs and Cost Effectiveness of Additive Manufacturing," *Spec. Publ. NIST SP - 1176*, Dec. 2014.

[2] W. E. Frazier, "Metal Additive Manufacturing: A Review," *J. Mater. Eng. Perform.*, vol. 23, no. 6, pp. 1917–1928, Apr. 2014.

[3] W. E. Frazier, "Direct digital manufacturing of metallic components: vision and roadmap," presented at the 21st Annual International Solid Freeform Fabrication Symposium, Austin, TX, Aug, 2010, pp. 9–11.

[4] D. D. Gu, W. Meiners, K. Wissenbach, and R. Poprawe, "Laser additive manufacturing of metallic components: materials, processes and mechanisms," *Int. Mater. Rev.*, vol. 57, no. 3, pp. 133–164, May 2012.

[5] H. Pohl, A. Simchi, M. Issa, and H. C. Dias, "Thermal stresses in direct metal laser sintering," in *Proceedings of the 12th Solid Freeform Fabrication Symposium, Austin, TX*, 2001.

[6] P. K. Rao, J. P. Liu, D. Roberson, Z. J. Kong, and C. Williams, "Online real-time quality monitoring in additive manufacturing processes using heterogeneous sensors," *J. Manuf. Sci. Eng.*, vol. 137, no. 6, p. 061007, 2015.

[7] L. Song and J. Mazumder, "Feedback control of melt pool temperature during laser cladding process," *Control Syst. Technol. IEEE Trans. On*, vol. 19, no. 6, pp. 1349–1356, Nov. 2011.

[8] C. Teng *et al.*, "A review of defect modeling in laser material processing," *Addit. Manuf.*, vol. 14, pp. 137–147, 2017.

[9] A. Vasinonta, J. L. Beuth, and M. L. Griffith, "A Process Map for Consistent Build Conditions in the Solid Freeform Fabrication of Thin-Walled Structures," *J. Manuf. Sci. Eng.*, vol. 123, no. 4, pp. 615–622, 2001.

[10] T.-L. Teng, C.-P. Fung, and P.-H. Chang, "Effect of weld geometry and residual stresses on fatigue in butt-welded joints," *Int. J. Press. Vessels Pip.*, vol. 79, no. 7, pp. 467–482, Jul. 2002.

[11] L. Facchini, E. Magalini, P. Robotti, A. Molinari, S. Höges, and K. Wissenbach, "Ductility of a Ti-6Al-4V alloy produced by selective laser melting of prealloyed powders," *Rapid Prototyp. J.*, vol. 16, no. 6, pp. 450–459, Oct. 2010.

[12] A. H. Nickel, D. M. Barnett, and F. B. Prinz, "Thermal stresses and deposition patterns in layered manufacturing," *Mater. Sci. Eng. A*, vol. 317, no. 1, pp. 59–64, Oct. 2001.

[13] F. Calignano, "Design optimization of supports for overhanging structures in aluminum and titanium alloys by selective laser melting," *Mater. Des.*, vol. 64, pp. 203–213, Dec. 2014.

[14] B. Cheng and K. Chou, "Geometric consideration of support structures in part overhang fabrications by electron beam additive manufacturing," *Comput.-Aided Des.*, vol. 69, pp. 102–111, Dec. 2015.

[15] E. Coatanéa, R. Roca, H. Mokhtarian, F. Mokammel, and K. Ikkala, "A Conceptual Modeling and Simulation Framework for System Design," *Comput. Sci. Eng.*, vol. 18, no. 4, pp. 42–52, Jul. 2016.

[16] H. Mokhtarian *et al.*, "A Conceptual Design and Modeling Framework for Integrated Additive Manufacturing," *J. Mech. Des.*, vol. 140, no. 8, p. 081101, 2018.

[17] P. Bridgman, "Dimensional Analysis, 1922," *Phil Mag*, vol. 2, no. 12, pp. 1263–1266.

[18] N. Shadbolt and P. R. Smart, "Knowledge Elicitation: Methods, Tools and Techniques," in *Evaluation of Human Work*, J. R. Wilson and S. Sharples, Eds. CRC Press, 2015, pp. 163–200.

[19] T. L. Saaty, "The Modern Science of Multicriteria Decision Making and Its Practical Applications: The AHP/ANP Approach," *Oper. Res.*, vol. 61, no. 5, pp. 1101–1118, Oct. 2013.

[20] M. Yan and P. Yu, "An Overview of densification, microstructure and mechanical property of additively manufactured Ti-6Al-4V—Comparison among selective laser melting, electron beam melting, laser metal deposition and selective laser sintering, and with conventional powder," in *Sintering techniques of materials*, InTech, 2015.

PUBLICATION V

Tracing the interrelationship between key performance indicators and production cost using Bayesian Networks

Suraj Panicker, Hari P.N. Nagarajan, Hossein Mokhtarian, Azarakhsh Hamedi, Ananda Chakraborti, Eric Coatanéa, Karl R. Haapala, and Kari Koskinen

Procedia CIRP, vol. 81 (2019)
10.1016/j.procir.2019.03.136

Available online at www.sciencedirect.com

ScienceDirect

Procedia CIRP 81 (2019) 500–505

www.elsevier.com/locate/procedia

52nd CIRP Conference on Manufacturing Systems

Tracing the Interrelationship between Key Performance Indicators and Production Cost using Bayesian Networks

Suraj Panicker[a]*, Hari P.N. Nagarajan[a], Hossein Mokhtarian[a], Azarakhsh Hamedi[a], Ananda Chakraborti[a], Eric Coatanéa[a], Karl R. Haapala[b], Kari Koskinen[a]

[a]*Automation Technology and Mechanical Engineering, Tampere University, Finland*
[b]*School of Mechanical, Industrial and Manufacturing Engineering, Oregon State University, Corvallis, Oregon, USA*

* Corresponding author. Tel.: (+358) 41-705-2584; *E-mail address:* suraj.panicker@tuni.fi

Abstract

Key performance indicators (KPIs) are used to monitor and improve manufacturing performance. A plethora of manufacturing KPIs are currently in use, with others continually being developed to meet organizational needs. However, obtaining the optimum KPI values at different organizational levels is challenging due to complex interactions between manufacturing decisions, variables, and desired targets. A Bayesian network is developed to characterize the interrelationships between manufacturing decisions, variables, and selected KPIs. For an additive manufacturing case, it is shown that the approach enables appropriate value estimation for decisions and variables for achieving desired KPI values and production cost targets in a manufacturing enterprise.

Keywords: Manufacturing performance indicators; Cost modeling; Bayesian networks; Additive manufacturing

1. Introduction

Manufacturing exists as a cornerstone of modern economic systems. Throughout the history of industrialization, society has progressed towards more efficient resource utilization with the help of technological advancements. Manufacturing enterprises, as they exist today, require transparent and integrated departments, such as sales, marketing, design, manufacturing, and quality control, which communicate from idea conceptualization to final product realization. Such integrated product development processes increase the number of stakeholders associated with each new product and, in turn, increase the number of decisions made across the production enterprise. Decisions on design constraints, choice of raw materials, choice of manufacturing processes, and required manufacturing process parameters are challenging to make and, at times, can be counterintuitive due to unforeseen tradeoffs. Thus, for efficient operation of a manufacturing enterprise, production decision (type of product, type of manufacturing process, manufacturing location and material supplier location, etc.), design decision (part dimensions and shape complexity), and manufacturing decision variables (process parameters) need to be identified, modeled, and compared against key performance indicators (KPIs) and manufacturing targets, such as production cost.

Manufacturing industry and academia have worked towards developing different KPIs to measure and monitor the success of an enterprise based on objectives of performance [1]. KPIs have been identified and developed for measuring performance in various domains, e.g., economic, environmental, social, product design, production, quality, and labour [2]–[4]. To efficiently measure, record, and monitor KPIs, decision makers

2212-8271
10.1016/j.procir.2019.03.136

must understand how individual stakeholder actions affect the various KPIs. However, the number of decisions, variables, and their interactions within an enterprise make it difficult to simultaneously observe and control changes in KPIs. Hence, mapping the interrelationships between KPIs, manufacturing decisions, manufacturing variables, and manufacturing targets is required to optimize KPI values and improve overall manufacturing performance. Towards that goal, a Bayesian network (BN) based monitoring strategy is proposed, which is well-suited to characterizing the complex interrelationships between manufacturing decisions, product design variables, manufacturing parameters, KPIs, and manufacturing targets (here, we choose production cost as the target) [5], [6].

A process-based cost model is used in this study [7]. The cost model is translated into a BN to estimate the most favourable manufacturing decisions, manufacturing variables, and process parameters for the chosen process for achieving specific KPI values, including cost targets. The approach is then used to estimate manufacturing variables (e.g., annual production ratio, product build time, and material use efficiency) to optimize specific KPI values. The BN strategy is demonstrated for production of a shell and a tailpipe for a turbine assembly [8], using wire and arc additive manufacturing (WAAM) and electron beam melting (EBM).

The manuscript is organized into several sections. Section 2 provides an overview of Bayesian networks. Section 3 describes the application of the BN methodology for the additive manufacturing case study. Section 4 discusses the results from the developed BN for the case study. Section 5 presents the conclusions of the work. Section 6 discusses limitations of the current model and future development efforts.

2. Bayesian Networks

Bayes' theorem describes the probability of occurrence of an event based on the prior knowledge of conditions that might have some relation to the event [9]. A BN uses this Bayesian inference to assign and update probabilities for a hypothesis as it is exposed to more evidence or information. A BN is often used as an inference tool, which is capable of using available information from a subset of variables in a system, to predict the behaviour of other parts of the same system [9]. In recent times, BNs have been employed in various disciplines such as engineering, natural sciences, medicine, sports, and economics, largely due to their advantages, as explained by Heckerman [10]: 1) ability to handle incomplete datasets by encoding statistical dependencies between the variables, 2) ability to learn causal relationships between the variables within a system to perform interventions and investigate predicted results, and 3) ability to model domain knowledge and data simultaneously, making it a sophisticated package for data analysis.

A BN uses Directed Acyclic Graphs (DAGs) to represent the dependencies within a system (comprising all the variables and decisions). Each manufacturing variable or decision is represented as a node in the BN. The dependency between variables or decisions are represented by arcs (unidirectional arrows) connecting the respective nodes. Parent nodes feed dependencies into the dependent child nodes, forming a hierarchy of decisions. Based on the dependencies between different variables, their joint probability distribution can be factorized into a set of conditional and marginal probability tables. The network uses these probability tables at each node to make inferences during simulations [11].

The causal relationships between nodes in a BN can be created using empirical data and machine-learning techniques. Alternately, knowing the interactions between variables from expert knowledge or literature, this information can be fed to the network in the form of connections (arcs) between nodes and the probability tables. In this research, cost models for products produced using additive manufacturing are translated into a causal graph using Dimensional Analysis Conceptual Modeling Framework (DACM) [12]. The resultant causal graph is used as a DAG for implementing the BN to provide interaction capabilities. The emphasis given to cause-effect relationships via the use of a causal graph provides an intuitive approach to explicitly evaluate the uncertainties in potential decisions and their outcomes with the use of probability tables. The rationale for implementing cost models in a BN is to leverage its ability of characterizing the impact of intrinsic and extrinsic factors on the different cost categories. Factors such as market forecasts, supply chain uncertainties, and market fluctuations can be modeled into the BN as extrinsic factors under certain boundary conditions. This approach will reduce the effective person-hours and effort required to estimate production costs for possible scenarios.

The different nodes of the BN are connected and their interactions are modeled using mathematical equations and conditional statements. Several cost modeling strategies, such as activity-based costing, product-based costing, process-based costing, bottom up costing, and top-down costing, have been developed for characterizing production cost [5], [13]–[15]. For the current case, a bottom-up, process-based costing method is used to evaluate the two manufacturing choices (WAAM and EBM) [7]. The methodology for translating deterministic cost models into a BN is explained in Section 3 using the additive manufacturing case, but the approach also applies for other processes.

3. Methodology and Case Study

The methodology developed herein facilitates modelling the manufacturing performance metrics for a product during early design by using a BN. The model herein characterizes manufacturing decisions, design and manufacturing variables, and KPIs into quantifiable production cost metrics for additive manufacturing processes. Production cost is modelled using six cost components: facility cost, capital cost, utilities costs, raw material cost, labour cost, and maintenance cost. Consumables cost is not considered in this study. Raw material transportation cost is added to examine the influence of raw material supplier location on production cost. The six cost components are dependent upon factors such as manufacturing location, type of manufacturing process, raw materials used, source of raw materials, and transportation modes, to name a few.

The first step in implementing a BN is to develop a holistic system model in which design and manufacturing variables, constraints, and decisions are defined. As noted above, the case

study considers the manufacture of a shell and tailpipe for a turbine assembly using WAAM and EBM. The functionality of the two additive manufacturing technologies have been discussed in prior studies [16]. WAAM uses an electric arc as the heat source and wire as the feedstock. The equipment considered in this study is a collaborative setup consisting of a six-axis ABB robot arm for the welding torch and Fronius welding equipment based on cold metal transfer (CMT) technology. In comparison, EBM is a powder bed fusion process, wherein an electron beam is used as the heat source and metal powder is used as feedstock. The electron beam scans over the powder following a pre-defined toolpath for each layer, heating it to a temperature at which the powder fuses based on tool path and layer profile information.

The geometries of the shell and tailpipe are predefined. Six KPIs are used to evaluate the performance of the system by considering social performance (labour productivity), environmental performance (energy intensity and percentage of recycled materials in manufacturing), production performance (order-to-delivery lead-time and setup rate), and production quality (scrap ratio) metrics. The different decisions for the system, KPIs, and key manufacturing variables and their values are reported in Table 1. The defined system model and cost models are translated into a DAG (Fig. 1) using DACM, and the BN is implemented using BayesiaLab 8 modelling software [17]. The network represents all variables, decisions, and targets as nodes. The decision nodes (green) are connected to manufacturing variables with arrows, which represent the interactions between each decision and the connected variable. The KPIs (blue) and cost categories (red) represent target nodes. Each manufacturing variable node's interaction with decisions and targets are modelled using system constraints and the deterministic cost models.

The probability tables are obtained using a sampling technique similar to the Monte Carlo method. The governing equations obtained through DACM are used to propagate several samples from the independent variable nodes (parent nodes) to the dependent variable nodes (child nodes). Sampling starts with defining the domain (value range) of the child nodes based on the domain of the parent nodes and the governing equations that determine the relationship between the parent and child nodes. The domains of the parent nodes and child nodes are then divided into multiple states. The user has the freedom to set multiple states and the range of each state can be normalized or set freely. The granularity of the results depends on the number of states and the ranges within these states. Next, a number of random sample values from each defined state of a parent node are obtained and the resultant value for each child node are calculated using the governing equations. A counting method is then used to count the number of samples that lie within each state of the child node. This count is used to calculate the conditional probability that a sample from a specific state of the parent node will result in the value of the child node being in a specific state. For example, we take 1000 samples from the first defined state of the parent node. Then, the corresponding values of the child node are calculated based on the sample values from the parent node and the governing equations.

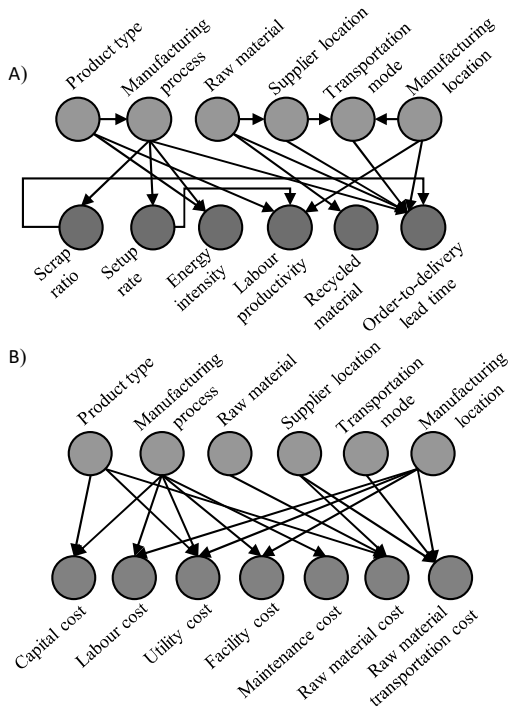

Fig. 1. Directed acyclic graphs (DAGs) with causal relationships between A) manufacturing decisions (green) and KPIs (blue) and B) manufacturing decisions (green) and cost targets (red).

Now, if 800 calculated values for the child node lie within the range of the first state of the child node, then the probability that the calculated value for a child node will be in the first state for a sample taken from the first state of the parent node is 80%. Using this method, conditional probability tables are computed for all the nodes in the network.

The final computed network allows the user to compare the impacts of different decisions on KPI values and production cost. For instance, selection of different production processes will result in use of different manufacturing equipment. This will in turn affect the facility cost, capital cost, maintenance cost, utilities costs, labour cost, production performance, and environmental performance of the system. Similarly, each of the other decisions is linked to several or all cost and performance metrics. Hence, it is important to measure, record, and visualize the impact of these decisions on cost and other performance metrics to make better choices. Based on the level of accuracy and granularity that is required for the BN, the production cost targets can be represented as a range or as precise cost estimates.

The usability of the developed method is demonstrated for estimating production cost and the above-mentioned KPIs for different manufacturing decisions. Two scenarios are chosen to evaluate BN performance and estimate target values. The results are presented and discussed in Section 4.

4. Results and Discussion

The developed BN is evaluated under two scenarios to understand how the decisions made (in green), the key performance indicators (in blue), and cost categories (in red) interact with each other. Scenario 1 defines the product type and type of manufacturing process; its impact on the cost and the performance indicators are observed by simulating the network. In the Scenario 2, the user is allowed to set target cost ranges for total production cost and labour cost; fix the range for one manufacturing variable, build time; and fix one KPI, order-to-delivery lead-time. The model responds to Scenario 2 by providing the user with the necessary decisions that should be made in order to attain the desired targets. In both the scenarios, with each decision made, the system computes the joint probability for the whole network based on the likelihood of occurrence of that particular choice. On the condition that evidence is introduced in any of the nodes, the system will then compute the posterior probabilities for all nodes within the network. The extent to which the nodes are affected by changes made to corresponding nodes depends upon the relationship between the nodes.

In the BN, prior to manually making any decisions for the decision nodes, the system autonomously presents an initial probability for choices of the decisions and variable nodes. This initial probability is the result of the probability distributions of the nodes, which propagate through the network. It is dependent on the interactions between the different nodes, the joint probability of the network, and the conditional probability table within each node.

Table 1. Bayesian model decisions, KPIs, and variable descriptions.

Decisions	**Choices**		
Product	Shell and Tailpipe		
Manufacturing process	WAAM and EBM		
Raw material	Titanium and Aluminium		
Manufacturing location	USA and China		
Raw material supplier location	USA, China, and India		
Transport mode	Rail, Road, and Sea		
KPI	**Description**		
Scrap ratio	Ratio between scrap quantity and processed product quantity		
Setup rate	Ratio between actual unit setup time and actual unit processing time		
Recycled material use	Percentage of materials used that are recycled input materials		
Energy intensity	Ratio of electricity generation and transmission losses (based on locational electricity mix) to the total direct energy required to manufacture the product [7]		
Order-to-delivery lead time	Latency between the initiation and execution of process		
Labour productivity	Ratio between value of monthly product shipped and monthly labour expenditures		
Variable	**Unit**	**Ranges / Discrete values**	
		EBM	**WAAM**
Material processing rate	kilograms/hour	0.2	2.9
Equipment floor space	square meters	4.46	24.15
Setup time	hours	1.3	4

This results in the choice of product as tailpipe (54.42%) compared to shell (45.58%) because the conditional probability that the shape complexity is two (2) corresponds more to the product tailpipe. Similarly, the choice of manufacturing process node favours EBM (54.42%) over WAAM (45.58%) for both products. EBM is capable of producing highly complex parts with better accuracy than WAAM and hence, a higher probability for EBM is calculated by the network for a shape complexity value of two (2) or higher.

For Scenario 1, we set the product type as *tailpipe* and the type of manufacturing process to be *WAAM* by providing evidence to the BN that the probability is 100% for *tailpipe* and *WAAM*. This evidence is provided solely for the sake of simulation. Users may make other similar choices, depending on their needs and the type of analysis required. Based on the provided evidence, we can see that the values for facility cost, capital cost, labour cost, and maintenance cost increase (Fig. 2). The increase in facility cost, capital cost, and maintenance cost is due to the larger equipment floor space and high equipment cost associated with the WAAM machine. The major change was seen in the medium (M) state range for capital cost ($1,900-$3,800) and maintenance cost ($400-$800) with increases in likelihood of occurrence of the medium state for the two cost components from the original values of 21.71% and 23.13% to 34.59% and 37.75%, respectively.

Manufacturing process selection is followed by the choice of raw material, which is chosen to be aluminium due to its low cost. Lack of granularity in the defined state ranges for the cost of raw materials node, however, prevents users from making inferences related to the raw material cost. It is prematurely set to be in the low (L) state range due to the prior decisions (product type and manufacturing process).

Nevertheless, based on the model, the unit price of the raw materials is low for aluminium, which is priced at an average of $56.60/kg, compared to titanium with an average of $410.00/kg. Hence, with better granularity in the states, the effect of raw material unit cost would be visible on the total raw material cost for the product.

The next decision is regarding the raw material supplier location and the manufacturing location. The choices with the highest probability are USA for the raw material supplier location and China for manufacturing location. For these two choices, the constraint nodes in the network ensure that the transport mode chosen is by sea. The immediate effect (Fig. 3) was observed in the increase in transportation time (736 hours or 30 days) and the cost of raw material transportation, which now lies in the high (H) state range ($40-$90 per product). In addition, choosing the manufacturing location as China reduces the labour cost significantly; the hourly labour rate for skilled labour in China is $3.22 versus $16.60 in the USA [18].

The total cost of manufacturing the goods in China with raw materials sourced from the USA has a likelihood occurrence of 87.95% in the low (L) state range (up to $21,897) and a mean value of $13,647. The alternative of having the manufacturing facility in the USA, sourcing materials from within the USA, and having the transport mode as rail results in an increased mean value for overall total cost ($13,835) (Fig. 4). This change is again due to the higher labour rates in the USA

compared to China. Therefore, the savings in transportation cost are dominated by increased labour costs, for this case.

In Scenario 2, an inverse evaluation is conducted to evaluate the effect of fixed cost targets and KPIs on the available choices for decisions. By defining the total cost of manufacturing to lie in the medium (M) state range ($21,897-$43,795), a significant change in the probabilities of certain decision choices is observed. The likelihood of manufacturing the shell using titanium as the raw material sees an increased probability (an increase of 38.13% for the shell and 37.43% for titanium). Next, setting the build time to the high (H) state range (227-342 hours) further confirms the manufacturing decisions of producing the shell using titanium, but also provides new information regarding which manufacturing process to consider. The analysis strongly suggests (100% likelihood) that EBM should be used for manufacturing the shell; EBM has a lower material processing rate (0.2 kg/hr) than WAAM (2.9 kg/hr) and thus, a high build time, but higher quality.

Another change observed is that labour cost has an increased tendency to lie in the high (H) state range ($3,900-$5,700) due to the longer build time. Setting the labour cost to the high state range, the model informs us that the manufacturing location should be in the USA. Lastly, the manufacturing facility should abide to strict delivery policies requiring low order-to-delivery lead times. This means that the setup time, build time, and transport time must be low. Therefore, we see an increase in the likelihood of the raw material supplier to be located in the USA and the transportation mode to be rail or road.

From the foregoing, it can be seen that using the BN model would enable industrial decisions makers to understand the consequences of the various decision choices on production performance metrics and cost targets. It is worth noting that the percentages for low, medium, and high ranges do not add up to 100% in some cases, due to presence of another range, called the filtered state. As the name suggests, the values in filtered states are outliers, which cannot physically exist in the real world.

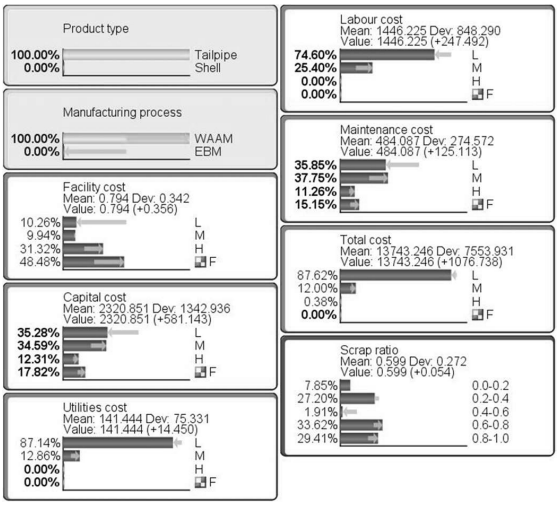

Fig. 2. Simulated results for fixed product (tailpipe) and manufacturing process (WAAM) in Scenario 1.

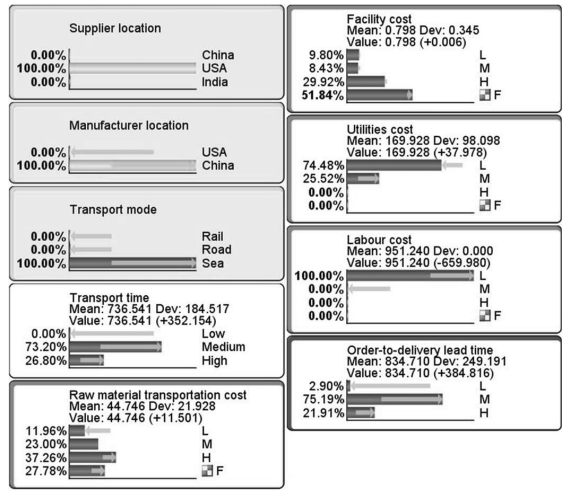

Fig. 3. Simulated results for fixed supplier location (USA) and manufacturing location (China) in Scenario 1.

For each parent node and its corresponding child nodes, the software computes values for all combination of numbers that fall in the ranges of the parent nodes, resulting in unfiltered ranges in computed values for the child nodes. These unfiltered values propagate throughout the model, and as the complexity and number of nodes increases in the model, the unfiltered ranges also compound. To reduce compounding we introduce filtered states to perform filtering.

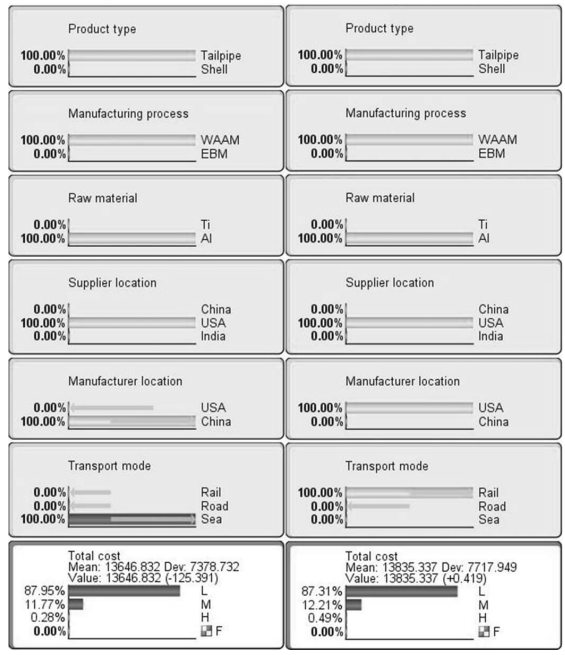

Fig. 4. Comparison of total production cost for set supplier location (USA) and manufacturing location (left - China, right – USA).

5. Conclusions

A Bayesian network (BN) as an interactive multi-criteria decision-making tool in manufacturing performance analysis was developed and demonstrated for an additive manufacturing case to characterize the influence of manufacturing decisions, variables, and constraints on manufacturing KPIs and targets. This method enables a decision maker to observe the effect of their decisions on target performance variables, and vice versa, to obtain information about the most probable variable values and decision choices. The interactive nature of the model makes it an effective tool for stakeholders at different levels of the enterprise to visualize the cause-effect relationships between their choices for performance targets, design constraints, and manufacturing variables.

The DACM framework enables integration of different forms of knowledge (e.g., expert opinion, qualitative models, and deterministic models) into a causal graph for developing the BN. This paper proposes using the DACM framework as a basis to systematically establish causal graphs and governing equations among the influencing variables. The BN is then established as a means to integrate decisions into the casual model and provide interactive analysis to the model. The simulated production cost and KPI values reported herein are not exact; rather, the model provides estimated ranges in which the costs are likely to lie. Hence, system-modelling using a BN offers a preliminary screening method to eliminate combinations of bad decisions. After narrowing down to a select combination of good decisions, real costs and KPI values can be estimated using deterministic methods. The methodology developed is generic and can be applied to any multi-criteria decision making problem supporting multiple types of decision processes.

6. Limitations and Future Work

Causal graphs of the production system, implemented in Bayesian networks (BNs), offer a powerful tool to characterize a complex system at different levels of detail and granularity. It is interesting to note that all nodes in a BN are linked to one another either directly or indirectly for computing the joint probability of the modelled system. During simulation, a marginal probability distribution of the states of the nodes can be displayed. The display shows the mean value for the state of a node where the probability of occurrence is maximum. The value displayed represents the mean of the entire range of a state in a node, and should not be considered to be exact.

Future research will leverage the ability of a combined DACM and BN approach to integrate different forms of knowledge/data. With growing concerns of industrial sustainability, such efforts can enable translation of sustainability reports of different corporations belonging to different types of industries into BN graphs (cause-effect graphs). The value for such research lies in the ability to understand, through visualization (graphs), the sustainability performance measures affecting variables specific to an industry, those specific to individual departments within an enterprise, and those variables with commonalities across different industries or departments. Such evaluations can help industry implement selective measures that target the impactful practices at each level of an organization as well as to implement measures that improve the overall sustainability performance across industries. It is essential for researchers, along with industry partners, to perform inference studies to understand which managerial decisions have a positive impact towards reaching the goals of the manufacturing enterprise. Insights from such inference studies will help in sustainability performance-based future sight and decision-making.

References

[1] Parmenter D. *Key performance indicators: developing, implementing, and using winning KPIs*. John Wiley & Sons, 2015.

[2] Ahmad MM and Dhafr N. "Establishing and improving manufacturing performance measures," *Robot. Comput.-Integr. Manuf.*, vol. 18, no. 3–4, pp. 171–176, 2002.

[3] Mahbod MA and Shahin A. "Prioritization of key performance indicators: An integration of analytical hierarchy process and goal setting," *Int. J. Product. Perform. Manag.*, vol. 56, no. 3, pp. 226–240, Mar. 2007.

[4] Amrina E and Vilsi AL. "Key Performance Indicators for Sustainable Manufacturing Evaluation in Cement Industry," *Procedia CIRP*, vol. 26, pp. 19–23, Jan. 2015.

[5] Dogan I and Aydin N. "Combining Bayesian Networks and Total Cost of Ownership method for supplier selection analysis," *Comput. Ind. Eng.*, vol. 61, no. 4, pp. 1072–1085, 2011.

[6] Khodakarami V and Abdi A. "Project cost risk analysis: A Bayesian networks approach for modeling dependencies between cost items," *Int. J. Proj. Manag.*, vol. 32, no. 7, pp. 1233–1245, 2014.

[7] Nagarajan HPN, Haapala KR and Raman AS. "A Sustainability Assessment Framework for Dynamic Cloud-based Distributed Manufacturing," *Procedia CIRP*, vol. 69, pp. 136–141, 2018.

[8] "Gas Turbine Engines – Exhaust Section," *Flight Mechanic*, 15-May-2016. [Online]. Available: http://www.flight-mechanic.com/gas-turbine-engines-exhaust-section/. [Accessed: 30-Dec-2018].

[9] Nielsen TD and Jensen FV. *Bayesian networks and decision graphs*. Springer Science & Business Media, 2009.

[10] Heckerman D, Geiger D and Chickering DM. "Learning Bayesian Networks: The Combination of Knowledge and Statsitical Data," *Mach. Learn.*, vol. 20, 1995.

[11] Koller D *et al. Introduction to statistical relational learning*. MIT press, 2007.

[12] Mokhtarian H *et al.* "A Conceptual Design and Modeling Framework for Integrated Additive Manufacturing," *J. Mech. Des.*, vol. 140, no. 8, p. 081101, 2018.

[13] Niazi A, Dai JS, Balabani S and Seneviratne L. "Product cost estimation: Technique classification and methodology review," *J. Manuf. Sci. Eng.*, vol. 128, no. 2, pp. 563–575, 2006.

[14] Southworth Z. "Bottom-up Cost Modeling for Vanadium Redox Flow Battery Component Manufacturing," M.S. Thesis, Oregon State University, Corvallis, OR, 2013.

[15] Brown MO. "A process based modeling approach for economic and environmental assessment of nano-assisted manufacturing," M.S. Thesis, Oregon State University, Corvallis, OR, 2011.

[16] Frazier W E. "Metal Additive Manufacturing: A Review," *J. Mater. Eng. Perform.*, vol. 23, no. 6, pp. 1917–1928, Apr. 2014.

[17] B. USA, "BayesiaLab 8 - Bayesian Networks for Research and Analytics." [Online]. Available: https://www.bayesialab.com. [Accessed: 28-Dec-2018].

[18] "May 2017 National Occupational Employment and Wage Estimates." [Online]. Available: https://www.bls.gov/oes/current/oes_nat.htm#51-0000. [Accessed: 10-Mar-2019].

PUBLICATION VI

A Dimension Reduction Method for Efficient Optimization of Manufacturing Performance

Ananda Chakraborti, Hari P.N. Nagarajan, Suraj Panicker, Hossein Mokhtarian, Eric Coatanéa, and Kari Koskinen

Procedia Manufacturing, vol. 38 (2019)
https://doi.org/10.1016/j.promfg.2020.01.070

Available online at www.sciencedirect.com

ScienceDirect

Procedia Manufacturing 38 (2019) 556–563

Procedia MANUFACTURING

www.elsevier.com/locate/procedia

29th International Conference on Flexible Automation and Intelligent Manufacturing (FAIM2019), June 24-28, 2019, Limerick, Ireland.

A Dimension Reduction Method for Efficient Optimization of Manufacturing Performance

Ananda Chakraborti[a]*, Hari P. N. Nagarajan[a], Suraj Panicker[a], Hossein Mokhtarian[a], Eric Coatanéa[a], Kari T. Koskinen[a]

[a]*Automation Technology and Mechanical Engineering, Tampere University, Tampere, Finland*

Abstract

Increased competitiveness in the manufacturing industry demands optimizing performance at each level of an enterprise. Optimizing performance in terms of indicators such as manufacturing cost requires knowledge of cost-inducing variables from product design and manufacturing, and optimization of these variables. However, the number of variables that affect manufacturing cost is very high and optimizing all variables is time intensive and computationally difficult. Thus, it is important to identify and optimize select few variables that have high potential for inducing cost. Towards that goal, a dimension reduction method combining dimensional analysis conceptual modelling framework and graph centrality theory is proposed. The proposed method integrates existing knowledge of the cost inducing variables, their interactions, and input-output relationship for different functions or behavior of a system, in the form of a causal graph. Propagation of optimization objectives in the causal graph is checked to identify contradictory influences on the variables in the graph. Following the contradiction analysis, graph centrality theory is used to rank the different regions within the graph based on their relative importance to the optimization problem and to cluster the variables into two optimization groups namely, less important variables and most important variables relative to optimizing cost. The optimization problem is formulated to fix less important variables at their highest or lowest levels based on their interaction to cost and to optimize the more important variables to minimize cost. The proposed dimension reduction method is demonstrated for an optimization problem, to minimize the production cost of the bladder and key mechanism for a high-field superconducting magnet at CERN, capable of producing a 16 Tesla magnetic field. It was found that the graph region representing the electromagnetic force and resultant stress generated during energizing of the magnet ranked highest for influence on the bladder and key manufacturing cost. An optimization of the stress and its associated variables to minimize the manufacturing cost is performed using a genetic algorithm solver in Matlab.

* Corresponding author. Tel.: +358-413692130.
E-mail address: ananda.chakraborti@tuni.fi

10.1016/j.promfg.2020.01.070

Keywords: Computer integrated manufacturing; Conceptual modelling; Dimension reduction; Multi objective optimization

1. Introduction

Continuous improvement has become means of subsistence for a successful manufacturing enterprise. In recent times, the growth of information and communications technology (ICT) and its integration into manufacturing has further enabled businesses to fulfill customer's needs in an economical and sustainable manner. To remain competitive in the market, manufacturers must ensure optimized utilization of resources, energy and consumables, as well as prolonged life of the product. Thus, optimization of a process or product design for performance improvement is crucial for an enterprise. Manufacturers measure performance with the help of key performance indicators such as cost, quality, productivity, etc. These indicators are often functions of design and manufacturing variables that need to be modelled and optimized. Hence, sufficient knowledge about the product design and manufacturing process is needed to model their influence on performance indicators. Difficulty arises when trying to model these performance indicators, which are inherently complex and span across multiple domains including product behavior, manufacturing process physics, and production planning. Moreover, optimizing a performance indicator require manufacturers to find optimal values for all influencing variables. Choosing optimal values for all variables irrespective of their level of influence on performance is computationally cost intensive. Dimension reduction in the field of design optimization or machine learning is not a new phenomenon. Nevertheless, there is a lack of systematic techniques that embed domain knowledge in manufacturing performance optimization models. Thus, a multi-domain approach is required with the help of conceptual modelling and simulation to optimize performance indicators. Such approaches would help manufacturers 1) to characterize interrelationships between variables in a system to model performance, 2) integrate knowledge of different domains for modelling performance indicators, and 3) to reduce the number of variables that are needed to optimize performance.

This research focuses on developing a new dimension reduction methodology, which combines graph based modelling of performance indicators across different domains using the dimensional analysis conceptual modelling framework (DACM), and variable clustering using the centrality concept in graph theory and network analysis. The method is tested with a case study of manufacturing the key and bladder mechanism for a new superconducting magnet at CERN. The remainder of the manuscript is organized as follows; Section 2 provides a background discussion on conceptual modelling, dimension reduction in optimization, and centrality concept of graph theory and network applications. Section 3 describes the developed methodology applied to the case study and briefly discusses the results of the case study. Finally, Section 4 describes the conclusions of the work and briefly discusses future development efforts.

Nomenclature

B	Magnetic Flux Density (Nm/A) $[MT^{-2}I^{-1}]$
q	Electric charge (C) [IT]
I	Electric current (A) [I]
J	Current density (I/mm^2) $[IL^{-2}]$
L	Inductance (H) $[ML^2T^{-2}I^{-2}]$
U	Total energy for self-Inductance $[ML^2T^{-2}]$
n	Number of poles
L_m	Length of the magnet (m) [L]
θ	Angle made by the conductor with the field (degree)
F_L	Lorentz force (N) $[MLT^{-2}]$
p_m	Magnetic pressure (N/mm^2) $[ML^{-1}T^{-2}]$
μ	Permeability (H m^{-1}) $[MLT^{-2}I^{-2}]$
σ	Normal stress (N/mm^2) $[ML^{-1}T^{-2}]$

σ_v	von Mises stress (N/mm^2) [ML^{-1}T^{-2}]
t	Time of current flow (sec) [T]
ε	Normal strain
τ	Shear stress (N/mm^2) [ML^{-1}T^{-2}]
δ_l	Elongation of the magnet due to F_L (mm) [L]
d_{key}	Diameter of the stainless steel key (mm) [L]
t_{key}	Thickness of stainless steel key lamination (mm) [L]
A_{key}	Cross-sectional area of the key (mm^2) [L^2]
V_{shell}	Volume of the key (mm^3) [L^3]
ρ_{SS}	Material density of stainless steel [ML^{-3}]
n_{key}	Number of keys
f	Feed rate of milling tool (mm) [LT^{-1}]
v	Velocity of milling tool (mm) [LT^{-1}]
k	Constant representing cost components within low importance variable list X_L
c_t	Tooling cost (€/unit)
c_m	Material cost (€/unit)
c_l	Labour cost (€/unit)
c_o	Overhead cost (€/unit)
t_s	Milling setup time (min)[T]
c_T	Motal cost of manufacturing of keys (€)

2. Background

2.1. Conceptual modelling and simulation

Conceptual modelling is the abstraction of a model from a real or proposed system [1]. DACM framework as a conceptual modelling mechanism originally developed as a specification and verification technique for complex systems, but has been applied to many different cases such as additive manufacturing [2], machine learning [3], and multidisciplinary design optimization [4]. The main aim of DACM is to extract and encode knowledge of different forms (expert literature, empirical/experimental, and equations) in the form of a causal graph. The DACM framework starts with functional modelling of the system and assigning of fundamental variables to the different functions of the model. The functions, associated variables, and representative equations are characterized in the causal graph in the form of the cause-effect relationship between the fundamental variables of the functional model. The mathematical machinery to check propagation of an objective in a causal network is based on the Vashy-Buckingham's Pi (π)-theorem and the dimensional analysis (DA) theory [5], [6]. An adjacency matrix or multiple domain matrix (MDM) can be obtained from the causal network representing multiple domains. A MDM is a systematic extension of the design structure matrix (DSM), popularly used in system decomposition, integration, and design of complex systems. This matrix encodes a rich data structure able to represent knowledge extracted from the multi-domain system variables [7]. In this research, the matrix representation is evaluated qualitatively to check for contradictory influences in the objective imposed by the system variables. The qualitative analysis is followed by a dimension reduction method to rank order the system variables and form the optimization objective function.

2.2. Dimension reduction

High dimensionality is a universal challenge during computational analysis in the field of science and engineering. In manufacturing, computationally expensive and resource demanding optimization methods are needed to simulate high-dimensional problems such as production planning, scheduling, and performance optimization. Shan and Wang [8] provided a survey of popular strategies such as decomposition, which is to break up the optimization problem into simpler and smaller steps, and screening of variables to identify more important and less important variables as potential means to tackle the high dimensionality in engineering problems. In this research, a screening using the

graph centrality theory and node ranking is performed to classify variables as either low impact or high impact depending on their influence on the performance objectives. Following the classification, the optimization problem is decomposed into two stages. First, the low impact variables are fixed at their highest or lowest values based on their connection to the target variables in the performance objectives. Second, the optimization is performed for only the high impact variables based on the performance criteria having fixed the low impact variable values. The screening using graph centrality and node ranking is presented in the next subsection 2.3.

2.3. Graph centrality and node ranking

In a graph-based representation of a system consisting of a large number of nodes, the user is often interested to know what the most important nodes are. This helps the user to direct their attention towards that part of the graph (or network) which has the most influence on the system represented. Graph centrality measures are used to rank nodes and find the most influential nodes within a complex network. Its most notable applications include wireless network applications, network traffic reduction, and social media network analysis. Many measures exist for graph centrality, Freeman [9] provides one of the earliest empirically based measures of centrality in complex networks. The author identifies three measures, namely, degree, betweenness, and closeness, which can be used to obtain a score for centrality in a graph. Borgatti and Everett [10] developed a unified framework for measuring centrality scores in complex social networks. They describe centrality as the node's contribution to the cohesiveness of the network. They also provide mathematical expressions for computing the centrality score in complex networks. The method of ranking the different nodes could be automated using a centrality measurement algorithm similar to the PageRank algorithm, proposed by Brin and Page [11] of Google. PageRank is a network ranking method developed to compute ranks of webpages in Google's search engine results. An improved version of this algorithm is used in applications that go beyond search engine ranking, which include impact analysis of graph-based system requirements and graph-based feature selection [12], [13]. In this article, a dimension reduction strategy is developed based on the causal graph representation of the system. Node ranking algorithm along with graph centrality measurements are used to identify most influential variables in the system. The variables in the causal graph are classified into two groups; high ranking/high impact variables and low ranking/low impact variables. Thus, only a smaller subset of the complete variable list that have high impact are used for optimizing the performance objectives, reducing computational cost. The methodology for dimension reduction using node ranking is explained using a case study of manufacturing the key and bladder mechanism for superconducting magnets in Section 3.

3. Combined Conceptual Modelling and Dimension Reduction Methodology

European Center for Nuclear Research (CERN) has been developing prototype designs of superconducting magnets which have the field strength of 16 Tesla (twice as much field strength compared to the current working designs operated in the Large Hadron Collider). In the conceptual design phase, three designs are under consideration for prototype manufacturing; the cosine theta design, the block design, and the common coil design [14]. In these three designs, the magnet and its support structure differ in size, performance, manufacturing, and assembly process. When the superconducting magnet is energized, electromagnetic forces try to expand the coil. The coil itself is unable to support these forces in tension. Hence, to counter these force during operation, and to have good control during assembly, a bladder and key (made of stainless steel, SS) mechanism is proposed by researchers to produce cost effective magnets [15]. The design and manufacturing of the various components which constitute the magnet becomes challenging considering that it is a multi-criteria design optimization problem. Larger the number of design variables, design constraints, material selection requirements, manufacturing parameters, and functional requirements of finished product, the bigger the optimization problem becomes computationally.

In this research, the cosine theta design structure for the magnet is used for the case study. The methodology developed is shown as a three step approach in Figure 1 which include, modelling the system using DACM, dimension reduction approach to find most influential variables, and solving the optimization problem. The DACM framework is used to model the behavior of the magnet (expansion of magnet coil due to electromagnetic force or Lorentz's force) during energizing.

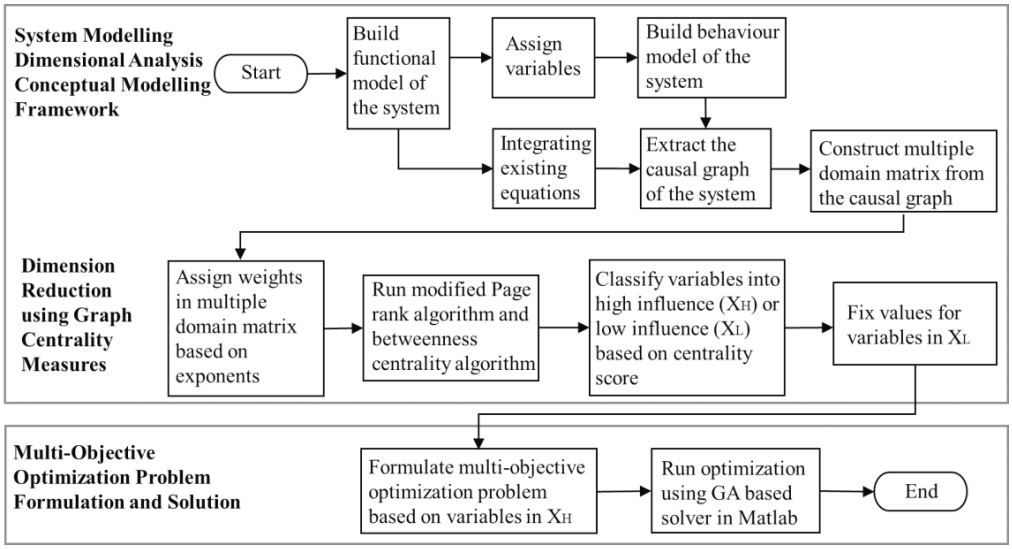

Figure 1: Combined conceptual modelling and dimension reduction methodology

The step-by-step conceptual modelling methodology using DACM is explained in earlier research [5]. The electromagnetic force is counterbalanced by the different support structures of the magnet to prevent magnet displacement. For simplification in this case study, it is assumed that the electromagnetic force is counterbalanced force by the pre-stress provided by the bladder and key mechanism. The functional model of the system is built from an abstract concept to a fidelity model based on elementary phenomena from the domain of classical electrodynamics and theory of failure as shown in Figure 2a. The resultant causal graph of the variables developed based on existing equations representing the different functions of the system is represented in Figure 2b. A simplified version of the cosine theta magnet design used in this case study is shown in Figure 2c. The causal graph maps the variables from the functional domain to the technical domain (used by designers to represent design parameters such as the geometry of the product and material), and from technical domain to process domain (used by manufactures to assign process parameters and compute cost of manufacturing). The nodes are color coded as green (independent variables), blue (intermediate variables), black/grey (exogenous variables), and red (target variables). The arcs that connects the nodes represent the interconnection between different variables as well the exponent of that connection from existing equations. A "+" is assigned on the node connection which denote the relationship, if increase in the n^{th} node increases the $(n+1)^{th}$ node and a "–" relationship if the increase in the n^{th} node decreases the $(n+1)^{th}$ node. Next, a multiple domain matrix is developed from the causal graph. The MDM is a sparse, square matrix representation of the system's structure that condenses knowledge of all the variables across the functional, design, and manufacturing process domains with their weights obtained from the causal graph (network). The MDM can be considered as a collection of design structure matrices (DSM) in each domain, mapping variables in the domain to itself, as well as variables from other domains to represent the entire structure of the system. The first column of the MDM consists of all the variables in the system. The MDM is a scalable matrix capable of handling very large structures, where each DSM can contain any finite number of variables. The matrix representation of the system facilitates application of ranking algorithms and graph centrality measures to find the most influential variables of the system.

A weighted PageRank algorithm and betweenness centrality scores are used to rank the nodes in the causal network based on the MDM. The PageRank algorithm computes a probabilistic rank vector that provides an importance estimate of all the nodes in the network based on the in-coming and out-going connections of the nodes in the causal graph. The PageRank algorithm is flexible and it can be modified to handle the weights in the causal network. A rank order for the nodes is obtained from the PageRank algorithm based on the measured centrality score. The betweenness centrality score is also computed for the MDM to validate the results obtained from PageRank algorithm.

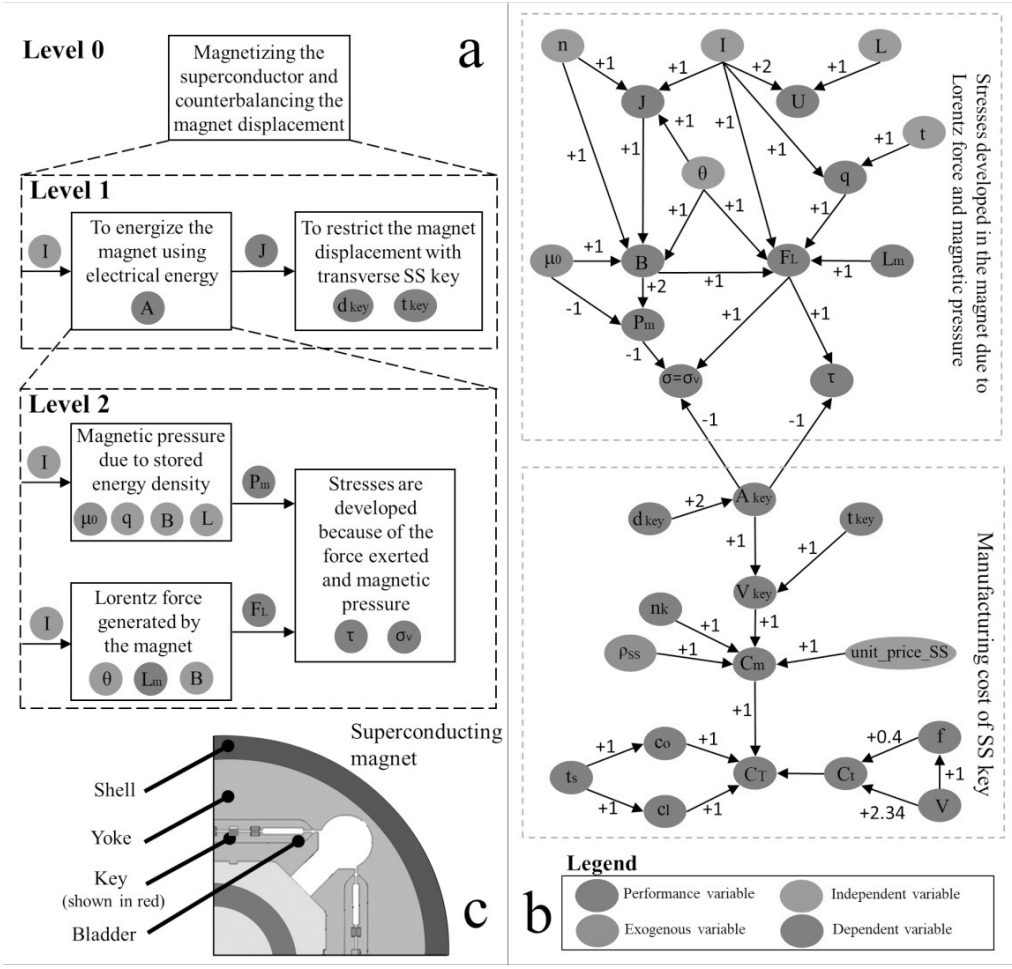

Figure 2: (a) Functional model describing expansion of magnet coil due to electromagnetic force; (b) Causal graph depicting magnet behaviour, and (c) Simplified cosine theta magnet design

Unlike PageRank, which is an Eigen vector centrality measure, the betweenness centrality is a measure of influence a node in a network has over the spread of information throughout the network [16]. The score measures the extent to which a node lies in the shortest path between the hub and the objective node. Higher the betweenness score implies the node is more central to the hub and objective nodes. Hence, betweenness score affirms the categorization of nodes as high importance and low importance nodes. The results of the PageRank algorithm and betweenness score are used to classify the variables into matrices X_H (high influence variables) and X_L (low influence variables). The results of weighted PageRank and betweenness scores of the variables are shown in Fig 3. A variable is considered to be of high importance if it has high score in both PageRank and betweenness centrality measures. The ranks are normalized based on the highest ranking node and a threshold of 0.3 is selected based on the distribution of ranks to categorize the variables. The high scoring variables are stored in X_H matrix and low scoring variables are stored in the X_L matrix. The X_L has low impact on the objective hence, the value of the variables are kept constant at its maximum or minimum depending on whether increase in the variable increases or reduces the performance objective (cost function). The variables in X_H matrix, i.e. $X_H = [B, F_L, \tau, \sigma_v, A_{key}, V_{key}, c_t, c_m, C_T]$, are considered for optimization of the total cost of manufacturing of the stainless steel key against the stress induced due to Lorentz force per magnet.

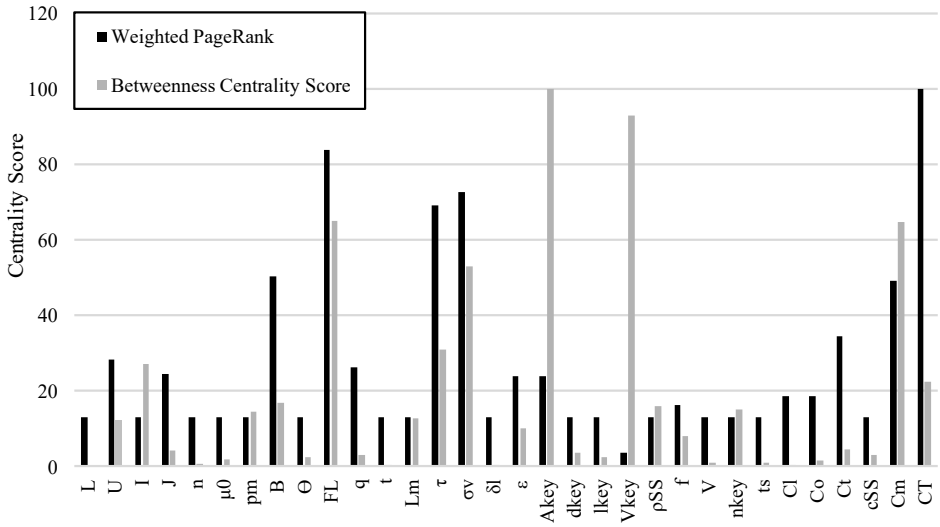

Figure 3: Centrality measure using PageRank algorithm and betweenness centrality score

The optimization problem is then formulated based on the mathematical function for cost of milling the key and the stress generated in the bladder and key mechanism due to the Lorentz force. The data used for optimization can be found in [14], [15]. The objective function for milling the key is as follows:

$$
\begin{aligned}
&f(X_H)\\
&\text{objective 1}\\
&\quad \min\ f(\sigma)\\
&\quad \text{where, } \sigma = \frac{4F_L}{\pi d_{key}^{\ 2}}\\
&\text{objective 2}\\
&\quad \min\ f(C_T)\\
&\quad \text{where } C_T = c_m + c_t\\
&C_T \approx \frac{1}{4}(\pi d_{key}^{\ 2}).l_{key}.\rho_{SS}.\text{unit\_price\_SS} + k\\
&\text{subjected to, } F_L \le 12000\\
&\qquad\qquad l_{key} \le 890\\
&\qquad\qquad d_{key} \le 1.5
\end{aligned}
$$

The variables are; $x_1=d_{key}$, $x_2=l_{key}$, the material is considered as stainless steel, SS304 and having standard values of density, unit price, and standard CNC milling parameters with carbide tools. The optimization is run with 'gamultiobj' (a genetic algorithm based solver in Matlab) solver to find manufacturing cost estimate against various levels of stress during energizing of the magnet using the high influence variables in X_H and for fixed values of low influence variables in X_L. From the optimization, the lowest cost obtained from crossover for machining all keys of a magnet was found to be €13.225,51 for a stress value of 191.083 MPa.

4. Conclusions and Future Work

Dimension reduction enables faster and cheaper optimization in the field of engineering design and manufacturing performance measurement. In this research, a dimension reduction methodology is proposed using the DACM

framework and graph centrality theory to estimate and optimize the manufacturing cost of new products in the conceptual design stage. The proposed method decomposes the optimization problem into two steps by categorizing variables into low importance variables whose values are prefixed during optimization step 1, and high importance variables, which are optimized using a solver (step 2). The methodology is demonstrated for optimizing the manufacturing cost of the bladder and key mechanism of a new high field superconducting magnet used by CERN. The two step optimization process reduces the effective number of variables that need to be optimized to get minimum manufacturing cost. The reduced variable list reduces the computation time during optimization and hence enables cheaper and faster optimization. Future research focusses on expanding the case study to include other components of 16 Tesla magnet and validation using real data from CERN's prototype magnet manufacturing.

References

[1] S. Robinson, "Conceptual modeling for simulation: issues and research requirements," presented at the Proceedings of the 2006 winter simulation conference, 2006, pp. 792–800.

[2] H. Mokhtarian *et al.*, "A Network Based Modelling Approach Using the Dimensional Analysis Conceptual Modeling (DACM) Framework for Additive Manufacturing Technologies," in *Proceedings of the ASME 2016 International Design Engineering Technical Conferences and Computers and Information in Engineering Conference*, Charlotte, NC, 2016, p. V01AT02A046 (9 p.).

[3] H. P. N. Nagarajan *et al.*, "Knowledge-Based Design of Artificial Neural Network Topology for Additive Manufacturing Process Modeling: A New Approach and Case Study for Fused Deposition Modeling," *Journal of Mechanical Design*, vol. 141, no. 2, pp. 021705-021705–12, Dec. 2018.

[4] D. Wu, E. Coatanea, and G. G. Wang, "Employing Knowledge on Causal Relationship to Assist Multidisciplinary Design Optimization," *Journal of Mechanical Design*, vol. 141, no. 4, p. 041402, 2019.

[5] E. Coatanéa, R. Roca, H. Mokhtarian, F. Mokammel, and K. Ikkala, "A Conceptual Modeling and Simulation Framework for System Design," *Computing in Science Engineering*, vol. 18, no. 4, pp. 42–52, Jul. 2016.

[6] E. Coatanéa, S. Nonsiri, T. Ritola, I. Y. Tumer, and D. C. Jensen, "A Framework for Building Dimensionless Behavioral Models to Aid in Function-Based Failure Propagation Analysis," *Journal of Mechanical Design*, vol. 133, no. 12, p. 121001, 2011.

[7] M. Maurer and U. Lindemann, "The application of the Multiple-Domain Matrix: Considering multiple domains and dependency types in complex product design," presented at the 2008 IEEE International Conference on Systems, Man and Cybernetics, 2008, pp. 2487–2493.

[8] S. Shan and G. G. Wang, "Survey of modeling and optimization strategies to solve high-dimensional design problems with computationally-expensive black-box functions," *Structural and Multidisciplinary Optimization*, vol. 41, no. 2, pp. 219–241, Mar. 2010.

[9] L. C. Freeman, "Centrality in social networks conceptual clarification," *Social Networks*, vol. 1, no. 3, pp. 215–239, Jan. 1978.

[10] S. P. Borgatti and M. G. Everett, "A Graph-theoretic perspective on centrality," *Social Networks*, vol. 28, no. 4, pp. 466–484, Oct. 2006.

[11] S. Brin and L. Page, "The anatomy of a large-scale hypertextual Web search engine," *Computer Networks and ISDN Systems*, vol. 30, no. 1–7, pp. 107–117, Apr. 1998.

[12] F. Mokammel, E. Coatanéa, M. Bakhouya, F. Christophe, and S. Nonsiri, "Impact analysis of graph-based requirements models using PageRank algorithm," presented at the 2013 IEEE International Systems Conference (SysCon), 2013, pp. 731–736.

[13] K. Henni, N. Mezghani, and C. Gouin-Vallerand, "Unsupervised graph-based feature selection via subspace and page rank centrality," *Expert Systems with Applications*, vol. 114, pp. 46–53, 2018.

[14] M. Sorbi *et al.*, "The EuroCirCol 16T Cosine–Theta Dipole Option for the FCC," *IEEE Transactions on Applied Superconductivity*, vol. 27, no. 4, pp. 1–5, Jun. 2017.

[15] S. Caspi *et al.*, "The use of pressurized bladders for stress control of superconducting magnets," *IEEE Transactions on Applied Superconductivity*, vol. 11, no. 1, pp. 2272–2275, Mar. 2001.

[16] M. E. J. Newman, "A measure of betweenness centrality based on random walks," *Social Networks*, vol. 27, no. 1, pp. 39–54, Jan. 2005.

PUBLICATION VII

Optimization driven design to explore and exploit the process-structure-property-performance linkages in digital manufacturing

Inigo Flores Ituarte, Suraj Panicker, Hari P.N. Nagarajan, Eric Coatanéa, and David W. Rosen

Unpublished Manuscript